Geopolymer, Next Generation Sustainable Cementitious Material − Synthesis, Characterization and Modeling

by

Mo Zhang

A Dissertation

Submitted to the Faculty

of the

WORCESTER POLYTECHNIC INSTITUTE

in partial fulfillment of the requirements

for the Degree of

Doctor of Philosophy

in

Civil and Environmental Engineering

May 2015

APPROVED:

Prof. Mingjiang Tao, Major Advisor

Prof. Aaron N. Deskins, Co-Advisor

Prof. Tahar El-Korchi

Prof. Rajib Basu Mallick

Prof. Jianyu Liang

ABSTRACT

Geopolymers have received increasing attention as a promising sustainable alternative to ordinary Portland cement (OPC). However, the relationship among the synthesis, geopolymerization process, microstructures, molecular strucutres and mechanical properties of geopolymers remains poorly understood. To fill this knowledge gap, this dissertation focuses on the correlation of chemical composition-reaction kinetics-microstructure-mechanical properties of geopolymers. This study also sheds light on the durability, environmental impact and engineering applications of geopolymers from practical perspectives.

The first part of this dissertation presents a comprehensive study on red mud-class F fly ash based geopolymers (RFFG). Firstly, RFFG with a high 28-day mechanical strength were successfully synthesized under the ambient condition of 23 ℃ and 40 to 50% relative humidity. A nominal Na/Al molar ratio of 0.6 ~ 0.8 with a Si/Al ratio of 2 was found to be a good starting chemical composition for RFFG synthesis. Secondly, the reaction kinetics and its relation to the mechanical properties of RFFG were investigated by monitoring the development of geopolymer gels, reaction rate, porosity and mechanical properties of RFFG samples cured at room temperature, 50 ℃ and 80 ℃ for up to 120 days. The asymmetric stretching FTIR band of Si-O-T (T is Si or Al) centered around 960-1000 cm^{-1}, which is the characteristic band of geopolymer gels, was observed to shift to a lower wavenumber at the early stage of the synthesis and shift to a higher wavenumber later on during the synthesis. The shift of Si-O-T band indicates that the geopolymerization took

place in three stages: dissolution to Al-rich gels at Stage I, Al-rich gels to Si-rich gels at Stage II and Si-rich gels to tectosilicate networks at Stage III. The mechanical strength of RFFG barely increased, increased slowly by a limited amount and developed significantly at these three stages, respectively. An elevated curing temperature enhanced the early strength of RFFG, whereas an excessively high curing temperature resulted in a higher pore volume that offset the early-developed strength. Lastly, the remaining mechanical properties of the RFFG samples after soaking in a pH = 3.0 sulfuric acid solution for up to 120 days and the concentration of heavy metals leached from RFFG samples after the soaking were measured. The RFFG samples' resistance against sulfuric acid was found to be comparable to that of OPC, and leaching concentrations of heavy metals were much lower than the respective EPA limits for soil contaminations. The degradation in mechanical properties of the RFFG samples during soaking in the acid was attributed primarily to the depolymerization and dealumination of geopolymer gels.

The second part of this dissertation is devoted to the investigation of nano-scale mechanical properties and molecular structures of geopolymer gels with grid-nanoindentation and molecular modeling. Four phases (e.g., porous phase, partially developed geopolymer gels, geopolymer gels and unreacted metakaolin or crystals) and their nano-mechanical properties were identified in metakaolin based geopolymers (MKG) with grid-nanoindentation technique. It was found that the proportion of geopolymer gels largely determines the mechanical strength of the resulting geopolymers while other factors (e.g., pores and cracks) also play some roles in macro-scale mechanical strength of geopolymers. The final setting time of the geopolymers increased with the increase in Si/Al ratio and the decrease in Na/Al ratio, while the proportion of geopolymer gels and macro-

mechanical strength of geopolymers increased with the increase in both Si/Al and Na/Al molar ratios, within the range of 1.2~1.7 and 0.6~1.0, respectively. In the molecular modeling, a combined density function theory (DFT)-molecular dynamic (MD) modeling simulation was developed to "synthesize" geopolymers. DFT simulation was used to optimize reactive aluminate and silicate monomers, which were subsequently used in reactive MD simulations to model the polymerization process and computationally synthesize geopolymer gels. The influence of Si/Al ratio and simulation temperatures on geopolymerization and resulting molecules of geopolymer gels was also examined. The computationally polymerized molecular structures of geopolymer gels were obtained. The distribution of Si_4(mAl) and radial distribution fuctions of Si-O, Al-O, O-O and Na-Al for the models were compared and qualitatively agreed well with the experimental results from nuclear magnetic resonance (NMR) and neutron/X-ray pair distribution function in previous literature. Three polymerization stages: oligomerization, ring formation and condensation, were identified based on the nature of polymerization process, which were found to be affected by the temperature and Si/Al ratio. A higher temperature enhanced the reaction rate while a lower Si/Al ratio resulted in more compact geopolymer networks.

The final part of this dissertation presents an experimental feasibility study of using geopolymer in shallow soil stabilization, in which a lean clay was stabilized with MKG at different concentrations. The study confirmed that MKG can be used as a soil stabilizer for clayey soils and the unconfined compressive strength, Young's modulus and failure strain are comparable to or even better than OPC when the MKG's concentration is higher than 11%. The binding effect of geopolymer gels on the soil particles was confirmed as the main mechanism for the improvement in mechanical properties of the stabilized soils with the

scanning electron microscopy imaging, energy dispersive X-ray spectroscopy analyses and X-ray diffractometry characterization.

ACKNOWLEDGEMENT

This Ph.D dissertation would not have been accomplished without the support from my family, friends, advisors, colleagues and collaborators.

Many thanks to my advisor Prof. Mingjiang Tao for his continuous support throughout my Ph.D journey. Prof. Tao gives me patient advising regarding my Ph.D study and provides me a friendly working environment and many opportunities to collaborate with the experts in different research fields. Without the encouragement and unconditional help from Prof. Tao, I could not have developed this multidisciplinary study or achieved so much. Thanks to my co-advisor Prof. Aaron Deskins for providing me guiding light in density functional theory and helping me in molecular dynamic simulations. Thanks to Prof. Guoping Zhang in UMassAmherst for his help and collaboration on my research.

Thanks to the lab managers Donald Pellegrino and Russ Lang for their help and creative designs for the experiments of geopolymers. I also would like to thank Dr. Boquan Li in Department of Mechanical Engineering, Douglas White in Department of Chemical Engineering, Andrew Butler in Instrument Core and Prof. Samuel Politz in Department of Biology & Biotechnology for their training and help in the analytical techniques. I benefitted from the aid of a number of undergraduate students: Peter Nowak, Adam Coen, Derrick Mann and Kevon Lumsden; as well as from my colleagues: Mengxuan Zhao, Xiongkong Yu and Hong Guo.

I also would like to thank the U.S. National Science Foundation for funding this research on geopolymers (Grant No. CMMI-1301048).

Acknowledgement

Especially, thanks to my parents who continuously support and put up with me during those tough time in the six years. Their encouragement is the most solid foundation for my study and life.

TABLE OF CONTENTS

Table of Contents

LIST OF FIGURES

List of Figures

LIST OF TABLES

CHAPTER 1 - INTRODUCTION

Concrete is arguably the most widely used construction material in the world. As the primary constitute of concrete, the annual production of Portland cement was 2.6 billion tons in 2006 [1]. The production increased by 54% from 2000 to 2006 [2], and is expected to increase at an annual rate of 0.8-1.2% due to the increasing consumption and growth in population and growing demand for civil infrastructure [3, 4]. However, the production of cement has raised serious concerns over energy consumption, greenhouse gas emissions and the depletion of raw materials. The production process of ordinary Portland cement (OPC), involving quarrying raw materials, transporting and crushing raw materials, clinker calcination at 1400~1450 ℃, and finish grinding, consumes about 3.2GJ energy per ton. In addition, the cement production contributes 5~7% to global CO_2 emission [5-8]. The stock of the raw material, limestone, for cement production becomes more limited. For example, *Cement Production in Vertical Shaft Kilns in China – Status and Opportunities for Improvement* published in 2006 reported the current known limestone deposits in China, the largest cement manufacture country, are only enough for cement manufacturing for another 59 years.

Therefore, the construction materials industry is always seeking sustainable materials to replace OPC in order to enhance sustainability of civil infrastructure by reducing CO_2 emissions and conserving energy. Geopolymer, as a family of inorganic aluminosilicate binders, provides a promising alternative to OPC because the following reasons: i. geopolymers have high mechanical strength and excellent durability; ii. the synthesis process for geopolymer consumes much less energy, especially for those made from

industrial wastes; iii. using geopolymer to replace OPC reduces the CO_2 emissions by 25~40%, and up to 80% [8-11]; and iv. abundant raw materials exist for the production of geopolymers from both natural minerals and industrial wastes.

However, it is difficult to optimize geopolymer synthesis with desired mechanical properties and performance largely due to poor understanding of the fundamental relationship among chemical composition of raw materials, microstructure, molecular structures, reaction kinetics, and mechanical properties of geopolymers.

1.1. LITERATURE REVIEW

1.1.1. Background of Geopolymers

Geopolymers are synthesized by alkali activation of aluminum- and silicon-rich solids [12]. During geopolymerization, silicate and aluminate tetrahedrons are polymerized by sharing all the oxygen atoms to form X-Ray amorphous or semi-crystalline molecular structures. Davidovits suggested to use polysialate as the chemical designation for these structures, which has three basic units as schematically illustrated in **Figure 1-1**: poly-sialate (PS), poly-sialate-siloxo (PSS), and poly-sialate-disiloxo (PSDS) [13].

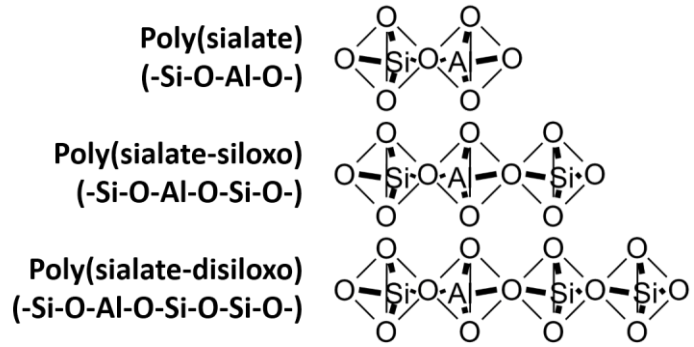

Figure 1-1. Three basic unit structures of polysialate as the chemical designation for geopolymer (redrawn from [13]).

A simplified chemical formula to represent geopolymer is $M_n\{-(SiO_2)_z - AlO_2\}_n$, where M is an alkali cation that balances the negative charge of Al^{3+} in tetrahedral coordinations, such as Na^+ or K^+; n is the degree of polymerization; and z is the Si/Al molar ratio in this geopolymeric structure, which is in the range of 1 to 3, with the upper limit of 300 [13]. The properties of geopolymers vary widely with Si/Al ratio: three dimensional and cross-linked networks are formed during geopolymerization process result in stiff and brittle properties when Si/Al ratio is lower than 3; while two dimensional and linearly-linked networks are formed in geopolymer systems and the resulting materials exhibit adhesive and rubbery properties when Si/Al ratio is higher than 3. The former geopolymers are similar to cementitious and ceramic materials in terms of mechanical properties and are of interest in the current study. The synthesis process of geopolymer is often approximated by the following two reaction formulas [13].

$$n(Si_2O_5, Al_2O_2) + 2nSiO_2 + 4nH_2O \xrightarrow{NaOH,KOH} n(OH)_3 - Si - O - Al(OH)_2{}^{(-)} - O - Si - (OH)_3 \quad (1.1)$$

$$n(OH)_3 - Si - O - Al(OH)_2{}^{(-)} - O - Si - (OH)_3 \xrightarrow{NaOH,KOH} (Na,K)^{(+)} - \left(\begin{array}{ccc} | & | & | \\ Si - O - & Al^{(-)} - O - & Si - O - \\ | & | & | \\ O & O & O \\ | & | & | \end{array} \right) + 4nH_2O \quad (1.2)$$

The raw materials (e.g., $(Si_2O_5, Al_2O_2)$and SiO_2) are firstly dissolved by alkali hydroxide solutions, such as NaOH and KOH, to release reactive aluminate and silicate oligomers, represented by $(OH)_3 - Si - O - Al(OH)_2{}^{(-)} - O - Si - (OH)_3$ in equation (1.1), which are polymerized to cross-linked networks in alkaline environments, as described in equation (1.2).

Geopolymers synthesized with different mix designs exhibit extraordinary properties as below:

- high mechanical strength [14, 15], high early mechanical strength gain [16, 17], high adhesive strength [18] and high surface hardness [19],
- high temperature- and fire-resistance [20-22],
- high resistance to chemical reagent and inorganic and organic acids [23-27],
- fast or slow setting depending on specific application requirement [28],
- low concentrations of leachable heavy or toxic metals [29, 30], and
- low porosity and micro- or nano-scaled pore size [31, 32].

Obviously, one single type of geopolymer cannot possess all of the above properties, but specific property or multi-properties can be achieved by tailoring geopolymer mix design and appropriate curing conditions. Because of the excellent properties mentioned above, geopolymers have received increasing attention for applications in geopolymer concretes [17, 33], sewer pipes [34], coastal infrastructures in marine environments [27], fire protection and acid resistance coating [20-22], toxic/radioactive waste immobilizations [30], military operations [35], railway sleepers [36], aircraft manufacture [37], and soil stabilization [38, 39]. Research studies were also conducted to explore the feasibility of using geopolymers as a synthetically biocompatible bone replacement material [40, 41], smart adhesive binders for healthy monitoring sensors [42] and foam concrete as lightweight thermal isolation construction materials [43] or low cost alternatives for porous ceramics [44].

There are abundant raw materials for geopolymer synthesis, most of which are industrial wastes, including blast furnace slag [45, 46], coal fired fly ash [33, 47-50] and metakaolin [51-55]. A number of other industrial wastes have also been used to synthesize

geopolymers, including red mud [56, 57], rice husk ash [56], palm oil fuel fly ash [58, 59], mine tailing [60], biomass fly ash [61], silica fume [62], clay sediment [63], electrolytic manganese residue [64], waste paper sludge ash [65], silica-rich tailing from vanadium extraction [66], volcanic ash [67], natural pozzolan [68], metahalloysite [69] and Pisha sandstone [70].

Solid raw materials are the main source of silicate and aluminate tetrahedrons, which are the reactive compounds participating in geopolymerization. Therefore, the physicochemical properties of raw materials, which govern the solubility and reactivity of the materials in alkali solutions, play an important role in the microstructure and mechanical properties of the resulting geopolymers. Besides the reactive constituents, the nonreactive fractions of the raw materials also affect mechanical properties of the geopolymers by their contents, gradation, and binding strength to geopolymer gels [71]. In this Ph.D. study, three types of solid raw materials: metakaolin, red mud and class F fly ash, were used to synthesize geopolymers. More details about these three materials are discussed in the following sections.

1.1.1.1. Red Mud

Red mud (RM), also known as bauxite residue, is the by-product of aluminum extraction from bauxite ores using the Bayer process [88]. During the Bayer process, a large amount of sodium hydroxide solution is used, which results in a high alkalinity and a high water content in bauxite residue (RM). The high alkalinity and slurry nature of RM make it difficult to dispose of this industrial waste. Before 1980s, marine disposal was the main approach to treat RM. However, due to the adverse environmental impact on oceans,

marine disposal was prohibited since 1980s when land-based disposal became the main storage approach for RM. However, land-based disposal also has a lot of issues, including high demand for areas and high cost for dewatering of red mud slurry, monitoring and maintenance of disposal ponds. RM is produced approximately 1.5 times the amount of produced aluminum. Due to an enormous demand of aluminum in various industrial fields, the global production of RM is tremendous [72]. About 2.6 billion tons of RM was accumulated globally in 2007, with an annual production of 2.7 million tons. By 2015, the global cumulated RM is estimated to reach 3 billion tons with an increasing annual production rate [73]. Therefore, how to reuse and recycle RM instead of disposal has become a crucial problem facing aluminum refineries.

Based on the data collected from global refineries, the pH value of untreated RM ranges from 9.2 to 12.8 with an average value of 11.3 $\pm$ 1.0. Alkaline anions present in red mud slurry include OH^-, CO_3^{2-}/HCO_3^-, $Al(OH)^{4-}/Al(OH)_3(aq)$ and $H2SiO_4^{2-}/H3SiO^{4-}$. Main chemical components in RM include Fe_2O_3, Al_2O_3, SiO_2, TiO_2, CaO and Na_2O with trace amount of other metal oxides, depending on the source of bauxite ores, of which 70% is in crystalline form and 30% is amorphous phase approximately [74].

Geopolymer synthesis requires alkaline solutions as the activator to dissolve raw materials and provide a basic environment for the polymerization of reactive silicate and aluminate oligomers. Given its high pH value and Al- and Si-rich nature, RM is an excellent solid material and alkali source for geopolymer synthesis, which can partially replace alkaline metal hydroxide solutions, the most expensive component in geopolymer manufacturing. As concrete is the most used construction material and geopolymer is a

promising cementitious binder, geopolymerization technology provides an excellent potential to reuse and recycle RM. Meanwhile, the large amount of inventory and annual production make RM a cheap and great raw material stock for geopolymer synthesis [74].

RM has recently been used in geopolymer synthesis by mixing with fly ash [75], rice husk ash [56], metakaolin [76] and granulated blast furnace slag [77]. The mechanical properties of the resulting geopolymers are comparable to those of OPC. Hajjaji et al. found that the addition of RM even had beneficial effect on the mechanical strength of metakaolin based geopolymer [76]. However, how to make the best use of RM in geopolymerization needs to be systematically studied.

1.1.1.2. Class F Fly Ash

Fly ash is one of the major by-products in powder with a spherical shape and a high amorphous content from coal fired power plants. The main chemical components in fly ash are SiO_2, Al_2O_3, Fe_2O_3, CaO, MgO, SO_3, Na_2O, K_2O and carbon residue. The chemical composition of each fly ash source is largely influenced by the coal source. There are generally four types of coals, including anthracite, bituminous, sub-bituminous and lignite. Fly ashes generated from bituminous coals or anthracites usually contain more than 70% $SiO_2+Al_2O_3+Fe_2O_3$ and 1-12% of CaO; while in those produced from lignites or sub-bituminous coals, the content of $SiO_2+Al_2O_3+ Fe_2O_3$ usually ranges between 50% and 70%, and the content of CaO is more than 20% [78]. According to the classification in ASTM C618, fly ashes are defined as Class C (CaO>20%) and Class F fly ash (CaO<20%), respectively [79]. The annual production of fly ash is 900 million tons [80]. Therefore, the disposal and storage of fly ash as industrial wastes became a serious environmental

problem and technical challenge. Nowadays, 20% to 30% of the fly ashes has been reused [81], a large proportion of which has been used in civil engineering applications due to the massive consumption of construction materials. Fly ashes, especially Class C fly ash which has relatively high concentration of CaO that can be hydrated to form calcium silicate hydrate (CSH), have been widely used to partially replace cement in concrete [78] and to mix with lime or cement in soil stabilizations [82].

Given its fine spherical shape and high content of amorphous silicates and aluminates, fly ash is an ideal raw material to synthesize geopolymers. The fly ash particles consist of solid spheres, hollow spheres (cenospheres) and those housing smaller spheres inside (plerosphere) [83]. Alkali solutions start to attack the shell of the ashes once they are in contact with fly ash spheres to dissolve reactive silicate and aluminate tetrahedrons [84]. During the course of the reaction, the alkali solutions penetrate inside the cenosphere and plerosphere and continuously dissolve the reactive fractions of fly ashes. At this stage, the interior space of the plerospheres are filled with smaller fly ash balls and activators, while the alkali solutions are attacking the ash particles from both inside and outside of the spheres. As the dissolved aluminate and silicate monomers accumulate, polymerization starts and geopolymer gels are formed. Therefore, the reaction rate usually increases with the decreasing fineness of fly ash particle size, which shortens the setting time and enhances the mechanical strength of the resulting geopolymers [85].

Palomo et al. observed that the amorphous fractions of fly ashes started to dissolve almost immediately when they were in contact with alkali hydroxide or/and silicate solutions using isothermal calorimetry [86]. Regardless of the concentration of the

activator solution, it took around 5 to 10 minutes to fully dissolve fly ashes with sodium hydroxide [86], and the dissolution was slightly slowed down with the addition of sodium/potassium silicates in the activator. Furthermore, Winnefeld et al. found that class F fly ash was more alkali reactive and more suitable for geopolymer synthesis because its amorphous content is higher than that of class C fly ash [87]. Class F fly ash based geopolymers with good mechanical properties have been obtained in various literature studies [47, 88-90]. In most of these studies, the geopolymers were cured at elevated temperatures since the reactivity of class F fly ash at ambient temperature is relatively low [91]. However, ambient temperature is more favorable for in situ concrete productions, and thus the reaction rate of class F fly ash and the synthesis of class F fly ash-based geopolymers under ambient conditions need to be further investigated.

1.1.1.3. Metakaolin

Metakaolin is a type of anhydrous aluminosilicate materials generated by calcination of kaolin at 500 to 800 ℃ [92-94]. Kaolinite, the main constituent of kaolin, with a chemical formula of $Al_2Si_2O_5(OH)_5$, is dehydroxylated at a temperature above 550 ℃. As a result, long-range ordered microstructures of kaolinite are broken down to form amorphous metakaolin. Metakaolin is structured by alternatively stacking silicate and aluminate layers, with additional lattice strain in aluminate layers, and thus the reactive aluminates are dissolved even faster than silicates [95]. The amorphous nature of metakaolin results in its high reactivity in alkaline solutions [96] and makes it an excellent raw material for geopolymer synthesis [97]. Panagiotopoulou et al. found that the dissolution potential of metakaolin in sodium and potassium hydroxides was the highest among most of

aluminosilicate raw materials, where 70% and 45% of metakaolin solids can be dissolved in NaOH and KOH (10M), respectively.

As two of the main solid materials used in this study, the suitability of fly ash and metakaolin for synthesizing geopolymers is reviewed. Firstly of all, compared to the other raw materials, such as blast furnace slag and class C fly ash, both metakaolin and class F fly ash have a very low CaO content, so using these two materials to synthesis geopolymer can largely exclude the contributions by CSH to the development of mechanical properties and microstructures.

For producing geopolymer-based concrete, class F fly ash is more advantageous because (i) the geopolymer synthesized with fly ash requires less water compared to the other raw materials, such as metakaolin and slag, due to its spherical shape, and results in a lower porosity and permeability, hence the reduced corrosion risk of the concrete [98]; (ii) the shrinking potential of fly ash based geopolymer is effectively decreased by the unreacted fly ash spheres which have a relatively larger particle size and a higher crystalline content, and act as micro-aggregates in the resulting geopolymers [99], and (iii) the lower price and a large stock make class F fly ash more favorable for producing geopolymer concrete that is in great demand. On the other hand, due to the laminar structure of metakaolin, the water requirement for metakaolin-based geopolymer is very high, leading to poor workability of the resulting geopolymer concrete. Metakaolin based geopolymer was found to be more sensitive to drying shrinkage [100, 101] compared to fly ash based counterparts. In addition, the price of metakaolin is much higher than the industrial wastes, such as fly ash and furnace slag. Therefore, metakaolin is less suitable for manufacturing

geopolymer concrete, especially at massive scale. However, metakaolin is more suitable for exploratory studies of geopolymer gels on microstructural properties due to its high reactivity in alkaline solutions, high proportions of resulting geopolymer gels, and less impurities left in the synthesized geopolymers. The higher reactivity of metakaolin firstly stems from its platy shape with a large surface area, compared to fly ash which has a spherical shape [102]. The surface area of metakaolin is in the range of 9-20m^2/g measured with N_2 sorption tests, while fly ash has a surface area between 0.6 to 4.2 m^2/g [43]. Secondly, the amorphous content and purity of metakaolin are higher than fly ash that contains a larger amount of crystals, such as quartz and mullite.

1.1.2. Mechanical Properties of Geopolymers

Mechanical properties are the most important indicators for geopolymers as cementitious binders for construction materials. Unconfined compressive strength (UCS) of cylindrical or cubic samples for geopolymers, geopolymer mortars and geopolymer concretes was determined in most of literature studies concerning mechanical properties of geopolymers. **Table 1-1** summarizes the UCSs of geopolymer samples synthesized from metakaolin and fly ash from previous literature studies [103-106]. In other literature studies on mechanical properties of geopolymers that are not included in **Table 1-1**, Na_2O/SiO_2 ratio and H_2O/Al_2O_3 ratio were also used to control the geopolymer synthesis. Criado et al. synthesized fly ash based geopolymers at a Na_2O/SiO_2 ratio of 1/0.69 at 85℃ for 7 days and 180 days and obtained UCS values of 55 MPa and 95 Mpa [107]; de Vargas et al. synthesized fly ash based geopolymers with a Na_2O/SiO_2 ratio of 0.4 at 80℃ for 7 days and 180 days and obtained UCS values of 5.3 MPa and 21.3 Mpa; and Fletcher et al. used

natural aluminosilicate materials to synthesize geopolymers at 90 ℃ for overnight with a UCS value of 10.9 Mpa [108]. It can be seen that the UCS value of geopolymers varies in a range of several MPa to more than 100 Mpa, depending on the chemical composition, curing temperature, curing time and raw material sources. In addition, UCS of geopolymers is also affected by water content, curing temperatures, alkali activators and curing humidity. These synthesis factors and their influence on the mechanical properties and geopolymerization process were reviewed in the following sections.

Table 1-1. UCS values of metakaolin- and fly ash-based geopolymers from previous literature [103-106].

Raw materials	Curing temperature (Time)	Na/Al Molar Ratio	Si/Al Molar Ratio	Compressive strength, MPa	Reference
Metakaolin	75°C (24 hours) and then ambient condition (7 days)	0.51	1.08	0.4	[103]
		0.72	1.08	2.2	
		0.72	1.50	6.2	
		1.00	1.08	4.4	
		1.00	1.50	23.4	
		1.00	2.00	51.3	
		1.29	2.00	53.1	
		1.29	2.50	64.0	
		1.53	1.50	19.8	
		1.53	2.50	49.0	
		1.53	3.00	2.6	
		2.00	2.00	11.8	
		2.00	3.00	19.9	
Metakaolin	70°C (24 hours)	1.00	1.92	67.0	[104]
		1.26	2.5	33.0	
		1.53	3.08	3.1	
		1.07	1.55	14.0	
Fly ash	85°C (2 hours)	1.00	1.50	11.0	[105]
		0.60	1.50	2.8	
		0.80	1.50	3.1	
		1.20	1.50	7.1	
		1.00	1.35	3.9	
		1.00	1.75	29.0	
		1.00	1.95	47.0	
		2.14	1.43	13.0	
		1.67	1.11	20.0	
		1.36	0.91	6.3	
Fly ash	95°C (6 hours)	2.00	1.00	102.1	[106]
		1.75	1.00	88.9	
		2.00	0.50	64.1	
		1.75	0.50	50.4	

1.1.3. Microstructure of Geopolymers

Because of their amorphous nature, geopolymer gels do not have a long-rang ordered atomic structure, and their X-ray diffraction pattern is usually a broad hump instead of

distinctive peaks. The hump spanning in 20 °-32 ° 2θ of XRD spectra is usually considered characteristic patterns of geopolymer gels [13, 109-112]. As shown in **Figure 1-2**, the XRD patterns of fly ash based and metakaolin based geopolymer are compared with those of the raw materials they were derived from. In all the geopolymer samples, the characteristic XRD humps of geopolymer gels are observed, although the position and intensity of the humps exhibit dependency on the raw materials and alkali activators. Comparing the XRD patterns of fly ash (**Figure 1-2** (a)) and metakaolin (**Figure 1-2** (b)), it can be observed that the hump between 16 °-27 ° 2θ (representing amorphous content) is weaker in fly ash than metakaolin, but the intensity of the crystalline peaks in fly ash are higher than those in metakaolin. This illustrates that the alkali reactivity of fly ash is lower than metakaolin, and thus more geopolymer gels would be formed from metakaolin than fly ash. Consistently, the hump of geopolymer gels in metakaolin based geopolymers is more intense than that in fly ash based geopolymers. The crystals in the raw materials still remained in the resulting geopolymers, including quartz, mullite, kaolinite and anatase, implying that the experimentally synthesized geopolymers are actually composite materials, which can be better demonstrated with scanning eletron microscopy (SEM)-energy dispersive X-ray spectroscopy (EDX) measurements.

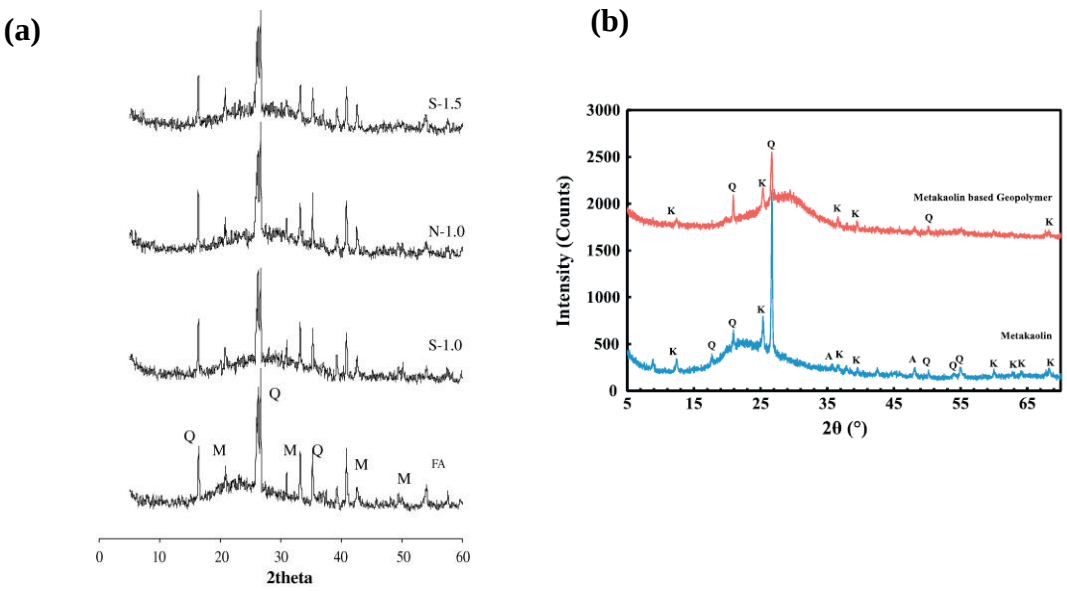

Figure 1-2. XRD patterns of (a) fly ash based geopolymers activated with different alkali activators [110] (S-1.5: 1.5 molar sodium silicate solution, N-1.0: 1.0 molar sodium hydroxide solution and S-1.0: 1.0 molar sodium silicate solution), (b) metakaolin based geopolymers [109] (Q: Quartz, M: Mullite, K: Kaolinite, and A: Anatase).

The backscattered SEM images of fly ash- and metakaolin-based geopolymers from two previous literature studies are shown in **Figure 1-3** (a) [113] and (b) [55], respectively, in which the phases can be clearly distinguished. In the fly ash based geopolymer (**Figure 1-3** (a)), unreactive components, including unburned carbon and Fe-oxide, unreacted fly ash spheres in different sizes (s: small, m: medium and l: large) are bound with geopolymer gels (arrows). In the metakaolin based geopolymer (**Figure 1-3** (b)), unreacted metakaolin and unreactive crystals, including quartz and anatase, are embedded in the geopolymer gels which account for a much larger proportion compared to those in the fly ash based geopolymer. Pores and micro-cracks are clearly observed in **Figure 1-3** (c) and (d) that are

the SEM images of fly ash- and metakaolin-based geopolymers taken with the secondary electron mode, respectively. The micromorphology of metakaolin based geopolymers (**Figure 1-3** (d)) [31] is more homogeneous than that of fly ash based geopolymers (**Figure 1-3** (c)) [114], which is in good agreement with the comparison between **Figure 1-3** (a) and (b) that more geopolymer gels were derived from metakaolin. Regardless of the raw materials, the experimentally synthesized geopolymer samples are composed of geopolymer gels, unreactive impurities, unreacted raw material residues, zeolite crystals (if formed), pores and microcracks.

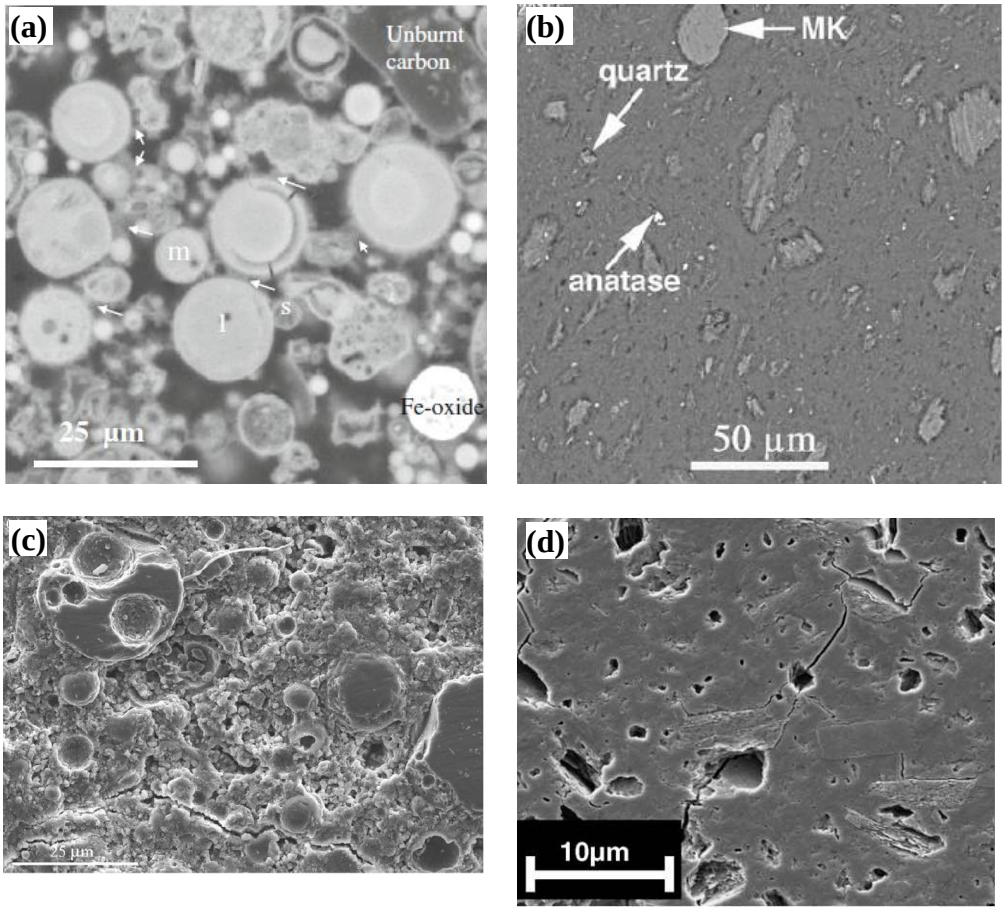

Figure 1-3. SEM images of (a) fly ash based geopolymers, (b) metakaolin based geopolymers in the back-scattered mode, (c) fly ash based geopolymers, and (b) metakaolin based geopolymers in the secondary electron mode [31, 55, 113, 114].

EDX has been used with SEM to estimate the chemical composition of different phases in geopolymers and qualitatively assess the formation of geopolymer gels. The continuous and gel-like structures in the SEM images of geopolymer samples are confirmed as geopolymer gels [71] with EDX, which usually has an estimated Si/Al ratio between 1.0 and 3.0 [90, 103, 115]. However, the EDX-estimated Na/Al is slightly less than 1.0 [103, 115], but can be much less or higher than 1.0 (0.2~4.5) depending on the chemical composition of the starting materials [90, 115], where the theoretical Na/Al molar ratio of geopolymer gels is 1.0 and Si/Al ratio ranges from 1.0 to 3.0 [31, 53, 55].

The chemical bonds related to Si, Al, O, H and alkali cations, as important structural parameters of geopolymers, have been investigated with Fourier transform infrared spectroscopy (FTIR) to assist the understanding of the formation and microstructure of geopolymer gels. FTIR is a nondestructive approach to characterize the microstructure of the materials by measuring infrared spectrum of absorption of a solid, gas or liquid in the range of 4000−400 cm^{-1} [116]. The chemical bonds in geopolymers that can be characterized with FTIR are summarized in **Table 1-2**. Most of the bonds appear in the FITR patterns in terms of broad bands or shoulder, instead of sharp peaks, confirmed the disordered microstructure of geopolymer gels. The most distinct FTIR band is the Si-O-T (T=Si or Al) asymmetric vibration band in the range of 900-1300 cm^{-1} [111, 117-127], which is usually assigned to the main band of geopolymer gels. The main band can be observed in raw materials because they are rich in Si and Al as well, which has a wavenumber higher than or close to 1000 cm^{-1}. The wavenumber of the main band in

geopolymers is always lower than that in the raw materials, although it is not fixed due to microstructural variations resulted by different chemical compositions, curing periods and curing temperatures. Therefore, the main bands of the raw materials and geopolymers are always compared against each other to reveal the formation of geopolymer gels. The main band shifts towards to a lower wavenumber when geopolymer is formed, such as the shift from 1054 cm^{-1}, 1080 cm^{-1} or 1100 cm^{-1} in raw materials to a wavenumber lower than 1000 cm^{-1} [112, 123, 128]. Prud'homme et al. tracked this main band shift to assess the reaction rate of geopolymers from the onset of the reaction [129]. Another band centered around 840-900 cm^{-1} was assigned to Si-OH and was used to confirm the formation of geopolymer gels by its appearance, which is only observed in geopolymers, but not in the raw materials [111, 124, 130, 131]. However, Rahier et al. [132] found that the Si-OH band disappeared in the highly developed geopolymer gels, which is attributed to the $Si(OH)_4$ attached to the intermediate Al or the free Si-O at the reactive sites of growing geopolymer gels. Some other FTIR peaks frequently observed in geopolymers include the bands around 1440 cm^{-1}, 3500 and 1600 cm^{-1}, which represent sodium bicarbonate and water, respectively. The sodium bicarbonate is formed by the reaction between the Na^+ and the atmospheric CO_2 when geopolymers were exposed to air [125, 126]. Water is usually left in pores or absorbed by the surface, and thus the decrease of bands for water can be used to infer the hardening of geopolymer samples [125, 131]. The other bands listed in **Table 1-2** are usually very weak, some of which are not observed in all the geopolymers or need to be identified with deconvolution techniques, such as the band for zeolites [125]. It should be noted that each of the FTIR bands varies with respect to frequency and intensity in the geopolymers synthesized from different raw materials under various synthesis conditions.

The Si-O-Al bending peak at 540~554 cm^{-1} was assigned to the geopolymer gels formed by the reaction between silicon aluminates and highly alkali solutions by Gao et al. [133], but was not observed in most of other studies. There is also some contradicting interpretation of the FTIR bands in the literature. Take the band centered around 870 cm^{-1} for example, which was assigned to the Al-O symmetric stretching in tetrahedrons by Andini et al., but is usually assigned to the Si-OH bond in the other literature studies [124, 130, 131]. Regardless of this discrepancy, these findings are in good agreement that the appearance of the band centered around 870 cm^{-1} can be used to indicate the formation of geopolymer gels. In the current study, this band is assigned to the Si-OH bond.

Table 1-2. FTIR bands assigned to geopolymers from previous literature studies.

Bond	Wavenumber (cm^{-1})	References
Si-O-T (T=Si or Al) asymmetric stretching band	900-1300	[111, 117-127]
Si-OH	840-900	[111, 124, 130, 131]
Sodium bicarbonate	~1440-1453	[125, 126]
Water	~3500 and ~1600	[125, 131]
AlO_2	680	[111]
Si-O bending vibration	~800-810, 475	[131, 134]
Si-O-Al bending	700, 569	[126, 133]
Al-O-T bending	540-555	[133]
Al-O Asymmetric stretching vibrations	~1400	[121]
AlO_4	750-900	[121] [126, 127, 134]
ν_4(O-Si-O) bending mode	454	[125]
Single Ring	710-733	[118]
Zeolite	509, 629, 665	[125]
3-membered and 4-membered Rings	1020-1070	[135]

Different cross-linked Si tetrahedrons and Al coordination are another type of microstructural parameter, which is experimentally accessible with the aid of nuclear magnetic resonance (NMR) technique. In geopolymer gels and the raw materials, the 4-, 5- and 6-coordinated Al can be characterized with solid-state ^{27}Al NMR. Examples of the ^{27}Al NMR spectra of metakaolin and the resulting geopolymer gels [136], and fly ash based geopolymers [137] are provided in **Figure 1-4** (a) and (b), respectively. As seen in the spectra of metakaolin (**Figure 1-4** (a)), the peaks observed at 58, 28 and 10ppm are assigned to the 4-, 6-, and 5-coordinated Al, respectively; while only a large peak at 58ppm and a small peak at 10ppm are detected in the geopolymer gels. Similar to the metakaolin based geopolymers, a large peak at 56ppm and two small peaks at 1.5ppm and 85ppm are observed for the 4-coordinated and 6-coordinated Al respectively in the fly ash based geopolymers (**Figure 1-4** (b)), except that the 6-coordinated Al has different frequencies in this case. The findings from the above literature studies indicate that the ^{27}Al NMR spectra of the well-developed gepolymers all have a major peak at 40-60ppm for Al(IV) and a small peak with a wavenumber lower than 10ppm for Al(VI). Depending on the raw materials and synthesis conditions, sometimes another small peak around 85ppm and a small peak around 30ppm can be observed for Al(VI) and Al(V) [108, 130, 137, 138], respectively, in geopolymer gels. On the other hand, the peaks for Al(IV), Al(V) and Al(VI) always appear in raw materials. The change in the ^{27}Al NMR spectra from the raw materials to the resulting geopolymers is often the indicator of the formation of geopolymer gels, especially for metakaolin based geoplymers. The distribution of Si tetrahedrons in aluminosilicate materials that can be characterized with ^{29}Si solid state NMR has been well defined in terms of Q_n(mAl) by Engelhardt and Michel [139], where Q is Si, n is the

number of the bridging oxygen connected to Al or another Si, and m is the number of Al connected to Si. The position of the $Q_n(mAl)$ in the ^{29}Si NMR spectra of ideal silicate glasses is listed in **Table 1-3** by Engelhardt and Michel [139]. The ^{29}Si NMR spectra of geopolymer gels usually showed broad and poorly defined features that need to be analyzed with deconvolution technique. After deconvolution, the detectable shifts of silicate tetrahedrons in geopolymers are those located at -88, -90, -97, -104, and -109ppm for $Q_4(4Al)$, $Q_4(3Al)$, $Q_4(2Al)$, $Q_4(1Al)$ and $Q_4(Al)$, respectively. There are also some weak peaks corresponding to monomers and dimers [106, 140], as shown in **Figure 1-4** (c) and (d). These spectra are the ^{29}Si NMR patterns of metakaolin [141] and fly ash based geopolymers [142], respectively.

Table 1-3. ^{29}Si NMR spectra of $Q_n(mAl)$ in ideal silicate glasses [139]

$Q_n(mAl)$	$Q_4(0Al)$	$Q_4(1Al)$	$Q_4(2Al)$	$Q_4(3Al)$	$Q_4(4Al)$
δ (ppm)	109	104	97	90	88
$Q_n(mAl)$	$Q_3(0Al)$	$Q_3(1Al)$	$Q_3(2Al)$	$Q_3(3Al)$	$Q_2(0Al)$
δ (ppm)	90	82	80	77	80
$Q_n(mAl)$	$Q_2(1Al)$	$Q_2(2Al)$	$Q_1(0Al)$	$Q_1(1Al)$	Q_0
δ (ppm)	73	73	74	70	70

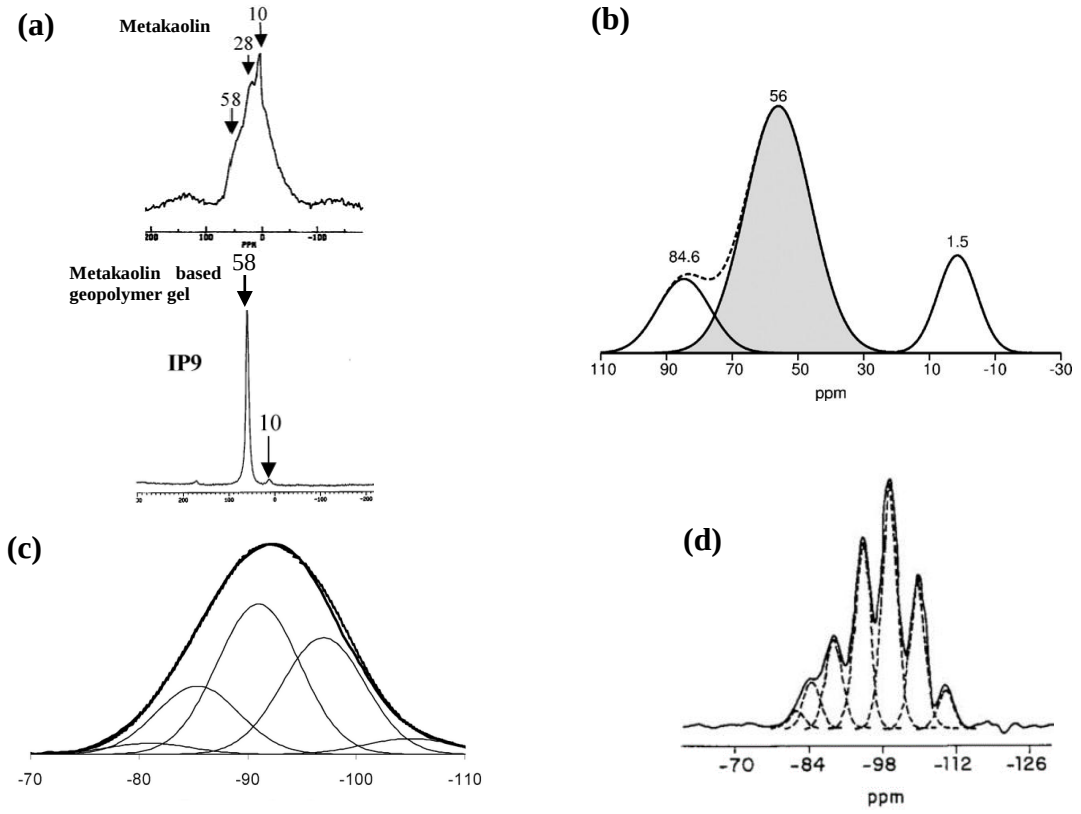

Figure 1-4. ^{27}Al NMR spectra of (a) metakaolin based geopolymers and metakaolin, (b) fly ash based geopolymers, and ^{29}Si NMR spectra of (c) metakaolin based geopolymers and (d) fly ash based geopolymers [136, 137, 141, 142].

Zhang et al. [126] used the ^{29}Si and ^{27}Al NMR and the FTIR spectra of raw materials and resulting geopolymer samples to indicate the formation of geopolymer gels and how the respective NMR and FTIR spectra relate to each other. The Si-O-T band was found to shift from 1086 cm^{-1} to 1006 cm^{-1}, which illustrated the formation of geopolymer gels, with a broadened width of the Si-O-T band implying a wider distribution of Q_n(mAl). Furthermore, the FTIR bands centered at 914, 798 and 697 cm^{-1} are assigned to 6-fold coordinated Al(VI)-OH, 6-fold coordinated Al(VI)-O and Si-O symmetrically stretching

band, respectively. The decrease in the intensity of these three bands suggests the conversion of the 6-coordinated Al(VI) in metakaolin to the 4-coordinated Al(IV) in geopolymer gels.

1.1.4. Porosity of Geopolymers

Pores, as an important aspect of geopolymers' microstructure, are not a part of geopolymer gels, but are formed during geopolymerization. The porosity of experimentally produced geopolymers has a significant impact on the mechanical properties, permeability and durability of geopolymeric materials. The pore volume and pore size distribution of geopolymers have been assessed with mercury intrusion porosimetry (MIP), N_2 adsorption-BJH analysis and microCT techniques. Based on the connectivity, the pores are classified as open pores and closed pores, where the latter cannot be measured by MIP or N_2 adsorption-BJH analysis. The pores can also be classified as gel pores (several nm to 0.02 μm) and capillary pores (0.1 to 1 μm or larger) based on their diameter [143]. Although the pore size is believed to be in the range of less than 10nm to approximate 10μm [144-146], the pore size distribution still varies depending on the raw materials and synthesis conditions. The pore size of fly ash based geopolymers measured with MIP by Kovalchuk et al. concentrated in the range of 0.5-5μm and 10-50μm [106], while the dominant pore sizes measured on another fly ash-based geopolymer by Ismail et al. with N_2 adsorption-BJH analysis were in the range of 1.7-8 nm and 10-100 nm [119]. The pores in fly ash based geopolymers consistently showed a bimodal distribution; while most of the pores in metakaolin based geopolymers distributed in the range of less than 10 nm to several μm [31, 52]. The connectivity, geometry and tortuosity of pores in geopolymers are

increasingly visualized and analyzed with the aid of microCT technology [147, 148]. The understanding of the development of pore volume and pore size distribution is important to establish the relationship of synthesis factors-microstructure-reaction mechanism-mechanical properties of geopolymers.

1.1.5. Geopolymer Gels

Geopolymer gels are the most important among the different components in experimentally synthesized geopolymers, which act as binding agent and largely govern the mechanical properties of the composite geopolymer. However, the mechanical properties of geopolymer gels and their distribution in the geopolymer matrix remain poorly understood. This is largely due to the fact that geopolymer gels exist at nano- to micro-scale within a complex composite matrix, and thus it is technically challenging to quantify mechanical properties of geopolymer gels and their distribution.

Pelisser et al., Skvara et al. and Steinerova et al. used nanoindentation to estimate the Young's modulus and hardness of geopolymers [149-151]. These studies shed light on micromechanical properties of geopolymer composites, but were not able to distinguish geopolymer gels in the composites for the lack of an effective approach to analyze the nanoindentation results. Since 2007, Ulm's group conducted several studies with the grid nanoindentation and statistical deconvolution techniques on cement pastes to investigate the micromechanical properties, nanoporosities and volumetric proportions of the phases present in Portland cement, including micro-pores, high-density CSH, low-density CSH and portlandite crystals [152-154]. The same techniques have been applied on geopolymers which also consist of multiple phases. Belena and Zhu explored the influence of curing

procedure on the micromechanical properties and volumetric distribution of different phases in geopolymers with the grid nanoindentation and deconvolution techniques [155]. They identified three phases in metakaolin-based geopolymers, including geopolymer gels, unreacted metakaolin and Quartz remained from the raw materials. Belena and Zhu also reported that the Young's Modulus and hardness of geopolymer gels cured under ambient conditions was in the range of 7-14 GPa and 0.2-0.5 GPa, respectively, and the volumetric proportion of geopolymer gels was between 83% and 89%, based on the analysis of the nanoindentation results. For unreacted metakaolin, the Young's modulus, hardness and volumetric proportion are 12-25 GPa, 0.5-1.0GPa and 7-13%, respectively, while these parameters for Quartz are 96-99 GPa, 14-15GPa and around 4%, respectively. Nemecek et al. used the same techniques on two geopolymers synthesized from fly ash and metakaolin respectively, and identified four phases in the fly ash-based geopolymers and two phases in metakaolin-based geopolymers by deconvoluting the probability density function (PDF) of elastic modulus [156]. They assigned the four phases in the fly ash based geopolymers to N-A-S-H gel (geopolymer gel), partly-activated fly ash, activated fly ash and nonactivated compact glass (unreacted components) with their elastic moduli in the range of 17.03 ± 3.48 GPa (50.7%) to 17.72 ± 3.75 GPa (77.5%), 26.06 ± 0.18 GPa (1.1%) to 29.95 ± 3.66 GPa (26.6%), 38.27 ± 10.13 GPa (17.5%) to 46.90 ± 7.76 GPa (17.6%) and 79.15 ± 14.34 GPa (5.1%) to 76.65 ±16.99 GPa (3.9%), respectively, where the percentage in the parentheses is the respective volumetric proportion. The two phases identified in the metakaolin-based geopolymers were geopolymer gels and unreacted metakaolin, respectively, with their elastic moduli around 17.72 ± 4.43 GPa (97.2%) and 43.91 ± 8.69 GPa (2.8%), respectively. However, the study by Nemecek et al. was conducted on a single

metakaolin-based or fly ash-based geopolymer sample, whose elastic moduli could be different once the synthesis conditions are changed. Belena and Zhu [155] noticed that the micromechanical properties (e.g., Young's Modulus and hardness) and volumetric proportion of geopolymer gels were higher for the samples cured at a higher humidity. On the other hand, Nemecek et al. found that (i) the ambient curing temperature resulted in more geopolymer gels and less partly-activated fly ash than the elevated curing temperature (80 ℃); and (ii) two more phases were observed in fly ash based geopolymer compared to the metakaolin counterpart due to the different reaction mechanisms of these two geopolymers. As evident from the above two studies, the micro-mechanical properties and volumetric proportion of geopolymer gels derived from the different samples can be discrepant. Comparing the results of the metakaolin based geopolymers in the above two studies, although the elastic modulus and volumetric proportion of geopolymer gels showed similarity, the properties of the other phases were inconsistent. Furthermore, one more phase was identified and assigned to unreacted crystal (Quartz) in Belena and Zhu's study, but not in Nemecek's. These discrepancies may be due to (i) the difference of the raw material source, chemical composition and curing procedure; and (ii) the deconvolution process, where the mechanical properties and proportions can vary appreciably if the PDF of elastic modulus and hardness were not carefully analyzed. Nevertheless, neither of these two nanoindentation studies had addressed the relationship between the characteristics of geopolymer gels and the macro-mechanical properties of the geopolymer composites.

1.1.6. Reaction Kinetics of Geopolymer Gel Formation

The reaction process from raw materials to geopolymers is complicated but is the key to reveal the relationship of chemical composition-reaction kinetics-microstructures-mechanical properties of geopolymers. To this end, numerous theoretical and experimental studies have been conducted. The earliest conceptual model of geopolymerization by Gluhhovsky [157] provides an overview of the process in three steps: (i) dissolution of aluminosilicate materials and release of reactive silicate and aluminate monomers; (ii) gelation of reactive monomers into aluminosilicate oligomers which reorganize into a more cross-linked system as the initial gels; and (iii) polycondensation and crystallization of the initial gels to form gepolymer gels. Provis et al. [158] further developed Gluhhovsky's model with their findings on the synthesis of geopolymers and zeolites, as depicted schematically in **Figure 1-5**. In the first step, the aluminosilicate materials (e.g., metakaolin and fly ash) are dissolved in alkali solutions; in the following step, aluminosilicate oligomers and polymerized silicate species are formed via the polymerization of silicate and aluminate monomers; subsequently, the aluminosilicate and silicate oligomers further polymerize into geopolymeric fragment (P) and aluminosilicate "nuclei" (N) in quasi- or nano-crystalline features; and eventually geopolymer gels (G) and zeolites (Z) are formed through the polycondensation of P and crystallization of N with remnant silicate monomers, respectively. In the resulting composite system, G and Z are inter-transformable under different conditions. In the entire process, the reaction steps often overlap and are intertwined with each other.

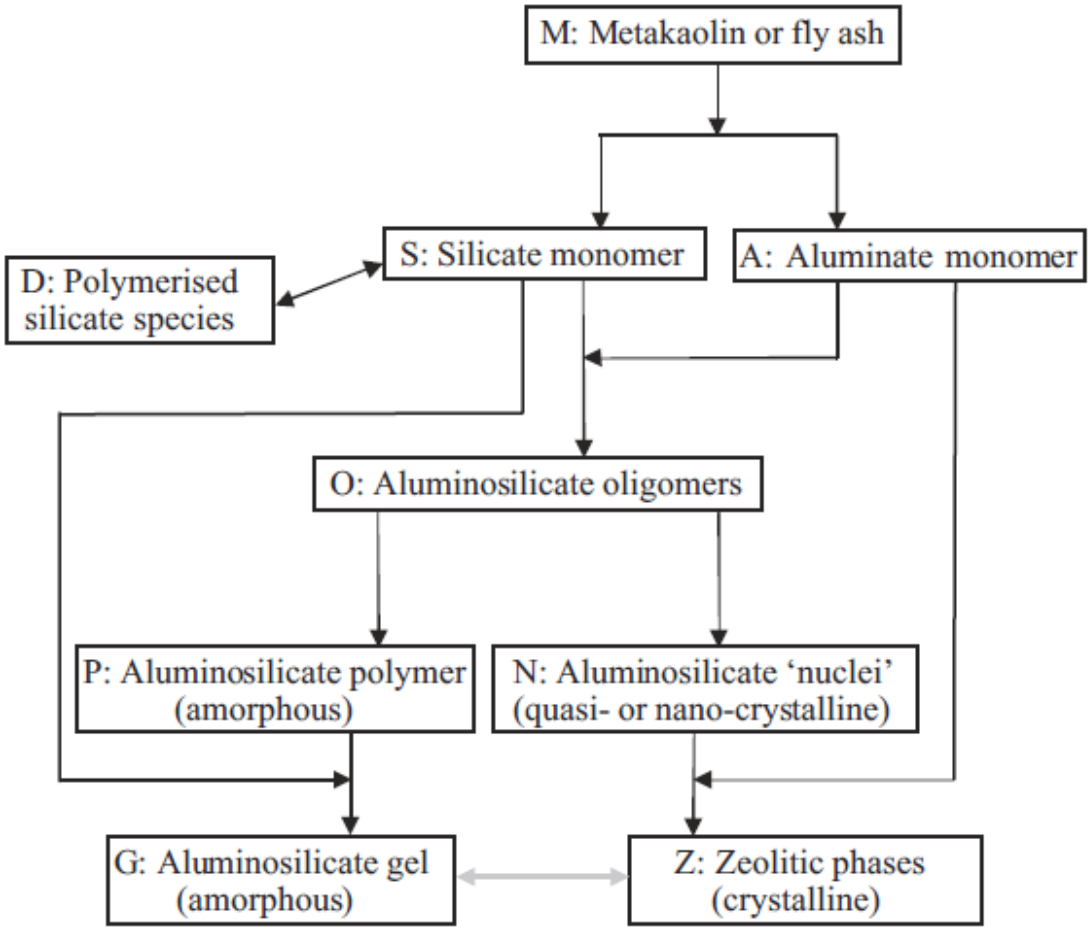

Figure 1-5. Conceptual model for geopolymerization process by Provis et al. [158].

The conceptual model in **Figure 1-5** quatitatively explains the reaction process from raw materials to geopolymers. However, the following two important aspects in the reaction are lack of emphasis. First of all, water is consumed in the dissolution process and released in following gelation and polycondensation processes [159-161]. Secondly, there are always unreacted materials and impurities remained in the final geopolymers as a part of fine aggregates, especially for the geopolymerization with fly ashes. These two aspects

have significant influence on the reaction kinetics and the final properties of experimentally synthesized geopolymers, such as microstructure, porosity and mechanical strength.

Reaction kinetics of geopolymer synthesis has been investigated from different perspectives, including reaction degree, reaction rate and the microstructural development of geopolymer gels with various analytical techniques. XRD has been used in many studies to examine the mineralogical change from the raw materials to geopolymers. Lyu et al. [128] observed the shift of an XRD hump from 19°-22° 2θ in metakaolin to 25°-28° 2θ in the resulting geopolymers and attributed this shift to the formation of geopolymer gels. Nasab et al. [112] observed that the center of a XRD hump shifted from ~25° 2θ in metakaolin to ~28° 2θ after geopolymerization. These studies can only qualitatively identify the formation of geopolymer gels due to their amorphous nature. Palomo's group estimated the reaction degree of geopolymers in three ways. Firstly, they conducted Rietveld analysis on the XRD patterns of the raw materials and the resulting geopolymers to estimate the difference between their amorphous content as the amount of geopolymer gels. Secondly, they dissolved the amorphous portions of the geopolymers by HCl attack and calculated the amount of the insoluble residue as the geopolymer gels. Lastly, they integrated the ^{29}Si NMR peaks of the characteristic Q_4(mAl) in geopolymers to estimate the reaction degree. The degrees of reaction estimated with these three methods were in good agreement [140, 142]. However, the reaction rate cannot be estimated, neither can a step-by-step reaction process be established from the above methods.

Provis and van Deventer developed a reaction kinetics model [158, 162], by using in-situ energy dispersive X-ray diffractometry (EDXRD) and ^{29}Si solid state NMR to monitor

the change in the microstructure of the geopolymers during the reaction process. White et al. used in-situ X-ray and neutron pair distribution function techniques to study the reaction kinetics of metakaolin based geopolymers [163, 164]. These atomic-scale characterizations provide an in-depth understanding of the formation of chemical bonds and the development of molecular structures of geopolymer gels during the reaction process [163, 164]. Although these methods are robust, some of the required devices and techniques, such as EDXRD, solid state NMR and peak integration, are not widely available.

In the recent years, Zhang's group conducted several experimental studies on reaction kinetics of metakaolin-based geopolymers with isothermal conductive calorimeter (ICC) [54, 123, 124]. Three ICC peaks were observed in geopolymerization process, which corresponded to the following three stages, as shown in **Figure 1-6**: the first peak usually appeared shortly after the onset of reaction, which was resulted from the heat released by the dissolution of metakaolin in strong alkaline solutions; the second peak was observed when another exothermic reaction occurred, suggesting the formation of oligomeric species in the aqueous phase of alumina/silica-hydroxy species; and the third peak, usually much less intense if appearing, was attributed to the polymerization/condensation reactions, implying that the reaction reached a thermally steady stage and large networks have consolidated [123]. A three-phase geopolymerization process was thus proposed by Zhang et al. based on the calorimetry results, including (i) dissolution of metakaolin into silicate and aluminate monomers; (ii) polymerization of the silicate and aluminate monomers to aluminosilicate oligomers that form geopolymer gels and zeolitic crystals; and (iii) reorganization of geopolymer gels and zeolitic crystals. The third step does not necessarily occur in every synthesis, which depends on the mix design and curing conditions, such as

alkali content and temperature. This reaction process model is consistent with the conceptual models by Gluhhovsky [157] and Provis et al. [158]. Zhang et al. [124] found that a higher reaction rate might hinder the further polymerization, and hence decrease the final degree of reaction for the metakaolin-based geopolymers in another study. They also pointed out that isothermal calorimeter is a valuable tool for qualitatively comparing reaction extent and reaction rate of geopolymers at the early stage. However, this technique is limited for the quantitative determination of geopolymerization degree because the thermodynamic parameters and the total heat release are unknown for geopolymers, especially those synthesized from industrial wastes [124].

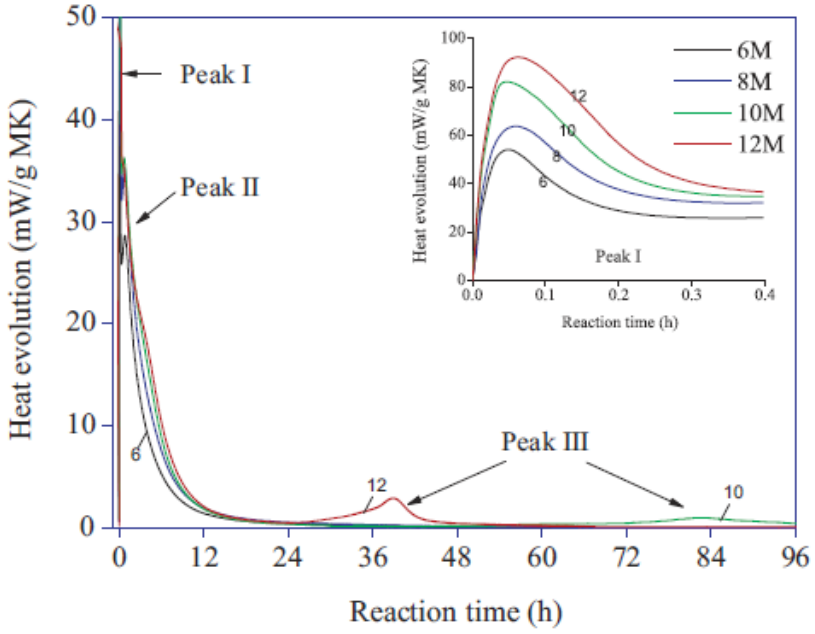

Figure 1-6. Heat release measured with isothermal calorimeter during the reaction of metakaolin based geopolymers synthesized with 6M, 8M, 10M and 12M NaOH at 40 ℃, by Zhang et al. [123].

As introduced in 1.1.3, FTIR is a more widely used technique for studying geopolymerization. In most of FTIR studies on the reaction kinetics of geopolymers, the wavenumber change of Si-O-T (T is Si or Al) band is considered as the indicator of the formation of geopolymer gels. With the aid of attenuated total reflectance-Fourier transform infrared spectroscopy (ATR-FTIR), closer time intervals can be applied to collect the chemical bonding information from the onset of alkali activation up to several months of curing to probe the kinetics of geopolymerization. Rees and the coworkers conducted two systematic studies on fly ash based geopolymers with ATR-FTIR to investigate the formation and aging of geopolymer gels, respectively. The changes in the wavenumber and intensity of Si-O-T bands centered around 1200-900 cm^{-1} were tracked from before the activation of fly ash up to 70 hours and 200 days, respectively. Their main findings were that the Si-O-T band shifted from 1055 cm^{-1} in fly ash to a lower wavenumber after the reaction started, and then became narrower and narrower (i.e., the Si-O-T bond became more ordered) with the polymerization progressing or gel aging [127, 165], as depicted in **Figure 1-7** (a) and (b). These geopolymers were synthesized with NaOH, while the authors found the Si-O-T band narrowed even sooner with the addition of soluble SiO_2 in the activator that increased the rate of polymerization. The effect of soluble SiO_2 on the geopolymerization will be reviewed in the following section.

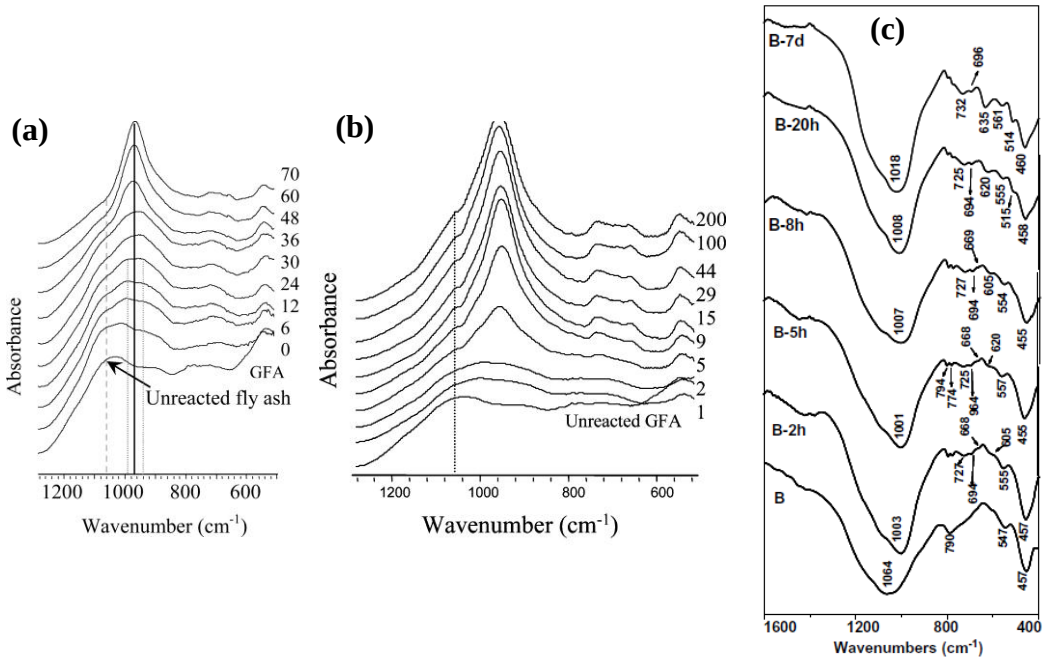

Figure 1-7. FTIR spectra of fly ash based geopolymers during the curing of (a) 70 hours [127] and (b) 200 days [165] in FTIR absorbance mode by Rees et al, and (c) 7 days in FTIR transmittance mode by Fernández-Jiménez and Palomo [166].

Another study by Fernández-Jiménez and Palomo indicates that the main band of Si-O-T shifted to lower wavenumbers firstly at the beginning of geopolymerization, and then shifted back to slightly higher wavenumbers [166], as illustrated in **Figure 1-7** (c). The shift of the main band is attributed mainly to the change of bond force constant of Si-O-T caused by the change of T-O-T angle and T-O length. The first shift towards a lower wavenumber was attributed to the substitution of a Si^{4+} for an Al^{3+} which results in a larger T-O-T angle and T-O length (i.e., the bond angle of Al-O-Si and bond length of Al-O is larger than Si-O-Si and Si-O, respectively), and thus a smaller bond force constant [106]. Another explanation for this band shift is the increase of the silicon sites with non-bridging oxygen (NBO) resulted by the dissolution of raw materials in the activators, illustrated in

a FTIR study on geopolymers by Lee and van Deventer [167]. This explanation was drawn based on the reduced molecular vibrational force constant of the $Si\text{-}O^{-}Na^{+}$ bond (i.e., silicon sites with NBO) compared to the Si-O-T bond (T: Si or Al). The other factors that may result in the change of this band include the increase of pore volume and pore size, compressive stress and hydrostatic pressure [134]. Conversely, the second shift of the main band towards a higher wavenumber is due to the formation of a more cross-linked tectosilicate network with the increasing participation of silicates in the polymerizations, which increases the Si-O-Si bonds and reduces the silicon sites with NBOs [168]. Therefore, these two consecutive shifts illustrates the precursor developed into an Al-rich system initially and then evolved towards a Si-rich system, which is more polymerized and denser than the Al-rich system [107, 127, 165, 169].

The change in 4-coordinated silicon sites during fly ash based geopolymer synthesis was investigated by Criado et al. [170] with ^{29}Si MAS-NMR to reveal the geopolymerization process. The deconvoluted NMR spectra of the fly ash activated by sodium hydroxide are present in **Figure 1-8** to illustrate the development of silicon sites. The peaks at -88, -93, -99, -104 and -108ppm were observed in the fly ash and the geopolymers cured for different periods, corresponding to the $Q_4(4Al)$, $Q_4(3Al)$, $Q_4(2Al)$, $Q_4(1Al)$ and $Q_4(0Al)$, respectively. The intensity of $Q_4(4Al)$ and $Q_4(3Al)$ peaks increased and that of $Q_4(1Al)$ and $Q_4(0Al)$ decreased in 8 hours after the activation of fly ash. This illustrates that the aluminosilicate components in the raw materials were dissolved to form smaller silicate oligomers. From the 8^{th} hour to the 7^{th} day of the reaction, the peak of $Q_4(2Al)$ became more intense with the decreased intensity of $Q_4(4Al)$ and $Q_4(3Al)$ peaks, demonstrating the polymerization of a more tectosilicate structure. Along the continuous

curing up to 180 days, a more distinct spectrum was resulted by a more ordered network of geopolymer gels, although the intensity and width of the peaks for the five silicon sites barely changed. In the geopolymer samples cured more than 7 days, the $Q_4(2Al)$ is the most dominant silicon site. The ^{29}Si NMR measurement can provide a good characterization of Q_4 during the geopolymerization, whereas the integrated interpretation of the microstructural development of geopolymer gels is not available.

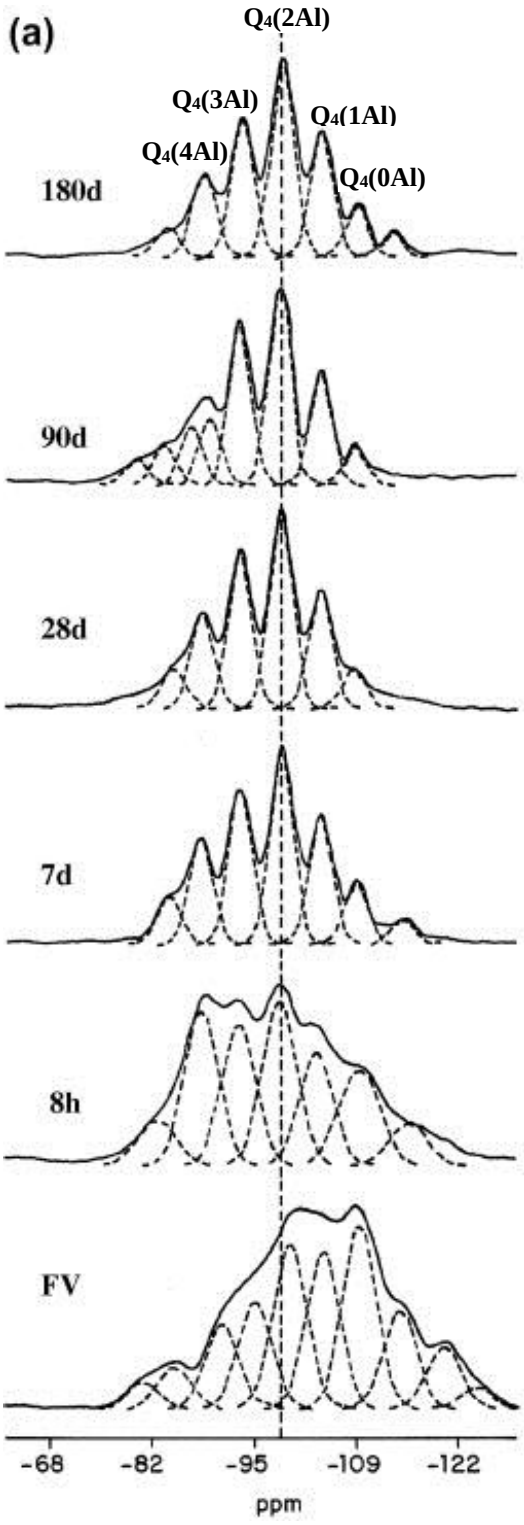

Figure 1-8. ^{29}Si NMR spectra of fly ash and the derived geopolymers cured for 8 hours to 180 days, by Criado et al.[170].

A great deal of research efforts has been devoted to understand the synthesis of metakaolin- and fly ash-based geopolymers. However, their reaction kinetics still remains poorly understood and the knowledge reported in the literature is not ready to be directly applied to the geopolymerization using the other raw materials, because of the significant effect of raw materials' properties on geopolymerization. For example, three heat release peaks were also observed in an ICC study on the reaction of fly ash based geopolymers, but the third peak occurred (if appeared) during the geopolymerization at a low intensity [85]. This is different from that in metakaolin-based geopolymer systems [54, 123, 124]. In addition, very few studies had addressed the relationship between the mechanical properties and the reaction degree at different reaction stages for geopolymers. Lastly, only a single curing temperature was applied, usually an elevated temperature between 40 ℃ and 90 ℃, which is not the most convenient curing temperature for in-site casting concrete that is widely used in civil engineering applications.

Many synthesis factors can influence the reaction kinetics, and thus the mechanical, physicochemical and microstructural properties of the resulting geopolymers. These factors include raw materials' properties (particle size distribution and amorphous content), type of activators (alkali hydroxide, alkali silicate and the mix of the above two), chemical compositions of the starting materials (Si/Al and Na/Al ratio) [115], and curing conditions (temperature, humidity and curing time). The effect of these factors on the final properties of geopolymers was reviewed in the next section.

1.1.7. Influence of Synthesis factors on Metakaolin- and Fly Ash-based Geopolymers

1.1.7.1. Chemical Composition of Raw Materials

The influence of chemical composition of raw materials, often characterized by Si/Al and Na/Al molar ratios, on properties of resulting geopolymers, has been investigated in numerous experimental studies on metakaolin- and fly ash-based geopolymers.

i. Si/Al Ratio

As depicted in the conceptual model in **Figure 1-5**, the availability of reactive silicates and aluminates governs the reaction kinetics, and thus the mechanical properties of the resulting geopolymers. However, Si and Al play different yet intertwining roles in the geopolymerization process. The reactive aluminates can significantly enhance reactions at the initial stage, including dissolution and gelation. This was observed by Fernández-Jiménez et al. [169], where the early reaction degree was higher for fly ash based geopolymers with a higher concentration of aluminum because (i) Al-O bond is more readily broken than Si-O bond in the dissolution process, and (ii) Si-O-Al bonds are more easily formed than Si-O-Si bonds in the following gelation process, with the former being energetically weaker [171]. In the subsequent polymerization process, a high aluminate concentration leads to a sufficient incorporation of Al to Si to form a dense geopolymeric network [169]. Silva et al. observed that the setting time of geopolymers decreased with the increasing Al concentration [172], while Cioffi et al. [173] found that geopolymer cannot solidify when the Al content was too small (SiO_2/Al_2O_3=6) due to the low degree of polycondensation. The comparison between the results obtained by Cioffi et al. [173]

and Andini et al. [47] implies that the higher dissolution rate of Al in metakaolin, caused by the strained bonds in its aluminate layer [9], is one of the reasons for the higher reaction rate of metakaolin than fly ash. Hajimohammadi et al. [168] explained the effect of Al concentration on the early reaction rate of geopolymerization from the microstructural point of view. They observed that the FTIR band of Si-O-T (T: Al or Si) shifted to a lower wavenumber and back to a higher wavenumber much sooner in the geopolymers with a higher concentration of reactive Al, indicating a higher reaction rate. With a large availability of reactive Al, the geopolymer precursor developed into Al-rich gels and then Si-rich gels in a short time period, which allowed these two gels to mix and form a relatively more homogeneous binder. On the other hand, in the geopolymer with a low concentration of reactive Al, the slow formation of the Al-rich gels and the subsequent Si-rich gels gave these two gels enough time to stabilize and condense individually, and thus it became difficult for the structure to evolve into a homogeneous binder. Consistently, the early strength of the former geopolymer (e.g., the one with a higher Al concentration) was much higher than that with a lower content of reactive Al after one-week curing.

Other than Al, soluble silicates in alkali activators also enhance the dissolution of Al^{3+} and Si^{4+} and thus the following polymerization processes, reported by Sindhunata et al. [174] and Dee and van Deventer [175]. Duxson et al. observed that more reactive aluminates incorporated with silicates and formed geopolymer gels [31, 175] as the concentration of the soluble silicates increased. Otherwise, the dissolutions of both Al and Si would be inhibited and the geopolymer slurry would solidify before sufficient geopolymer gels were formed to bind the unreacted materials, and thus a low mechanical strength would be resulted [175]. On the other hand, Criado et al. found that the addition

of silicate solutions higher than SiO_2/Na_2O=0.50 slightly decelerated the development of geopolymer gels at the early stage, due to the slow formation rate of more polymerized silicate species. Nonetheless, a high concentration of soluble silicates resulted in denser and Si-rich geopolymer gels with a higher mechanical strength, which offset the negative effect of the delayed polymerization to some extent [176, 177]. Criado et al. explained this reaction kinetics with the ^{29}Si NMR analysis on the geopolymers. Larger clusters increased (e.g., Q^2_{cycle}: Si sites connected with 2 bridging oxygen in a cyclic molecule) and led to Si-rich gels when soluble silicates with an appropriately high concentration ($SiO_2/Na_2O \approx$ 0.69) was added to geopolymers [112, 170]. Meanwhile, Si monomers and dimers (e.g., Q^0 and Q^1: Si sites connected with 0 and 1 bridging oxygen, respectively) declined [112, 170]. However, when the concentration of soluble silicates was too high (e.g., SiO_2/Na_2O>0.69) [176, 177], the initial dissolution was slowed down and a colloidal system was formed; or the polymerization process was even inhibited when it was extremely high (e.g., SiO_2/M_2O>2.00, where M is K or Na) [174]. Large oligomers were formed in those highly concentrated silicate environments, which precipitated on the surface of raw materials and prohibited the further dissolution of aluminate tetrohedrons. As a result, the polymerization of geopolymer gels was retarded or even stopped due to the insufficient monomeric aluminates and colloidal nature of the silica concentrated systems [174].

It should be noted that the effect of silicate and aluminate concentration on mechanical strength of geopolymers need to be considered holistically as Si/Al ratio or SiO_2/Al_2O_3 ratio since the reactive silicates and aluminates are incorporated with each other to form geopolymeric networks. Hajimohammadi et al. pointed out that the role of silicates in the

development of geopolymer gels and strength at later stages is more important than Al [168]. In their study, the geopolymer with a high Si/Al ratio had a higher development of mechanical strength at later stage (2 and 3 weeks' curing), although its early strength was lower. This observation is consistent with the reaction model of fly ash based geopolymers proposed by Fernández-Jiménez et al. [169], as shown in **Figure 1-9**. Although the strength starts to form at the Al-rich stage (gel 1 in **Figure 1-9**), it increases by a much higher value at the Si-rich stage (gel 2 in **Figure 1-9**). This may be attributed to the properties of different microstructures in geopolymeric framework. The 3D polymeric structures poly(sialate-siloxo) (PSS, -Si-O-Si-O-Al-) and poly(sialate-disiloxo) (PDSD, -Si-O-Si-O-Si-O-Al-) are more stable and rigid than poly(sialate) structures (PS, -Si-O-Al-). With a high Si/Al ratio, the formation of Si-O-Si bonds, as well as PSS and PDSD, is more dominant in the resulting geopolymers, while the formation of PS is more favorable vice versa [178].

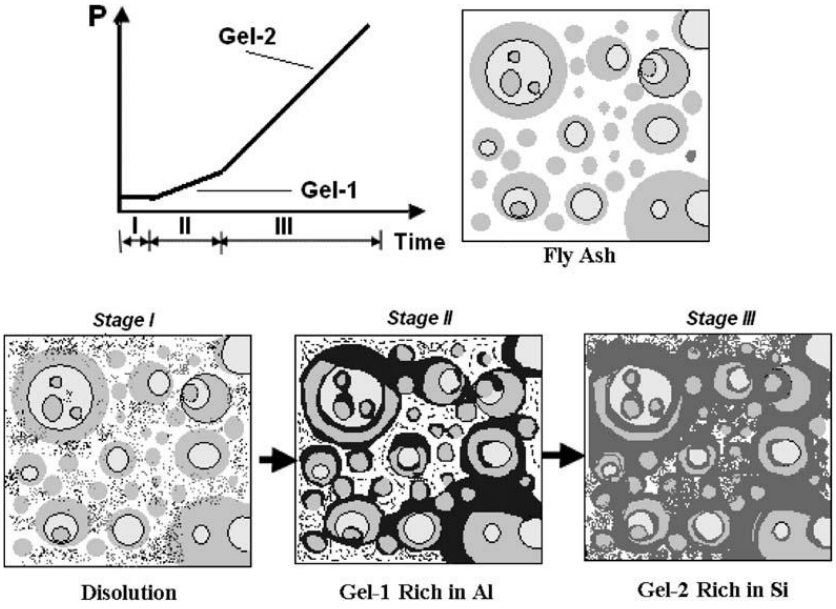

Figure 1-9. Schematic reaction model of mechanical properties (P) evolution along the reaction for fly ash based geopolymers [169].

Both the polycondensation degree and mechanical strength of geopolymers were found to increase with Si/Al ratio [31, 47, 101, 105, 169, 172, 173], but not monotonically. The optimal Si/Al ratio for geopolymers with a high strength is believed to be around 1.90~2.00 [31, 101]; and a higher or lower value than this range would reduce the strength. An appropriate Si/Al ratio (around 1.90~2.00) can dissolve a higher number of small aluminosilicate oligomers, such as monomers and dimers, which are highly reactive and able to fully participate in the condensation before hardening. Thus, the synthesized geopolymer gels would be denser [31] and their mechanical strength would be higher [179], whereas an excessively high Si/Al ratio (much higher than 2.00) is detrimental for geopolymerization and thus mechanical strength [115].

The increase in the degree of polycondensation with the increasing Si/Al ratio is illustrated with the microstructural change of the metakaolin- and fly ash-based geopolymer samples in **Figure 1-10**. As shown in the SEM images, with the increase of Si/Al ratio up to 1.9 and 1.95 for metakaolin- and fly ash-based geopolymers, the following observations can be obtained: (i) the microstructure of geopolymers are more homogeneous and compact; and (ii) the proportion of unreacted raw materials is lower, such as the platy shaped particles of metakaolin and spherical particles of fly ash. For the metakaolin based geopolymer with a Si/Al ratio of 2.15, its micromorphology becomes more porous and has more cracks than that with a Si/Al ratio of 1.90. These defects in the geopolymer with a Si/Al ratio higher than 1.90 are responsible for its reduced mechanical strength.

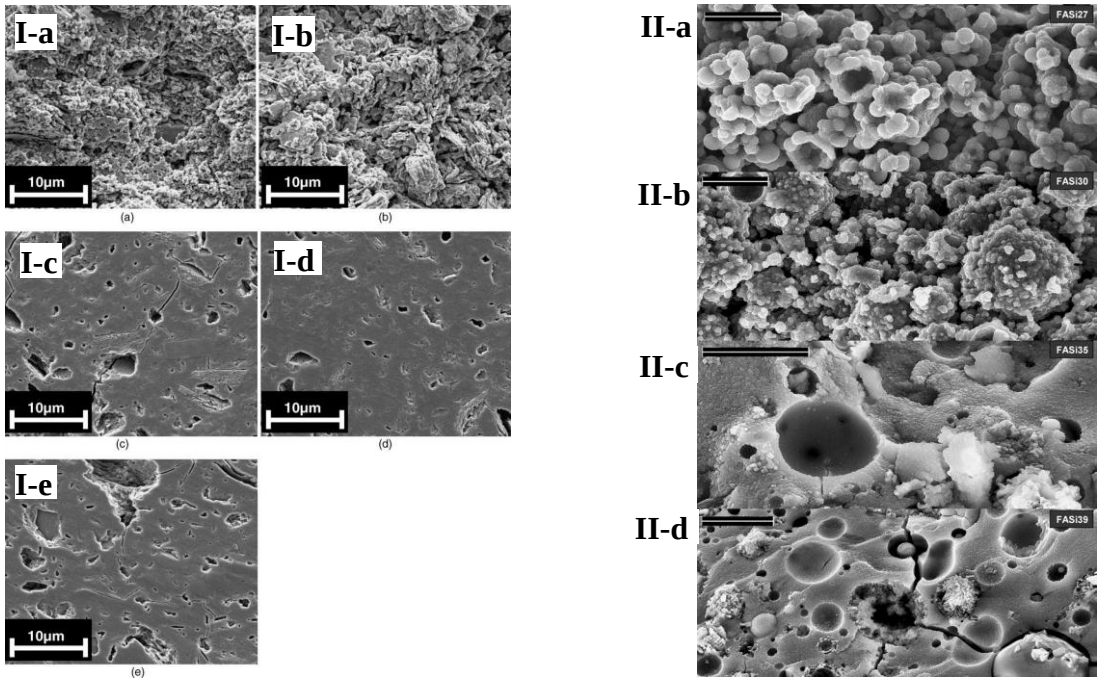

Figure 1-10. SEM Images of metakaolin based geopolymers with Si/Al ratio of (I-a) 1.15, (I-b) 1.40, (I-c) 1.65, (I-d) 1.90, and (I-e) 2.15 [31]; and fly ash based geopolymers with SiO_2/Al_2O_3 ratio of (II-a) 2.70, (II-b) 3.00, (II-c) 3.50, and (II-d) 3.90 [105].

The porosity, as another important factor affecting mechanical properties of geopolymers, is also affected by Si/Al ratio. A high silicate concentration led to more even distribution of geopolymer gels in the matrix, and thus resulted in more isolated pores [31, 143]. Conversely, geopolymer gels synthesized from a low silicate concentration are only formed and limited around the unreacted particles, leading to more capillary (large) pores. The coalescence of small pores into large pores is inhibited with the increase in silicates during the condensation process. In this case, a larger amount of small pores can form, rather than the large pores, resulting in a low permeability of the geopolymer. This is beneficial for the durability of the geopolymer because a low permeability prevents geopolymeric materials from being corroded in aggressive environments [31, 143]. Furthermore, it was found that the cumulative pore volume of geopolymers decreased with the increasing Si/Al ratio. Therefore, a low concentration of soluble Al leads to a more compact geopolymeric structures with finer pores, while an Al-rich geopolymer system is prone to form larger pores and a higher cumulative pore volume, which in turn increases the cracking risk of the geopolymers. This implies that a high concentration of Al in geopolymer precursors is detrimental for its long-term mechanical strength and durability, despite the positive effect of high Al concentration on the geopolymerization rate and early strength development.

The influence of Si/Al ratio on the drying shrinkage potential of metakaolin-based geopolymers was carefully studied in the literature [100, 101]. Increasing Si/Al ratio is detrimental for drying shrinkage resistance of metakaolin-based geopolymers at ambient temperature [31, 115], although a relatively higher Si/Al ratio (Si/Al $\approx$ 1.9~2.0) is beneficial for a higher degree of polymerization and strength development. Therefore, increasing Si/Al ratio can improve the mechanical performance of metakaolin-based

geopolymers in the early age, which would compromise the drying shrinkage resistance in the longer curing time [101].

The mechanical properties of geopolymers are affected by Si/Al ratio in a complex manner, with multiple competing mechanisms involved, which remains far from well understood.

ii. Alkali Cations (Na^+ or K^+)

Besides reactive silicates and aluminates, the alkaline cations play an important role in geopolymerization process. In the dissolution process, the alkali solution, which is the main source of alkali cations, is essential to dissolve reactive silicate and aluminate tetrahedrons. In the following polymerization process, the alkali cations incorporate with $Al(OH)_4^-$ to balance the negative charge of the polymerized aluminosilicate networks. Therefore, the availability of alkaline cations is a vital factor for geopolymerization and the properties of the resulting geopolymers. The commonly used alkaline cations are Na^+ and K^+. Steveson investigated the effect of these two types of cations on the geopolymerization with fly ash [105] and metakaolin [179]. He observed that: (i) the Na-geopolymers set faster than K-geopolymers, (ii) the micromorphology of Na-geopolymers was smoother than K-geopolymers, (iii) the pore volume in Na-geopolymers was lower than K-geopolymers, (iv) the mechanical strength of Na-geopolymers was higher than K-geopolymers after two hours' curing at 85°C, and (v) the microstructure of K-geopolymers was denser than Na-geopolymer. These findings are similar in both fly ash- and metakaolin-based geopolymers and in good agreement with the observations by Rahier et al. [180] and Phair and van Deventer [181]. van Jaarsveld and van Deventer [182] found that the initial reaction rate

of Na-geopolymer was higher while the structure of K-geopolymer was denser, which implied that the behavior of Na^+ and K^+ is different during geopolymerization process: Na^+ favors the dissolution process and K^+ enhances the condensation. However, Steveson believed that the mechanical strength of K-geopolymers could be higher if the curing time is extended (>2 hours). His speculation was confirmed by van Jaarsveld and van Deventer [182] in a study that the 14 days' compressive strength of K-fly ash based geopolymers was higher than the Na counterparts, which they thought was due to higher specific surface areas of K-geopolymers. Cioffi et al. also found that K-metakaolin based geopolymers had higher compressive strength than the Na counterparts at different curing temperatures from 25℃ to 85℃ [173]. Conversely, Duxson et al. observed that the K-meatakaolin based geopolymers had a lower strength than the Na counterparts when Si/Al = 1.15 and 2.15, while K-metakaolin based geopolymers were stronger when Si/Al = 1.40~1.90 [51]. The same research group also found that the strength of geopolymers tended to decrease with the increasing addition of K^+ in the geopolymers activated by the mix of Na^+ and K^+ [31]. In another study by Duxson et al. with the same sample matrix, potassium was found to result in a more disordered structure with a larger amount of Al-O-Al bonds which can weaken the geopolymeric networks [141].

The setting time of geopolymers increased with the increase of SiO_2/Na_2O ratio observed by Gao et al. [133]. However, Cheng and Chiu [183] observed the final setting time increased with the increasing concentration of KOH in their studies on the geopolymers synthesized with the mix of KOH and Na_2SiO_3. This is due to the increasing concentration of OH^- associated with the cations, which sped up the dissolution rate of aluminate and silicate tetrahedrons but extended the polycondensation process. However,

when the concentration of cations is too high, the polymerization is so fast that the resulting geopolymer gels precipitate on the surfaces of the unreacted materials and inhibit any further dissolutions, and then the geopolymers would flash set [99] without having mechanical strength fully developed. This phenomenon was observed in van Jaarsveld and van Deventer's study [182] on fly ash based geopolymers. For both K-geopolymers and Na-geopolymers, the setting speed decreased with the increase of M_2O/SiO_2 (M: Na or K) when the $Na_2O/SiO_2<0.9$ and $K_2O/SiO_2<0.8$, respectively. Rattanasak and Chindaprasirt confirmed this trend in their study that the dissolution of both Si^{4+} and Al^{3+} in 10M NaOH was higher than that in either 5M NaOH or 15M NaOH [110]. On the other hand, a high concentration of alkali cations has a positive effect on the polymerization process. Rowles and O'Connor [115] found that the degree of polymerization decreased and more unreacted materials (e.g., metakaolin) remained in the resulting geopolymers with the decrease of alkaline concentration, as demonstrated by the increasing intensity of Al(IV) (a representative Al coordination in metakaolin) sites with ^{27}Al NMR characterization. Consistent with the above findings, Rahier et al. observed that the reaction rate decreased with the increase of Si/Na ratio [132].

Rowles and O'Connor [103] investigated the effect of chemical composition on the mechanical and microstructural properties of metakaolin based geopolymers activated by NaOH with different Si:Al:Na molar ratios. The SEM images of the MKG with low, medium and high strength are shown in **Figure 1-11**, which were synthesized at the nominal Si:Al:Na ratio of 1.50 : 1.00 : 0.72, 1.50 : 1.00 : 1.50 and 2.50 : 1.00 : 1.29. Their findings suggested that the optimal Si:Al:Na is 2.50:1.00:1.29, at which the mechanical strength was maximized and the microstructure of geopolymer was more homogeneous

than the other ones. Na^+, which is coupled with OH^-, in terms of Na/Al ratio, was found to play important roles in the reaction and the mechanical properties. In the geopolymer system activated by NaOH, a low Na^+ concentration cannot provide enough OH^- to dissolve silicate and aluminate tetrahedrons from raw materials or sufficient Na^+ to incorporate with $Al(OH)_4^-$ for the polymerization. However, an excessively high Na^+ concentration (a Na/Al ratio much higher than 1.29) left excessive sodium in the geopolymer to weaken the polymerized structures.

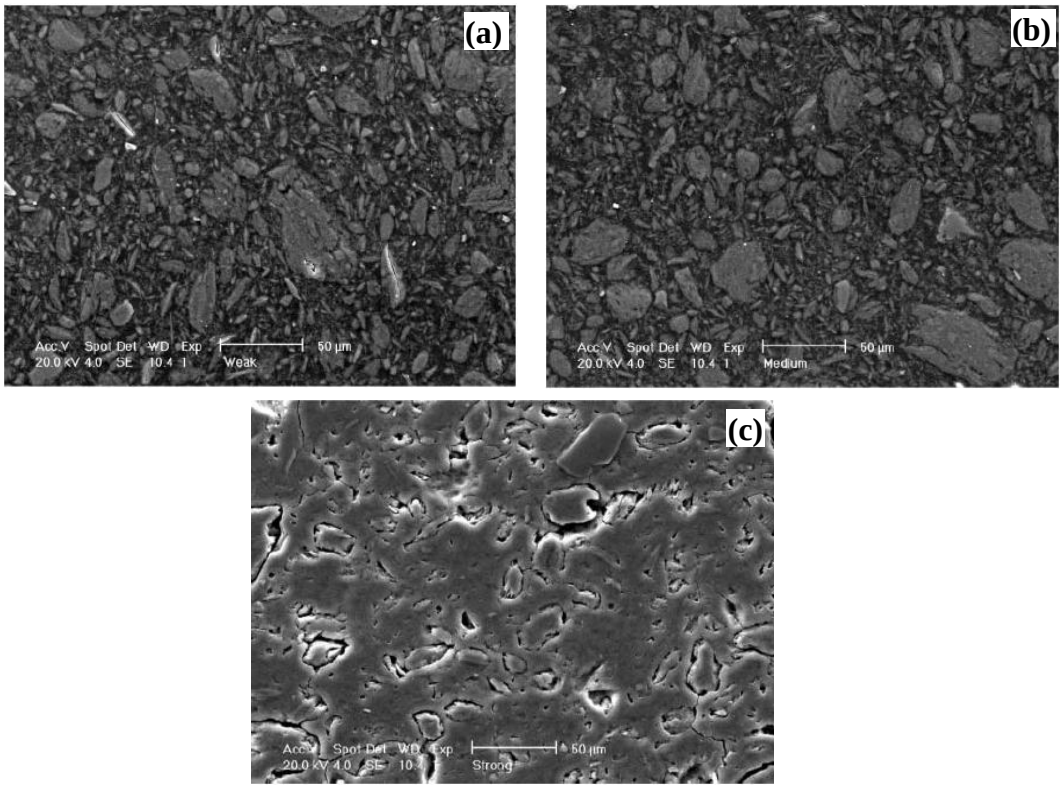

Figure 1-11. SEM micrographs for the aluminosilicate polymers with nominal Si :Al : Na molar ratios, based on the starting compositions, of (a) 1.5 : 1.0 : 0.72, (b) 1.5 : 1.0 : 1.5 and (c) 2.5 : 1.0 : 1.29, which correspond to low, medium and high strength samples, respectively [103].

This finding was also confirmed in the study by Gao et al. [133] on metakaolin based geopolymers with SiO_2/Na_2O molar ratios ranging from 1.00 to 2.00. The mechanical strength of the geopolymer increased with the decrease of SiO_2/Na_2O ratio (increase of Na^+ concentration) within the range of 1.00 to 1.50 and then decreased. Steveson [105, 179] observed the same effect of Na^+ concentration on mechanical strength in his studies, where the optimal Na/Al ratio was 1.20 and 1.00 for metakaolin- and fly ash-based geopolymers, respectively. Rowles and O'Connor [115] found that the optimal Na/Al molar ratio for the mechanical strength of metakaolin based geopolymers was 1.00. Conversely, Hos et al. [184] observed that the mechanical strength of the geopolymer significantly increased with the decreasing Na/Al ratio with an optimal value of 0.36, much lower than the theoretical Na/Al of 1.00. The discrepant findings regarding the effect of Na/Al ratio on mechanical strength the geopolymers may be attributed to the difference in the raw materials. Metakaolin and fly ash were used in the former studies that are not fully reactive, and a melt-quenched aluminosilicate was used by Hos et al. which is purer and highly reactive. Steveson found that the charge-balancing role of Na was dominant in fly ash based geopolymers and the dissolution role was dominant in metakaolin based geopolymers [105, 179]. Furthermore, the influence of the concentration of alkali cations on the mechanical strength of geopolymers varies with the Si/Al ratios. It was found by Duxson et al. [51] that the strength of metakaolin based geopolymers decreased with the concentration of M (M: Na and/or K) at Si/Al=1.15, increased at Si/Al=1.40~1.90, and had no trend at Si/Al=2.15.

As seen from the above literature studies, the effect of alkali cations on the geopolymerization and the properties of the resulting geopolymers is complex and depends

on other factors, such as raw materials, Si/Al ratios and curing time. However, the dosage of alkali cations has to be adjusted based on the concentration of Si and Al since the main function of alkali cations is to balance the negative charge of the geopolymeric networks.

1.1.7.2. Curing Temperature

The mechanical strength of geopolymers usually increases with the curing temperature, while the temperature higher than 80 ℃ seems detrimental for the strength development [50, 84, 87, 185]. This can be attributed to the dissolution rate of the raw materials, which increases with the curing temperature, especially for class F fly ash, of which the reactivity is relatively low at room temperature. Skvara et al. [137] found that the reaction degree of class F fly ash based geopolymeric system at 20 ℃ for 70 days is equivalent to that at 60 ℃ for 1 day. In addition, the reaction energy of class F fly ash-based geopolymers at room temperature was approximately twice that of OPC [186]. The dissolution rate of metakaolin in alkali solutions and the subsequent geopolymerization rate can be accelerated with elevated temperatures, and thus the setting time of the geopolymers decreased [52, 185, 187]. However, the final degree of geopolymerization is not necessarily higher at higher curing temperatures. For instance, Zhang et al. found that a higher curing temperature led to a sooner appearance of the first peak but not a quicker second peak in the geopolymer's ICC spectra. The first and the second peaks correspond to the dissolution and polymerization process, respectively. In addition, their study indicates that the curing temperature only had a significant effect on the reaction rate, but not the final degree of reaction or mechanical strength [123], when the nominal Na/Al ratio was less than 1. Curing temperature was also found to be less relevant to the polymerization process after

the precursor was set [89, 174]. From the reaction kinetics point of view, Palomo's group conducted an NMR study on fly ash based geopolymers and found that less Al participated in the geopolymerization at elevated temperatures [188], which can be one reason for the relatively low reaction degree of the geopolymers. Finally, for the porosity of resulting geopolymers, elevated curing temperatures are more likely to result in a higher cumulative pore volume and thus a lower density for the geopolymers, due to the accelerated water evaporations during the heating [52, 173, 189, 190]. However, Sindhunata et al. found that there were more cavities with larger pore sizes in the geopolymer synthesized at lower temperatures [174]. Therefore, the influence of temperature on the porosity of geopolymers remains to be further investigated.

1.1.7.3. Water Content and Curing Humidity

Water plays an important role in geopolymerization process, as it is consumed during the dissolution of raw materials, and released during the subsequent polymerization processes. Water content can affect the mechanical properties of the resulting geopolymers mainly from two aspects. Firstly, water content alters the reactivity of the precursor. A relatively high water content is favorable for the initial reaction that is dominated by the dissolution, but can be harmful for the formation of geopolymer gels during the later stages of geopolymerization [113]. However, an excessive amount of water in geopolymer precursors reduces the reaction rate due to the dilution effect that makes the collision and reaction among reactive ions less frequently or likely [132]. Secondly, water introduces pores into geopolymer matrix. During polymerization, water is extracted from the geopolymer molecules and trapped in the matrix of the unreacted constituents, such as

semi-reacted hollow fly ash spheres. Pores are left in the geopolymer matrix after water is evaporated during the hardening. Although a higher water content enhances the dissolution of aluminate and silicate tetrahedrons, increase the degree of geopolymerization and thus the mechanical strength, but the introduced higher porosity can offset and even override the mechanical improvement [53, 105, 179]. Conversely, the reduction of water content in metakaolin-based geopolymer precursor usually leads to the decrease in pores and thus improves mechanical properties of the resulting geopolymers, including compressive strength, Young's modulus, fracture toughness and modulus of rupture [55]. In general, the mechanical strength of geopolymer increased with the decrease of water content [105, 179, 182]. Therefore, the water content of the geopolymer precursor should be kept as low as possible while its workability is ensured.

Curing humidity also has important influence on the final properties of the resulting geopolymers. Either too high or too low humidity was found to be detrimental to the geopolymerization process and result in geopolymers with a high porosity [106]. Due to a fast water evaporation, large size pores and drying shrinkage cracks are prone to form when geopolymers are cured at a low humidity [99, 106]. However, Zhang et al. [99] found that the dissolved reactants would be leached out with water to inhibit the further reaction for the geopolymers cured at an excessively high relative humidity. Although a high humidity was beneficial for preventing carbonation, it resulted in a higher cumulative pore volume and less polymerized structures than intermediate curing humidity, observed by Kovalchuk et al.[106]. Maintaining a proper curing humidity is particularly important for the geopolymers with a low reaction rate, such as class F fly ash based geopolymers at ambient

temperature, since cracks or pores are prone to form before a high strength is developed during the prolonged curing period.

1.1.8. Computational Modeling of Geopolymers

Although numerous experimental studies have been conducted on geopolymers, the molecular structure of geopolymer gels and the geometric configuration of geopolymeric networks are still not readily accessible by experimental techniques, due to the composite nature of experimentally synthesized geopolymers, the amorphous nature of geopolymer gels, and intertwining reaction processes, where the pure geopolymer gel and each of the reactions (e.g., dissolution, polymerization and condensation) cannot be separated. However, the abovementioned information is the key to understand the relationship of chemical composition-reaction kinetics-microstructure-mechanical properties of geopolymers.

With the aid of molecular simulations, the molecular strcture of geopolymer and the chemistry of geopolymerization kinetics can be investigated at molecular or atomic scale. The properties of geopolymer gels would not be affected by the other impurities in the molecular models, while each single reaction process can be simulated independently or tracked. Zhang's group used semi-empirical AM1 method in a series of studies to simulate the possible pathways of the dissolution of metakaolin in alkali solutions, ion reorientation process and polycondensation process in geopolymerization [191-193]. In the simulation of ion reorientation process [192], they examined 3 paths for the reorientation between 2 clusters (silicate monomers and/or aluminate monomers) and 4 pathways for the reorientation between 3 clusters. They found that the hybrid Si-Al reorientation was the

dominant path. In the simulation of polycondensation process [193], the authors simulated the polymerization of 5 monomers in the paths towards a chain, sheet and framework structure, respectively, and found the framework path was dominant. In these two studies, they verified the simulation results with the ^{29}Si MAS NMR results of metakaolin based geopolymer, where 95% of the silicon tetrahedral sites are belong to Q_4(4Al) (-82 to -83.5ppm) and Q_4(2Al) (-88 to -89.5ppm), which are Si-Al hybrid orientated clusters and existed in cross-linked aluminosilicate frameworks. However, the scale of the models is too small to represent the microstructure of geopolymer gels or describe the geopolymerization process comparable to those in experimental synthesis. Yang et al. [194] simulated the aluminosilicate oligomers with a Si/Al ratio of 1 to 6 using density functional theory (DFT) method, and compared the stability of isomers by measuring their relative energies. The obtained energetically stable oligomers can be used as building blocks for the simulation of geopolymerization, including open chain clusters, such as silicate and aluminate monomers, aluminosilicate dimers, trimmers, tetramers, pentamers and hexamers, and 3-, 4-, 5- and 6-membered closed rings. They used some of these oligomers in the following DFT study on the polymerization of aluminosilicate clusters, which is the fundamental reaction for the synthesis of geopolymer and zeolite. They calculated the energy of the reaction between silicate monomer, aluminate monomer or aluminosilicate dimer and some ring oligomers, including four, six, double four and double six rings [195] with DFT method, and obtained energetically favorable polymerization paths in geopolymerization processes. However, DFT modeling is only limited to smaller molecular systems (e.g., those composed of hundreds of atoms) and thus is incapable of simulating large molecular systems such as geopolymers, which requires a prohibitive

computation time. White et al. [196] modeled the deprotonation and dimerization of silicate and aluminate monomers and their dependence on pH values with DFT simulations. The DFT simulation results were used in their subsequent Monte Carlo simulations to investigate the influence of silicate concentration on the dissolution and polymerization processes of Na-metakaolin based geopolymer, which was activated with three alkali solutions [197]. The snapshots of the Monte Carlo models of Na-metakaolin based geopolymer activated with NaOH along the simulation are presented in **Figure 1-12**. This simulation study elucidated the dissolution and polymerization mechanisms of metakaolin based geopolymers that cannot be characterized with physical experiments otherwise. However, the dissolution and polymerization processes were not separated in the simulation, as their models shown in **Figure 1-12**, so the effect of their interaction and remnants of metakaolin on the simulation results cannot be eliminated. In addition, this simulation focused more on the dissolution process, where the molecular structure of geopolymer gels is not available. Lastly, the geopolymers synthesized from different raw materials are intrinsically different, the models and the resulting geopolymers with metakaolin as the starting material might not be directly applied to other raw materials-based geopolymers.

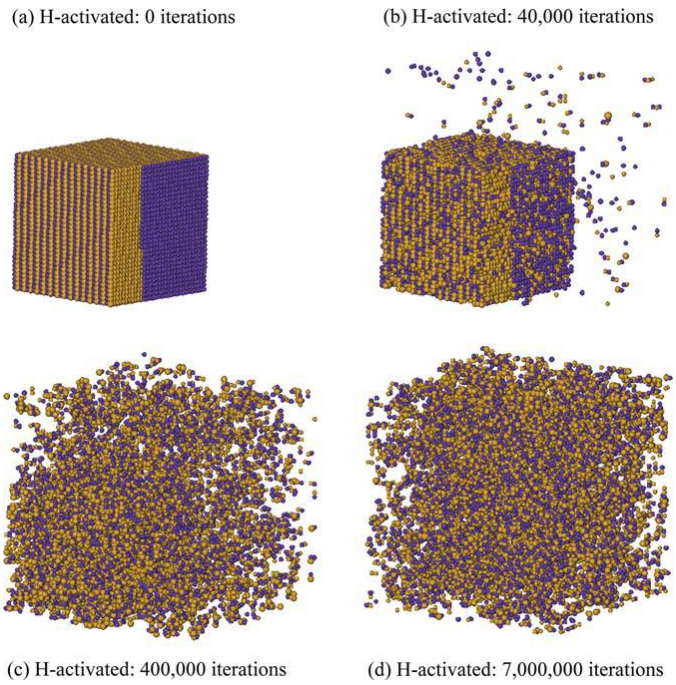

Figure 1-12. Three-dimensional snapshots of the clusters presented in the hydroxide-activated (H) geopolymer gels at various stages (number of iterations) during the simulation. The metakaolin particle is the only cluster present at the beginning of the simulation (iteration 0), as displayed in (a). Yellow spheres represent silicate sites and purple spheres are aluminate sites.

Most of the previous molecular simulations are limited to the early stages of the entire geopolymerization process or in a small scale, and thus the realistic 'geopolymeric' or 'close-to-geopolymeric' molecular structures comparable to those synthesized in the laboratory are still unknown [198]. However, geopolymer gels with different molecular structures govern largely the mechanical and physicochemical properties of geopolymer composites. On the one hand, linearly linked networks result in cohesive and rubbery properties, while those with cross-linked networks exhibit cementitious and ceramic properties; one the other hand, each molecular structure has its own applicability: poly-sialate [–SiO_4–AlO_4–] is good at thermal insulation, poly-sialate-siloxo [–SiO_4–AlO_4–

SiO_4–] has high strength and capability to solidify toxic wastes, and poly-sialate-disiloxo [–SiO_4–AlO_4–SiO_4–SiO_4–] is favorable in fire-resistance and has high bonding strength. To this end, it is important to understand the molecular structure and chemical formula of geopolymer gels, which determine the microstructure, and thus the properties of geopolymers.

1.1.9. Durability of Geopolymers in Sulfuric Acid

Sulfuric acid resistance has been a main durability issue of many Portland cement concrete structures when they are used in sewer systems or simply exposed to acid rain. As a promising alternative for OPC, the durability of geopolymers in such aggressive environments is also a concern. Via the comparison to OPC, it was found that geopolymers have a better performance after a long-term exposure to sulfuric acid [23, 199, 200]. Bakharev [23] investigated the deterioration mechanism of geopolymers in acidic environment by analyzing the microstructure change of fly ash based geopolymers after the immersion in 5% sulfuric acid. Bakharev concluded that the mechanical degradation of geopolymer in acids may be attributed to (i) the depolymerization of geopolymer gels by breaking the Si-O-Al bonds with acids, (ii) the formation of silicic acid from the released silicate monomers, (iii) the polymerization of siliceous polymers and zeolites with the silicate and aluminate monomers, and (iv) the replacement of alkali cations (Na^+ and/or K^+) by hydrogen or hydronium ions in geopolymeric frameworks. Allahverdi and Skvara [201, 202] found that the change in geopolymers in the sulfuric acid at a high concentration (pH=1.0 and 2.0) and a low concentration (pH=3.0) is different. In the geopolymer samples immersed in pH 1.0 and pH 2.0 sulfuric acid solutions, (i) the breaking of Si-O-Al bonds

and the ion replacement of Na^+ and K^+ by H^+ and H_3O^+ are the main deterioration mechanisms, and (ii) gypsum was formed, which prevented the geopolymer from being further corroded. In contrast, leaching of Na^+, Ca^{2+} and dealumination are the main deterioration mechanisms for the geopolymers immersed in the pH 3.0 sulfuric acid solution, but no gypsum deposition was found. The formation of gypsum was also reported by Thokchom et al. [199, 200], who found that the resistance of fly ash based geopolymer can be improved by increasing the concentration of Na_2O during synthesis. Bakharev found [23] that the geopolymers synthesized with NaOH have more crystalline phases and a better resistance to sulfuric acid, while the introduction of K^+ tends to lower the acid resistance of the geoplymers. Furthermore, the resistance of fly ash based geopolymers to sulfuric acid can be improved by increasing Si content in the recipe, increasing the content of calcium which can form gypsum to resist further acid corrosions, or decreasing water content which makes the resulting geopolymer denser [203]. Palomo et al. [96] tested the resistance of metakaolin based geopolymers to sulfuric acid with a 0.001M sulfuric acid ($pH \approx 2.75$). The flexural strength of the geopolymer samples showed little decrease after the immersion of 7 to 90 days, and increased after immersing for 90 to 270 days. They found that geopolymer gels kept forming during the immersion and a part of the amorphous phases was converted to faujasite crystals after the immersion of 180 days, which acts as a reinforcement in the geopolymer. Ariffin et al. monitored the performance of the geopolymer synthesized from the mix of pulverized fuel ash and palm oil fuel ash in 2% sulfuric acid for 18 months, which was barely affected and much better than OPC. The excellent acid resistance of the geopolymers was attributed to the more cross-linked microstructure compared to OPC. It can be seen that geopolymers have higher resistance

to sulfuric acid than OPC, regardless of the raw materials, whereas the mechanisms for the good resistance are not entirely the same.

1.1.10. Soil Stabilization

Soil stabilization is a process to improve the properties of the soils, such as strength, workability, plasticity and texture. The widely used stabilization processes include mechanical and chemical stabilization. By applying mechanical stabilization, the soils are blended with two or three admixtures or compacted to improve their workability and mechanical properties. The chemical stabilization is accomplished by blending chemicals and emulsions, such as binders and water repellents, and compacting to improve soil behavior, or by deep mixing and grouting. Well-established chemical stabilizers include lime, cement, asphalt, and fly ash, among which lime and cement are the most widely used. However, the energy consumption and CO_2 emission of the production of Portland cement and lime are high. A more sustainable and effective soil stabilizer is always sought in geotechnical engineering.

Cristelo et al. [38, 39] explored the effect of fly ash-based geopolymer in deep soft soil improvement by grouting. They mixed 20% to 50% fly ash with soils and grouted the warm activator (50 ℃) prepared by mixing of sodium metasilicate and 10, 12.5 or 15 molal NaOH with the soil-fly ash mix at an activator/(soil + fly ash) ratio between 0.4 and 0.5 (0.8 and 0.9 for 50% fly ash scenario). After 28 days and 1 year curing, they tested the compressive strength of the soil samples, which obtained a great improvement in the strength. They found that the strength of the soils increased with the increasing fly ash content [38] and decreasing calcium content [39]. Although the studies by Cristelo et al. showed promising

results on soil stabilization with geopolymers, there are still some concerns on their studies. Firstly, the same results in lab experiments were not able to repeat in their field tests by jet grouting. This may be due to the different grouting processes they applied in the lab and in the field, where they mixed the soil and fly ash first and then grouted the solids with the activator for the lab experiments, but they mixed the fly ash and activator first and then grouted the geopolymer with soils in the field tests. Secondly, the fly ash contents (the lowest content of 20%) they used were relatively high, which increased the consumption of alkali and silicate solutions correspondingly, and thus the cost of this technique. Lastly, the issues on the stabilization of shallow soil were not addressed in their studies.

1.1.11. Potential Applications

Other than the alternative to OPC as a cementitious binder in concrete manufacture, more applications of geopolymer as a construction material have been explored. Some of the most promising ones are reviewed herein. First of all, using geopolymers as fire-resistance coating for buildings has been widely studied because geopolymers have a much better thermal resistance than OPC. Zhang et al. [204] found that the bending and compressive strength of fly ash-metakaolin based geopolymer paste, mortar and concrete after the exposure to any high temperature between 100 ℃ and 800 ℃ are much higher than that of the OPC counterparts. In addition, class F fly ash-based geopolymer was found to retain a higher mechanical strength than metakaolin-based geopolymer after exposed to high temperatures due to its lower porosity. The mechanical strength of fly ash based geopolymers even increased after heating because of high iron content presented in the fly ashes, as shown in the studies by Zhao et al., Rickard et al. and Kong et al. [205-209].

Using geopolymer to produce lightweight construction materials is another potential. Geopolymers were used to produce geopolymer foam concretes by using autoclaves or aeroclaves as fire prevention and incombustible materials [108, 210-213]. In the above literature studies, the thermal conductivity and mechanical strength of geopolymer foam concretes were found to be comparable to OPC counterparts. More importantly, because of high temperature resistance of geopolymers, the geopolymer-based foam concrete can retain or even increase its mechanical strength after exposed to high temperatures up to 1000 ℃ [43]. In the contrast, the hydration products in OPC exhibit irreversible degradation while being exposed to any temperatures higher than 200 ℃, and dramatic strength reduction upon 600 ℃. Zhang et al. [43] suggested that geopolymer foam concrete synthesized at low temperatures with a proper concentration of gas-release agent is more sustainable and cost effective than OPC foam concrete. Particularly, fly ash based geopolymer is more suitable for producing foam concrete than metakaolin or slag, because of its lower degree of shrinkage [43].

Some other potential applications of geopolymers have also been investigated, such as in the construction of oil wells and CO_2 sequestration wells [214, 215]; immobilization of toxic metals released during mining, including Pb^{2+}, Cr^{3+}, As^{2+}, Cd^{2+}, at different efficiencies; radioactive waste cleanup; adhesives to ceramic tiles [216]; and fiber reinforced composites with polypropylene, glass, basalt, wollastonite and steel fibers, which exhibited improvement on the properties such as flexural strength, toughness, reduction of water absorption and penetration, and high temperature- and alkali-resistance [217-220].

1.1.12. Sustainability of Geopolymer Compared to OPC

The energy consumption of OPC is mainly attributed to calcination of raw limestone at a temperature higher than 1400 ℃ and production of cement from clinker. The total energy consumption of one ton of OPC is approximately 3.2 GJ while the clinker factor (e.g. proportion of clinker in cement [221]) of 0.77 is assumed [43]. Another environmental concern on OPC is the vast CO_2 emission during the manufacture. The production of 1 ton OPC emits about 821.1 to 1150kg [222-224] CO_2, of which 60% is attributed to the decomposition of limestone ($CaCO_3 \rightarrow CaO+CO_2$) and 40% to the fuel combustion. Due to the increasing demand of concrete in housing and the other infrastructure, the annual global production of cement is expected to increase from 2.8 billion tons currently to 4 billion tons, and thus the energy and CO_2 emission issues will become more severe. The cement and concrete industry keeps seaching solutions to these problems, such as improving the manufacture techniques to reduce the energy input and CO_2 output, and blending industrial wastes (e.g., granulated blast furnace slag and fly ash) with OPC instead of 100% OPC to decrease the clinker factor [43]. Van den Heede and De Bellie reported that the improved technologies can reduce the CO_2 emission up to 17% [6], while Flower and Sanjayan found that the blended cement can decrease the CO_2 emission by 13% to 22% [225]. Nonetheless, the reduction of the environmental influence by these approaches is still limited.

Geopolymer provides a promising solution for the sustainable challenges of cement concrete. During the production of geopolymer, the consumption of energy and emission of CO_2 are mainly attributed to solid raw materials, activators (e.g., alkali hydroxide and silicate solutions), and curing process. Most of the solid raw materials are industrial wastes,

which barely add any energy consumption or CO_2 emission. Although the preparation of metakaolin requires the calcination of kaolinite at the temperature of 500 ℃ to 800 ℃ [92-94], the induced energy consumption or CO_2 emission are much less than those by the combustion of limestone at >1400 ℃. The production of alkali hydroxide and silicate solution is the most energy intensive portion of geopolymer production [5], which need a large amount of electricity for the chlorine–alkali (chlor-alkali) process and energy due to the high temperature (up to 1400 ℃) request for the melting of sand and soda ash, respectively [226]. However, the proportion of alkali activators is very small, generally less than 10 wt% in geopolymer syntheses, and will not introduce a big increase of energy consumption or CO_2 emission [43]. The curing of geopolymers is even much less energy or CO_2 intensive, which usually requires a temperature in the range of room temperature to 85 ℃.

Habert et al., McLellan et al., and Turner and Collins [5, 8, 226] investigated the sustainability of geopolymers in terms of energy demand, global warming impact (CO_2) and cost through life-cycle evaluation studies. Based on the comparison between the fly ash based geopolymer cured at elevated temperatures (60 ℃~80 ℃) and OPC for the production of 1 m^3 concrete with the same strength, the estimated CO_2 emission from geopolymer concrete is 9% lower than OPC concrete, while geopolymers emit 25.2% less CO_2 than OPC [226]. In the study by Habert et al., the CO_2 emitted by fly ash based geopolymer concrete was estimated to be 45% less than that by OPC concrete [5], in good agreement with the estimation by Gabel and Tillman [227]. Duxson et al. [10] reported that geopolymer binder can achieve 80% less CO_2 emission than OPC and require a much lower water demand. McLellan et al. [8] estimated that the cost for geopolymer production can

be 7% lower to 39% higher than OPC, whereas Delton estimated that geopolymer production required 48% more energy and 67% more cost than 100% OPC [228]. As shown in the above literature studies, the most apparent environmental advantage of geopolymers over OPC is the reduction of CO_2. However, the evaluations by different studies exhibit discrepancy, which may be due to the variability in the assumption on transportation, raw materials, mix design and curing scenarios. In addition, several aspects for the lift-cycle evaluation were missed in the abovementioned studies, including the cost and environmental benefits brought by the better durability of geopolymer compared to OPC, the lower thermal conductivity of geopolymer [43, 161] that leads to a lower operational energy and CO_2 emission by housing which contributes the most to the total energy consumption and CO_2 emission [229], and the reduction of cost and environmental impact resulted by the disposal and treatment of industrial wastes by geopolymerization.

1.1.13. Conclusions

Geopolymer is a promising sustainable alternative to OPC because of its outstanding mechanical properties, low energy consumption and low CO_2 emission. Due to its high strength, low porosity, good chemical resistance and excellent fire resistance, its potential applications in concrete, soil stabilization, chemical/fire protective coating and pipes in sewer systems have been widely investigated and promising results have been obtained. However, it is still practically difficult to control or tailor the synthesis and properties of geopolymers. This is largely because the properties of synthesized geopolymers are largely influenced by various synthesis factors, including chemical composition of the starting materials (e.g., Si/Al ratio and Na/Al ratio) and curing conditions (e.g., temperature and

humidity). However, the understanding of these effects remains poorly understood because they are complex and often intertwined.

To understand the reaction kinetics, microstructure and mechanical properties of geopolymers and tailor the geopolymer synthesis for desired properties, numerous experimental and computational studies have been conducted. The formation of geopolymer gels can be confirmed qualitatively by XRD, SEM-EDX; the geopolymerization process from raw materials to the resulting geopolymer has been better understood by monitoring the chemical and molecular changes with FTIR, NMR, in-situ X-ray/neutron PDF; the reaction rate and its dependence on synthesis factors, such as temperature, chemical composition (Si/Al and Na/Al ratio) and alkali concentrations, have been investigated with ICC; and the investigation of reaction mechanisms with molecular modeling has shed light on the feasible reaction pathways and oligomers for polymerization of geopolymer gels. A great deal of strides has been achieved on geopolymerization processes, for which a three-step conceptual model, including dissolution, gelation-polymerization and condensation-crystallization, has been developed. In addition, this introduction has reviewed the durability of geopolymers in sulfuric acidic environment, the sustainable advantages of geopolymers compared to OPC and the potential applications in deep soil stabilization, foam concrete, fiber reinforced concrete and the other niche techniques. Nevertheless, the molecular configuration of geopolymer gels has not been identified, and its correlation to the mechanical properties of experimentally synthesized geopolymers and the geopolymerization kinetics remains unknown. These are the key to successfully tailor the geopolymer synthesis for a good mechanical strength. Furthermore, with the addition of another industrial waste, such as

red mud, the reaction process, development of microstructure and mechanical properties, and durability can be changed. Lastly, the feasibility of geopolymer in shallow soil stabilization has never been explored.

1.2. RESEARCH MOTIVATIONS AND OBJECTIVES

This study was driven by three main motivations: (i) helping to fill the knowledge gap in the understanding of the chemical composition-reaction kinetics-microstructure-mechanical properties relationship for geopolymer technology through an integrated multi-scale experimental and computational approach; (ii) using red mud, a massively produced and hard-to-treat industrial waste, associated with fly ash to synthesize geopolymers and examine the durability and environmental impact of the resulting geopolymers; and (iii) exploring the effectiveness of geopolymer in shallow soil stabilization.

The main objectives of this work include:

(i) To study the synthesis conditions, mechanical properties, reaction mechanisms and environmental impact of red mud-class F fly ash based geopolymers to facilitate their future applications in civil engineering. The microstructures of geopolymers were characterized by SEM-EDX, XRD and Micro-CT; and the reaction mechanisms of geopolymers were investigated with FTIR and ICC.

(ii) To obtain the mechanical properties of geopolymer gels at nanoscale, volumeric distribution of different phases in geopolymers and their effect on the mechanical properties at macro-scale with the aid of nanoindentation technique.

(iii)To predict the molecular structures of amorphous geopolymer gels and understand the polymerization process via molecular simulation.

(iv)To explore the feasibility of geopolymers as the next-generation soil stabilizer.

1.3. OUTLINE OF DISSERTATION

This dissertation consists of eight chapters. A critical and comprehensive literature review on geopolymers was presented in Chapter 1, with the focus on geopolymer synthesis, microstructural characterization and reaction mechanisms. The influence of curing condition (e.g., temperature, water content and humidity) and chemical composition (e.g., content of Si, Al and Na^+ or K^+) on the mechanical strength and microstructures (e.g., micromorphology, mineralogy and porosity) of the resulting geopolymers, as well as the reaction kinetics that have been largely investigated with mechanical tests, XRD, SEM-EDX, FTIR, NMR, MIP and ICC was reviewed. The raw materials used for the geopolymer synthesis in this dissertation were also introduced, including metakaolin, red mud and class F fly ash. The achievement and problems of literature studies on the molecular simulations, potential applications, acid resistance and environmental evaluation of geopolymers were also reviewed.

Chapters 2, 3, and 4 were devoted to synthesis and characterization of the geopolymers from two abundant industrial and fuel energy wastes, namely class F fly ash and red mud. The influence of synthesis factors, including nominal chemical composition of starting materials, curing conditions and fly ash sources, on the mechanical properties and microstructure of red mud-class F fly ash based geopolymer was studied and detailed in Chapter 2. In Chapter 3, the reaction kinetics of red mud-class F fly ash based geopolymer was investigated by using FTIR to analyze the chemical bonding change of geopolymers cured at different temperatures for the curing time up to 120 days, and correlated to the

development of mechanical strength. In Chapter 4, durability and leaching tests were conducted on the red mud-class F fly ash based geopolymers by soaking the samples in sulfuric acid and deionized water to evaluate their long-term performance and potential environmental impact.

In Chapter 5 and 6, experimental and computational studies were performed to shed lights on nano-scale mechanical properties and molecular structure of geopolymer gels. The grid nanoindentation technique was applied on metakaolin based geopolymer samples to probe the Young's modulus and hardness of geopolymer gels at nano-scale, their dependence on curing time and nominal chemical composition of the raw materials, and their correlation to the mechanical properties of geopolymers at macro-scale. In Chapter 6, density functional theory-based first principle simulations and reactive molecular dynamic simulations were performed to simulate the geopolymerization process and predict the molecular structure of geopolymer gels. The simulations were focused on the polymerization and condensation process from aluminate and silicate monomers to "geopolymeric" molecular structures.

To further broaden the potential applications for geopolymer, an exploratory research study on the feasibility of geopolymers as the next-generation soil stabilizer was presented in Chapter 7. The metakaolin-based geopolymer was used to stabilize a lean clay. The stabilized soils were compared to the OPC stabilized soils and were characterized with SEM-EDX and XRD to examine the improvement of the mechanical properties and its mechanisms.

Chapter 8 summarizes the major findings from this research study and provides some recommendations for future studies.

CHAPTER 2 - SYNTHESIS FACTORS AFFECTING MECHANICAL PROPERTIES, MICROSTRUCTURE, AND CHEMICAL COMPOSITION OF RED MUD-FLY ASH BASED GEOPOLYMERS

2.1. INTRODUCTION

Geopolymer is a family of aluminosilicates synthesized by alkali activating Si- and Al-rich materials and polycondensing tetrahedral silica and alumina [13, 75]. As an emerging class of cementitious materials, geopolymer has received increased attention from the construction material research community recently, due to its excellent mechanical properties, low energy consumption, and low CO_2 emission. Thus, geopolymer provides a viable and sustainable alternative to replace ordinary Portland cement (OPC), with a broad range of potential applications in concretes, soil stabilization, protective coating, and waste encapsulation [20, 39, 230-233]. The molecular formula of geopolymer gel can be simplified as the following [75]:

$$M_n\{-(SiO_2)_z - AlO_2 -\}_n$$

where *M* is an alkali cation that balances the negative charge for AlO_4^-, such as K^+ or Na^+, *n* the degree of polycondensation, and *z* the Si/Al molar ratio that is in the range of 1 to 15, with a limit of up to 300 [13, 75]. The geopolymerization process can be simplified as a series of reactions that interact with each other: (1) Reactive silicate and aluminate tetrahedra are dissolved from aluminosilicate raw materials in alkali hydroxide solution and/or alkali silicate solution; (2) The released Si- and Al-tetrahedra are polycondensed

into amorphous or semi-crystalline oligomers; and (3) Different types of oligomers further polymerize and harden into synthetic aluminosilicates, also called geopolymer gels [161, 234].

In principle, a wide range of materials, including the natural minerals and industrial byproducts that are rich in amorphous silica (SiO_2) and/or alumina (Al_2O_3), are potential sources to synthesize geopolymers. For instance, metakaolin [103, 235, 236], natural aluminosilicate minerals [237, 238], fly ash [14, 49, 239], granulated blast furnace slag [30, 240], red mud [56, 75, 241], rice husk ash [56, 242], and their mixtures [91], have been used to successfully synthesize geopolymers. Therefore, geopolymer technology also provides a sustainable approach to reuse industrial byproducts and wastes. Fly ash, the major waste from coal power plants, consists of fine particles that are mostly amorphous and soluble in alkali solutions. With an annual production of around 500 million tons globally [243], fly ash is considered as the fifth largest raw material resources [244]. In recent years, both class C fly ash (CFA, with a Ca content of > 20 wt.%) and class F fly ash (FFA, with a Ca content of < 20 wt.%) [245], have been used as raw materials in geopolymer synthesis. Red mud (RM), also known as bauxite residue, is the industrial waste of alumina extraction from bauxite ores via the Bayer process [73]. RM has high water content and high alkalinity with an average pH value of 11.3 ± 1.0 because a large amount of alkali is used to extract alumina. Due to these characteristics and its elevated heavy metal concentration, safe and economical disposal or treatment of RM remains a major challenge for alumina refineries. At present, RM is usually disposed into on-site waste lakes for further dewatering, consolidation, and storage. This process is very costly due to the regulatory requirements for long-term environmental monitoring and

maintenance. As reported in 2011, over 2.7 billion tons of RM is stored in land-based repositories globally, and its annual production rate is 120 million tons per year [73]. Therefore, the reuse of RM has been a main focus of many research efforts [246]. Red mud, when mixed with other Si- and Al-rich materials [46, 56, 75, 247], has been used in geopolymer synthesis for its strong alkalinity [248]. Therefore, RM-based geopolymer can have additional economic benefits by reducing the consumption of alkali activator, which is the most expensive raw material required for geopolymer synthesis.

According to previous work [90, 106, 125, 126], the mechanical properties of geopolymers are affected by many factors, such as the characteristics of raw materials (e.g., Si/Al and Na/Al ratios, the content of amorphous compounds, and particle size), curing conditions (e.g., curing temperature [52, 106, 190], curing time and curing humidity [100, 249]). With different coal sources and treatment processes used in different coal power plants, the properties of fly ash vary significantly. However, the influences of the aforementioned synthesis conditions on the mechanical and microstructural properties of RM-FFA based geopolymers (RFFG) have barely been studied systematically. Furthermore, these influences are difficult to predict because: (i) there is a lack of the information about a good starting chemical composition (e.g., nominal Si/Al and Na/Al ratios) of raw materials for synthesizing geopolymers because of highly variable chemical properties of RM and FFA from different sources; (ii) ambient temperature and humidity need to be confirmed as a suitable curing condition for the RM-FFA based geopolymers because the geopolymerization rate of FFA at room temperature is low [91]; and (iii) reliable long-term mechanical properties of RM-FFA based geopolymers need to be re-

confirmed. The above knowledge gap hinders the engineering implementation of RM-based geopolymerization as a sustainable approach for recycling RM and FFA.

In this study, geopopolymers were synthesized from RM and three FFA sources to: (i) study the effect of physical and chemical properties of FFA, nominal Si/Al and Na/Al molar ratios of raw materials and curing time on the mechanical properties of resulting geopolymers (i.e., unconfined compressive strength, Young's modulus, and failure strain); and (ii) identify a good starting chemical composition of raw materials for RM-FFA based geopolymers. Such an understanding can help obtain geopolymers with exceptional mechanical properties and durability by adjusting the constituents of raw materials. In addition, the influence of curing temperature and pre-curing time at a 100% relative humidity (RH) was investigated to further understand the curing condition-microstructure-mechanical properties relationship. The microstructural and mineralogical properties of the geopolymers were also characterized by scanning electron microscopy (SEM), X-ray diffraction (XRD), and energy-dispersive X-ray spectroscopy (EDX) to shed lights on the correlation between the chemical composition of geopolymer gels and their mechanical properties. Finally, the current study will facilitate the engineering application of RM-FFA based geopolymers as a construction material, and its findings will also provide a practical guide to synthesize geopolymers from other raw materials that were not examined in this study.

2.2. MATERIALS AND METHODOLOGY

2.2.1. Materials

The raw materials used for geopolymer synthesis include RM and three FFA sources. Moist, soil-like RM was acquired from Alcoa World Alumina, LLC. The received RM was first oven-dried at 100 ℃, and then ground until all particles passed through a No. 100 sieve (i.e., mesh opening size of 0.152 mm), in order to better control the synthesis process and facilitate geopolymerization. FFAs were obtained from two coal power plants: Headwater Resources Inc. (denoted as HW) and Boral Material Technologies Inc. (denoted as B1 and B2, which were two different batches acquired at different time). The particle size distributions of these raw materials in **Figure 2-1** show that the RM is the finest component and HW FFA is slightly finer than B1 and B2 FFA. The median particle sizes (D_{50}) are 16, 20, and 25 μm for HW, B1, and B2 FFA, respectively, while the D_{50} of RM is 1.9 μm. The chemical compositions of the raw materials are listed in **Table 2-1**. RM is largely composed of SiO_2, Al_2O_3, Fe_2O_3, and CaO, along with some trace elements. The major constituents of HW, B1, and B2 FFA are SiO_2 and Al_2O_3, of which the amorphous phases are the main reactive components for geopolymerization. The alkali activator was the mixture of sodium hydroxide solution with a NaOH concentration of 50 wt.%) and 2 M sodium trisilicate solution.

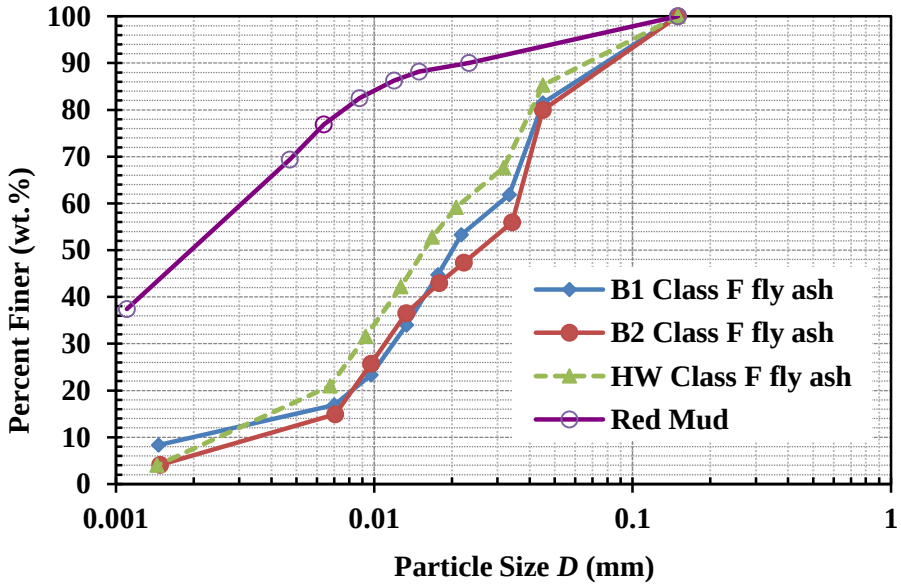

Figure 2-1. Particle size distributions of raw materials used for geopolymer syntheses.

Table 2-1. Chemical and physical properties of red mud and class F fly ash.

Properties	RM	HW FAA	B1 FFA	B2 FFA
Chemical Composition (wt.%)				
SiO_2	22.82	57.91	53.72	52.50
Al_2O_3	15.06	27.44	28.43	28.24
Fe_2O_3	17.34	6.32	7.97	8.60
CaO	12.24	1.30	1.68	1.57
MgO	0.27	--	0.85	0.92
Na_2O	4.37	--	0.35	0.30
K_2O	1.19	--	2.44	2.63
SO_3	--	0.21	0.12	0.92
MnO	0.36	--	--	--
P_2O_5	2.43	--	--	--
TiO_2	3.43	--	--	--
Loss in ignition	15.75	2.15	2.43	3.08
Specific Gravity	2.93	2.39	2.30	2.29
Median particle size (μm)	1.9	16.0	20.0	25.0

2.2.2. Synthesis Process

For each sample set, a RM to FFA mass ratio of 1:4 was used based on the following considerations: (1). Previous research results indicate that the strength decreases with the increase in RM fraction [75]; and (2) it is desirable to use RM at a maximum amount to partially replace the expensive alkali solutions. The nominal Na/Al molar ratios between 0.6 and 1.0 with a fixed nominal Si/Al molar ratio of 2 were used, based on previous literature studies for geopolymers with a high strength and preliminary experimental results by the authors [55, 100, 103, 125]. The nominal Si/Al and Na/Al molar ratios were calculated from the chemical composition of raw materials and activator solutions. As reported by Steveson and Sagoe-Crentsil [105], the mechanical strength of fly ash based geopolymers is higher when the geopolymer precursor is drier. Therefore, the water content was kept as low as possible while adequate workability was still maintained for the sample preparation. The water content was defined as:

$$Water\ content = \frac{Weigh\ of\ water\ in\ the\ activator + Weight\ of\ extra\ water}{Weight\ of\ solid\ raw\ materials + Weight\ of\ activator} \quad (2.1)$$

Because the water content is dependent on the chemical composition of the raw materials (e.g., Si, Al, and Na concentrations), different sample sets cannot have the same water content while their Si/Al and Na/Al ratios are kept the same. The latter (i.e., Si/Al and Na/Al molar ratios) was the major synthesis factors to be investigated in this study. Nevertheless, water contents among different sample sets were kept as close to each other as possible. **Table 2-2** shows the water contents of different sample sets, at which these mixes reached roughly equivalent consistency during mixing. The nominal chemical composition of each sample set was achieved by adjusting the sodium hydroxide

solution/sodium trisilicate solution ratio that is in the range of 0.22 to 0.43, and the water content was controlled by adding the predetermined amount of deionized water.

Table 2-2. Summary of synthesis parameters for the geopolymer samples investigated in this study.

Sample Set and Study Objectives	Sample	Fly Ash Resources	Na/Al Molar Ratio	Water Content	Curing Temperature (℃)	Curing time at 100% RH (Days)	Total Curing Period (Days)
A: Chemical composition vs. mechanical properties	B2-NA7	B2	0.7	27%	~23	0	28
	B2-NA8		0.8	26%			
	B2-NA10		1.0	28%			
B: Influence of curing temperature and fly ash properties	HW-T23	HW	0.6	23%	~23	0	28
	HW-T50				50		
	HW-T80				80		
	B1-T23	B1	0.6	21%	~23	0	28
	B1-T50				50		
	B1-T80				80		
	B2-T23	B2	0.7	23%	~23	0	28
	B2-T50				50		
	B2-T80				80		
C: Influence of precuring time at 100% RH	HW-R0	HW	0.6	23%	~23	0	28
	HW-R1					1	
	HW-R3					3	
	HW-R5					5	
	HW-R7					7	
D: Influence of total curing period	HW-P14	HW	0.6	23%	~24	0	14
	HW-P21						21
	HW-P28						28
	HW-P49						49
	HW-P91						91
	HW-P180						180
	B2-P14	B2	0.7	27%	~23	0	14
	B2-P21						21
	B2-P28						28
	B2-P49						49
	B2-P91						91
	B2-P180						180

The alkali activator solution was premixed and cooled down to room temperature, and poured into a mixer. The RM and FFA were dry mixed, and then blended thoroughly with the activator for about 30 minutes to obtain geopolymer precursor with a slurry to paste consistency. The precursor was then poured into cylindrical molds, which have an inner diameter of 40 mm and a height of 100 mm, with an aspect ratio of 2.5 to minimize the end effects in unconfined compression testing. Before curing, all samples were vibrated in molds for about 5 minutes to remove air bubbles introduced during mixing and pouring. Three replicates were prepared for each sample set.

As summarized in **Table 2-2**, different synthesis schemes and curing conditions were designed to investigate the effect of fly ash properties, Na/Al molar ratio, and curing conditions (i.e., curing time at ambient conditions, pre-curing time at 100% RH, and curing temperature) on the mechanical and microstructural properties of RFFG. The ambient condition herein and in the following sections is referred to the temperature of 23 ℃ and RH of 40% to 50%. The specific objective of each sample set is also summarized in **Table 2-2**. The sample identifier nomenclature is: *FFA source-synthesis factor + the value of synthesis factor (or n)*. For Sample Set A, NA stands for Na/Al molar ratio and *n* is the nominal Na/Al molar ratio of the starting materials (7, 8, and 1 stand for 0.7, 0.8 and 1.0, respectively); for Sample Set B, T stands for curing temperature and *n* is the temperature value in Celsius; for Sample Set C, R stands for relative humidity and *n* is the curing days at 100% RH; and for Sample Set D, P stands for curing period and *n* is the curing days.

The samples of HW-T80, B1-T80 and B2-T80 were sealed in plastic bags and curried in an oven at 80 ℃ for 1 day, and cured at ambient conditions for the next 27 days before compression tests. The samples of HW-T50, B1-T50 and B2-T50 were sealed and cured at 50 ℃ in an oven for 7 days, and continued to cure at ambient conditions for the next 21 days. For Sample Set C, they were sealed and pre-cured in a 100% RH curing room for 0, 1, 3, 5, and 7 days, respectively, and then further cured at ambient conditions for a total curing time of 28 days. The rest of the samples were cured at ambient conditions for different time as shown in **Table 2-2**. The ambient conditions were achieved with the assistance of a plastic chamber equipped with a humidifier to keep the RH in the range of 40~50%. Preliminary experimentation found that a RH of lower than 40% resulted in cracking of geopolymer samples, and a RH higher than 50% caused carbonation on the sample surface that was detrimental for strength development.

2.2.3. Mechanical and Microstructural Characterization

To investigate mechanical properties of RFFG, including unconfined compressive strength (UCS), failure strain (ε_f), and Young's Modulus (E), unconfined compression tests were conducted on the samples in an Instron loading frame at a constant rate of 0.5 in./min. The sample's top surface was covered with a cardboard to reduce the effect of uneven surface formed during curing.

Chemical and microstructural properties of the raw materials and geopolymers were also examined. The mineralogical composition of RM and FFAs were characterized by XRD in a Rigaku Geigerflex X-ray powder diffractometer using a Cu Kα radiation emitted at a voltage of 37.5 kV and a current of 25 mA. The XRD data were collected from 5 °to

70 °2θ at scan speed of 0.05 °/step and 1.0 sec/step, which were analyzed with the software MDI Jade 5.0. The micromorphology of the raw materials and the geopolymer samples were examined with a JEOL JSM-7000F field emission SEM in backscatter mode. The chemical composition of the characteristic structures within the selected geopolymer samples was estimated based on the EDX measurements with an OXFORD INCA X-act instrument. Small pieces of the geopolymer samples after unconfined compression tests were used in the SEM-EDX test. The external surfaces of the cylindrical samples were avoided for microstructure evaluation, because excessive oxidation might have occurred on sample surfaces during curing, which is not representative of the bulk geopolymer [71].

2.2.4. ANOVA Analysis

Statistical analyses with the one-way analysis of variance (ANOVA) method were conducted with the IBM SPSS v.17 on the mechanical property data that do not show a clear trend. The standard significance α of 0.05 was assumed for all the statistical tests, which means that, if the *P*-value of a statistical test is less than 0.05, at least one of the population means is different from the others; otherwise the difference among the population means is not statistically significant [250].

2.3. RESULTS AND DISCUSSION

2.3.1. Micromorphology of Raw Materials

SEM micrographs in **Figure 2-2** indicate that FFA consists of solid and hollow spherical particles; and RM particles are flaky-shaped with visible agglomerates of a few micrometers (μm) in size, which are probably formed by grinding. The particle size of RM

is smaller the FFAs, which agrees with the particle size distribution curves shown in **Figure 2-2**.

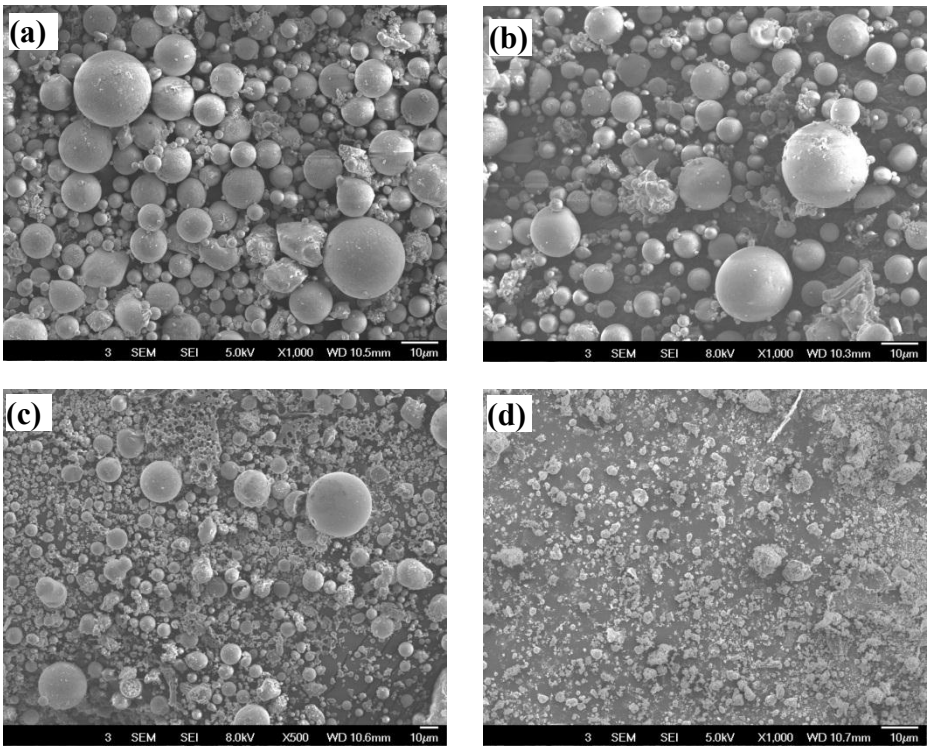

Figure 2-2. SEM images of raw materials used to prepare geopolymers: (a) B1 FFA; (b) B2 FFA; (c) HW FFA; and (d) RM.

2.3.2. Mechanical Properties of Geopolymers

2.3.2.1. Correlation between Mechanical Properties and Chemical Composition

The mechanical properties of RM-B2 FFA geopolymers synthesized at different initial Na/Al molar ratios are summarized in **Table 2-3**. **Table 2-3** also includes the estimated Si/Al and Na/Al molar ratios of the resulting geopolymer gels based on EDX measurements. The geopolymers, except for B2-NA10, have compressive strength comparable to that of OPC. The estimated chemical composition of geopolymer gels is quite different from the

initial values. Such a discrepancy is expected because: (i) not all the silica and alumina in the raw materials are amorphous (i.e., reactive); (ii) only part of the reactive silica and alumina participated in geopolymerization and eventually became part of the synthesized geopolymer gels; and (iii) the EDX measurement-based ratios reflect most of the silica and alumina present in geopolymer gels instead of the quantities in the whole geopolymer samples. As expected, UCS and E values increased with the Na/Al ratios of geopolymer gels, because a higher Na/Al molar ratio represents a higher degree of geopolymerization. One function of Na^+ cations is to balance the negative charge of 4-coordinate Al^{3+} and the amount of Na and Al should be the same in ideally stoichiometric chemical composition of geopolymer gels. The EDX Na/Al molar ratios shown in **Table 2-3** are higher than 1. This is because the EDX tested areas might include some constituents with a higher Na content (e.g., zeolite crystals) and/or a lower Al content (e.g., fly ash). However, there is no apparent trend of the mechanical properties against the Na/Al ratios of the starting materials. This implies that the mechanical properties were more dependent on the chemical composition of the geopolymer gels other than the starting materials. However, only qualitative interpretation can be made with the limited data. The results indicate that the RM-B2 FFA based geopolymer samples achieved the maximum UCS values at the starting Na/Al ratio of 0.8. The optimal Na/Al molar ratios of starting materials exhibit slight dependence on fly ash sources, whose values are 0.6 and 0.7 for RM-HW FFA based and RM-B1 FFA based geopolymers, respectively.

Table 2-3. The EDX and UCS results of RM-B2 FFA based geopolymers with different starting Na/Al molar ratios cured at ambient conditions for 28 days.

Sample	Starting Si/Al[a]	Starting Na/Al[a]	EDX Si/Al[b]	EDX Na/Al[b]	UCS (MPa)	E (GPa)	ε_f (%)
B2-NA7	2.0	0.7	3.1	1.5	10.5	0.36	2.87
B2-NA8	2.0	0.8	3.6	1.6	13.5	0.56	2.37
B2-NA10	2.0	1.0	2.8	1.3	6.1	0.18	3.23

[a]The starting Si/Al and Na/Al are the nominal Si/Al and Na/Al molar ratios calculated based on the chemical composition of the starting materials respectively; and [b]the EDX Si/Al and Na/Al are the Si/Al and Na/Al molar ratios of the resulting geopolymer gels estimated from the EDX measurements.

Both UCS and E values increased with the Si/Al ratio of geopolymer gels, while ε_f value decreased. The normalized UCS values (i.e., UCS values divided by the respective maximum UCS value) are plotted against the Si/Al ratios of geopolymer gels in **Figure 2-3**, along with the results reported in previous studies. The two sample sets reported by Steveson et al. [105, 179] were FFA based and metakaolin based geopolymers, respectively, cured at 85 ℃, while the one by Duxson et al. [31] was metakaolin based geopolymer cured at 40 ℃. Ahmari et al. [251] reported FFA-ground waste concrete based geopolymers cured at ambient temperature, of which the optimal Si/Al ratio is the closest to the optimal value in this study. As shown in **Figure 2-3**, the mechanical strength of the geopolymers increased with the Si/Al ratios within a reasonable range. The maximum UCS in this study was obtained at a higher Si/Al ratio than the others in the literature. This discrepancy might be due to the fact that: (i) different raw materials and curing conditions were used in these studies; and (ii) the Si/Al ratios in this study were estimated on the basis of the EDX experimental measurements, while the Si/Al ratios from the literature were estimated from the nominal composition of raw materials.

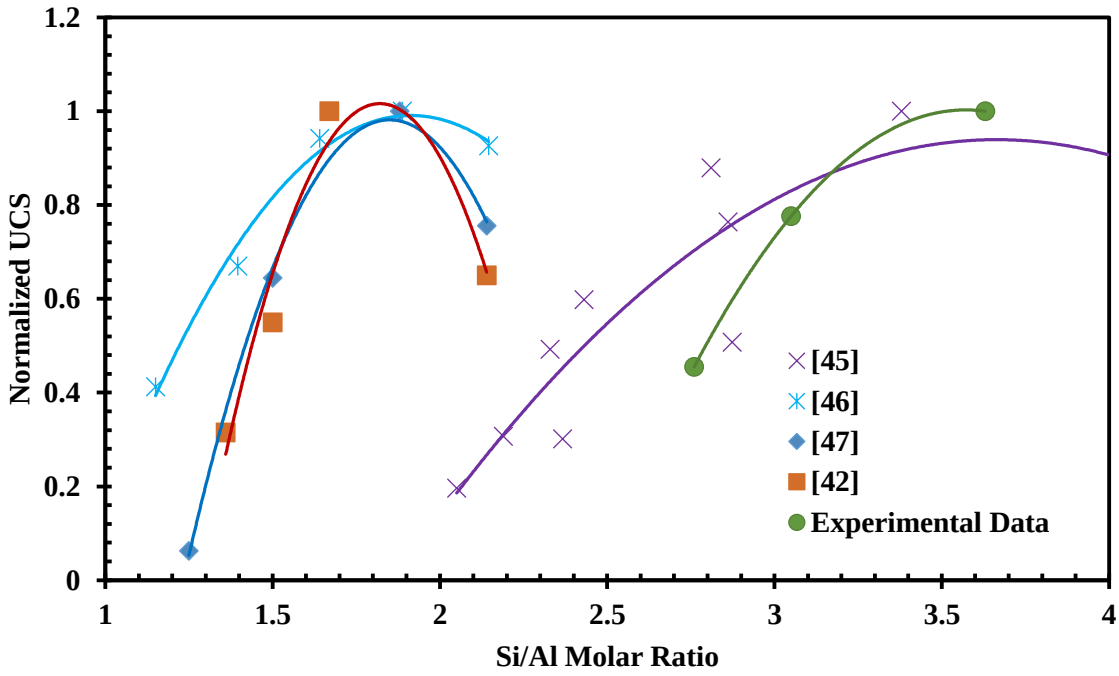

Figure 2-3. Normalized UCS vs. Si/Al molar ratio (estimated based on EDX Measurements) of sample set A in the current study and previous studies reported in literature [31, 105, 179, 251].

2.3.2.2. Influence of Curing Temperatures and Fly Ash Properties

To study the influence of curing temperature on the mechanical properties of geopolymer, Samples Set B were cured at ambient temperature, 50 ℃ and 80 ℃, respectively. In addition, three sample batches were synthesized with three different raw material mixes to examine the influence of fly ash sources, as shown in **Table 2-2**.

The UCS, ε_f, E and bulk density (ρ) of all the samples cured for 28 days are shown in **Figure 2-4** (a) to (d). The values shown in **Figure 2-4** are the average of three samples with the standard deviation. The UCS of the samples cured at room temperature ranges from 11.3 to 21.3 MPa, which is comparable to almost all types of Portland cement listed

in ASTM C150 with the compressive strength of 8-21 MPa [252]. The mechanical strength of the geopolymers synthesized in this study also generally agrees with the results reported by Zhang et al. [75], although they used Class C fly ash and a different red mud source to synthesize geopolymers.

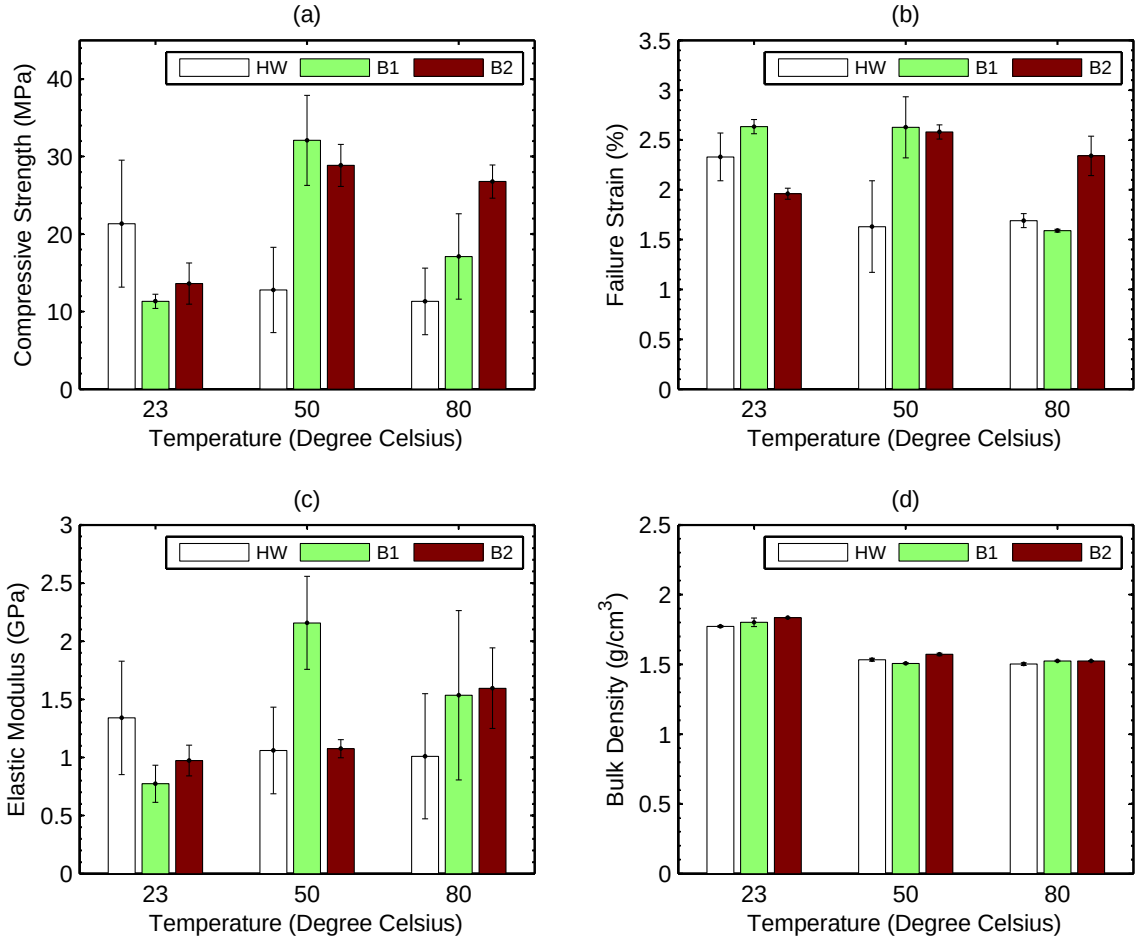

Figure 2-4. Mechanical properties of geopolymers cured at different temperatures: (a) UCS; (b) ε_f; (c) E; and (d) ρ (the legend is used to explain FFA sources). The error bars represent one standard deviation, which applies to other figures as well.

The influence of curing temperature on UCS, E, and ε_f all depend on FFA sources. For RM-HW FFA based geopolymers, the average UCS and E decreased with curing temperature; whereas for RM-B1 FFA and RM-B2 FFA based geopolymer samples,

elevated curing temperatures resulted in higher average UCS and E values than ambient temperature. The ε_f of HW-T23 is higher than HW-T50 and HW-T80; while the ε_f values of B1-T23 and B1-T50 are higher than B1-T80; however, the ε_f of B2-T50 is the highest among the three RM-B2 FFA based geopolymer samples. The density of the samples cured at elevated temperatures is lower than that at room temperature, as shown in **Figure 2-4** (d), which might be caused by more water evaporated at higher temperatures.

The trends in mechanical properties of the geopolymer samples observed in **Figure 2-4** are the reflection of the intertwined effects of raw material properties and curing conditions during complex geopolymerization processes. During the synthesis process, curing temperature, water content, particle fineness and crystallinity of the FFA sources, affect the degree of geopolymerization and hence the mechanical properties of the resulting RFFG. For each sample set synthesized from the same FFA source, the geopolymer samples cured at 80 ℃ show slightly lower mechanical strength than those cured at 50 ℃. The strength reduction of geopolymers cured at the temperature higher than 80 ℃ was also reported in the previous studies [14, 87]. This might be caused by the quick loss of moisture that has detrimental effect on the mechanical strength development of geopolymers. RM-HW FFA based geopolymer samples have higher mechanical strength than B1 and B2 FFA counterparts cured at ambient temperature. This is probably because HW FFA has finer particle size that is easier to dissolve, as shown in **Figure 2-1**, and thus a higher degree of geopolymerization can be achieved in HW FFA based geopolymer. Previous studies showed the crystallinity plays a more important role in geopolymerization and thus mechanical properties of geopolymers at an elevated temperature [253, 254]. However, this might not be the case in this study. RM-HW FFA based geopolymer showed lower

mechanical strength than the B1 and B2 FFA counterparts cured at 50 ℃, yet HW FFA has a higher crystalline content than B1 and B2 FFA, as shown in the subsequent sections. The discrepancy in their UCS values at 50^{o}C might be attributed to the different particle fineness of the FFAs used in this study. The coarser particles of B1 and B2 FFA, which were not dissolved in the mixing process, might be dissolved and react at 50 ℃ during the curing. The finer particles of HW FFA dissolved and polymerized at a higher degree in the mixing process might adhere to the surface of unreacted particles and block the interior crystals from being dissolved and participating in the further geopolymerization reaction. The effect of amorphous and crystalline contents of FFA on the mechanical properties of the resulted geopolymer needs to be further investigated with the aid of analytical XRD technique.

2.2.2.3. Influence of Pre-curing Time at 100% Relative Humidity

The Sample Set C of RM-HW FFA based geopolymer were pre-cured at 100% RH for different time periods to identify a reasonable curing humidity associated with ambient temperature.

The UCS, ε_f, E and ρ values of these samples and the control group HW-R0 are shown in **Figure 2-5** (a)-(d). The highest average UCS and ε_f values were achieved when the samples were pre-cured at 100% RH for 3 days. The average E values initially decreased with increasing curing period at 100% RH until 3 days, and remained nearly constant afterwards. However, there are no apparent trends in **Figure 2-5** due to data scattering. These mechanical results were further interpreted by ANOVA analysis to understand their statistical trend.

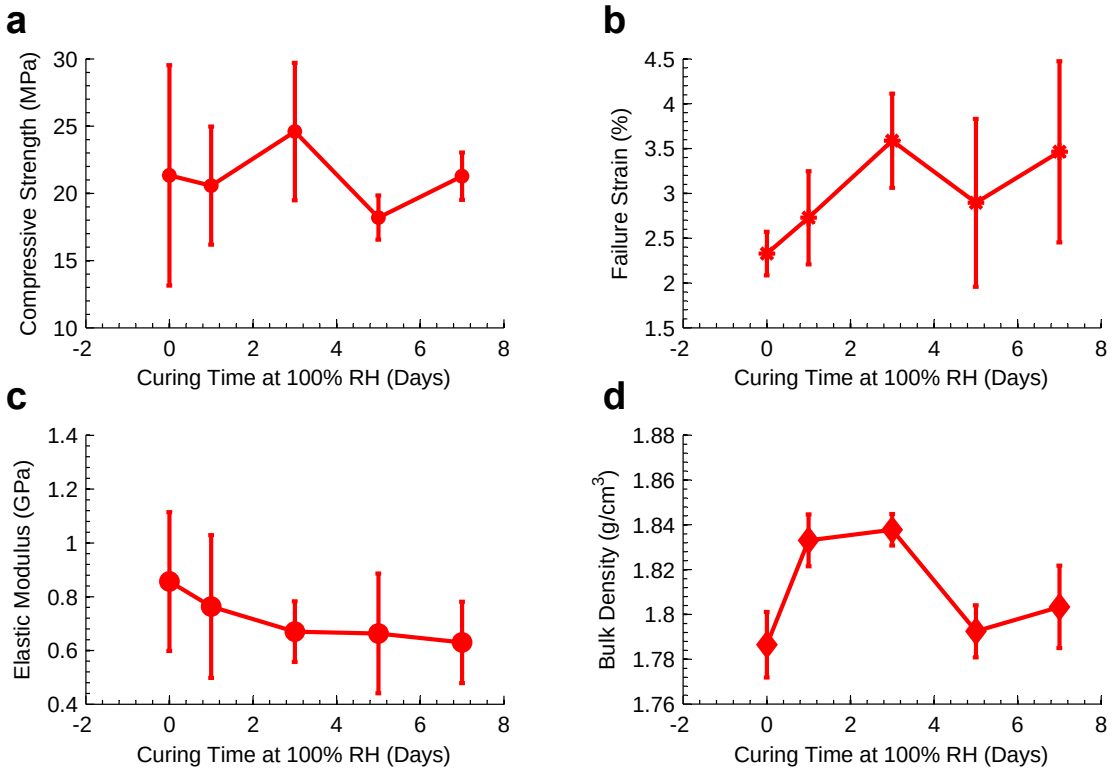

Figure 2-5. The mechanical properties of RM-HW FFA based geopolymer precured at 100% RH for different periods: (a) UCS (b) ε_f; (c) E and (d) ρ.

The P-values of the ANOVA analyses for UCS, ε_f and E are 0.631, 0.604 and 0.795 respectively, all larger than 0.05. This indicates that no apparent statistical difference in each measured mechanical property of RM-HW FFA based geopolymers was caused by different pre-curing time at 100% RH. Therefore, ambient RH is the preferable curing humidity for both practical applications and desired mechanical properties of RFFG.

2.2.2.4. Influence of Total Curing Time

Figure 2-6 (a)-(d) show the mechanical properties and bulk density of the geopolymer samples of Sample Set D cured for up to 180 days, (see **Table 2-2** for sample information). The UCS of RM-HW FFA based geopolymer samples increased quickly during the initial

28 days curing, and remained largely constant afterwards; and the UCS of RM-B2 FFA based geopolymer kept increasing within 91 days, and remained constant thereafter (see **Figure 2-6** (a)). The UCS values of RM-B2 FFA based geopolymers were lower than those of the RM-HW FFA counterparts when the curing time was shorter than 49 days. The quicker early strength development of RM-HW FFA based geopolymes can be attributed to finer particles of HW FFA compared to B2 FFA (see **Figure 2-1**), which possesses larger reaction surfaces leading to a higher degree of reaction. On the other hand, the ANOVA analysis results, which are 0.304 and 0.177 respectively, indicate no statistical difference in the UCS values of these two sample sets after they were cured for more than 91 days.

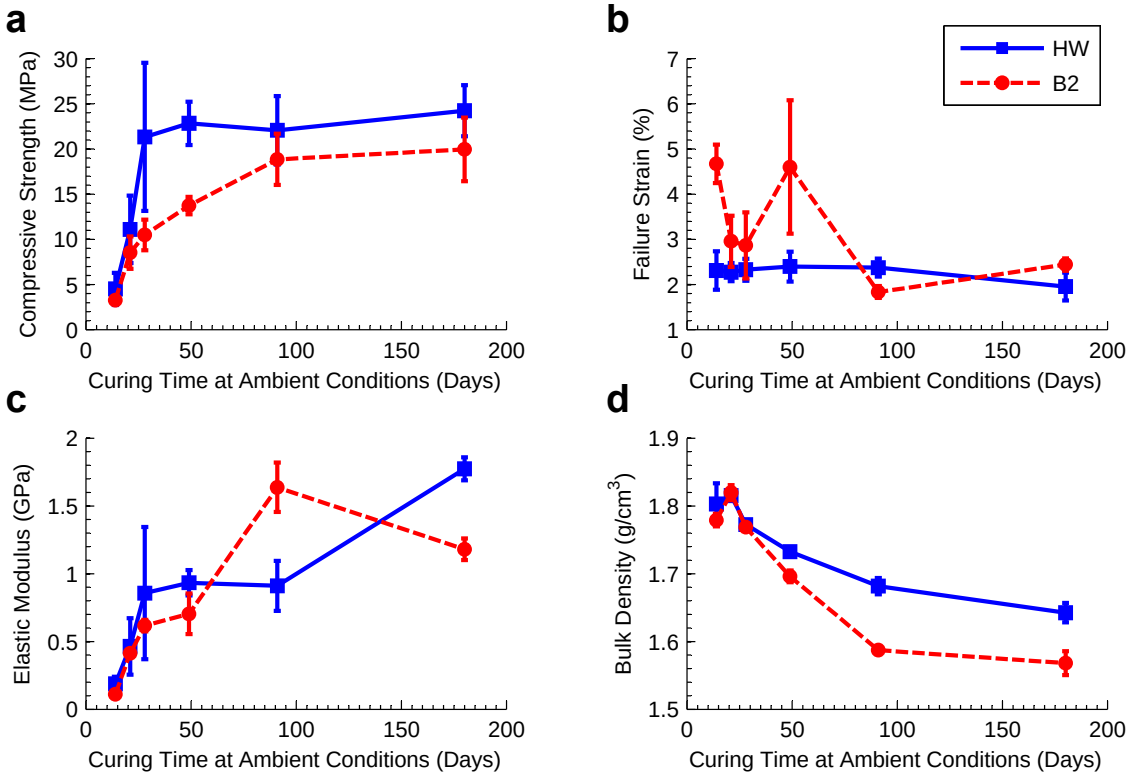

Figure 2-6. The mechanical properties of RM-HW FFA and RM-B2 FFA based geopolymers cured at ambient conditions for different curing time periods: (a) UCS; (b) ε_f; (c) E; and (d) ρ (the legend is used to explain FFA sources).

The ε_f of RM-HW FFA based geopolymer (see **Figure 2-6** (b)) remained relatively constant during the whole curing period, which illustrates that the ductility of this geopolymer is barely affected by the extended curing time. On the other hand, the ε_f of RM-B2 FFA based geopolymer decreased with curing time except for the outliner on the 49th day. The difference in these two curves further elucidates the dependence of ductility on the FFA properties. The E values of these two geopolymers increased with the extended curing time, which have not reached their steady state even for 180 days curing. The decreasing trend of density of these two sample sets (**Figure 2-6** (d)) probably resulted from the continuous water evaporation during curing at ambient conditions.

The results in **Figure 2-6** illustrate that RFFG do not degrade with prolonged curing and its strength and stiffness can further improve. This implies that the mechanical properties of the RFFG are likely to remain steady or even be enhanced during the service.

2.3.4. Microstructural Properties of Geopolymers

2.3.4.1. Influence of different fly ash sources

The SEM micrographs of selected geopolymer samples of HW-T23, B1-T23 and B2-T23 are shown in **Figure 2-7** (a)-(c). Geopolymer gels are identified in all three samples, of which the microstructure is continuous and homogenous with some crystals embedded in the gel matrix. Based on the EDX spectra, the estimated Si/Al molar ratios are 5.05, 2.51 and 2.3, and the estimated Na/Al molar ratios are 2.15, 0.93 and 0.90 for HW-T23, B1-T23 and B2-T23, respectively. The estimated Na/Al and Si/Al molar ratios are similar between B1-T23 and B2-T23, which might be due to the similarity between B1 and B2 FFA that were produced from the same power plant. However, the estimated Si/Al and Na/Al ratios

of HW-T23 are much higher than the other two samples. This might be because the detected areas in HW-T23 sample may consist of other components besides geopolymer gels, such as fly ash particles with a Si/Al ratio of >3, and zeolite crystals with a Na/Al ratio of >1.0. The microstructure of the final RFFG composites seems similar regardless of FFA sources. However, the difference in the EDX measurements illustrated the chemical composition of the geopolymer gels is highly dependent on the FFA properties.

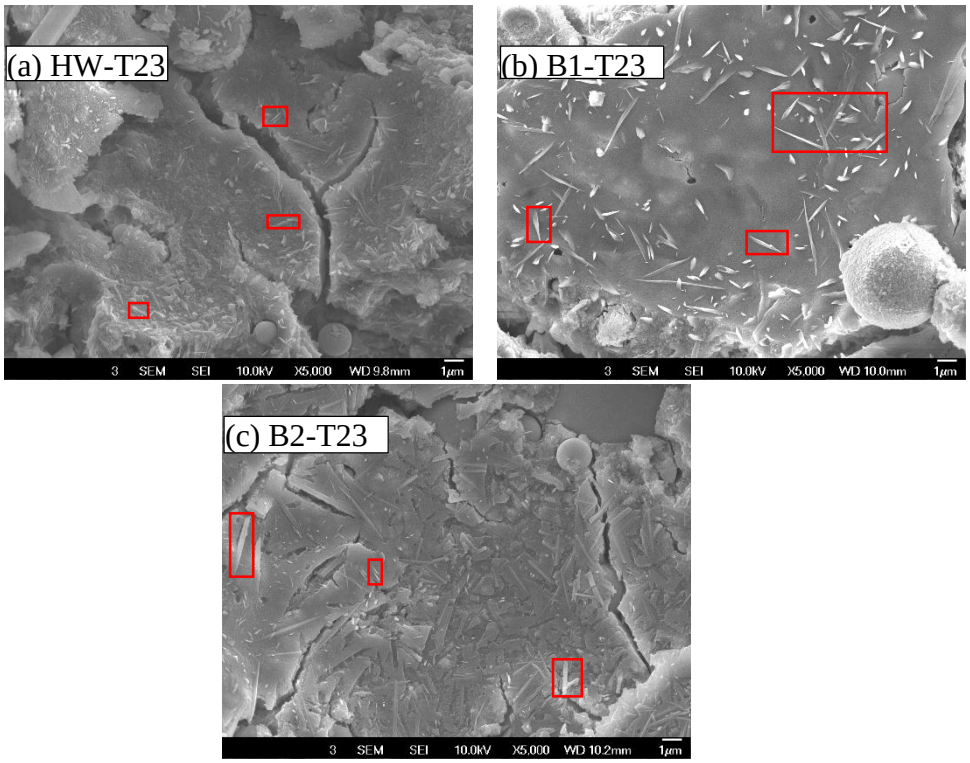

Figure 2-7. SEM micrographs of (a) HW-T23; (b) B1-T23; and (c) B2-T23. (The selected areas by the rectangles indicate crystals.)

2.3.4.2. Influence of curing temperature

Figure 2-8 (a)-(c) show the SEM images and the corresponding estimated chemical compositions based on the EDX results of the selected geopolymer samples of B2-T23, B2-T50 and B2-T80, respectively. As seen in the SEM images, all the geopolymer samples consist of geopolymer gels, unreacted FFA spheres and RM flakes, crystals, micro-pores, and micro-cracks. This indicates the composite nature of geopolymers, which has also been reported in previous studies [75].

The unreacted FFA is distinguishable because of its spherical feature, which is also confirmed by the EDX spectra of the spheres that show oxygen, silicon and alumina, but no sodium. This agrees well with the chemical composition of B2 FFA summarized in **Table 2-1** that the amount of Na is small and undetectable with EDX. Continuous and homogenous geopolymer gels with microcracks and some semi-spherical dents surround the FFA spheres. The dents might be formed after the fly ash spheres were removed during the unconfined compression tests or SEM sample preparations, while the microcracks might be formed by the drying process during curing or loading process during compression tests. Due to the heterogeneity of RM and FFA, it is likely that the geopolymer gels with different degree of geopolymerization were resulted within the geopolymer samples. This probably explains the spatial difference in the EDX measured Si/Al and Na/Al ratios at different spots (see the inset table in **Figure 2-8**). In addition, the surrounding area might affect these tested spots, which could be unreacted raw materials or non-reactive impurities and crystals with very different Si/Al and Na/Al ratios than those of geopolymer gels. Nevertheless, most of the selected spots in geopolymer gels have a

Na/Al ratio around 1 and a Si/Al ratio in the range of 1-3, which is a typical range for geopolymer gels.

As observed in **Figure 2-8**, the higher the curing temperature is, the more homogeneous is the geopolymer morphology. Some needle- or leaf- shaped crystals are found in **Figure 2-8** (b) and (c) for the geopolymers cured at 50 ℃ and 80 ℃, but fewer in **Figure 2-8** (a) for the counterpart cured at room temperature. Based on their shapes and chemical compositions estimated from the EDX results shown in the inserted table, the crystals probably belong to zeolites (e.g., (c)4). Zeolite crystal formation in geopolymer systems at elevated curing temperature was also reported by previous literature study [179]. Higher temperature accelerated the motion of existing oligomers in the goepolymer precursor to further condense to crystalline-like structure. The consumption of the oligomers triggered the release of more reactive Si- and Al-tetrahedra and generated more oligomers to participate in the geopolymerization. In other words, higher temperature promoted the reaction of the geopolymer system. More homogeneous morphology and the formation of crystalline components illustrate a higher degree of geopolymerization, which might be the reasons for higher strength, ductility and stiffness of B2-T50 and B2-T80 geopolymers, as shown in **Figure 2-4** (a) and (b). Similar findings were also reported by previous work [247]. However, as discussed previously in Section 2.3.2.2, the influence of curing temperature is intertwined with raw materials' properties, such as particle fineness and amorphous contents.

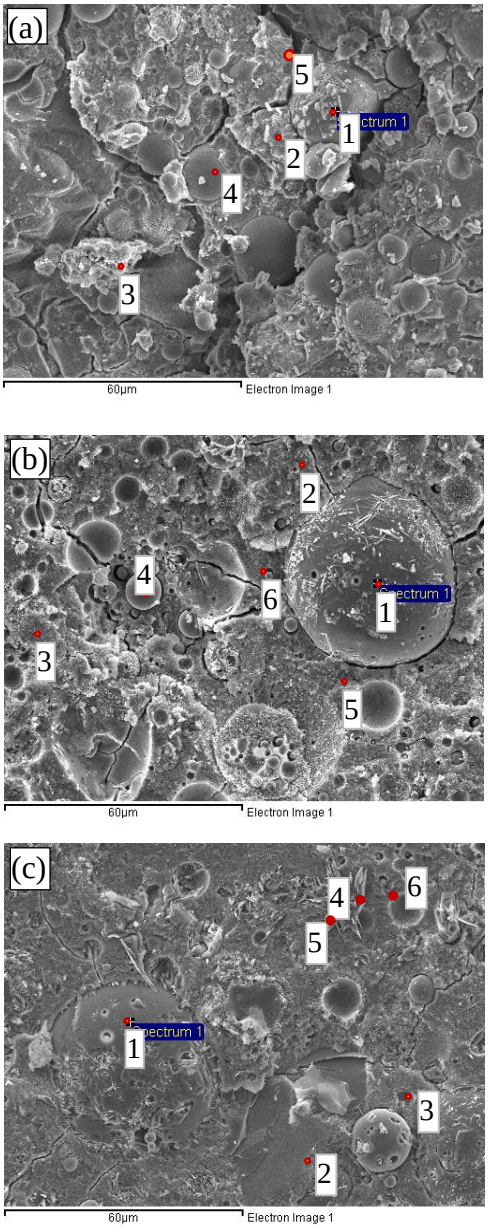

EDX Spot	Si/Al Molar Ratio	Na/Al Molar Ratio	Constituent
(a) 1	1.7	NA	Fly Ash
(a) 2	3.3	2.7	Geopolymer Gel
(a) 3	4.0	1.4	Geopolymer Gel
(a) 4	1.4	NA	Fly Ash
(a) 5	3.2	1.8	Geopolymer Gel
(b) 1	2.0	NA	Fly Ash
(b) 2	5.0	6.7	Geopolymer Gel
(b) 3	1.8	4.2	Geopolymer Gel
(b) 4	1.2	NA	Fly Ash
(b) 5	4.0	3.6	Geopolymer Gel
(b) 6	3.5	0.8	Geopolymer Gel
(c) 1	2.1	NA	Fly Ash
(c) 2	2.9	2.3	Geopolymer Gel
(c) 3	4.3	5.9	Geopolymer Gel
(c) 4	0.9	1.9	Zeolite
(c) 5	1.9	0.9	Geopolymer Gel
(c) 6	1.0	0.8	Geopolymer Gel

Figure 2-8. SEM-EDX results of geopolymer samples: (a) B2-T23; (b) B2-T50; and (c) B2-T80 (The inserted elemental molar ratios are estimated on the basis of EDX measurements; NA: not available.).

2.3.5. Mineralogical Composition of Geopolymers

Figure 2-9 shows the XRD patterns of RM, FFAs, and the RFFG samples cured at ambient conditions for 28 days. Only the patterns in the range of 15° to 40° are shown in **Figure 2-9**, because no characteristic peak was detected in the rest of diffraction angles. As seen in the XRD patterns, the crystalline silica and alumina components in the raw materials are mainly quartz and mullite. RM is highly crystalline that shows peaks of calcite, hematite and quartz, which agree well with the chemical compositions in **Table 2-1**, with relatively high concentrations of Fe and Ca in RM. Therefore, the solubility of RM in an alkali activator solution is probably low, and it might only act as inactive fillers and partially contributes to the high alkalinity required for geopolymer syntheses. All the FFA spectra show the existence of broad humps that represent amorphous components, implying that FFAs are the major reactive raw materials in the alkali activation. The crystalline content in HW FFA, especially the quartz around 27 º, is higher than that in B1 and B2 FFA, as seen in the area encompassed by the peaks in **Figure 2-9**. Therefore, the solubility of HW FFA in alkali solutions is lower than B1 and B2 FFA, agreeing well with the previous study [255]. In the XRD patterns of HW-T23, B1-T23, and B2-T23 geopolymer samples, there is a broad hump in the range of 17 º to 38 º, which is the typical XRD pattern for the amorphous geopolymer. However, because of the high peak of quartz, the geopolymer hump is less apparent, especially in HW-T23. Some peaks from the raw materials remained in the corresponding geopolymer patterns, but with reduced intensity, which is attributed to the unreacted crystalline contents, such as the quartz around 21 °and 33 °, and the Mullite around 35 °. The peaks from the remaining calcite and hematite in all the geopolymer patterns are invisible because RM proportion in the raw material mix was low (20 wt.%).

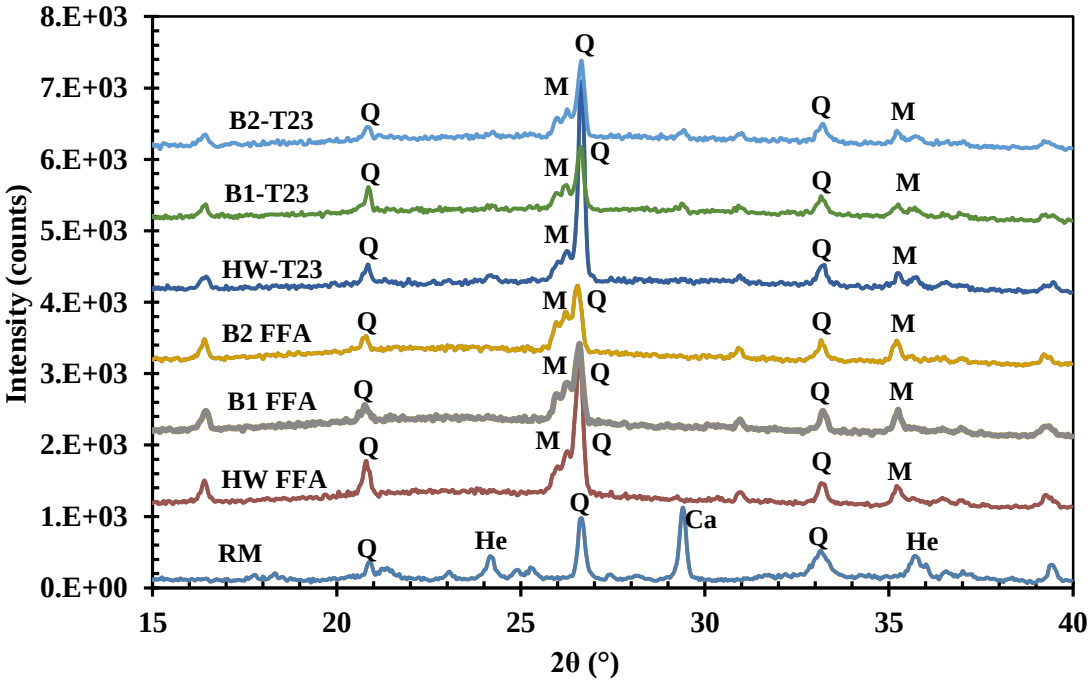

Figure 2-9. XRD patterns of raw materials and the RFFG synthesized with the mixes of RM and different FFA sources cured at ambient conditions for 28 days (Na: Nacrite, Q: Quartz, He: Hematite, Ca: Calcite, B: Berlinite, and M: Mullite).

2.4. CONCLUSIONS

In this study, geopolymers were successfully synthesized from two abundant industrial wastes, red mud and class F fly ash, via the alkali activation by the mixture of sodium hydroxide and sodium trisilicate solutions. The mechanical properties (UCS, E, and ε_f) and microstructure of the resulting geopolymers are affected by multiple factors: curing temperature, curing time, fly ash sources, and chemical composition of raw materials. The influences of the above factors are complicated and often intertwined.

Pre-curing at 100% RH has little improvement on the mechanical properties of RM-HW FFA based geopolymers, which implies that ambient curing condition is more

practical for synthesizing RM-FFA based geopolymers. Additionally, for prolonged curing of up to 180 days at ambient conditions, the UCS and E of the RFFG samples continuously increase with curing time, while the ε_f generally remains constant. These trends provide confidence to the long-term performance of synthesized geopolymers in field engineering applications.

The formation of amorphous geopolymer gels was confirmed from the XRD and SEM characterization. The XRD patterns of raw materials and resulting geopolymers indicate that the crystallized components in the raw materials are more difficult to dissolve and hence those unreactive crystals remain as fillers in the resulting geopolymer composites. SEM micrographs also confirm the composite nature of the final geopolymer products, regardless of raw materials or curing temperature. This explains the complexity and multiple factor dependence of the mechanical properties of the geopolymers.

The Si/Al and Na/Al ratios of geopolymer gels estimated based on the EDX measurements are quite different from the nominal chemical composition of the raw materials, with the former ratio having a stronger correlation with the mechanical properties of RFFG. The nominal Na/Al molar ratio of 0.6-0.8 with the nominal Si/Al ratio of 2 used in this study seems to be a good starting point for synthesizing geopolymers from different sources of raw materials. Due to the complexity associated with heterogeneous composite nature of the resulting geopolymers, it is still difficult to pinpoint the optimal chemical compositions for producing geopolymers with desired properties, and more quantitative studies are required to further advance the understanding of the relationship of raw materials, synthesis conditions, and geopolymer properties.

The ambient condition-based geopolymerization technology developed in this study can provide a sustainable approach to recycle and reuse two abundant industrial wastes, RM and FFA. Furthermore, the RFFGs can be used as a ‘greener’ alternative to ordinary Portland cement for applications in various engineering fields.

CHAPTER 3 - REACTION KINETICS STUDY ON RED MUD-FLY ASH BASED GEOPOLYMERS

3.1. INTRODUCTION

Geopolymer is a type of aluminosilicate inorganic polymers synthesized by activating silicate and aluminate rich materials with alkali solutions [13, 75]. As a family of aluminosilicate materials, geopolymer's chemical formula is simplified as $M_n\{-(SiO_2)_z - AlO_2 -\}_n$, where M is an alkali cation to balance the negative charge introduced by $Al(OH)_4^{-1}$, which can be sodium (Na^+) or potassium (K^+), and thus the stoichiometric M/Al ratio is 1 for geopolymer; n is the polymerization degree; and z is Si/Al ratio, varying in the range of 1 to 15, and up to 300 [13, 75]. In geopolymeric structures, silicate tetrahedrons and aluminate tetrahedrons are linked by sharing oxygen atoms to form different networks that affect the properties of the resulting geopolymers siginificantly. Therefore, the Si/Al ratio, z, is a vital parameter for the final product, which is usually lower than 3 for the geopolymers used as cementitious and ceramic materials [13, 75].

Geopolymer has many extraordinary properties, such as a high mechanical strength [14, 15], good chemical and thermal resistance [20-27, 29], and low toxic composition [29, 30]. Also because of its low energy requirement and CO_2 emission during the production, geopolymer has become a sustainable alternative to ordinary Portland cement (OPC). It is applicable in concrete as a cementitious material [17, 33], toxic/heavy metal immobilization [30], protective coating [20-22] and soil stabilization [39, 109]. Geopolymers have been successfully synthesized with metakaolin [103, 235, 236] and

many industrial wastes that are rich in Si and Al. For instance, fly ash [14, 49, 239], granulated blast furnace slag [30, 240], red mud (or bauxite residue) [56, 75], rice husk ash [56, 242], palm oil fuel fly ash [58, 59], mine tailing [60], biomass fly ash [61], silica fume [62], and the mix of the abovementioned materials have been used as raw materials for synthesizing geopolymers. Among these industrial wastes, red mud (RM) has attracted more attention to mix with other Si- and Al-rich materials for geopolymer synthesis in the recent years [46, 56, 57, 71, 75-77, 241, 247] because: (i) Si and Al are two of the main chemical components in RM that is suitable for geopolymer synthesis; (ii) the high alkality remained in RM after the aluminum extraction by NaOH boiling of bauxite ores with the Bayer process can substitute a portion of alkali activator, which is the most expensive raw material for geopolymer synthesis [73]; and (iii) the high average pH value of 11.3 ± 1.0 and the large inventory (e.g., globally 2.7 billion tons in 2007) with an annual production of 120 million tons make the disposal and treatment of RM a major challenge for aluminum refinery [73]. A sustainable approach to reuse RM has been reported by Zhang et al. [57], in which RM has been successfully used to synthesize geopolymer by mixing with class F fly ash (FFA). Zhang et al. [57] also investigated the effect of chemical composition (e.g., Si/Al and Na/Al molar ratios), curing conditions (e.g., curing temperature, humidity and time) and the properties of FFA on the mechanical and microstructural properties of the resulting geopolymers [57]. In addition, the formation of geopolymer gels was confirmed with SEM images and EDX spectra, and a good starting chemical composition of raw materials was recommended for the synthesis of RM-FFA based geopolymer (RFFG) with a high strength. However, the reaction kinetics of RFFG and its correlation to the development of mechanical properties remain unknown. Furthermore, the porosity, as an

important factor affecting the strength of geopolymers, was not considered in the previous study by the authors.

As the prerequisite knowledge to tailor geopolymer synthesis, the geopolymerization kinetics has been widely investigated. Palomo's group assessed the reaction degree of geopolymers by conducting X-ray diffractometer (XRD), HCl attack and solid state ^{29}Si nuclear magnetic resonance (NMR) on the fly ash based geopolymers [140, 142]. Provis and van Deventer developed a reaction kinetics model [158, 162, 256], by monitoring the microstructure of the geopolymer during the reaction process with the in-situ energy dispersive XRD and ^{29}Si solid state NMR. In their model, the geopolymerization process was divided into the following three stages: dissolution of the Si- and Al-raw materials at Stage I, polymerization of the silicate and aluminate oligomers at Stage II, and condensation and crystallization for aluminosilicate clusters at Stage III. Water molecules were consumed at the first stage, and extracted in the last two stages, while all the reactions steps are interactive with each other [257]. White et al. investigated the reaction kinetics of metakaolin based geopolymers by analyzing the interatomic arrangement during the reaction process with in-situ X-ray and neutron pair distribution function techniques [163, 164]. Rees et al. interpreted the development of geopolymer gels by monitoring the change in the Si-O-T bonds in fly ash-based geopolymers [127, 134, 165] with Fourier transform infrared spectroscopy (FTIR). Fernández-Jiménez and Palomo indicated that the alkali activated raw materials developed into Al-rich gels first and then converted to Si-rich gels during the geopolymerization by tracking the Si-O-T bond with FTIR [166]. Criado et al. further studied the effect of the chemical composition and curing conditions on the reaction kinetics of fly ash based geopolymers by using FTIR, ^{29}Si NMR and XRD characterization

[140, 170, 176]. Zhang et al. studied the reaction degree and rate at the early stage of geopolymerization and their dependence on curing temperature and alkali content [54, 123, 124] by measuring the heat release during the reaction with isothermal conduction calorimeter (ICC). The porosity of geopolymers has been measured with the BET analysis and mercury intrusion porosimetry analysis [52, 173, 189, 190]. Pores are left in the hardened geopolymers either by the air induced in the mixing during the synthesis, or by the pore water evaporation during hardening. It was found that the formation of both pores and geopolymer gels can be enhanced by elevated curing temperatures [190], and thus they have conflicting influences on the mechanical properties of geopolymers, which further complicate the synthesis processes. The results from these studies seem promising on the understanding of geopolymerization kinetics. However, most of these results were obtained on the metakaolin-, fly ash- or furnace slag-based geopolymeric systems, which may not be applicable to the geopolymers synthesized from the mix of RM and FFA. On the other hand, most of the previous studies focused on the early stages of geopolymerization, rather than its implication to the mechanical properties and microstructural change of geopolymers after aging. Therefore, the relationship of reaction kinetics-porosity-mechanical properties of RFFG and its dependence on the curing temperature are the main focus of the current study. The microstructural development and reaction rate of RFFG at different curing temperatures along the curing up to 120 days were monitored with the aid of FTIR, ICC and XRD to investigate the reaction kinetics. The unconfined compressive strength, failure strain and Young's modulus of the RFFG were determined at corresponding curing time instants to provide insight into the reaction kinetics of RFFG from the perspective of mechanical properties. Besides, the pore size distribution and

morphology of the pores in the RFFG were measured with N_2- Barrett, Joyner and Halenda (BJH) and MicroCT-X ray techniques to provide the information of porosity and how it relates to the reaction kinetics and the mechanical properties' development of the geopolymers.

3.2. MATERIALS AND METHODOLOGY

3.2.1. Materials

FFA from Headwater Resources Inc. and RM from Alcoa World Alumina, LLC. were used as solid raw materials to synthesize geopolymers. The soil like RM was dried in an oven at 100°C to remove the remaining moisture and then ground with a kitchen mill until all the particles passed a No. 100 mesh (i.e., the opening size of 152 μm) to facilitate the geopolymerization. RM and FFA have a median particle size of 1.9μm and 16.0μm respectively, and their chemical compositions are listed in **Table 3-1**. The major constituents in RM are SiO_2, Al_2O_3, Fe_2O_3 and CaO, and in FFA are SiO_2 and Al_2O_3. The alkali activator was prepared with a sodium hydroxide solution at NaOH concentration of 50 wt.% from Fisher Science Inc. USA, deionized water and a 2M sodium trisilicate solution that was prepared by dissolving sodium trisilicate pellets from Sigma Aldrich Inc. USA in deionized water.

Table 3-1. Chemical composition of class F fly ash and red mud used to synthesize geopolymers

Chemical Composition (wt.%)	Red Mud	Class F Fly Ash
SiO_2	22.82	57.91
Al_2O_3	15.06	27.44
Fe_2O_3	17.34	6.32
CaO	12.24	1.30
MgO	0.27	--
Na_2O	4.37	--
K_2O	1.19	--
SO_3	--	0.21
MnO	0.36	--
P_2O_5	2.43	--
TiO_2	3.43	--
Loss in ignition	15.75	2.15

3.2.2. Geopolymer Sample Preparation and Final Setting Time Determination

RFFG was prepared at a Si/Al molar ratio of 2.0 and a Na/Al molar ratio of 0.6 according to a previous study by the authors for RFFG with a high mechanical strength [57]. NaOH solution, sodium trisilicate solution and deionized water were mixed at a ratio of 7:3:3 firstly, and then added to the solid raw materials that were dry mixed at RM:FFA ratio of 1:4 for 30 minutes. The water content of the precursor, i.e., the proportion of the water in the activator, was adjusted to 23%, which was the lowest amount that can provide a good workability. The water content was kept as low as possible because a lower water content is more favorable for producing fly ash based geopolymers with higher mechanical strength [105].

To prepare the samples for unconfined compression tests, the geopolymer slurry was poured into PVC cylindrical molds with an inner diameter of 25mm and a height of 62.5mm after mixing. The height to diameter ratio of 2.5 was selected for eliminating the end effect

in the unconfined compression testing. The samples were vibrated for 5 minutes to remove the air bubbles entrained in the mixing and pouring. They were sealed in plastic bags subsequently and cured at room temperature (~23 ℃), 50 ℃ and 80 ℃, respectively, to investigate the influence of curing temperature on the reaction kinetics and development of mechanical properties of RFFG. For room temperature curing, the samples were placed in a plastic chamber equipped with a humidifier for the first 14 days' curing. The relative humidity was maintained 40%~50% that was suggested for geopolymers with a high mechanical strength in the previous studies [52, 57]. Except for those samples tested after curing for 49 hours (the final setting time for room temperature cured samples, i.e., 2 days), 7 days and 14 days, the samples were demolded after 14 days and continued to be cured in the chamber until testing. For the elevated curing temperatures (50 ℃ and 80 ℃), the samples were cured for 7 days and 1 day in a 50 ℃ oven and a 80 ℃ oven, respectively; then they were moved from the oven to the curing chamber, unsealed, demolded, and continued to be cured until testing. Three replicates were prepared for each of the sample sets that are summarized in **Table 3-2**. Some extra cylindrical samples were prepared for XRD and FTIR powder specimens. In **Table 3-2**, curing temperature and curing time are used to designate the samples, where T is short for temperature followed with the temperature value in Celsius while h and D stand for hour(s) and days, respectively, preceded with the respective curing time.

Table 3-2. RFFG samples prepared for mechanical and microstructural characterizations

Sample	Curing Temperature	Tests
T23-1h, T23-7h, T23-24h, T23-40h, T23-2D, T23-7D, T23-14D, T23-28D, T23-49D, T23-90D and T23-120D	23 ℃ (Room Temperature)	Unconfined Compression Tests (excluding the samples before final setting) FTIR and XRD
T50-1h, T50-2h, T50-7h, T50-24h,T50-2D, T50-7D, T50-14D, T50-28D, T50-49D, T50-90D and T50-120D	50 ℃ in the first 7 days, and 23 ℃ (Room Temperature) in the following curing	
T80-1h, T80-2h, T80-7h, T80-24h,T80-2D, T80-7D, T80-14D, T80-28D, T80-49D, T80-90D and T80-120D	80 ℃ in the first day, and 23 ℃ (Room Temperature) in the following curing	

Note: T, h, and D stand for temperature, curing time in hour(s), and curing time in days, respectively. For each curing temperature, the samples cured for 7, 28 and 49 days were used for N_2-BJH measurement, and those cured for 49 days were used in MicroCT characterization.

The final setting time of the RFFG samples cured at different temperatures were determined with the Vicat needle method developed for cement based on the ASTM standard C191-13 [258]. According to this standard, the final setting time is defined as the time elapsed between the contact of the geopolymer and the time when the needle does not leave a complete circular impression in the paste surface. The geopolymer is more fluid than cement paste and would leak out from the joint between the conical ring and the plate which are used to hold the cement in ASTM C191-13 [258]. Therefore, the apparatus was slightly modified by using a short piece of PVC pipe that has the same height and a similar volume as the conical ring. The bottom of the PVC pipe was sealed with non-adsorptive tapes to hold the geopolymer slurry. The geopolymer samples in the PVC pipes were sealed with plastic bags and cured under the same conditions as the corresponding compression

testing samples. The final setting time was measured every 10 minutes after the geopolymer slurry was poured into the PVC pipe. For those cured at elevated temperatures, the samples were sealed and put back into the oven after every measurement.

3.2.3. Mechanical and Microstructural Characterizations

Unconfined compression tests were conducted on the cured cylindrical samples with an Instron loading frame at a constant loading rate of 0.5 in./min. The top surface of the samples was covered with a cardboard to reduce the influence of the uneven surface formed during the curing on the testing results. With the force and deformation obtained from the compression tests, the unconfined compressive strength (UCS), failure strain and Young's modulus were calculated.

The microstructural and mineralogical changes of the RFFG along curing time were characterized with FTIR and XRD, respectively. Before the final setting, about 5 gram geopolymer slurry was taken from a UCS sample every 1 hour during the first 7 hours' curing, and then at 24 hours and 40 hours. These samples were subsequently dried in a plastic vial to extract the free water in the slurry and stop the geopolymerization reaction using the freeze-dry procedure: the geopolymer slurry was frozen immediately with liquid nitrogen after packed in the vial, stored in a freezer at -26 ℃ overnight and then dried with a lyophilizer. The dried samples were ground using an agate mortar and pestle into fine powders that pass through a sieve with an opening size of 45μm. After the final setting, the crushed compression testing samples were ground into fine powders with a particle size <45μm and kept in a desiccator to remove the remaining moisture prior to FTIR and XRD testing. The surfaces of the cylindrical samples were avoided during sampling to reduce

the effect of carbonation during the exposure to air. For the raw materials, their FTIR samples were prepared by mixing the <45μm portion of RM and FFA at the ratio of 1:4 for 24 hours. The FTIR spectra were obtained with a BrukerOptics Vetex70 FTIR spectrometer with the transmittance mode in the range of 500~1600 cm^{-1} at the resolution of 2 cm^{-1}. The powder samples were scanned with a Rigaku Geigerflex X-ray powder diffractometer using a CuKα radiation with a voltage of 37.5 kV and a current of 25 mA at 1 sec/step to obtain the XRD spectra. The mineralogy data were collected from 6° to 70° 2θ at 0.02 °/step and analyzed with MDI Jade 5.0.

3.2.4. Porosity and Heat Release during Geopolymerization

The pore size distribution and cumulative pore volume of the RFFG samples cured at different temperatures for 7, 28, and 49 days were measured by nitrogen isotherms with the BJH method, in order to examine the influence of porosity on the mechanical development of RFFG. The measurements were taken on the crushed compression RFFG samples with a size about 10mm×10mm×10mm using a Coulter SA3100 Series Surface Area and Pore Size Analyzers. The surface portions of the samples were avoided because there may have invisible drying cracks that can be mistaken for pores by BJH measurements.

The porosity of the RFFG samples cured for 49 days at different temperatures was also estimated from the images obtained with MicroCT-X ray technique, along with the morphology of the pores.

The heat released during the reaction of RFFG was measured with TAM Air isothermal calorimeter at 25℃ (room temperature), 50℃ and 80℃ using the intermixing mode. The

mix of RM and FFA at a ratio of 1: 4 was first placed in an ampoule which is sealed by a stopper assembled with a mini mixer and two syringes. The solid materials and the activator solutions held in the syringes were maintained in the calorimeter until the setup reached a thermal equilibrium at the reaction temperatures. The mixer was started once the activator was injected and the heat flow was immediately collected at a 50-second interval. At the same time, the heat flow of the control cement powder under the same condition was recorded to provide a baseline for the RFFG samples.

3.3.RESULTS AND DISCUSSION

3.3.1. Final Setting Time and Mechanical Properties of RFFG

The final setting time of the RFFG samples cured at room temperature, 50 ℃ and 80 ℃ are 49 hours, 7 hours and 1.3 hours (140 minutes), respectively. This illustrates that the RFFG samples were solidified faster at higher curing temperatures. The 2 day mechanical testing results were obtained after the samples were cured for 49 hours to be consistent with the RFFG cured at room temperature.

The mechanical properties of the RFFG samples cured at room temperature (~23℃), 50℃ and 80℃ for from the final setting time to 120 days, including UCS, failure strain and Young's modulus, along with their bulk density are presented in **Figure 3-1**. Regardless of the curing temperature, the UCS and Young's Moduli increased with curing time until 28 days, when they reached a statistically steady state level that is comparable to or even higher than that of OPC (around 10 MPa) (see **Figure 3-1** (a) and (c)). The only exception is the Young's modulus of the samples cured at 23℃, which decreased after 90 days' curing, as depicted in **Figure 3-1** (c). The failure strain of the RFFG cured at 23 ℃

for 2 days is extremely high because the sample was very soft and highly deformable. As the curing proceeded, the RFFG cured at 23℃ became stiffer and deformed much less upon compression, with a failure strain of 4.2% after 7 days' curing. Except for T23-2D, the failure strain of the RFFG samples was statistically constant along the curing time, showing no curing temperature dependence (see **Figure 3-1** (b)). Due to the water evaporation that took place primarily at the early stage of the curing, the bulk density of all the RFFG samples decreased along the curing time until 28 days, after which the density kept nearly constant (**Figure 3-1** (d)). At each curing time instant, the bulk density decreased with the curing temperature, implying the more pore water evaporation at elevated curing temperatures. The mechanical properties, especially at early stage of the curing before 28 days, exhibit dependence on curing temperatures to different extents. UCS values of the samples cured at 23°C, 50°C and 80°C for 2 days are 0.56 ± 0.01 MPa, 5.00 ± 1.79 MPa and 8.89 ± 3.37 MPa, respectively. The failure strains of these samples are 17.11 ± 0.29%, 2.21 ± 0.23% and 4.07 ± 0.84%, and the Young's Moduli are 0.004 ± 0.0003 GPa, 0.44 ± 0.14 GPa and 0.32 ± 0.09 GPa, after curing for 2 days, respectively. The mechanical properties of these samples at the early stage illustrated that the elevated curing temperature significantly increased the early strength and stiffness of RFFG, where the compressive strength generally increased with the curing temperature, as shown in **Figure 3-1** (a). The UCSs of the samples cured at 23°C, 50°C and 80°C for 49 days, which represent a stable state level, are 14.24 ± 3.00 MPa, 16.71 ± 4.20 MPa and 12.61 ± 3.76 MPa, respectively. Statistically, the UCS of the RFFG samples follows the order of 50°C>23℃>80℃ from high to low values, with respect to curing temperature. This indicates that a moderate temperature such as 50°C is the most favorable for the strength

development of RFFG. Although a higher curing temperature such as 80°C is more beneficial for the early strength gain, it is less beneficial for long-term strength development, even compared to room temperature. This can be attributed to the influence of other factors (e.g., pore volume) on mechanical properties of resulting geopolymers and its dependency on curing temperature, which will be further discussed in the following sections. The initial strength of the RFFG samples cured at room temperature developed at a much slower rate than that of the samples cured at elevated temperatures, but its long-term strength is comparable statistically to that of the 50℃ counterpart. In addition, the other mechanical properties (e.g., failure strain and Young's Modulus) of the RFFG samples cured at room temperature are statistically similar to those of the RFFG samples cured at elevated temperatures. Therefore, room temperature curing is more preferred, especially from the perspective of in-situ applications of RFFG in civil engineering.

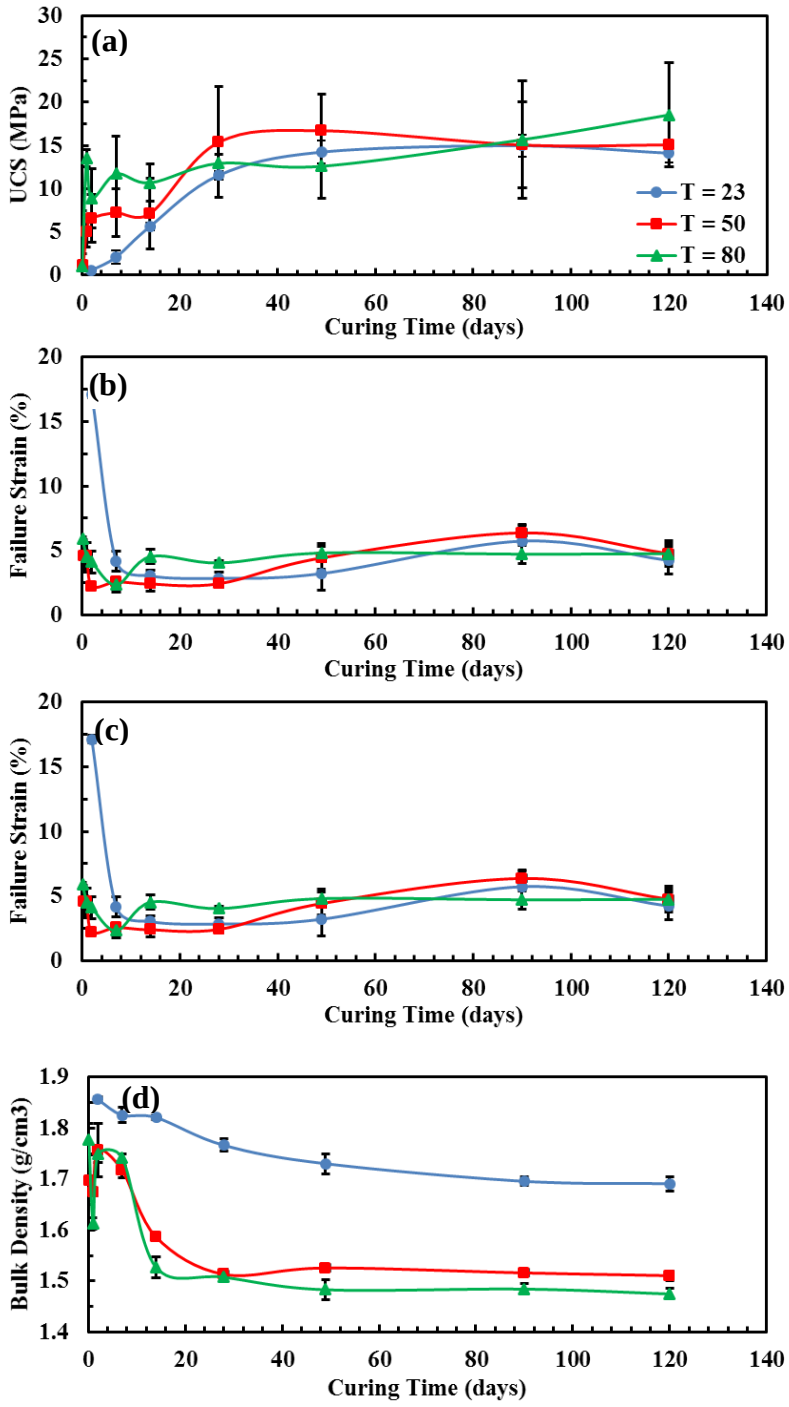

Figure 3-1. Effect of curing temperatures on (a) unconfined compressive strength, (b) failure strain, (c) Young's modulus and (d) bulk density during the curing time up to 120 days. Note that the error bars represent the standard deviation for all the plots.

3.3.2. Heat Release in the Reaction

The normalized heat flow of the RFFG samples at room temperature, 50 ℃ and 80 ℃ was measured with ICC and is plotted in **Figure 3-2**. Two peaks of the heat flow were detected in the RFFG at room temperature and 50 ℃, while only one peak in the sample at 80 ℃. The first peak appeared almost immediately when the reaction started, which was generated by the dissolution of the raw materials. The second peak was resulted from the polymerization of the reactive silicates and aluminates, which is more distinct in the samples at room temperature, but overlapped with the first peak in the sample at 50 ℃. This illustrates that the elevated temperature accelerates the polymerization. Therefore, the undetectable second peak in the RFFG at 80 ℃ might be due to the overly fast polymerization that made the first and second peak of the released heat fully overlapped. The intensity of the first peak increased with the temperature, indicating that the dissolution degree is significantly enhanced by the elevated temperature. The higher dissolution degree of the raw materials at higher temperatures provides more reactive silicates and aluminates for the following reaction steps, and thus accelerated the final setting and development of the early strength of the RFFG samples.

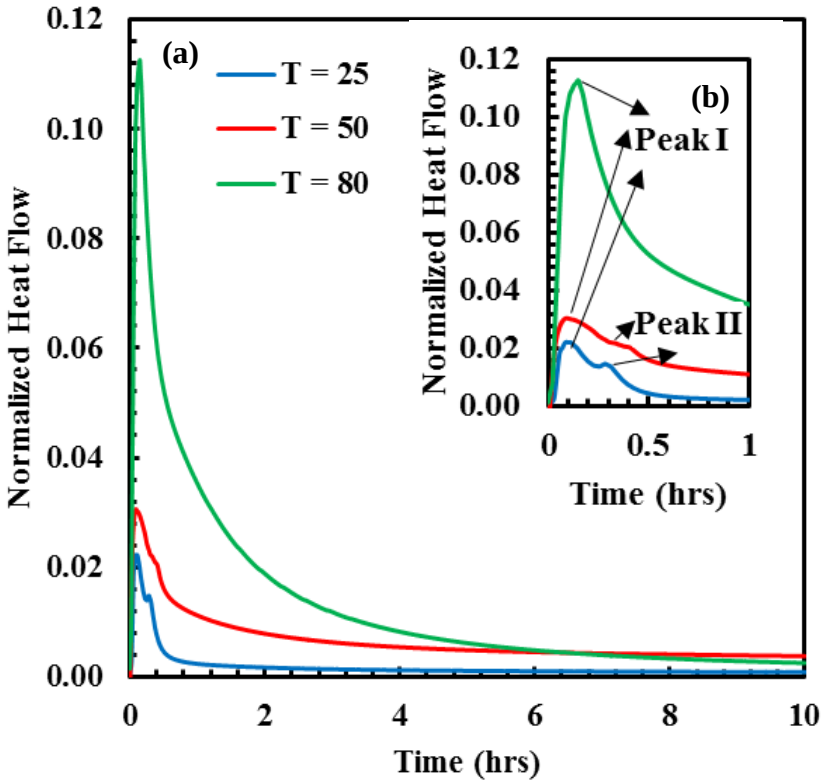

Figure 3-2. (a) Normalized heat release during the reaction of RFFG samples at room temperature, 50 ℃ and 80 ℃, and the first and second peaks are enlarged in (b).

3.3.3. Microstructural Characterization by FTIR

The change in chemical bonding of the RFFG samples cured at different temperatures was characterized with FTIR to shed light on the reaction kinetics and strength development of the samples during the course of curing process from right after the mixing of the precursor to 120 days. The characteristic FTIR spectra of the raw materials (20% RM + 80% FFA) were also included to provide the baseline value for understanding the shift of characteristic bondings. For the samples cured at room temperature, with a final setting time of 2 days, their FTIR spectra after the curing of 1, 7, 24 and 40 hour(s) are shown in **Figure 3-3** (a).

For the RFFG samples cured at 50°C and 80°C, whose final setting time is 7 hours and 1.3 hours respectively, they were solidified much faster than those cured at room temperature. Accordingly, the spectra at closer FTIR sampling intervals were obtained to capture the chemical bonding change during the initial stage of the curing.

The major FTIR band observed in all the RFFG and raw material samples is centered between 1200 cm^{-1} and 900 cm^{-1}, which is identified as the asymmetric stretching vibration of Si-O-T (T: Si or Al) and designated as the "main band" in the followed texts [127, 165]. The change in the position and intensity of this Si-O-T band was used to characterize the formation of geopolymer gels [52, 118]. The main band was centered at 1031.9 cm^{-1} in the raw materials and shifted to a lower wavenumber after the onset of the reaction, as shown in **Figure 3-3**. For room temperature cured samples, the main band shifted to 1001.0 cm^{-1} after 1 hour curing, implying that the raw materials were dissolved in the alkali activators. During the curing time from 1 hour to 2 days (49 hours), this band shifted to 968.2 cm^{-1} and became narrowed gradually. These changes were caused by the continuous increase of silicate sites with non-bridging oxygen (NBOs) or substitution of tetrahedral Al in the silicate networks, which was also observed in the other literature [259-261]. From the 2^{nd} day to 14^{th} day, this band became broader and the center shifted from 968.2 cm^{-1} to 1003.0 cm^{-1}. This was due to the decreasing Si-O-T bond angle and increasing molecular vibrational force constant, as a result of more Si-O-Si bond formed that accounted for a large proportion of small oligomers, such as monomers and dimers [106]. After 14 days curing, the Si-O-T band stabilized at a frequency in the range of 972.1 cm^{-1} to 987.5 cm^{-1} with a stable intensity. The shift of Si-O-T band after 14 days is more likely caused by the

enlarged and more compact molecular networks that resulted in an improvement on the mechanical strength, as shown in **Figure 3-1** (a). The shift of main band illustrated the three stages of the geopolymerization: Stage I-dissolution of raw materials − Al rich gel (the main band shifting from 1031.9 cm^{-1} to 968.2 cm^{-1}), Stage II-Al rich gel – Si rich gel (the main band shifting from 968.2 cm^{-1} to 1003.0 cm^{-1}), and Stage III-Si rich gel – cross linked tectosilicate geopolymer gels (the main band shifting from 1003.0 cm^{-1} to 976.0 cm^{-1}). These three stages occurred during the curing period from right after the mixing to 2 days, 2 days to 14 days, and 14 days to 120 days, respectively, for room temperature cured RFFG samples. These three shifting stages were also observed in the 50°C samples and 80°C samples. For the 50°C samples, these three stages happened during the period from right after the mixing to 7 hours, 7 hours to 14 days and 14 days to 120 days, while the Si-O-T band shifted from 1031.9 cm^{-1} to 970.2 cm^{-1}, 970.2 cm^{-1} to 993.1 cm^{-1} and 993.1 cm^{-1} to 987.5 cm^{-1}, respectively. For the 80°C samples, the Si-O-T band shifted from 1031.9 cm^{-1} to 981.8 cm^{-1} and 981.8 cm^{-1} to 989.5 cm^{-1}, and then stabilized around 989.5 cm^{-1} in the period from right after the mixing to 140 minutes, 140 minutes to 2 days and 2 days to 120 days, respectively. Clearly, the shift of the main band in the RFFG samples cured at room temperature and 50℃ is more similar. The main band in 80℃ cured RFFG samples changed in the similar way, but within a shorter time period. As seen in **Figure 3-3**, the Si-O-T band is in range of 972.1 cm^{-1} to 991.4 cm^{-1} and consistent for RFFG samples cured at different temperatures, which is more stable in position and intensity for the samples cured at higher temperatures.

A band between 1436.9 to 1444.7 cm^{-1}, 1433.1cm^{-1}~1438.9cm^{-1} and 1436.9cm^{-1}~1442.7cm^{-1} was observed in the RFFG samples cured at room temperature, 50 ℃ and 80 ℃, respectively. This band is assigned to the asymmetric stretching of the O-C-O bonds in CO_3^{2-} formed by the reaction between the excessive Na^+ and the atmospheric CO_2 in the geopolymer powder samples when they were exposed to air [107, 123, 262, 263]. This band was not observed in the raw materials or the samples with a constant bulk density, in which the free water is almost evaporated. Therefore, a liquid environment is absent for bringing the Na^+ to the surface of the samples to react with CO_2. For the FTIR samples treated with the freeze-dry process, the Na^+ in the geopolymer precursor reacted with the CO_2 and formed Na_2CO_3 during the drying process. Therefore, the O-C-O band is more intense and narrower in the RFFG specimens sampled before the final setting compared to the other samples. For the RFFG samples cured at room temperature, 50 ℃ and 80 ℃, the intensity of the O-C-O band significantly decreased with the curing time, and became a broad shoulder after 7 days, 24 hours and 140 minutes, respectively. This implies that Na^+ was consumed in the reaction and not adequate to form the carbonates after the abovementioned curing time. Apparently, the elevated temperature accelerated the participation of Na^+ in the early stage reaction.

The bending vibration of O-H [47] was observed at 1410.0 cm^{-1} to 1411.9 cm^{-1}, 1406.1 cm^{-1} to 1410.0 cm^{-1} and 1410.0 cm^{-1} to 1411.9 cm^{-1} in the RFFG samples cured at room temperature, 50 ℃ and 80 ℃ before their respective final setting, respectively. The free water in the samples was mostly evaporated after the samples set, while the O-H band cannot be identified after the final setting, except for the room temperature samples, in which this O-H band was still detectable after 7 days' curing. This illustrates the slow

evaporation rate of water at room temperature, which may inhibit the formation of geopolymer gels in the polymerization process [113, 138]. This can be one reason why the mechanical strength and Young's modulus of room temperature cured samples developed much slower compared to the other two sample groups in the first 7 days, as demonstrated in **Figure 3-1** (a).

Another small band observed in the range of 864.1 to 881.5 cm^{-1}, 864.1 to 866.0 cm^{-1} and 864.1 to 868.0 cm^{-1} for the samples cured at room temperature, 50 ℃ and 80 ℃, respectively, is assigned to the bending vibration of Si-OH [124, 130, 132], which was not found in the raw materials. The previous study found two types of structures may result in this band: (i) the SiO_4 groups attached to the intermediate type of Al, or (ii) the free $Si\text{-}O^-$ that appeared at the reactive sites of growing polymers [132]. The Si-OH band usually appeared in the incompletely formed polymers that can reduce the mechanical properties of the resulting geopolymers, but disappeared upon dehydration [126, 132]. This band was observed at the beginning of the reaction for each RFFG sample group, and faded during the reaction. This is consistent with the findings in the previous research, indicating that the molecular arrangement became more ordered and the bending vibration of $Si\text{-}O^-$ tended to be less intense as the aluminosilicate gels underwent polymerization [118]. **Figure 3-3** also indicates that the band of Si-OH disappeared faster when a higher curing temperature was used. In other words, the elevated curing temperature accelerated the consumption of reactive components, and thus the polymerization process.

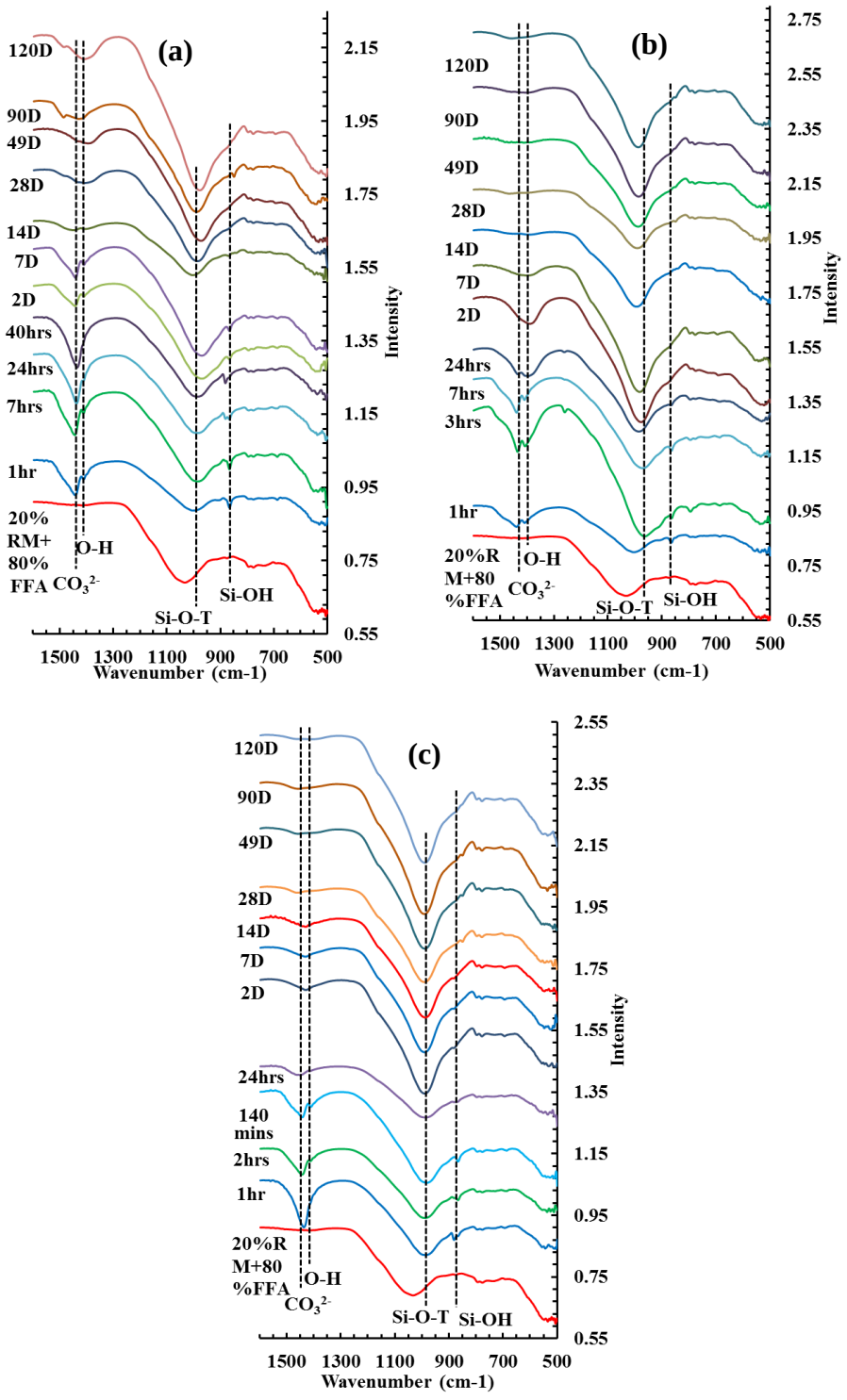

Figure 3-3. FTIR spectra of RFFG samples cured at (a) room temperature, (b) 50 ℃ and (c) 80 ℃ from right after the mixing to the curing time up to 120 days, and 20%RM+80%FFA is the mix of the raw materials for synthesizing RFFG.

To assess the effect of Si-O-T bond, the main constituent for the geopolymeric frameworks, on the mechanical strength, the frequency of the main band is plotted against the curing time and compared with the UCS of the RFFG samples. For each curing temperature, the 3 stages of the shift of Si-O-T band are marked in **Figure 3-4**. At Stage I, the frequency of the main band decreased from 1031.9 cm^{-1} in the raw materials to a wavenumber lower than 1000 cm^{-1}, indicating that the raw materials were dissolved in the activators and released the silicate and aluminate monomers that further developed into an Al-rich gel. During this stage which ended at the respective final setting time, the mechanical strength have barely been developed, (0.56 ± 0.01 MPa for the samples cured room temperature, 1.12 ± 0.09 MPa for 50 ℃ and 1.02 ± 0.28 MPa for 80 ℃), as depicted in the UCS curves in **Figure 3-4**. At Stage II, the main band shifted to a higher wavenumber. This is attributed to Al-rich geopolymer precursor turning into a Si-rich gel which includes more Si-O-Si bonds. The formation of the Si-rich gel was found to be mainly responsible for the strength development of the geopolymer [166, 169]. Consistently, the mechanical strength of the samples increased during this stage. The UCS values at the end of Stage II (14 days for room temperature, 7 days for 50 ℃, and 49 hours for 80 ℃ cured RFFG) were around 5.67 ± 0.25 MPa, 7.22 ± 2.77 MPa and 8.89 ± 3.77 MPa for room temperature, 50 ℃, and 80 ℃ cured RFFG samples, respectively. Subsequently, the wavenumber of the main band decreased and kept nearly constant at Stage III. The shift of Si-O-T bands towards to a lower frequency may be caused by a more ordered geopolymer gel network developed from the Si-rich gels with a lower molecular vibrational force constant along the polycondensation [118]. In the meanwhile, the more crosslinked networks in the

geopolymer enhanced the mechanical properties of RFFG samples, as the UCS increased further and then became stable at Stage III. The development of the Si-O-T bond illustrated by the shift of the FTIR band around 1000 cm^{-1} agreed well with the conceptual model of geopolymerization: (i) RM and FFA were firstly dissolved in the alkali activator and the system became Al-rich gels initially, (ii) the gel turned into a Si-rich system along the polymerization while the mechanical strength started to develop, and (iii) the geopolymer gels further condensed into a more cross-linked and compact framework structure which provides a higher mechanical strength. The faster change of the Si-O-T band in the samples cured at 80 ℃ compared to the room temperature and 50 ℃ counterparts elucidates a high curing temperature can increase the reaction rate, especially at the early curing stage. However, a faster reaction rate and a higher early strength do not necessarily translate into a higher long-term mechanical strength.

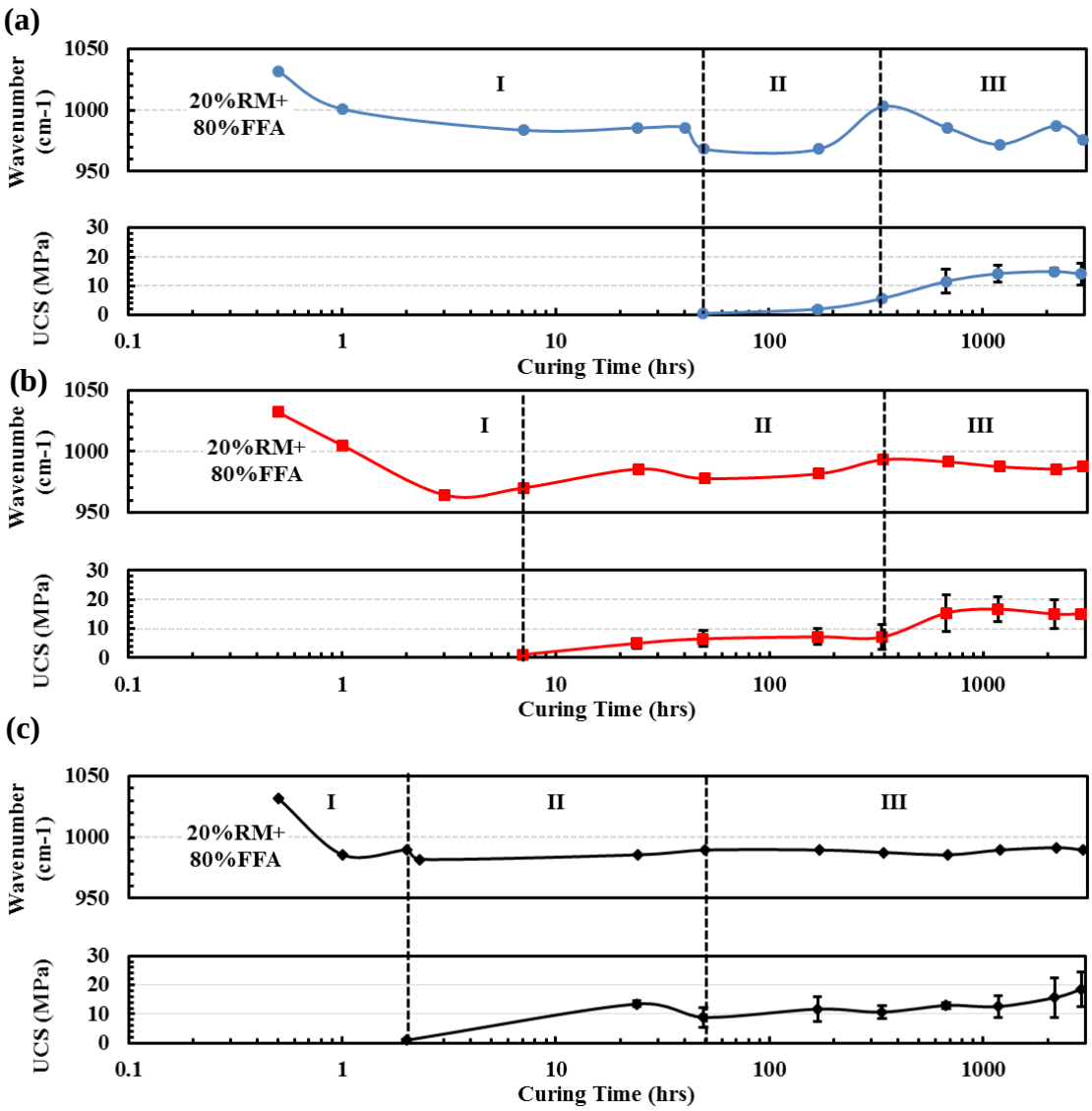

Figure 3-4. Correlation between the wavenumber shift of Si-O-T band and the development of UCS of RFFG samples cured at (a) room temperature (23 ℃), (b) 50 ℃ and (c) 80 ℃.

3.3.4. Mineralogical Characterization by XRD

The mineralogical change of the RFFG samples during the curing period at different curing temperatures was compared to the raw materials via XRD spectra in **Figure 3-5**. The RFFG

samples' designations are made with the curing temperature in Celsius and the curing time in hour(s) (hr(s)) or day(s) (D). Although XRD was conducted at the same curing time instants as the FTIR samples, only the spectra that exhibit apparent difference are plotted and compared with those of the raw materials. The minerals in RM and FFA are shown in **Figure 3-5** as well as those remained in the geopolymer samples. The crystalline change in RFFG samples does not show noticeable dependence on the curing temperature, and thus the minerals are only remarked in **Figure 3-5** (c). The main crystals identified in RM include Nacrite, Quartz, Mulite, Kaolinite, Calcite and Hemite, while those in FFA are Mulite, Quartz and Kaolinte. These identified crystals are consistent with the chemical composition of the raw materials summarized in **Table 3-1**. The minerals remained in the RFFG samples are mainly from the FFA that is the majority (80%) of the raw materials used to synthesize RFFG samples, for all the three curing temperatures. A hump between 16° to 30° 2θ and centered at 22 °is observed in the XRD pattern of FFA. A similar hump is observed in the geopolymer precursors after the onset of the reaction, regardless of the curing temperature, as shown in 23-1hr, 50-1hr and 80-1hr XRD patterns. This hump barely has any difference before the samples reached their respective final setting. As the curing proceeded, the width of this hump extended to 16°~38° 2θ and the center shifted to 26 °~27 ° after 28 days', 7 days' and 2 days' curing for the samples cured at room temperature, 50°C and 80°C, respectively. The shift of this hump agrees with the findings in previous studies on reaction mechanisms [13, 112, 128, 131] that verified the formation of geopolymer gels. This characteristic XRD hump for geopolymer gels remained stable in the following curing, as shown in **Figure 3-5**. The appearance of this XRD hump also verified that the formation of geopolymer gels occurred at a slower rate at room

temperature compared to elevated temperatures. This is consistent with the effect of the curing temperature on the development of UCS and Young's Moduli, as demonstrated in **Figure 3-1** (a) and (c).

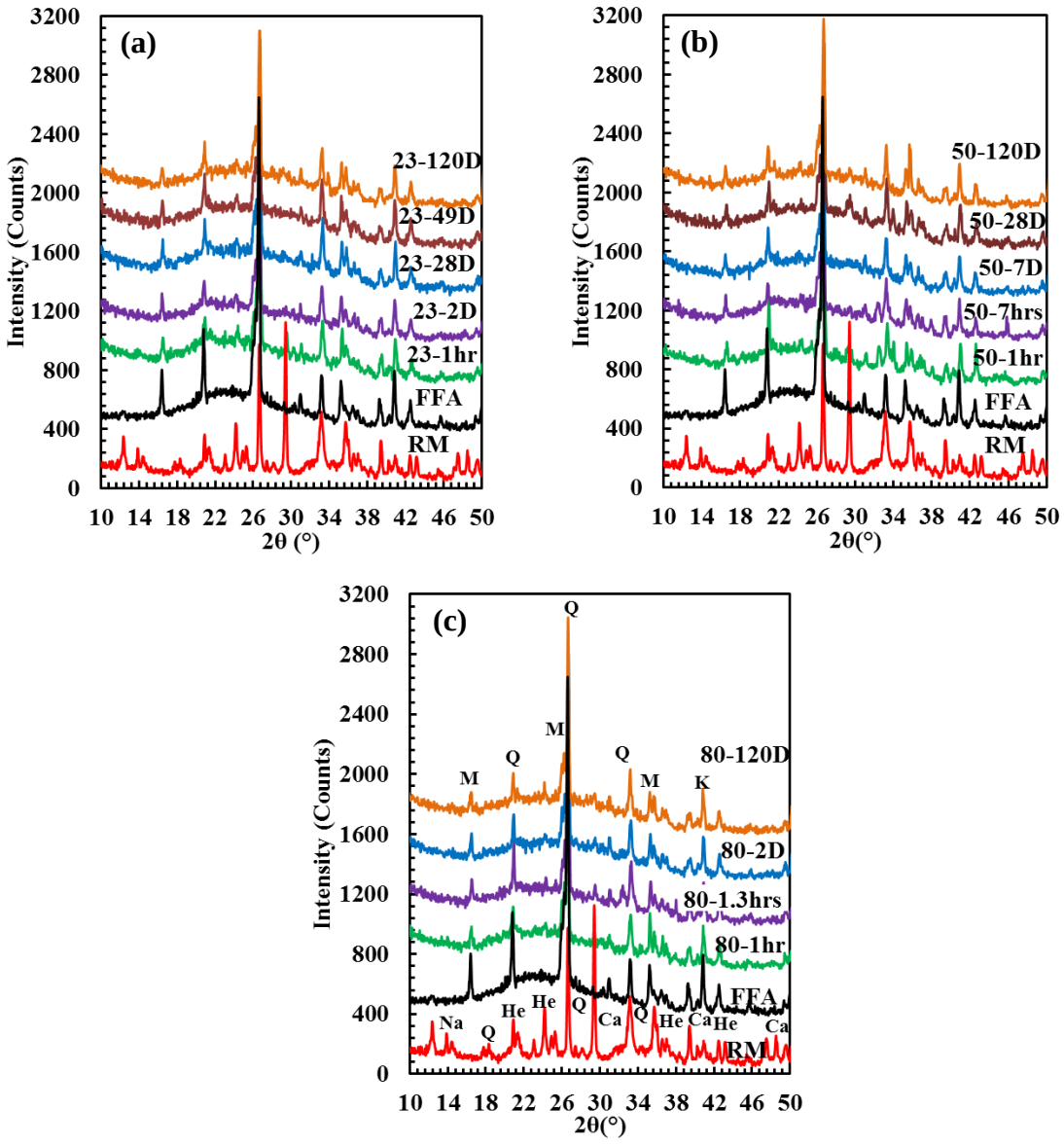

Figure 3-5. XRD spectra of RFFG samples cured at (a) room temperature, (b) 50 ℃ and (c) 80 ℃ (Q: Quartz, M: Mulite, K: Kaolinite, Na: Nacrite, He: Hematite, and Ca: Calcite).

3.3.5. Porosity

The pores formed in the RFFG samples cured at room temperature, 50 ℃ and 80 ℃ for 49 days were visualized by 2-Dimensional (2D) scanning with MicroCT in over 2500 cross-sections, of which a random section for each of the samples is shown in **Figure 3-6**. The bright spots indicate the pores while the darkest ones represent heaviest elements, such as metals.

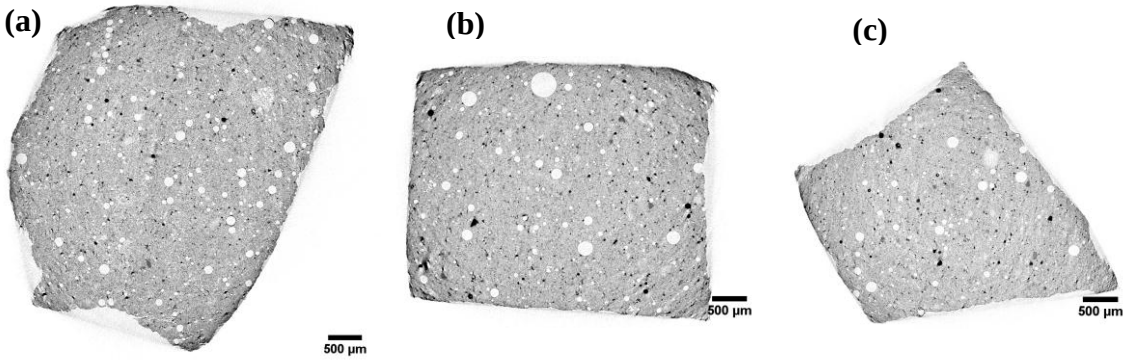

Figure 3-6. Cross-sectional images of the RFFG samples cured for 49 days at (a) room temperature, (b) 50 ℃ and (c) 80 ℃ acquired with MicroCT. Note that the bright spots indicate the pores while the darkest ones represent heaviest elements, such as metals.

The 2D fraction of the total, closed and open pores on the area of the scanned cross-sections were calculated and plotted in **Figure 3-7** for the RFFG samples cured at room temperature, 50 ℃ and 80 ℃ for 49 days. The closed pores are the majority in all the samples while the open pores are only a small fraction. The RFFG samples cured at 80 ℃ has more pores than the other two sample groups, with the latter two groups having similar pore volumes. This agrees well with the lower mechanical strength of the RFFG samples cured at 80 ℃ for 49 days compared to the counterparts cured at room temperature and 50 ℃, as shown in **Figure**

3-1 (a), in spite of the highest early strength of 80 ℃ cured RFFG samples. The higher pore volume of the 80 ℃ cured RFFG samples may be introduced by the faster water evaporation at higher curing temperature and the accelerated water elimination from the geopolymeric networks due to the higher reaction rate (**Figure 3-3** (c)).

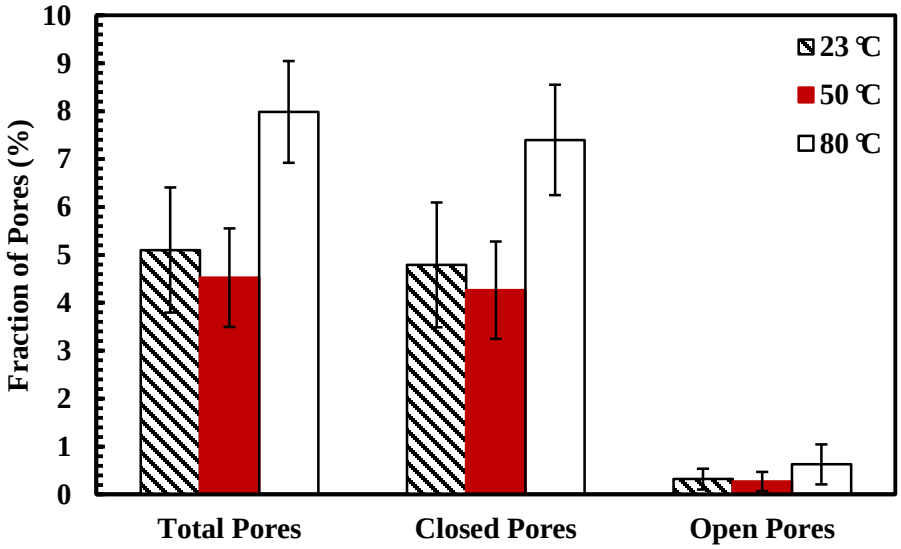

Figure 3-7. Fraction of total, closed and open pores on the cross-sections in the RFFG samples cured at 23 ℃ (room temperatures), 50 ℃ and 80 ℃ for 49 days estimated from 2D microCT scanning.

The pore size distribution and 3-dimensional (3D) volume of the open pores were also characterized by the BJH analysis of the N_2 adsorption-desorption data on the RFFG samples cured for 7, 28 and 49 days at 50 ℃, respectively. As expected, the open pore volume of the RFFG cured at 50 ℃ decreased with the curing time (**Figure 3-8** (b)). As the curing proceeded, the percentage of larger size pores progressively decreased. This trend agrees well with the development of mechanical strength which increased with the curing

time from 7 days to 49 days, illustrating that the decreasing pore volume is favorable for a high strength of RFFG.

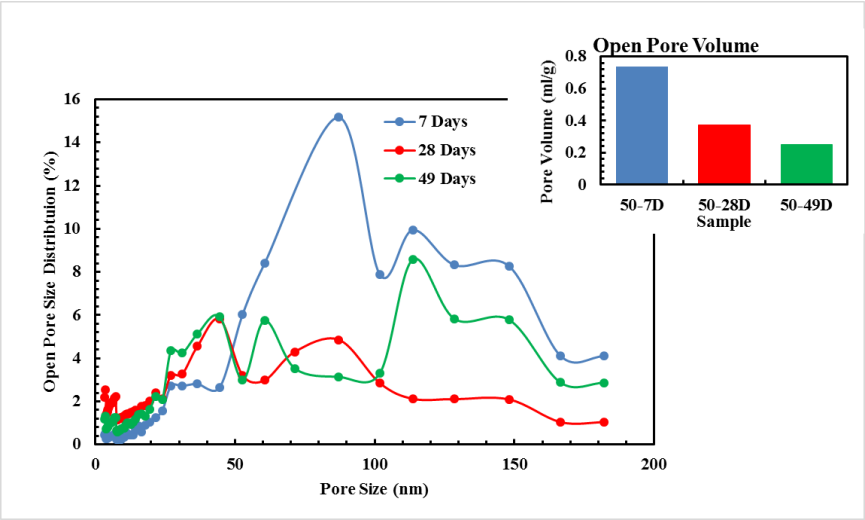

Figure 3-8. Open pore size distribution and pore volume of the RFFG cured at 50 ℃ for 7, 28 and 49 days, tested with N_2-BJH technique.

3.4. CONCLUSIONS

The correlation of mechanical properties-development of geopolymer gels-porosity of RFFG and its dependence on the curing temperature were investigated in this study. The UCS and Young's Modulus of all the RFFG samples increased with the curing time, while the failure strain was steady during the curing of 120 days, regardless of the curing temperatures. The formation of geopolymer gels in the samples cured at different temperatures was verified with the FTIR and XRD spectra. The geopolymer gel was developed in a three stage process based on the shift of the Si-O-T bands during the curing of RFFG from the raw materials to the samples cured for 120 days. The Si-O-T band shifted from a high wavenumber (1031.9 cm^{-1}) to a wavenumber lower than 1000 cm^{-1} in Stage I

while the raw materials were dissolved and the precursor developed to Al-rich gels. Subsequently, the Si-O-T band gradually shifted to a relatively higher wavenumber in Stage II while the Al-rich gels kept growing and started to form Si-rich gels. In the third stage, the Si-O-T band gradually shifted back to a relatively lower wavenumber while the Si-rich gels kept growing and converted to more cross-linked networks. During the first stage which is from the mixing to the final setting of the samples, the raw materials were dissolved and Al-rich gels started to form, while the strength was barely developed. During the second stage, the Al-rich gels continued to grow which was gradually converted to Si-rich gels, and the mechanical strength increased by a relatively limited extent. In the third stage, the Si-rich gels kept growing into more cross-linked aluminosilicate structures, and the strength increased in a great amount and stabilized. This correlation between the development of geopolymer gels and mechanical strength agreed well with the findings from previous research that the Al-rich gel is responsible for the early strength development and the Si-rich gel enhances the mechanical strength more significantly in a long term [169]. In addition, the decrease of both the pore volume and the proportion of large size pores along the curing is consistent with the increasing mechanical strength for the RFFG samples.

The curing temperature plays an important role in the development of the microstructure and mechanical properties of RFFG. First of all, the dissolution of raw materials is accelerated by the elevated temperature, verified by the ICC measurement on the heat released during the geopolymerization at room temperature, 50 ℃ and 80 ℃. The elevated temperature enhanced the development of geopolymer gels, where each of the three stages of geopolymerization occurred faster at a higher curing temperature. The

higher geopolymerization rate at elevated temperature was also qualitatively confirmed with the faster formation of the XRD pattern of geopolymer gels, the hump between 16 °~38 ° 2θ. As a result, the final setting time of the RFFG samples decreased with the increase of curing temperature. More importantly, the mechanical strength of the samples cured at 50 ℃ and 80 ℃ developed faster than that of the samples cured at room temperature. However, the pore volume of the RFFG formed at an excessively high temperature, 80 ℃ in this case, was higher than those of the samples cured at room temperature and 50 ℃. Therefore, the higher early mechanical strength of the RFFG cured at 80 ℃ resulted by the faster development of geopolymer gels at early stage was compromised by the higher pore volume. This explained well the long term strength of the RFFG samples cured at 80 ℃ is statistically lower than that of the samples cured at room temperature and 50 ℃.

This study indicates that the development of geopolymer gels is the most important factor governing the solidification rate and mechanical properties of the resulting RFFG, which is significantly affected by the curing temperature. Besides geopolymer gels, pore volume and pore size of geopolymers, which are affected by curing temperature, also play important roles in the development of mechanical strength, especially the long-term strength. Based on the results of this study, the synthesis and curing conditions of RFFG can be adjusted for different application requirements, such as a fast gain of mechanical strength, high long-term strength and low porosity.

CHAPTER 4 - DURABILITY AND HEAVY METALS' LEACHING BEHAVIOR OF RED MUD-FLY ASH BASED GEOPOLYMERS IN SULFURIC ACID SOLUTIONS AND DEIONIZED WATER

4.1. INTRODUCTION

Geopolymer is a type of aluminosilicate materials with an amorphous or semi-crystalline microstructure. In geopolymeric structures, silicate and aluminate tetrahedrons are polymerized and exist in three basic repeating units: poly-sialate (PS, -Si-O-Al-), poly-sialate-siloxo (PSS, -Si-O-Si-O-Al-), and poly-sialate-disiloxo (PSDS, -Si-O-Si-O-Si-O-Al-) [13]. The molecular structure of geopolymers can be simplified as $M_n\{(SiO_2)_z - AlO_2 -\}_n$, where *z* is the Si to Al ratio, ranging from 1 to 3 for cementitious geopolymers, *n* is the degree of polycondensation and *M* is an alkali cation that balances the negative charge of the geopolymeric network introduced by $Al(OH)_4^{-1}$, such as sodium (Na^+) and potassium (K^+) [13]. Because of their high mechanical strength, low energy consumption and low CO_2 emission during the production process, geopolymers lead themselves to a promising and sustainable alternative to ordinary Portland cement (OPC) as construction materials.

Geopolymers are synthesized by activating Si- and Al-rich raw materials with alkali hydroxide and/or alkali silicate solutions at ambient or slightly elevated temperatures. Many silicate and aluminate rich materials have been used to synthesize geopolymers with high mechanical strength, including metakaolin [103, 138, 236], natural aluminosilicate

minerals [237, 238], fly ash [47, 88-90], granulated blast furnace slag [30, 240], red mud [56, 57], rice husk ash [56] and palm oil fuel ash [58, 59], most of which are industrial wastes. Given the massive demand for cement in the construction industry, geopolymerization technology also provides an effective way to recycle and reuse these industrial by-products.

Red mud (RM), also known as bauxite residue, is one of the main byproducts of aluminum extraction from bauxite ores via the Bayer process. The inventory of RM was 2.7 billion tons by 2011 and is growing at a rate of 120 million tons per year [73]. The NaOH solution used in the Bayer process results in a high alkalinity and a high water content for RM, which has a pH value of 11.3 ± 1.0. In addition, RM is known to contain substantially elevated levels of several trace and toxic metals native to many bauxite ores, including iron, manganese, copper, zinc, cadmium, lead, chromium, and nickel [73]. These characteristics make it difficult to safely dispose and treat RM for aluminum refineries. Currently, RM is disposed into on-site waste lakes for further dewatering, consolidation, and storage, which are very costly due to mandatory environmental monitoring and maintenance associated with the disposal practice. On the other hand, the high alkalinity and high content of Si and Al of RM make it favorable for geopolymer synthesis, because it can partially replace alkali hydroxide, one of the most expensive raw materials in geopolymer synthesis.

Fly ash is one of the main byproducts from coal combustion in power plants, which is classified into class F and C fly ash according to the ASTM standard C618 [78, 79]. Class F fly ash (FFA) is produced by the combustion of bituminous coals or anthracites. Its main

chemical constituents are SiO_2, Al_2O_3, and Fe_2O_3 (with their total amount around 70%) and has less than 20% CaO. Class C fly ash (CFA) is the residue from sub-bituminous coals and lignites with the total amount of SiO_2+Al_2O_3+Fe_2O_3 ranging in 50%~70% and more than 20% CaO. Both types of fly ash contain trace amount of heavy metals, such as As, Cd, Co, Cr, Pb, Sb and Zn [264]. The annual production of fly ash is 900 million tons globally [80], which makes the disposal of fly ash a great challenge. Because of its high amorphous silicate and aluminate contents, fly ash is the one of the most widely used raw materials for synthesizing geopolymers. In the recent years, geopolymers have been successfully synthesized with the mix of fly ash and RM [57, 75, 241]. In a previous study by the authors, the effect of the chemical composition of raw materials, curing temperature, curing humidity and curing time up to 180 days on the mechanical properties and microstructure of red mud-class F fly ash based geopolymers (RFFG) were systematically studied [57, 75, 241]. The chemical composition of Si/Al=2.0 and Na/Al=0.6~0.8 and room curing condition (e.g., temperature of ~23 ℃ and relative humidity of 40%~50%) were recommended for synthesizing RFFGs with a high mechanical strength.

The durability of geopolymers and the resulting mortars and concretes need to be evaluated, such as the resistance to acid attack [23, 200-202, 265], alkaline silicate reaction [266-268] and freeze and thaw cycles [269, 270], in order to ensure its long-term performance in engineering applications. Particularly, the resistance of geopolymers to sulfuric acid has been examined due to the frequent exposure of concretes to acid rain [271], sewage [272, 273] and sulfur-rich soils [203]. Palomo et al. [96] and Ariffin et al. [274] found that metakaolin- and blended ash-based geopolymers had better acid resistance than OPC by soaking the concrete samples in 2% and 0.001M sulfuric acid (pH ≈ 2.75), and

testing the remaining compressive strength and flexural strength, respectively. Allahverdi and Skvara [201, 202] examined different deterioration mechanisms of fly ash based geopolymers in sulfuric acid with different pH values (1.0, 2.0, and 3.0) by measuring the changes in mass and microstructure. Bakharev [23] investigated the deterioration mechanism of fly ash based geopolymers in a 5% sulfuric acid by monitoring the changes in their mechanical properties and microstructure. Thokchom et al. [199, 200] investigated the effect of Na_2O concentration on the resistance of fly ash based geopolymers to sulfuric acid. The depolymerization and dealumination of geopolymer gels were found to be the primary reasons for the degradation of mechanical properties of geopolymers after sulfuric acid attack from the studies mentioned above. Nonetheless, the majority of these studies were conducted on metakaolin and fly ash based geopolymers. With the participation of RM in the geopolymerization, the durability of the derived geoplymers may be different, and thus the resistance of RFFG to sulfuric acid needs to be systematically examined. In addition, due to the heavy metals present in RM and FFA, it is important to investigate leaching behavior of these heavy metals in RFFG samples and to determine whether an excessive amount of heavy metals will be leached from the geopolymers.

In this study, RFFG samples were soaked in a sulfuric acid solution of pH=3.0 and deionized water of pH=7.0 for from 1 day to 120 days. Unconfined compressive strength, Young's modulus, failure strain and flexural strength of the soaked samples were measured and compared with the unsoaked counterparts and the OPC control samples. The soaked samples were characterized with X-ray diffractometer (XRD), scanning electron microscopy (SEM) and Fourier transform infrared spectroscopy (FTIR) to examine the influence of the acid attack on the mineralogy and microstructure, respectively. The level

of heavy metals leached from both cylindrical and powder RFFG samples in sulfuric acid solution and deionized water was determined using an atomic absorption spectrophotometer (AA). The effect of curing temperature of RFFG samples on the leaching behavior of heavy metals was also investigated.

4.2. MATERIALS AND METHODOLOGY

4.2.1. Materials

FFA from Headwater Resources Inc. and RM from Alcoa World Alumina, LLC. were mixed at 4:1 to synthesize geopolymers. The soil like RM were dried in an oven at 100°C to remove the remaining moisture and then ground with a kitchen mill until all the particles passed a No. 100 mesh (i.e., the opening size of 152 μm) to facilitate the geopolymerization. The median particle sizes of RM and FFA are 1.9μm and 16.0μm respectively and their chemical compositions are summarized in **Table 4-1**. The major constituents in RM are SiO_2, Al_2O_3, Fe_2O_3 and CaO, and in FFA are SiO_2 and Al_2O_3. A 50 wt.% sodium hydroxide solution from Fisher Science Inc. USA, 2M sodium trisilicate solution and deionized water were mixed at a proportion of 3:7:3 as the activator solution. The 2M sodium trisilicate solution was prepared by dissolving sodium trisilicate pellets from Sigma Aldrich Inc. USA in deionized water. A sulfuric acid at pH of 3.0 was prepared by diluting 17.8 M sulfuric acid with deionized water to soak the RFFG samples. Deionized water at pH=7.0 was used as another soaking solution to compare with the sulfuric acid regarding the influence of solution on the leaching behavior of heavy metals. Type II OPC samples with its chemical composition given in **Table 4-1** were also prepared as the control group to provide reference values regarding the resistance against sulfuric acid.

Table 4-1. Chemical compositions of RM, FFA and cement (heavy metals at trace amount were not detectible)

Chemical Composition	Red Mud (wt.%)	Class F Fly Ash (wt.%)	Type II (MH) Portland cement
SiO_2	22.82	57.91	19.8
Al_2O_3	15.06	27.44	4.8
Fe_2O_3	17.34	6.32	3
CaO	12.24	1.3	61.9
MgO	0.27	--	3.8
Na_2O	4.37	--	0.61
K_2O	1.19	--	--
SO_3	--	0.21	3
MnO	0.36	--	--
P_2O_5	2.43	--	--
TiO_2	3.43	--	--
Loss in ignition	15.75	2.15	2.24

4.2.2. Geopolymer Sample Preparation

RFFG samples were synthesized at Si/Al and Na/Al molar ratios of 2.0 and 0.6, respectively, which are recommended in the previous study for achieving good mechanical properties of RFFG [57]. The Si/Al and Na/Al molar ratios were calculated on the basis of the contents of Si, Al and Na in the solutions and the solid raw materials. For durability testing, two groups of RFFG samples with different sizes and shapes were prepared using two types of molds: a cylindrical mold with an inner diameter of 40.0mm and height of 100.0mm for unconfined compressive strength tests and a rectangular mold with the size of 100.0mm(L) ×25.4mm(W) ×17.7mm(H) for three-point bending tests. RM and FFA were mixed with the alkali activator for 30 minutes, poured into the molds, vibrated for 5 minutes to remove the air bubbles introduced during the mixing and cured at room temperature

(~23 ℃) and a relative humidity of 40%~50% for 28 days. The control OPC cylindrical samples were prepared at a cement/water ratio of 0.35 and cured at room temperature and 100% relatively humidity for 28 days. For leaching test, small cylindrical samples with an inner diameter of 25.4mm and a height of 63.5mm were used. Extra small cylindrical samples were used to ground into powder with a particle sized less than 45 μm to be used in the leaching tests. The samples were prepared in the same way as the durability testing samples, whereas the curing temperature of room temperature and 80 ℃ were used to investigate the effect of curing temperature on the leaching behavior of heavy metals in RFFGs in the sulfuric acid. For 80 ℃ curing, the samples were sealed in plastic bags immediately after vibration and put in an oven at 80 ℃ for one day, and then cured at room temperature with a RH of 40%~50% for another 27 days.

4.2.3. Sulfuric Acid Exposure

For the durability test, the RFFG samples were soaked in a sulfuric acid (pH=3.0) and deionized water (pH=7.0) at the solid/liquid volumetric ratio of 1/4 for 1, 7, 28, 56, 90 and 120 days before testing their mechanical properties. The OPC control samples were soaked in the same leachants for 1 and 7 days for short-term exposure and 120 days for long-term exposure. A pH meter was used to monitor pH values of the soaking solutions during the course of soaking. The soaking solutions were refreshed every day in the first 3 days of soaking when their pH value increased quickly, and every 7 days from the 7^{th} day to the end of the soaking. The dimensions and weight of the samples were measured when the leachants were refreshed to monitor the physical change of the samples during acid

exposure. The samples were wiped with paper towels before the measurements. Three replicates were used for each soaking period.

4.2.4. Mechanical Property Testing, FTIR, and XRD

Unconfined compression tests were conducted on the cylindrical samples (40.0mm×100.0mm) after soaking in sulfuric acids for various time periods using an Instron loading frame at a constant loading rate of 0.5 in./min for determining their unconfined compressive strength (UCS), failure strain and Young's modulus. The top surface of the samples was covered with a piece of cardboard to reduce the end effect on the testing results. The prismatic samples were tested with three-point bending tests according to the ASTM standard C78 [275] for the flexural strength of RFFG samples.

FTIR and XRD characterizations were conducted to investigate the change in chemical bonding and mineralogy of the RFFG samples after being exposed to sulfuric acids. Chunks of the samples after mechanical tests were ground to powder with an agate mortar and pestle until their particle sizes were less than 45μm. The FTIR spectra were obtained with a BrukerOptics Vetex70 FTIR spectrometer with the transmittance mode in the range of 500~1600 cm^{-1} at a resolution of 2 cm^{-1}. The powder samples were scanned with a Rigaku Geigerflex X-ray powder diffractometer using a CuKα radiation with a voltage of 37.5 kV and a current of 25 mA at 1 sec/step to obtain the XRD spectra. The data were collected from 6°to 70°2θ at 0.02 °/step and analyzed with MDI Jade 5.0.

4.2.5. Leaching Tests

Two types of samples were used for the leaching tests: (i) small cylindrical samples (25.4mm × 63.5mm); and (ii) powder samples ground from the cured small cylindrical

samples. The powders were ground to the particle size less than 45μm following the same procedure as the FTIR and XRD samples. The samples were soaked in the sulfuric acid and deionized water at the volumetric ratio of 1:20 [276] for 4, 8, 12, 16 and 24 hours and 3, 7, and 14 days, respectively. The powder samples were soaked in a 50mL glass vial and rotated to expedite the leaching rate, while the cylinders were soaked statically to mimic the practical scenarios. Two replicates were used for each sample set. The leachate was collected and pressure filtered using a filter paper with an opening of 0.45μm for atomic absorption spectroscopy (AA) tests. The concentration of Cu, Pb, Cr, Cd, As, Al and Fe in the collected leachate was measured with AA tests.

4.3. RESULTS AND DISCUSSION

4.3.1. Mechanical Properties of Durability Testing Samples

Unconfined compressive strength (UCS), Young's modulus, failure strain and bulk density of the RFFG samples after the soaking for up to 120 days are presented in **Figure 4-1**. The mechanical properties of the RFFG samples soaked for a short term of 1 and 7 days and a long term of 120 days are compared with those of the control OPC samples. As shown in **Figure 4-1** (a), the UCS values of the RFFGs did not decrease statistically after the one-day soaking, while the UCS of the OPC samples lost about 30% after soaking in deionized water, and lost about 10% after soaking in sulfuric acids based on their mean values. After 7 days' soaking in the acid, the UCS of the RFFG samples decreased from 10 ± 1.6 MPa to 6.7 ± 1.9MPa, and maintained 10.8 ± 0.6 MPa after 7days' soaking in the water, with 1.6, 1.9 and 0.6 being the respective standard deviations. For the OPC samples, the acid and water soaked samples have the UCS reduced from 9.3 ± 2.8 MPa to 8.5 ± 2.8 MPa and

6.3 ±4.6 MPa, respectively. After the soaking of 28, 56 and 120 days, the UCSs of RFFG samples maintained at 6~7MPa statistically, regardless of the leachants. After the long term soaking in the acid for 120 days, the UCS of RFFG samples lost up to 30% statistically. The UCSs of the OPC samples after the long term soaking in the acid and water were 8.0 ±2.3 MPa and 7.3 ±1.2 MPa, respectively. The UCS lost of OPC during the long term acid exposure is about 14% statistically, lower than that due to the short term exposure. This might be due to low permeability of OPC which prevented the samples from the further adsorpting liquid or acid and the strength slightly developed. It should be noted that the sustained UCS values of the RFFG and OPC samples are statistically similar, although a larger strength loss occurred in the RFFG samples after exposed to the acid and/or deionized water The failure stain of both the RFFG and OPC samples increased after soaking, as demonstrated in **Figure 4-1** (b). The failure strain of RFFG samples increased from 2.2% to 3.5~4.0% after soaking in the sulfuric acid for 1, 7 and 28 days, and further increased to ~5% after soaking longer than 56 days. For the RFFG samples soaked in the deionized water, the failure strain after soaking for different periods is similar; while the samples soaked for 28 and 56 days have a lower failure strain. The failure strain of OPC samples increased by ~1% (from 3.6% to 4.4% and 4.8% for soaked in the acid and water, respectively) after one-day soaking and kept constant statistically after soaking for longer periods. Both the RFFG and OPC samples show apparent decrease in Young's modulus after soaking in the acid and water, illustrating that the stiffness is affected more significantly by the acid attack compared to strength and ductility. The bulk density of the RFFG samples increased from 1.7g/cm^3 to 1.9g/cm^3 after one-day soaking in the sulfuric acid and deionized water due to the adsorption of liquids, and decreased to 1.8g/cm^3 after

a longer soaking. The OPC samples have a higher density than the RFFGs and barely show any change after soaking, regardless of pH values of the leachants and soaking periods. As illustrated by the unconfined compression testing results, the RFFG samples had similar durability to the control OPC samples exposed to low pH sulfuric acid and deionized water solutions.

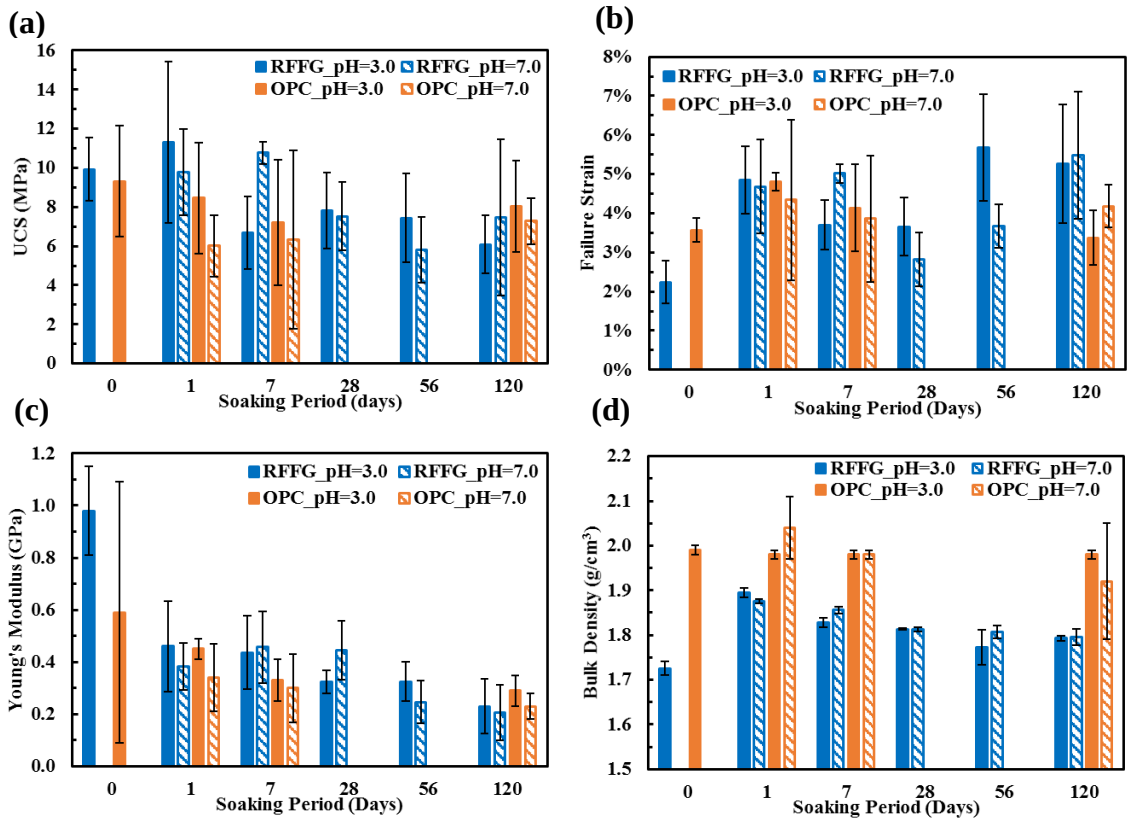

Figure 4-1. Change in (a) UCS, (b) failure strain, (c) Young's modulus and (d) bulk density of RFFG and OPC samples after soaking in sulfuric acid (pH=3.0) and deionized water (pH=7.0) for up to 120 days.

The flexural strength of the prismatic RFFG samples before and after the soaking in the sulfuric acid and deionized water is plotted against soaking time in **Figure 4-2**. After the

first day soaking, the flexural strength decreased from ~7MPa to ~4Mpa and barely further reduced statistically. The loss of flexural strength is about 45% of its initial value, higher than the UCS loss, illustrating that the flexural strength of the RFFG samples is more adversely affected by the soaking. This might be due to the different formation mechanisms of flexural strength and UCS. Flexural strength is estimated based on the tensile stress induced during the test which is mainly affected by the binding force between the particles and geopolymer gels. UCS is also contributed by the interaction among the particles besides the adhesive strength of geopolymer gels. Therefore, although the deterioration of both flexural strength and UCS of the RFFG samples is attributed to the partial dissolution of geopolymer gels and leaching of the alkali cations from the geopolymer samples during the soaking, the UCS was degraded less than flexural strength by the depolymerization.

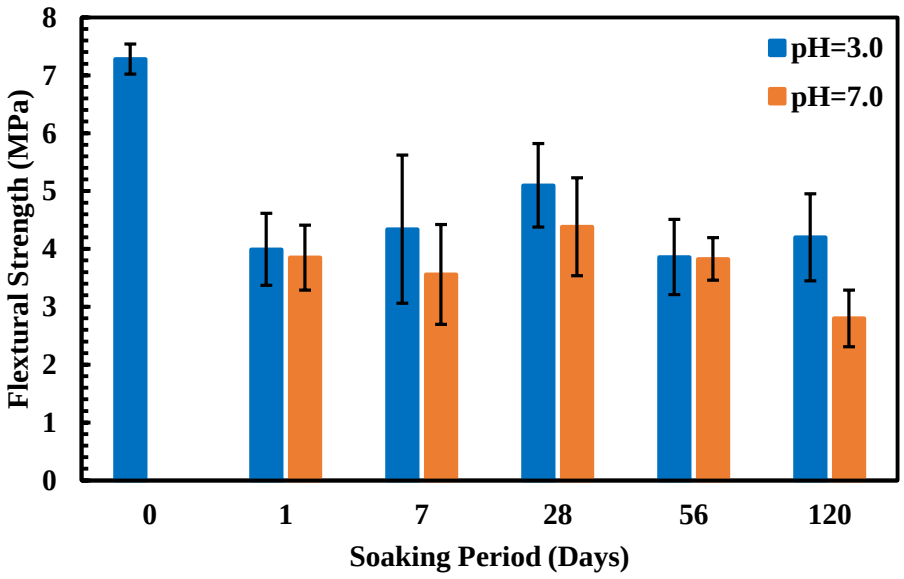

Figure 4-2. Variation of flexural strength of RFFG samples soaked in sulfuric acid (pH=3.0) and deionized water for 0 to 120 Days.

The normalized weight of the cylindrical RFFG and OPC samples soaked in the sulfuric acid and deionized water for 120 days is plotted as a function of the soaking time. The weight was normalized via dividing the weight of the soaked sample by its weight prior to soaking. As shown in **Figure 4-3**, the weight of the RFFG samples increased appreciably after the first day soaking, due to a large amount of solutions adsorbed by the pores in the samples. From the 2nd day to the 21st day, the weight started to decrease gradually from ~1.08 times to ~1.05 times the respective initial weight, due to the partial dissolution of the geopolymers, whereas no apparent visual degradation on the samples was observed. After the 21st day, the weight of the RFFG samples stayed constant through the soaking for 120 day, implying that no further dissolution happened. This is consistent with that the respective UCS values of the samples soaked for longer than 28 days barely had further decrease (**Figure 4-1** (a)). However, the Young's modulus of the RFFG samples kept decreasing after the soaking for longer than 28 days. Therefore, the deterioration mechanisms of strength and stiffness during soaking are different and need further investigation. On the other hand, the weight change of the OPC samples soaked in the sulfuric acid is different from that in the deionized water, as plotted in **Figure 4-3**. In the first 14 days' soaking in the acid and water, the weight of the OPC samples barely changed. During the longer soaking, the weight of OPCs in the sulfuric acid reduced by ~2% while the OPCs in the deionized water gained about ~2% weight.

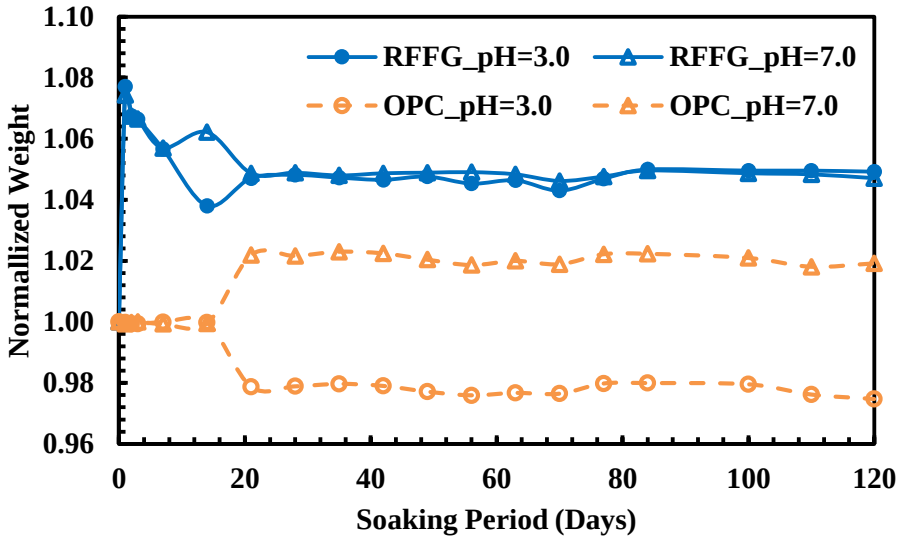

Figure 4-3. Weight of the cylindrical RFFG and OPC samples along the soaking period of 120 days.

4.3.2. Changes in Microstructure and Mineralogy of Durability Testing Samples

The SEM images of the RFFG samples before and after soaking in the sulfuric acid and deionized water are compared in **Figure 4-4**. Since the most mechanical strength was lost after one-day soaking, only the SEM images of the samples soaked for 1 day are shown. Note that the micro-morphologies of the RFFG samples soaked for longer than 1 day were similar to their 1-day counterparts. In the unsoaked sample, the unreacted particles are wrapped and bound with geopolymer gels, where the pores and cavities are observed in the geopolymer matrix, as shown in **Figure 4-4** (a). In the samples soaked in the acid and water for 1 day, the particles are still bound with the gels, while those close to the cavities are loosely compacted. The "geopolymer gel wrapping" is less apparent in the soaked samples, which implies that the liquid was adsorbed along the capillary pores where the geopolymer

gels nearby was partially dissolved, as circled in **Figure 4-4** (b) and (c),. Other than these, no apparent morphological difference is observed among these three samples.

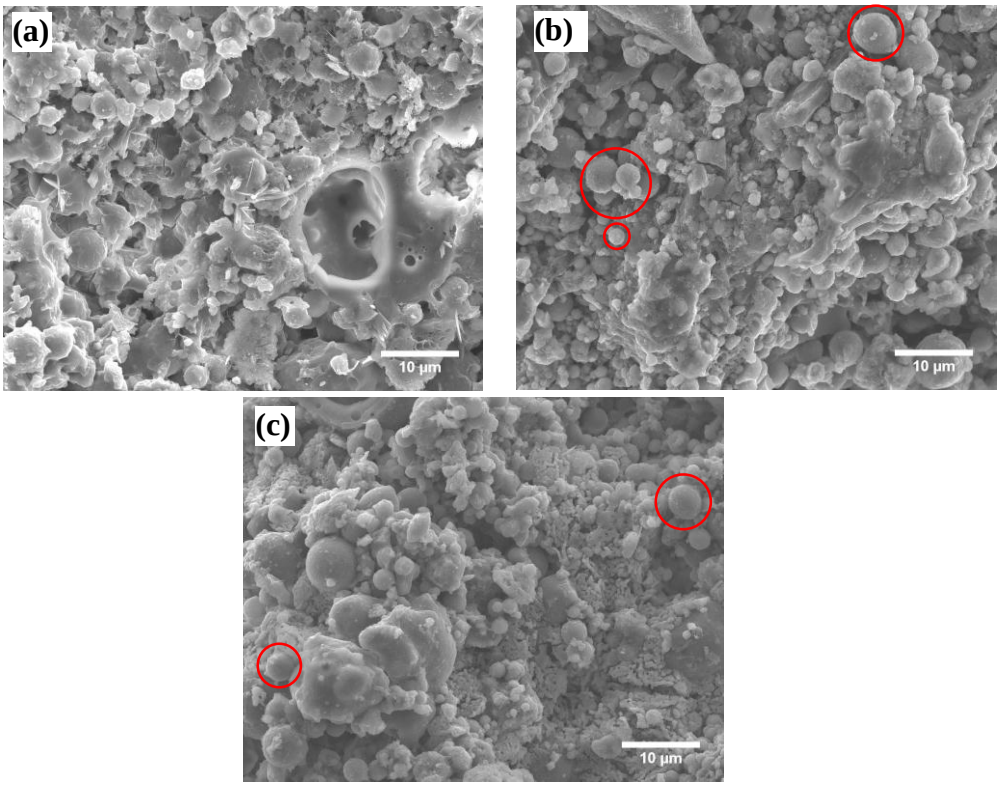

Figure 4-4. SEM images of RFFG samples (a) before soaking, (b) soaked in sulfuric acid (pH=3.0) and (c) deionized water (pH=7.0) for 1 day.

The mineralogical change of the RFFG samples before and after soaking in sulfuric acid and deionized water was characterized with XRD. Since different soaking time does not seem to affect the change in mineralogy of the soaked samples, only the XRD spectra of those soaked for 1, 56 and 120 days are compared with those of the unsoaked sample, as shown in **Figure 4-5** and **Figure 4-6** in the sulfuric acid and deionized water, respectively. The minerals in the RFFG samples did not change after the soaking, indicating that the

crystalline phases in the geopolymer were not dissolved by the leachants. However, the hump between 17°~38° 2θ, which is the characteristic XRD pattern of geopolymer gels, shifted to 15°~32° 2θ after the first day's soaking. This shift implies the partial dissolution of geopolymer gels in the sulfuric acid. This hump is gradually narrowed to 15°~30° 2θ after 56 days' soaking, and shows a decrease of intensity after 120 days' soaking, as illustrated by the enlarged view in **Figure 4-5** (b). For the RFFG samples soaked in the deionized water, the change of the XRD spectra is similar to that of the samples soaked in the acid, while the hump of geopolymer gels exhibits slightly less change after the sample was soaked for a longer periods (i.e., 56 and 120 days) compared to those soaked in the sulfuric acid, as shown in **Figure 4-6** (b). This elucidates that the partial dissolution of geopolymer gels by the sulfuric acid is slightly more than the deionized water. Nonetheless, the slightly higher dissolution of geopolymer gels in the acid did not result in a higher deterioration in the mechanical properties for the RFFG samples.

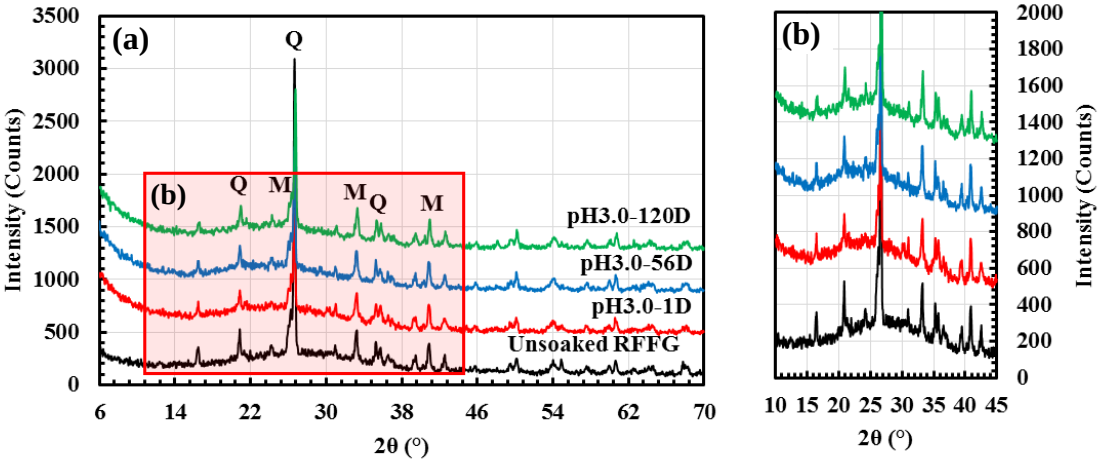

Figure 4-5. XRD spectra of (a) RFFG samples before and after soaking in the sulfuric acid at pH=3.0 for 1, 56 and 120 days with the spectra between 10° and 45° 2θ enlarged in (b). (Q: Quartz and M: Mullite).

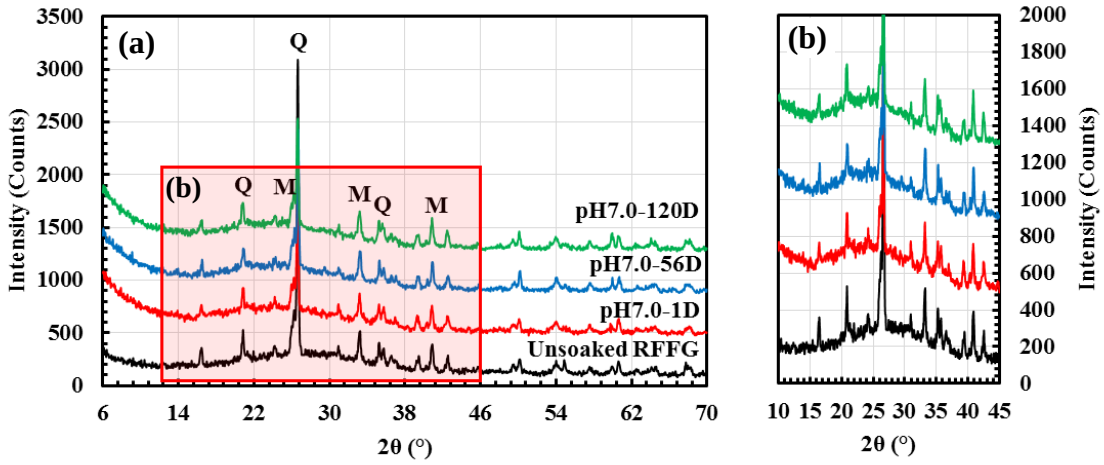

Figure 4-6. XRD spectra of (a) RFFG samples before and after soaking in the deionized water at pH=7.0 for 1, 56 and 120 days with the spectra between 10 ° and 45° 2θ enlarged in (b). (Q: Quartz and M: Mullite).

The partial dissolution of geopolymer gels by the sulfuric acid and deionized water was also confirmed by the FTIR characterization by using the same sample sets as in the XRD characterization, as shown in **Figure 4-7**. The asymmetric stretching vibration band of Si-O-T often assigned to geopolymer gels, where T is Si or Al, is observed in the unsoaked RFFG samples. The center of this band shifted from 972 cm^{-1} to a higher wavenumber in the range of 987~993cm^{-1} and 987~989cm^{-1} after the samples were soaked in the sulfuric acid and deionized water, respectively. This shift is caused by the dealumination and depolymerization by the attack of the leachants to the RFFG samples, which agrees well with the findings by Bakharev in the study on the resistance of fly ash based geopolymers exposed to sulfuric acids [23]. The wavenumber of Si-O-T band did not further increase when the soaking time increased, illustrating that the geopolymer gels were barely further

dissolved during the prolonged soaking periods. Another small peak around 870cm^{-1} appeared in the samples after soaking is also attributed to the dissolution of geopolymer gels [23].

The XRD and FTIR characterization results are consistent with the changes in mechanical properties of the RFFG samples after soaking in the sulfuric acid of pH=3.0 and deionized water. The deteriorating effect of the leachants on geopolymer gels and mechanical properties of soaked RFFG samples are summarized as follows: (i) the decreasing mechanical strength (e.g., UCS and flexural strength) and Young's modulus of the RFFG samples can be attributed to the partial dissolution of geopolymer gels by the leachants; (ii) neither further dissolution of geopolymer gels was observed during the soaking longer than 1 day, nor did the RFFG samples had further appreciable decrease in their mechanical strengths; and (ii) the deteriorating effect of the sulfuric acid on the mechanical properties of the RFFG samples is similar to that of deionized water within the 120 days' exposure.

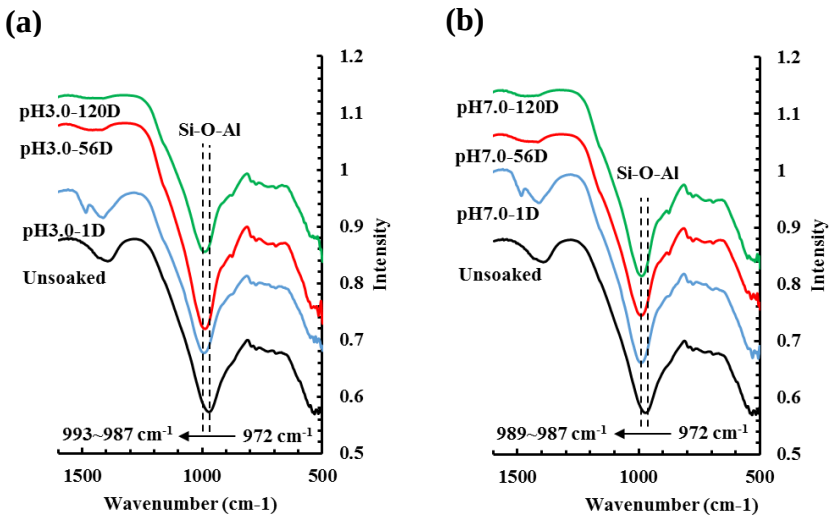

Figure 4-7. FTIR spectra of unsoaked RFFG sample and RFFG samples soaked in (a) sulfuric acid (pH=3.0) and (b) deionized water (pH=7.0) for 1, 56 and 120 days. The vertical dotted lines indicate the position of the asymmetric stretching vibration band of Si-O-T for geopolymer gels.

4.3.3. Leaching Behavior of Heavy Metals in RFFG Samples

In the collected leachates of the RFFG samples during soaking, Al, Fe and As were detected with AA tests, as well as other trace heavy metals: Cu, Cr and Cd. The concentrations of Al and As leached from different RFFG samples are plotted as a function of soaking time in **Figure 4-8**. In general, the concentration of leaching Al and As increased with the soaking time, regardless of RFFG sample size. Except for Al, the concentration of the leaching heavy metals did not show further increase after 7 days' soaking. For both the powder and cylindrical RFFG samples, the concentration of Al leached from the samples cured at room temperature was higher than that cured at 80 ℃ when the soaking time was shorter than 16 hours. This illustrates that the dealumination of room temperature cured RFFG was faster than RFFG samples cured at the elevated temperature. However, the

concentration of leached Al from the powder samples cured at 80℃ exceeded the room temperature counterpart when the soaking time was longer than 7 days. The leaching Al from the 80℃ cured cylindrical samples reached a similar concentration to that from the room temperature cured counterparts, as shown in **Figure 4-8** (b) at the end of the soaking. For the samples cured at room temperature, the level of Al leached by the sulfuric acid was similar to that by the deionized water. On the other hand, for the powder RFFG samples cured at 80℃ more Al was leached out by the sulfuric acid than the deionized water.

Arsenic (As) was leached from the powder samples very fast, whose concentration in the leachate after 4 hours' soaking was in the range of 1~1.5ppm, showing little dependence on the curing temperature of the RFFG samples or the pH value of the leachants. For the cylindrical samples cured at room temperature, the leaching As was less than 0.7ppm when the soaking time was shorter than 24 hours, which was undetectable in the leachate of the samples cured at 80℃. As the soaking continued, the concentration of As leached from the cylindrical samples increased to a similar level to that from the powder counterparts. The effect of pH value on the leaching behavior of As is insignificant for both the powder and cylindrical samples.

Iron (Fe) leached from the powder samples followed a similar trend to Al along the soaking time, but at much lower concentrations (<4ppm), while Fe leached from the cylindrical samples is negligible (<0.015ppm). The concentration of other heavy metals: Cu, Cr and Cd, leached from both powder and cylindrical RFFG samples was very low and did not show any change along the soaking time. Therefore, the leaching behavior of heavy metals: Fe, Cu, Cr and Cd is not presented herein for conciseness.

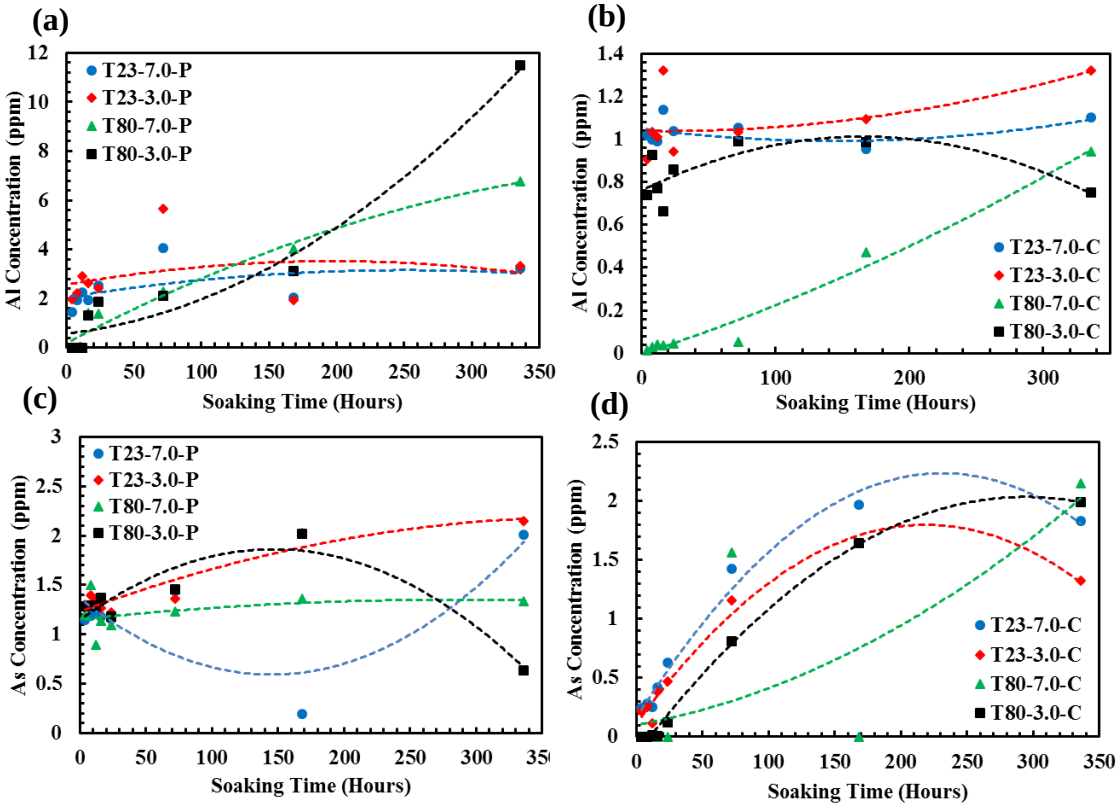

Figure 4-8. Concentration of Al leached from (a) powder RFFG samples, (b) cylinderical samples, As leached from (c) powder RFFG samples and (d) cylinderical RFFG samples cured at room temperature and 80 ℃ soaked in sulfuric acid (pH=3.0) and deionized water (pH=7.0) for 4 to 336 hours (14 days). Note that the samples are designated by curing temperature (T23: 23 ℃, room temperature or T80: 80 ℃)-pH value of the leachant (3.0: sulfuric acid or 7.0: deionized water-sample form (C: cylinder or P: powder).

The maximum concentration of heavy metals detected in the leachate during the soaking is presented in **Figure 4-9**. It should be noted that Al might have not reached the theoretical maximum level, which is the concentration of Al in the RFFG samples from the raw materials (see **Table 4-1**), by visually checking its leaching curve in **Figure 4-8** (a). The maximum concentrations of Al and Fe leached from the powder samples are much higher than those from the cylinder samples, while the highest concentrations of As leached from

these two types of samples are similar. The maximum concentrations of Cu, Cr and Cd leached from the powder samples are all similar to those from the cylindrical counterparts, which are all at trace level (<0.15ppm). As shown in the plot, more heavy metals leached in the sulfuric acid than the deionized water, especially for Al. This verifies that the dealumination effect by sulfuric acid is more intense than the deionized water, although no apparent difference in the mechanical deterioration was observed between the samples soaked in these two leachants in the durability tests. The maximum concentrations of Cu, Cr, Cd, and As leached from the RFFG samples are much lower than their respective contamination limits in soils by US EPA, which are 45, 212, 2 and 5.6 ppm, respectively [277].

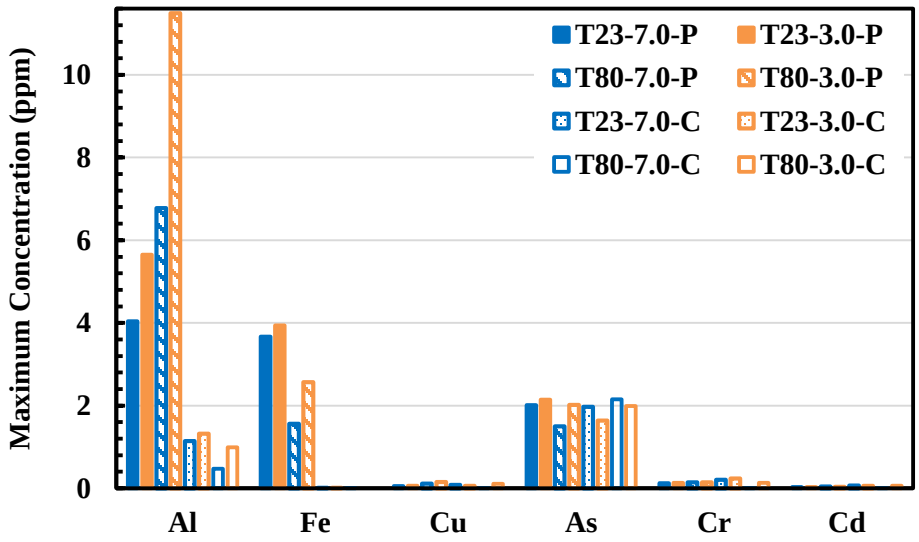

Figure 4-9. Maximum concentrations of the detectable heavy metals leached from the powder and cylindrical RFFG samples cured at room temperature and 80 ℃. Note that the samples are designated by curing temperature (T23: 23 ℃, room temperature or T80: 80 ℃)-pH value of the leachant (3.0: sulfuric acid or 7.0: deionized water-sample feature (C: cylinder or P: powder).

4.4. CONCLUSIONS

The durability and leaching behavior of heavy metals of red mud-class F fly ash based geopolymers (RFFG) exposed to a sulfuric acid of pH = 3.0 and deionized water at pH = 7.0 were investigated in this study. UCS, Young's modulus and flexural strength of the RFFG samples decreased by ~30%, ~70% and 45% after the exposure to the sulfuric acid for 120 days, respectively, which are comparable to the deterioration of respective mechanical properties of the control OPC samples. The failure strain slightly increased after the samples were exposed to the acid. The mechanical strength of the RFFG samples decreased after 1 day's soaking appreciably, but no further decrease in mechanical strength of the samples was observed during the rest of the soaking period. Young's modulus of the samples gradually decreased with the increasing soaking time.

The deterioration of the mechanical properties of the RFFG samples is attributed mainly to the partial dissolution of geoplymer gels, which is verified by the SEM, XRD and FTIR characterization results. The extended soaking did not cause further dissolution of geopolymer gels, indicated by the qualitative comparison of the XRD and FTIR spectra among the RFFG samples soaked for different periods. Furthermore, the change in the mechanical, physical and microstructural properties of the RFFG samples along the soaking in the sulfuric acid is similar to that in the deionized water, although the dealumination effect of the sulfuric acid is more intense than the water.

The concentrations of As, Cu, Cr and Cd detected in the leachate of the RFFG samples were all much lower than the respective contamination limits in soils by the US EPA standard, even for the leachate of the powder RFFG samples. In addition, the curing

temperature did not have much influence on the leaching behavior of heavy metals in the RFFG samples soaked in sulfuric acid or deionized water.

Based on current study, RFFGs were found to have resistance against a low pH value sulfuric acid and deionized water comparable to ordinary Portland cement. Mechanical properties and durability of RFFGs can be further improved by optimizing their synthesis, chemical composition and curing conditions. Furthermore, the use of the red mud-fly ash based geopolymers in civil engineering projects that may be exposed to a sulfuric acidic environment will not introduce heavy metals at an excessive level to the surrounding soils. Therefore, red mud-fly ash based geopolymerization technology not only produces a more economical and ‘greener’ alternative to ordinary Portland cement, but also lend itself to recycle and reuse two abundant industrial wastes: red mud and fly ash.

CHAPTER 5 - EFFECT OF CHEMICAL COMPOSITION ON GEL FORMATION AND NANOSCALE MECHANICAL PROPERTIES OF GEOPOLYMERS

5.1. INTRODUCTION

Geopolymer has attracted increasing attention as a sustainable alternative to ordinary Portland cement for its high strength, good durability, low energy consumption and low CO_2 emission during the production. Geopolymer is formed via the polymerization of silicate and aluminate tetrahedrons by sharing all the oxygen atoms, which has an amorphous or a semi-crystalline molecular structure with a simplified chemical formula $M_n\{-(SiO_2)_z - AlO_2\}_n$, where M is an alkali cation that balances the negative charge introduced by the Al^{3+} in tetrahedral coordination, such as Na^+ or K^+; n is the degree of polymerization; and z is the Si/Al molar ratio in this structure, which is in the range of 1 to 3, and up to 300 [13]. For geopolymers with cementitious binder-like properties, z is between 1 and 3, which have three basic aluminosilicate structures that repeat in geopolymeric network: polysialate (-Si-O-Al-O-, PS), polysialate-siloxo (-Si-O-Al-O-Si-O-, PSS) and polysialate-disiloxo (-Si-O-Al-O-Si-O-Si-O-, PDSD), where PSS and PDSD are more stable and rigid than PS [178]. Geopolymer is usually synthesized by using powdery Si- and Al-rich materials activated with alkali hydroxide or/and silicate solutions. The solid raw materials were first dissolved in the activator to release reactive silicate and aluminate monomers or small oligomers. Along with the dissolution, the reactive components are polymerized to larger clusters, such as chain and ring structures. As the reaction proceeds, the clusters are further polycondensed to more cross-linked networks,

which are the geopolymer gels that act as binding agents in the resulting geopolymers [157, 158]. At the last stage, zeolite can be formed via the crystallization of the clusters under some circumstances, such as a high concentration of soluble silicate [170] and high temperatures [278]. Water is consumed at the first reaction stage, and released at the following stages and left pores in the final geopolymer matrix [53]. Therefore, the experimentally synthesized geopolymers usually have a composite nature, which consist of geopolymer gels, unreacted raw materials, zeolitic crystals (if available) and micro- or undermicro-cracks and pores that are formed due to the water evaporation or introduction of air.

Geopolymers have been successfully synthesized with many Si- and Al-rich materials, including metakaolin [103, 138, 236], fly ash [47, 88-90], ground blast furnace slag, red mud [56, 57], rice husk ash [56] and palm oil fuel ash [58, 59], most of which are industrial wastes. Because of its high mechanical strength [14, 15], excellent fire- and chemical-resistance [20-27] and low content of leachable heavy or toxic metals [29, 30], geopolymer has been widely studied for its potential applications in concrete [17, 33], soil stabilization [38, 39, 109], fire protective coating [20-22], toxic/radioactive waste encapsulation [30] and sewer pipes [34]. However, it is still difficult to tailor the properties of geopolymers during synthesis since they are influenced by multiple synthesis factors, such as the properties of raw materials [85], chemical composition (e.g., Si/Al and Na/Al ratios) [31, 47, 101, 105, 169, 172, 173], water content [113] [132], curing temperature [50, 84, 87, 185] and humidity [99, 106]. The microstructure, the properties and proportion of geopolymer gels play important roles in governing the macro-mechanical properties of the geopolymers, and thus the characteristics of geopolymer gels at micro- or nano-scale have

to be well understood to adjust the geopolymer synthesis and achieve desired properties. The microstructure and formation processes of geopolymer gels have been investigated with scanning electron microscopy (SEM) [53], energy dispersive X-ray spectroscopy (EDX) [90, 103, 115], X-ray diffractometer (XRD) [13, 109-112], Fourier transform infrared spectroscopy (FTIR) [127, 165, 166], nuclear magnetic resonance (NMR) [142, 170, 279] and isothermal conduction calorimeter (ICC) [123, 124]. SEM-EDX can obtain a morphological but qualitative characterization of the microstructure of geopolymers; XRD can be used to examine the mineralogical change after the geopolymerization and provide indirect evidence for the formation of geopolymer gels; FTIR and NMR tests provide analytical results of the atomic arrangement of geopolymer gels; and ICC measurements can monitor the heat released during the geopolymerization process and qualitatively assess the reaction rate. Based on the results of mechanical tests and NMR characterization, Fernández-Jiménez et al. [169] divided the development of geopolymer gels into two stage: (i) Al-rich gels were formed through the polymerization of the reactive silicate and aluminate tetrahedrons first at the early stage; and then (ii) Al-rich gels grew into Si-rich gels gradually at the later stage. They also found that the development of the mechanical strength of geopolymers occurred mainly during the second stage because Si-rich gels have a higher strength than Al-rich counterparts. This development of geopolymer gels described by Fernández-Jiménez et al. is also supported by the FTIR results [107, 127, 165, 169]. In these studies, the authors tracked the change in the wavenumber of the asymmetric stretching vibration band of Si-O-T (T is Si or Al), which is a characteristic FTIR band of geopolymer gels, along the reaction process. Since Si-O-Si has a lower bond angle and bond length compared to Si-O-Al, its vibrational constant is higher than Si-O-Al

bond's, and thus the geopolymer gels rich in Si-O-Si show the Si-O-T band at a higher wavenumber. The Si-O-T band of geopolymer gels observed in these studies always shifted to a lower wavenumber first and then back to a higher one. However, a quantitative characterization of mechanical properties at micro- or nano-scale and the proportion of geopolymer gels cannot be obtained with these analytical techniques due to the amorphous nature of geopolymer gels, which are indistinguishable from the other components presented in composite geopolymers.

The grid-nanoindentation technique has been applied to investigate mechanical properties (e.g., Young's modulus and hardness) of the heterogeneous materials, such as cement paste, natural rock, shale and bones [153, 154, 280]. Based on grid indentation results, the volumetric distributions of multiple phases in a heterogeneous material can be estimated with the aid of deconvolution analysis on the histogram of Young's modulus or hardness. Given that geopolymer gels are in the order of several nanometers to micrometers [278], grid nanoindentation and deconvolution analysis were conducted on metakaolin- and fly ash-based geopolymers to investigate mechanical properties and volumetric distribution of geopolymer gels [155, 156]. Beleña and Zhu [155] conducted grid nanoindentation on two metakaolin-based geopolymers with different curing procedures. Based on the statistical deconvolution analysis of 8×15 (=120) indents, they identified three phases in the geopolymers, including geopolymer gels, metakaolin and crystalline minerals. They found that the Young's modulus and hardness of geopolymer gels varied in the range of 7 GPa ~ 14 GPa and 0.2 GPa ~ 0.5 GPa, respectively, while the proportion of geopolymer gels ranged between 83% and 89%, depending on synthesis procedures. Němeček et al. [156] applied the grid nanoindentation technique on a metakaolin based

geopolymer (MKG) cured at ambient temperature and two fly ash based geopolymers (AAFA) cured at ambient temperature and 80 ℃. They identified four phases in AAFA, which are N-A-S-H gels (also known as geopolymer gels), partly-activated slag, nonactivatd slag and nonactivated compact glass in ascending order of their Young's modulus; and two phases in MKG, including geopolymer gels and unreacted metakaolin. They found that the Young's modulus of geopolymer gels is irrelevant of the raw materials or curing temperatures, which is around 17 GPa with a standard deviation of 3 ~ 5 GPa. The volumetric proportion of geopolymer gels, on the other hand, shows dependence on the curing temperature and raw materials, which is 50.7%, 77.5% and 97.2% in heat-cured AAFA, ambient-cured AAFA and heat-cured MKG, respectively. However, the correlation between the proportion of geopolymer gels and mechanical properties of geopolymers at macro-scale was not investigated, nor is the influence of chemical composition of raw materials on the resulting geopolymer gels.

In this study, metakaolin based geopolymers were synthesized with different Si/Al and Na/Al ratios cured for from the final setting time to 28 days. They were characterized with mechanical tests, grid nanoindentation and FTIR to (i) determine mechanical properties, including Young's modulus and hardness, of geopolymer gels at nano-scale and distinguish the multiple phases of geopolymers; (ii) estimate the proportion of geopolymer gels and examine its effect on macro-mechanical properties of geopolymers; (iii) investigate the effect of chemical composition of raw materials on reaction rate, development of geopolymer gels and macro-mechanical properties of geopolymers. The final setting time was measured by the Vicat needle test for each geopolymer sample to examine the effect of chemical composition on the reaction rate. FTIR was conducted on the geopolymers

during the curing to reveal the development of geopolymer gels and its dependence on the chemical composition of the raw materials. The results from this study reveal the influence of volumetric proportion and microstructure of geopolymer gels on the macro-mechanical properties of MKG at different reaction stages. This multi-scale study also sheds light on the relationship of chemical composition-formation of geopolymer gels-mechanical properties of geopolymers at macro-scale.

5.2. MATERIALS AND METHODOLOGY

5.2.1. Materials and Geopolymer Sample Preparation

Metakaolin (MK) from Advanced Cement Technologies, LLC, was used to synthesize geopolymers to reduce the intervening effect of impurities in the raw materials. The chemical and physical properties of the MK are summarized in **Table 5-1**, with SiO_2 and Al_2O_3 as the dominant constituents. The majority of the silicate and aluminate in MK is in amorphous nature due to the high temperature calcination (> 550 ℃) during the production of MK from kaolinite. In addition, the platy shaped and fine MK powders have a high contact area with the solutions. Therefore, the reactivity of MK in the alkali activator is very high.

Table 5-1. Chemical composition and physical properties of metakaolin

Chemical composition	
SiO_2 (wt%)	52.20
Al_2O_3 (wt%)	43.11
Fe_2O_3 (wt%)	1.53
CaO (wt%)	0.07
MgO (wt%)	0.06
Na_2O (wt%)	0.07
K_2O (wt%)	0.22
SO_3 (wt%)	0.99
Moisture content (wt%)	0.33
Loss on ignition (wt%)	0.18
Physical properties	
Amount passing No. 325 sieve (wt%)	92.9
Blaine Fineness (m^2/kg)	2690

A sodium hydroxide solution (NaOH~50%, and H_2O~50%) from Fisher Science Inc. USA and a reagent grade sodium silicate solution (Na_2O~10.6%; SO_2~26.5%, 1.39g/mL at 25 ℃) from Sigma Aldrich Inc. USA were mixed with deionized water at the predetermined proportions to prepare alkali activators and adjust Si/Al and Na/Al ratios of the geopolymer precursors. Metakaolin based geopolymer (MKG) samples were prepared with seven Si/Al molar ratios and four Na/Al molar ratios, ranging from 1.2 to 2.2 and 0.6 to 1.2, respectively. The effect of chemical composition on the formation of geopolymer gels and mechanical properties of the resulting geopolymer at nano- and macro-scale was investigated with the samples listed in **Table 5-2**. The Si/Al or Na/Al ratio was used to designate the MKG sample sets, represented as SA and NA respectively, followed by a number that is 10 times the respective molar ratio used for the geopolymer synthesis (see **Table 5-2**). The sample sets with varying Si/Al ratios have a fixed Na/Al ratio around 1.0 that is the theoretical Na/Al ratio for geopolymers [31, 53, 55], and those with varying Na/Al ratios have a fixed

Si/Al ratio of 1.7. The Na/Al ratio (1.07 ≈ 1.1) of SA17 (NA11) sample sets has been verified as a good starting chemical composition of MKG synthesis in the previous experiments by the authors, which is very close to 1.0 and was not changed in this study. These nominal chemical compositions were calculated with the content of Si, Al and Na in the activators and metakaolin. The water content of all the geopolymer sample sets was adjusted to 41%, except for the samples with a Si/Al ratio of 2.2, for which 43% is the lowest water content that can be reached.

Table 5-2. Metakaolin based geopolymer samples prepared with different Si/Al and Na/Al molar ratios

Sample Set	Si/Al (molar ratio)	Na/Al (molar ratio)	Water Content	Objectives	Curing Conditions	Curing Period
[a]SA12	1.2	1.0	41%	Effect of Si/Al ratio	Room temperature (~23 ℃), and 40% ~50% RH	Final setting time (FS), 7 days (7D) and 28 days (28D)
SA14	1.4	1.0	41%			
SA16	1.6	1.0	41%			
SA17	1.7	1.1	41%			
SA18	1.8	1.0	41%			
SA20	2.0	1.0	41%			
SA22	2.2	1.0	43%			
[b]NA06	1.7	0.6	41%	Effect of Na/Al ratio		
NA08	1.7	0.8	41%			
NA11	1.7	1.1	41%			
NA12	1.7	1.2	41%			

Note: [a.] SA stands for Si/Al molar ratio and [b.] NA for Na/Al molar ratio.

5.2.2. Sample Preparation for Mechanical Properties and Final Setting Time Tests

Metakaolin was thoroughly mixed with the activators for 30 minutes and poured into two types of molds to prepare the samples for mechanical property and the final setting time

tests, respectively. For the mechanical property testing samples, the molds were made with 100mm (height) × 40mm (diameter) PVC pipes at a height/diameter ratio of 2.5 to reduce the end effects of the cylindrical samples during unconfined compression tests. The final setting time of MKG samples was determined by adopting the Vicat needle method specified in ASTM standard C191-13 [258] for the setting time of hydraulic cement. According to this standard, the final setting time is defined as the time elapsed between the contact of the geopolymer and the moment when the needle does not leave a complete circular impression in the paste surface. The apparatus used in ASTM C191-13 to hold cement slurries is a conical ring and a non-adsorptive plate. For geopolymer precursors, a short piece of PVC pipe with the bottom sealed by non-adsorptive tapes was used, due to the more fluid nature of the geopolymer precursors that would otherwise leak out from the joint between the conical ring and the plate. The PVC pipe has the same height and a similar volume to those of the conical ring. After pouring, both types of the samples were vibrated for 5 minutes to remove the air bubbles introduced during the mixing. These samples were then sealed in plastic bags and cured at room temperature (~23 ℃) in a plastic frame equipped with a humidifier to maintain a relative humidity of 40%~50%. The final setting time was measured every 10 minutes with the Vicat needle [258] after the geopolymer slurry was poured into the PVC pipe. The samples for mechanical property tests of each recipe (**Table 5-2**) were cured for the final setting time, 7 days and 28 days, respectively, with 3 replicates prepared for each curing period.

5.2.3. Characterization of Mechanical Properties and Microstructure of MKG Samples

Mechanical properties of the cured MKG cylindrical samples at macro-scale, including unconfined compressive strength (UCS), Young's modulus (E_m) and failure strain (ε_f), were tested with an Instron loading machine at a constant loading rate of 0.5 in./min. The top surface of the samples was covered with a cardboard to reduce the influence of the uneven surface formed in the curing on the testing results.

After the compression testing, small chunks of the crushed samples were ground into fine powders that have a particle size less than 45 μm with an agate mortar and pestle for FTIR analysis. The exterior portion of the MKG samples was avoided to reduce the effect of carbonate formed during the exposure to the air. The MK powders were also characterized with FTIR to provide baseline spectra and compare with those of MKG samples. The FTIR spectra were obtained with a BrukerOptics Vetex70 FTIR spectrometer with the transmittance mode in the range of 500~1600 cm^{-1} at the resolution of 2 cm^{-1}.

5.2.4. Grid Nanoindentation

Mechanical properties of MKG samples at nano-scale, including Young's modulus (E_n) and hardness (H), were characterized with grid-nanoindentation tests. The samples for nanoindentation were prepared by cold mounting the crushed samples after the compression testing with epoxy in a plastic mold, which has an inner diameter of 25mm that is the same size of the nanoindentation sample holder. The PELCO® epoxy resin was mixed with a hardener at a ratio of 3:1, and then poured into the mold, in which a piece of MKG chunk was placed. After hardened for 24 hours, the sample surface was polished

using a series of silica carbonate papers in descending order of fineness of 60, 120, 240, 320 and 600 grit to obtain a flat surface, and then further polished with a series of Al_2O_3 pastes in descending order of the particle size of 1 micrometer, 300 nanometers, and 50 nanometers. The Al_2O_3 particles remained in the pores of the samples during the polishing were removed by using the ultrasonic bath.

The polished samples were tested using Nano Indenter® XP with a Berkovich indenter. To obtain a statistical analysis of the nano-mechanical properties of this heterogeneous composite, three areas of each MKG sample that show different phases under the 40× optical microscopy were selected to conduct the nanoindentation. Within each chosen area, 100 indents in 10×10 grids with a 7-μm spacing between two indents were taken. Therefore, a total of 300 indents were carried out on each sample. The maximum penetration depth of the indentation was set to 500nm. The nanoindentation was conducted in the Continuous Stiffness Measurement (CSM) mode, where a harmonic loading, as sketched in **Figure 5-1**, was applied on the surface of samples with a loading rate of 50 nN/s and a frequency of 55 Hz [281].

Based on the analysis procedure for nanoindentation testing developed by Oliver and Pharr [282], the hardness of the indented sample can be determined as follows:

$$H = \frac{P_{max}}{A} \tag{5.1}$$

Where P_{max} is the maximum load (**Figure 5-1**) and A is the projected contact area.

The Young's modulus can be determined with the following equation:

$$E_n = \frac{(1-\nu^2)E_i}{E_r E_i - (1-\nu_i^2)} \quad (5.2)$$

Where E_n and ν are the Young's modulus and Poisson's ratio of the indented sample and ν was assumed to be 0.18 for all the MKG samples, E_i and ν_i are the Young's modulus and Poisson's ratio of the indenter. For a diamond indenter, E_i=1141GPa and ν_i =0.07 [282]. E_r is the reduced modulus, also called indentation modulus, which is defined as follows:

$$E_r = \frac{S\sqrt{\pi}}{2\beta\sqrt{A}} \quad (5.3)$$

Where *S* is the contact stiffness, β is a constant depending on the geometry of the indenter. For Berkovich indenter, β=1.034. The contact stiffness with CSM technique can be measured at any point along the loading curve, instead of the unloading point in the linear loading mode. *S* can be calculated as follows [281]:

$$S = \left[\frac{1}{\frac{P_{OS}}{h(\omega)}\cos\phi - (K_S - m\omega^2)} - K_f^{-1}\right]^{-1} \quad (5.4)$$

Where P_{OS} is the amplitude of the oscillating force, *h(ω)* is the displacement response, ω is the loading frequency, ϕ is the phase angle between the oscillating force and the displacement response, *m* is the mass of the indenter, K_s is the spring constant of the leaf springs that support the indenter, and K_f is the stiffness of the indenter frame.

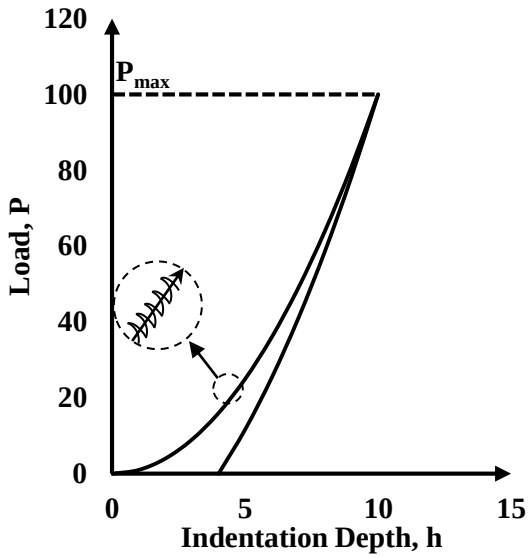

Figure 5-1. Schematic illustration of the CSM loading cycle, redrawn from [281].

5.2.5. Deconvolution technique

The statistical deconvolution technique proposed in [156, 283] was applied to estimate the Young's modulus (E_n) and hardness (H) of each phase in the MKG samples based on the histograms of E_n and H, respectively, with an alternative minimization criterion.

Firstly, the experimental histograms of E_n and H were plotted with all the effective measurements that were divided into N^{bins} bins at an equal spacing b. For all the samples, the proportion of effective measurements was higher than 90%, i.e., $N^{exp} > 270$, where the failure of the measurements can be caused by the defects on the samples' surfaces and the surrounding vibration that lasted longer than the drifting time (1 hour in this study). For the MKG samples measured in this study, 0.5 GPa and 0.05 GPa were used as the b value for the histograms of E and H, respectively, to obtain a sufficient resolution. Accordingly, the experimental probability density function (PDF) can readily be determined as follows:

$$p_i^{exp} = \frac{f_i^{exp}}{N^{exp}} \cdot \frac{1}{b} \quad (5.5)$$

Where p_i^{exp} is the experimental PDF of bin *i*, f_i^{exp} is the frequency of the values (e.g., Young's modulus or hardness) within bin *i* in the overall effective indentation measurements, N^{exp}, and $i = 1, \ldots, N^{bins}$.

Based on the experimental histograms constructed with an appropriate bin size, m phases in the MKG samples can be distinguished. E_n or H of each phase was assumed to follow a normal distribution,

$$p_r(x) = \frac{1}{\sqrt{2\pi s_r^2}} exp \frac{-(x-\mu_r)^2}{2s_r^2} \quad (5.6)$$

Where p_r is the theoretical PDF of the r-th phase, $r = 1, \ldots, m$, *x* is the property of interest (i.e., E_n or H in this study), μ_r and s_r are the arithmetic mean value and standard deviation of all *x* values within the r-th phase, respectively, which are defined as

$$\mu_r = \frac{1}{N_r}\sum_{k=1}^{N_r} x_k \,; s_r^2 = \frac{1}{N_r - 1}\sum_{k=1}^{N_r}(x_k - \mu_r)^2 \,; k = 1, \ldots, N_r \quad (5.7)$$

Where N_r is the number of *x* in the r-th phase, x_k is the values of E_n or H of the indents in the r-th phase.

The volume fraction of the r-th phase is $f_r = \frac{N_r}{N^{exp}}$, and the theoretical PDF for all the effective measurements is $p^{the}(x) = \sum_r^m f_r p_r(x)$. It should be noted $\sum_i^m f_r = 1$. The theoretical PDF of each phase was determined by the following minimization criterion:

$$min \sqrt{\sum_i^m (p_i^{exp} - p^{the}(x_i))^2} \quad (5.8)$$

The derived phase number, *m*, varied from 2 to 4 due to the varying degrees of reaction of the MKG samples synthesized with different chemical compositions and curing periods.

5.3. RESULTS AND DISCUSSION

5.3.1. The Final Setting Time

The final setting time of the MKG samples synthesized with different chemical compositions was determined firstly. As plotted in **Figure 5-2**, the final setting time of the MKG samples increased with the increase in Si/Al molar ratio and the decrease in Na/Al molar ratio. Most of the samples set within 1 day, except for the samples SA20, SA22 and NA06, which set after 48 hours, 9 days and 15 days, respectively. As can be seen in the figures, the final setting time of the MKG with a Si/Al ratio larger than 2.0 or Na/Al ratio lower than 0.8 increased significantly, which will further be discussed in Section 5.3.4.

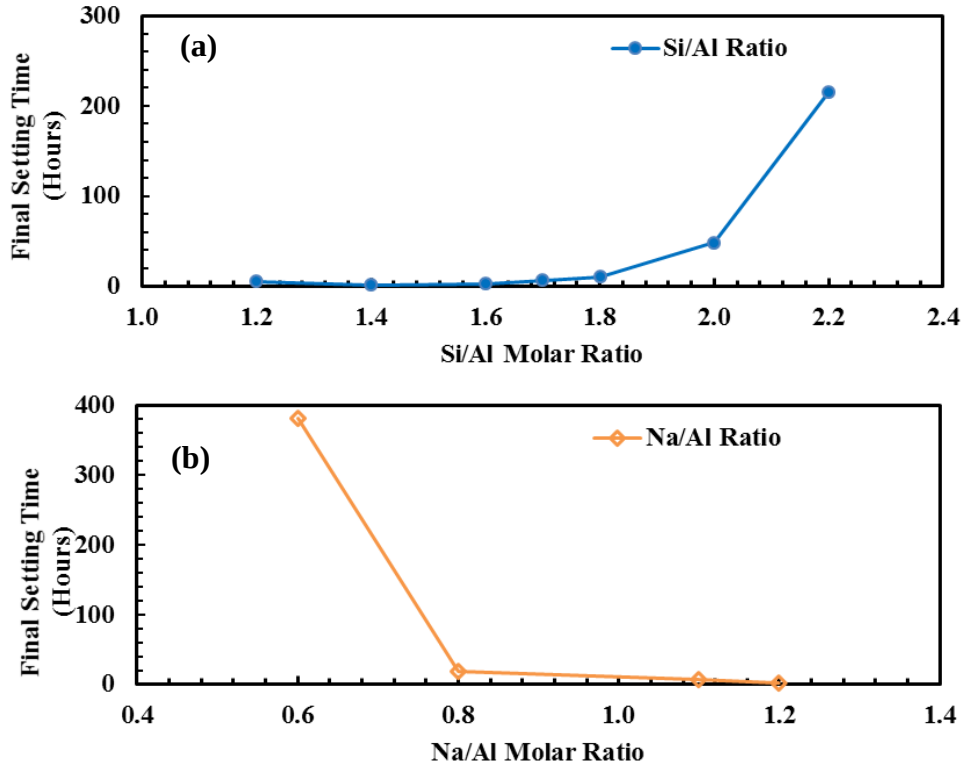

Figure 5-2. The final setting time of MKG samples with different (a) Si/Al molar ratios, and (b) Na/Al Molar ratios.

5.3.2. Mechanical Properties

Unconfined compressive strength (UCS), Young's modulus (E) and failure strain (ε_f) of the MKG samples cured for the final setting time (FS), 7 days (7D) and 28 days (28D) are plotted against Si/Al and Na/Al molar ratios in **Figure 5-3** and **Figure 5-4**, respectively. Note that the final setting time for different MKG sample sets is different and can vary significantly from one sample set to another, as shown in **Figure 5-2**. SA12 samples (with a Si/Al ratio of 1.2) were too crumbled to be tested after the final setting time, and cracked after 28-day curing, so only the results after 7 days' curing are plotted in **Figure 5-3**. SA22

samples (with a Si/Al ratio of 2.2) set after 9 days, and therefore only the results of FS and 28D cured samples are available. Similarly, only the results at FS and 28 days of NA06 samples (with a Na/Al ratio of 0.6), which set after 382 hours (i.e., 15 days and 22 hours), are presented in **Figure 5-4**; and the NA12 samples (with a Na/Al ratio of 1.2) cracked after 28 days' curing, and thus the corresponding mechanical properties were not measured.

In general, UCS and E increased with the Si/Al ratio in the range from 1.2 to 1.7, and then decreased when the Si/Al ratio was higher than 1.8. There is no consistent trend of UCS with the curing time, and the development of the mechanical strength shows apparent dependence on the Si/Al ratios. The UCS of sample SA14, SA16 and SA17 (with a Si/Al ratio of 1.4, 1.6 and 1.7, respectively) developed fast, where their strengths after the final setting time are statistically similar to that of the respective samples cured for 7 and 28 days. The only exception is SA16, of which the UCS after the final setting time is slightly lower than the 7 days and 28 days counterpart. For the samples with a Si/Al ratio lower than 1.4 or higher than 1.8, the UCS after the final setting time is very low or even not available (SA12). For SA18, SA20 and SA22, the slow UCS development is consistent with the long final setting time (see **Figure 5-2** (a)). Although the early strength of SA18 and SA20 is low, their UCS kept increasing along the curing and achieved a relatively high level after 7 and 28 days curing. These findings agreed well with that in the study by Hajimohammadi et al. [168] and the geopolymerization model built by Fernández-Jiménez et al. [169]. They found that the geopolymer with a relatively lower Si/Al ratio (a higher content of Al), an Al-rich gel with a large amount of Si-O-Al bonds was formed faster, and thus an early strength developed quicker (e.g., SA14, SA16 and SA17). When the Si/Al ratio is high, the mechanical strength developed slower but can reach a higher value in a

long term, due to the lower formation rate of the Si-O-Si bonds which, however, have a higher strength than the Si-O-Al bonds. In this case, SA18 and SA20 could not develop a higher strength than SA17 after 28 days curing. This might be due to the deterioration on the MKG samples, such as drying cracks formed during the curing. The UCS of SA12 after 28 days is not available due to the cracks; while for SA22, the UCS after 28 days is still very low, illustrating that either too low or too high Si/Al molar ratio cannot result in high mechanical strength. Young's modulus of the MKG samples after the final setting time apparently decreased with the Si/Al ratios. After 7 days and 28 days curing, the E_m of the MKG samples with a Si/Al ratio at 1.6~1.7 increased more than the other samples. The relation between the development of E_m and Si/Al ratio is also consistent with the findings by Hajimohammadi et al. [168] and Fernández-Jiménez et al. [169]. The failure strain of the MKG samples presents less dependence on the curing time or the Si/Al ratio, as shown in **Figure 5-3** (c). It is only distinct that the ε_f after the final setting time is higher than that after 7 days or 28 days curing, while the ε_f of SA22 is extremely high because this sample set was very soft and deformable after the final setting time.

For the MKG cured for the final setting time, the UCS and E_m increased, while ε_f decreased with Na/Al ratio, as illustrated in **Figure 5-4**. After 7 days and 28 days curing, the strengths of the samples with a Na/Al ratio of 0.8 and 1.1 are similar, which are both higher than that with a Na/Al ratio of 1.2. The Young's moduli of the samples cured for 7 and 28 days increased with the Na/Al ratio and then maximized at Na/Al=0.8 and 1.1, respectively. Again, the effect of Na/Al ratio on the failure strain of the MKG samples was not apparent, as shown in **Figure 5-4** (c).

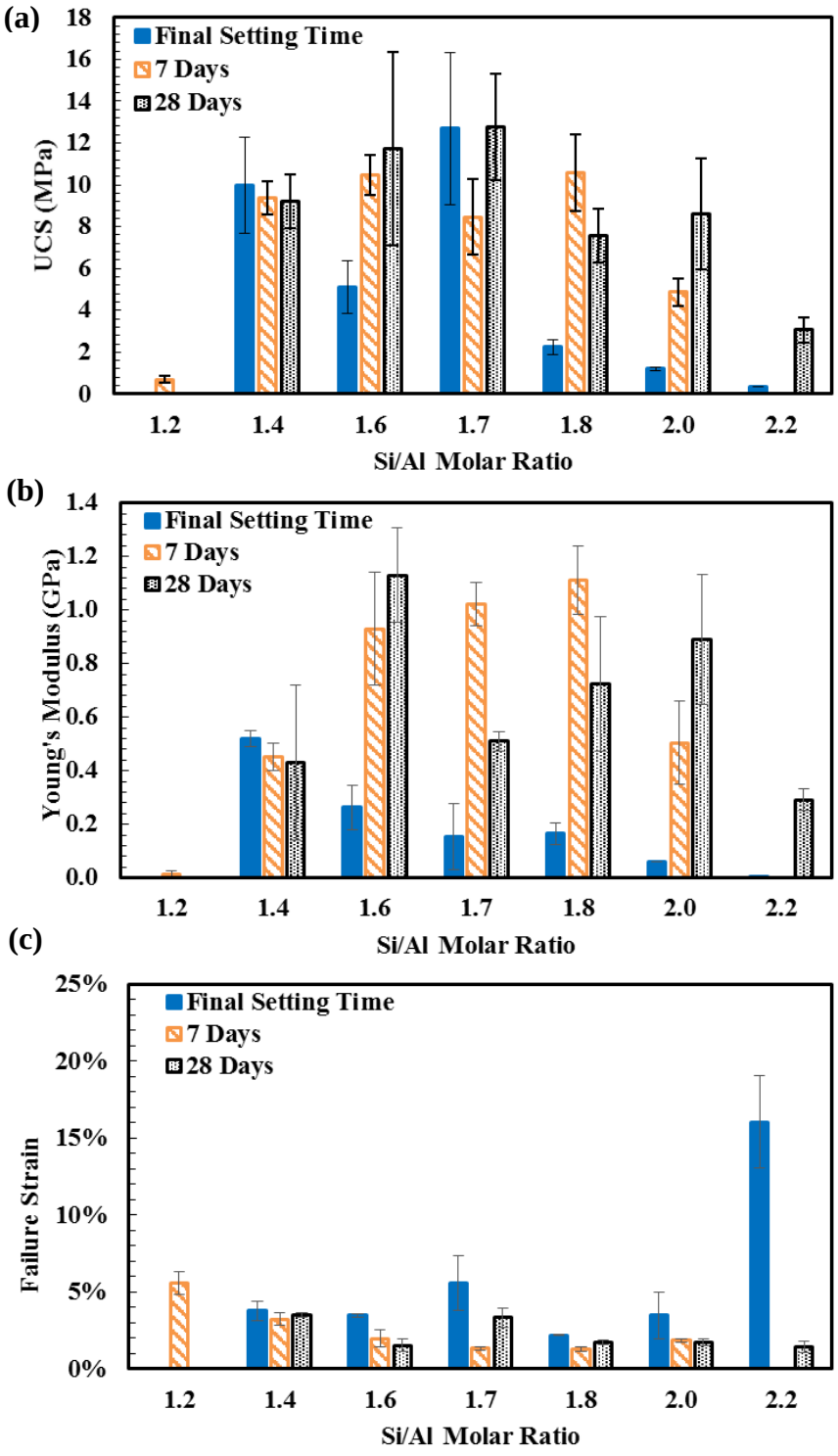

Figure 5-3. Effect of Si/Al molar ratio on (a) UCS, (b) Young's modulus and (c) failure strain of MKG samples cured for the final setting time, 7 days and 28 days, where the error bars are the standard deviations.

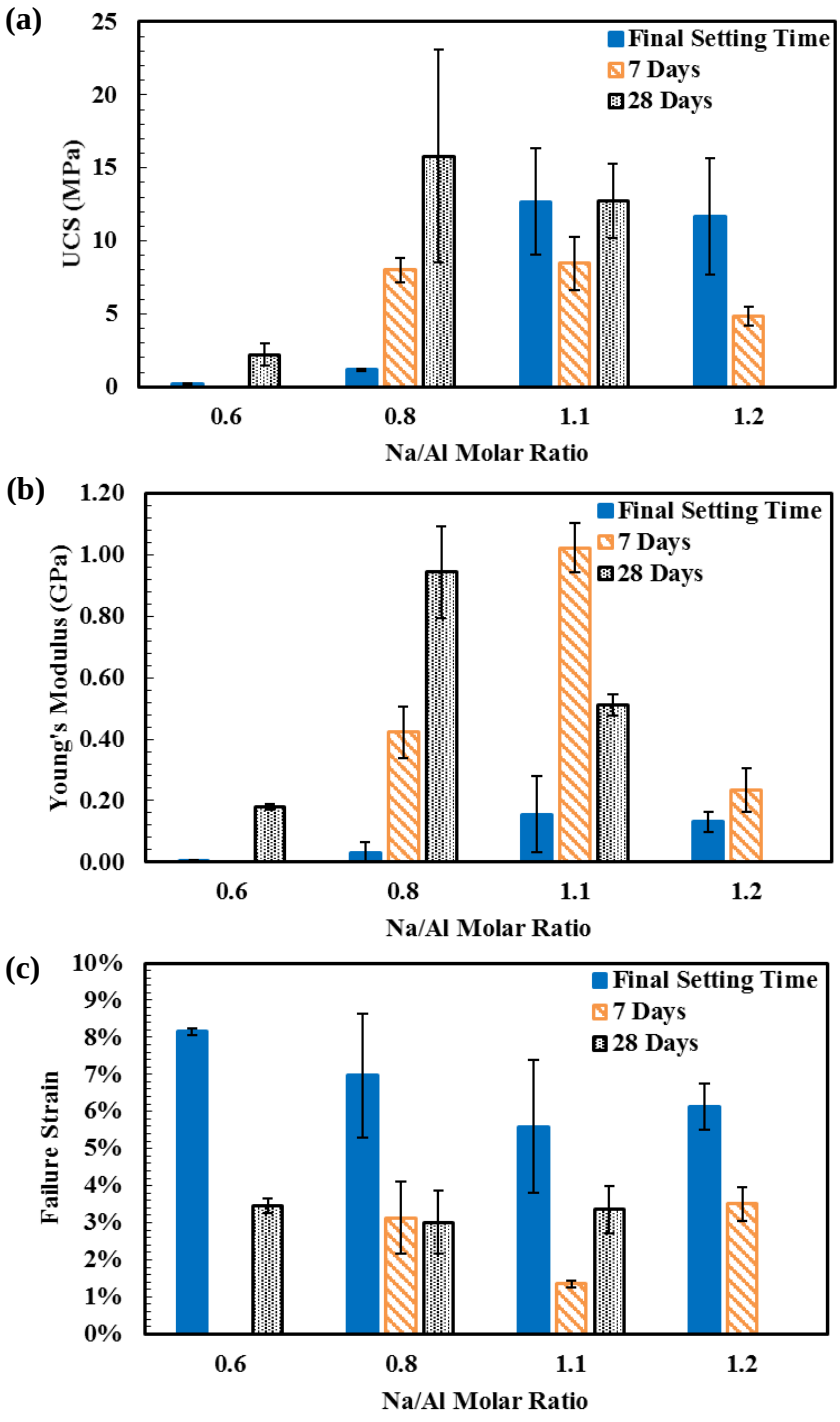

Figure 5-4. Effect of Na/Al molar ratio on (a) UCS, (b) Young's modulus and (c) failure strain of MKG samples cured for the final setting time, 7 days and 28 days, where the error bars are the standard deviations.

5.3.3. Mechanical Properties at Nano-Scale

Young's moduli (E_n) and hardness (H) at nano-scale were measured with the grid nanoindentation on the effective indentations (>270). The experimental PDF and the deconvolution results of SA18 (Si/Al = 1.8 and Na/Al = 1.0) cured for 7 days and SA16 (Si/Al = 1.6 and Na/Al = 1.0) cured for 28 days are shown in **Figure 5-5** as examples. For SA18, four phases are identified. Their Young's moduli are 5.5 ± 1.9 GPa (66.3%), 9.6 ± 0.4 GPa (9.9%), 12.7 ± 1.7 GPa (12.8%), and 21.5 ± 6.1 GPa (11.0%), respectively, with the volumetric proportion of each phase in the parentheses; and the hardness values are 0.3 ± 0.2 GPa (64.6%), 0.8 ± 0.2 GPa (6.9%), 3.2 ± 1.2 GPa (13.1%), and 4.5 ± 0.4 GPa (15.4%), respectively. For this sample, the volumetric fraction of each phase estimated based on Young's modulus and hardness agrees well. For SA16 sample set, as shown in **Figure 5-5** (c) and (d), four phases were derived based on E_n and three phases based on H. The four phases based on E_n PDF have Young's modulus values of 0.7 ± 0.5 GPa (20.6%), 2.6 ± 1.3 GPa (23.7%), 9.4 ± 3.0 GPa (30.6%) and 21.4 ± 13.4 GPa (25.1%); while the three phases based on H PDF have the hardness of 0.05 ± 0.02 GPa (38.4%), 0.14 ± 0.1 GPa (33.1%) and 2.0 ± 0.7 GPa (28.5%), respectively. It should be noted that the porous phase with E_n < 2 GPa and H < 0.1 GPa was identified in SA16, but not in SA18, which appeared in some other samples. However, the mechanical properties exhibited significant dependence on the samples: (i) the phases derived from the deconvolution analysis of the mechanical properties (E_n or H) are not always reliable, of which the number varies within 2~4 for different samples; (ii) the phases derived from E_n is not always the same as those from H; and (iii) different phases can be derived from different samples. Four phases were

categorized based on the statistical analysis of both E_n and H of all the measured samples and the consideration of the results in the previous studies [155, 156]:

(i) Porous phase: $E_n < 2$ GPa and $H < 0.1$ GPa;

(ii) Partly developed geopolymer gels: 2 GPa $\leq E_n < 5.5$ GPa and 0.1 GPa $\leq H < 0.35$GPa;

(iii) Geopolymer gels: 5.5 GPa $\leq E_n < 25$ GPa and 0.35 GPa $\leq H < 1.5$ GPa; and

(iv) Unreacted metakaolin or crystals: $E_n \geq 25$ GPa and $H \geq 1.5$ GPa.

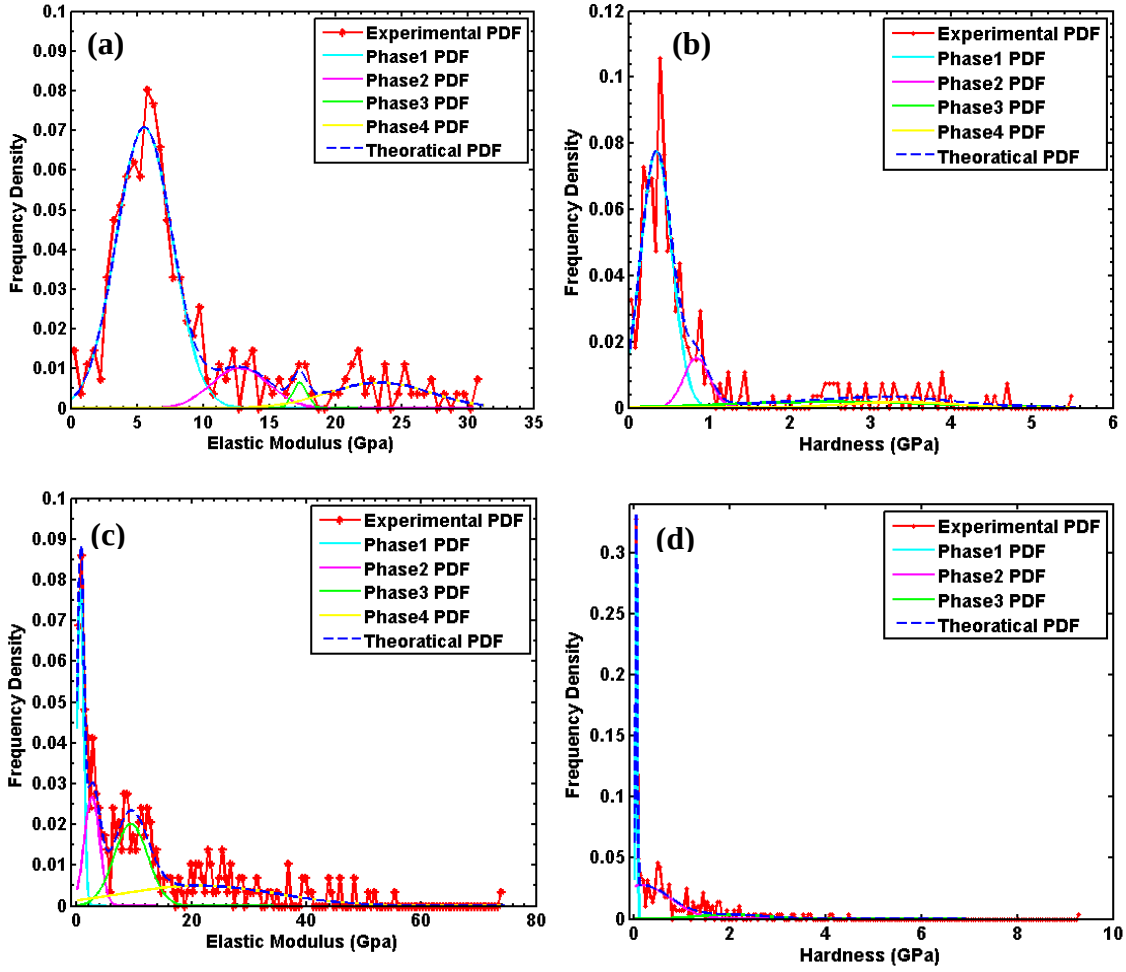

Figure 5-5. Deconvolution results of the PDF of (a) Young's moduli and (b) hardness for SA18 (Si/Al=1.8 and Na/Al=1.0) cured for 7 days, and the PDF of (c) Young's moduli and (d) hardness for SA16 (Si/Al=1.6 and Na/Al=1.0) cured for 28 days.

The volumetric distributions of these four phases for all the indented MKG samples are listed in **Table 5-3**. For SA20 and SA22 after the final setting, the samples were too soft to prepare a flat and smooth surface for indentation, so the indentation results for these two sets are unavailable. In each of the samples, geopolymer gels are identified and dominant in most of the samples that have a high compressive strength. The partly developed

geopolymer gels are the second major phase in the samples. Most of the samples have a low proportion of porous phase, except for SA12 cured for 7 days, NA06 cured for 28 days and NA08 cured for its final setting time, which all have a very low strength. The porous phase in these samples may contain cracks that formed during the curing. It should be noted that SA12 cracked after curing for 28 days, implying invisible cracks may have formed in the counterpart cured for 7 days. Furthermore, most of the indented samples after their final setting time have unreacted metakaolin at 5%~25%. After the curing of 7 days, the proportion of the unreacted metakaolin always decreased. However, some of the sample sets (e.g., SA14, SA20 and NA08) cured for 28 days have a higher proportion of the fourth phase ($E_n \geqslant 25$ GPa and $H \geqslant 1.5$ GPa) than their counterparts cured for 7 days. For these samples, the fourth phase might contain crystals converted from the geopolymer gels during the curing, which also have a high stiffness and hardness. As summarized in **Table 5-3**, the proportion of geopolymer gels generally increased, while the proportion of the partly developed geopolymer gels decreased with the curing time.

Table 5-3. Volumetric distribution of different phases in indented MKG samples

Sample	Curing Time	Porous phases (%)	Partly developed geopolymer gel (%)	Geopolymer gel (%)	Unreacted metakaolin or crystals (%)
		E_n<2GPa H<0.1GPa	2GPa≤E_n<6GPa 0.1GPa≤H<0.35GPa	6GPa≤E_n<25GPa 0.35GPa≤H<1.5GPa	E_n≥25GPa H≥1.5GPa
SA12	7 days	28.4	56.3	15.4	0.0
SA14	1.5 hrs	0.0	80.0	14.5	5.5
	7 days	0.0	87.9	12.1	0.0
	28 days	0.0	66.4	27.5	5.0
SA16	2.7 hrs	0.0	58.9	16.5	24.5
	7 days	6.2	38.4	46.6	8.9
	28 days	20.6	23.7	55.7	0.0
SA17	6.7 hrs	0.0	0.0	77.1	22.9
	7 days	0.0	9.7	87.0	3.3
	28 days	0.0	4.4	95.6	0.0
SA18	10 hrs	5.1	81.8	3.7	9.5
	7 days	0.0	66.3	33.7	0.0
	28 days	0.0	9.4	89.0	1.7
SA20	7 days	0.0	71.2	22.3	6.5
	28 days	5.6	0.0	87.1	7.3
SA22	28 days	0.0	0.0	8.8	91.2
NA06	28 days	33.8	39.4	16.2	10.6
NA08	18.3 hrs	65.5	0.0	21.4	13.1
	7 days	0.0	0.0	96.3	3.7
	28 days	7.6	0.0	72.5	19.9
NA11	6.7 hrs	0.0	0.0	77.1	22.9
	7 days	0.0	9.7	87.0	0.0
	28 days	0.0	4.4	95.6	0.0
NA12	1.3 hrs	0.0	0.0	76.6	23.4
	7 days	0.0	0.0	94.2	5.8

5.3.4. FTIR Characterization of Metakaolin based Geopolymers

The FTIR spectra of metakaolin and the MKG samples after the final setting are compared in **Figure 5-6** to illustrate the effect of Si/Al and Na/Al ratios on the chemical bonding of geopolymers. In metakaolin, two bands at 1076.3 cm^{-1} and 794.6 cm^{-1} are assigned to asymmetric stretching band of Si-O-T (T: Si or T) and 4-coordinated Al-O band, respectively. After geopolymers set, the Si-O-T band was observed to shift from 1076.3 cm^{-1} in metakaolin to 962.5~1003.0 cm^{-1}, indicating the formation of geopolymer gels [118, 127]. Four-coordinated Al-O, which is a characteristic bond in metakaolin, can only be found in SA12 and NA06 sample sets that were too weak to be tested for mechanical properties after the final setting, implying a low degree of reaction in these two samples. In SA12, SA18, SA20, SA22, NA06 and NA08 sample sets, the bands around 1440 cm^{-1}, 1410 cm^{-1}, 866 cm^{-1} are observed, which were generated by carbonates, O-H bonds and Si-OH bonds, respectively. The carbonates were formed by the reaction between CO_2 in the air and the Na^+ that did not participate in the geopolymer gel networks. The band of O-H is always observed to be associated with CO_3^{2-}, implying that the Na^+ was diffused to the samples' surfaces and reacted with CO_2 [235]. The appearance of the Si-OH band is the evidence of small aluminosilicate oligomers, such as monomers and dimers, in the geopolymers [235]. The carbonates and Si-OH bonds suggest a low degree of reaction of these samples at this early stage and thus a low mechanical strength of the resulting geopolymers [126, 132]. Consistently, SA12, SA18, SA20, SA22, NA06 and NA08 after the final setting all have a very low UCS value, as shown previously in **Figure 5-3** and **Figure 5-4**, and a low content of geopolymer gels, as provided in **Table 5-3** (3.7%~21.4%). Another FTIR band around 680 cm^{-1} corresponding to the AlO_2 group in geopolymer gels

is found in SA14, SA16, SA17 (NA11) and NA12, which have a high mechanical strength (**Figure 5-3** and **Figure 5-4**) and a high proportion of geopolymer gels in the range of 76.6% ~ 86.6% (**Table 5-3**). Although SA14 only has 14.5% of geopolymer gels, but its proportion of partly developed geopolymer gels is as high as 80.0%, which can be one reason for its high UCS.

For the MKG samples cured for 7 days and 28 days, the bands of CO_3^{2-}, O-H and Si-OH disappeared while the band of AlO_2 group was observed. This observation suggests the further development of geopolymer gels along the curing time in all these samples, in good agreement with the change in the proportion of geopolymer gels presented in **Table 5-3**. However, the development of geopolymer gels is dependent on the chemical composition of the sample sets, illustrated by the change of the FTIR bands. The FTIR spectra of SA12 and NA06 barely changed after the curing of 7 days or 28 days, indicating that it is hard to form geopolymer gels at these chemical compositions (Si/Al=1.2, Na/Al=1.0 for a very low Si concentration; and Si/Al=1.7, Na/Al=0.6 for a very low Na concentration). The Si-O-T band, also known as the main band of geopolymer gels, did not show apparent change during the later curing period (e.g., from 7 days to 28 days) in SA14, SA16, SA17 (NA11) and NA12 sample sets, illustrating the limited further development of geopolymer gels, which is consistent with the results of mechanical property measurements (**Figure 5-3** and **Figure 5-4**) and nanoindentation results (**Table 5-3**). On the other hand, the intensity of the Si-O-T band in SA18, SA20, SA22 and NA08 sample sets became more intense after the curing of 7 days and 28 days, showing the increasing content of geopolymer gels in these sample sets, which agrees well with the increasing

volumetric proportion of geopolymer gels (**Table 5-3**) and macro-mechanical strength (**Figure 5-3** and **Figure 5-4**) of these samples.

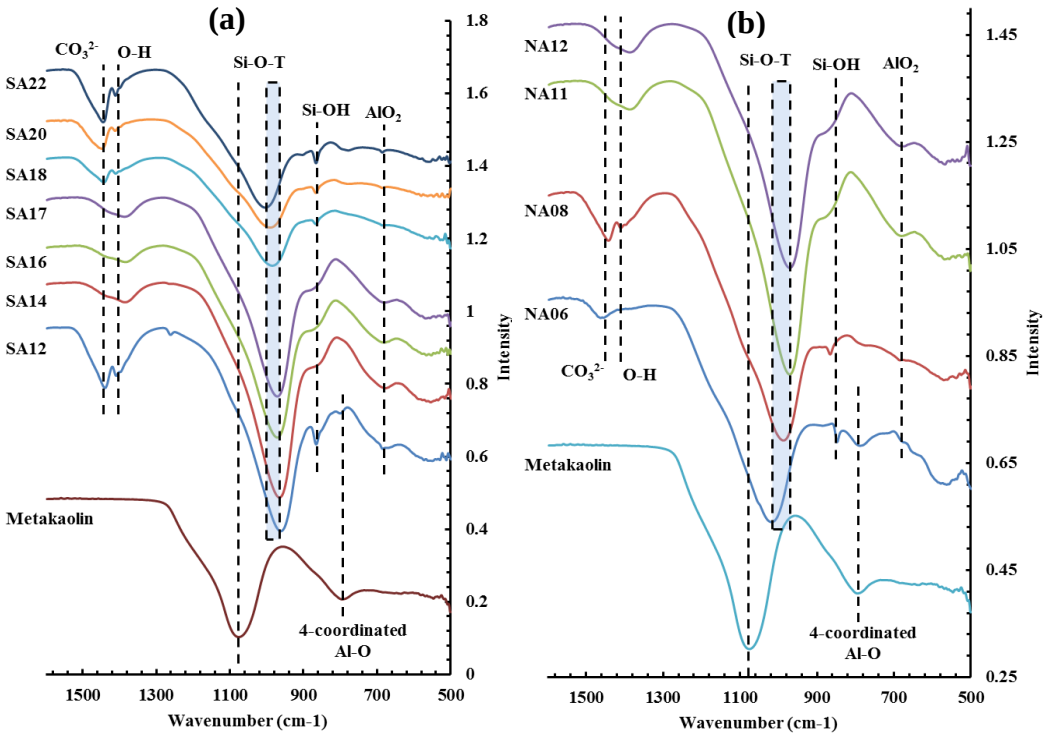

Figure 5-6. FTIR spectra of metakaolin and MKG samples synthesized with different (a) Si/Al molar ratios and (b) Na/Al molar ratios after the final setting.

5.3.5. Effect of Si/Al and Na/Al Ratios on Reaction Rate and Microstructure of Geopolymers

The wavenumber of the main band Si-O-T and the volumetric proportion of geopolymer gels in the samples cured for the final setting time, 7 days and 28 days are plotted as a function of Si/Al ratio and Na/Al ratio in **Figure 5-7** and **Figure 5-8**, respectively. The final setting time is also included in these figures to provide a reference for their early stage

reaction. As depicted in **Figure 5-7** (a) and **Figure 5-8** (a), the wavenumber of the Si-O-T FTIR band and the final setting time both increase with the increasing Si/Al molar ratio, and decrease with the increasing Na/Al molar ratio. Si-O-Si bonds have a lower bond angle and bond length, thus a higher molecular vibrational force constant, than Si-O-Al bonds [106], so the increase in the wavenumber of Si-O-T band indicates the formation of a higher content of Si-O-Si bonds. The trend of the final setting time and the Si-O-T with the Si/Al ratio is in good agreement with the previous findings by Cheng and Chiu, Silva et al. and Gao et al. [133, 172, 183]. Silva et al. found that a higher Al concentration (a lower Si/Al ratio) or a higher release rate of Al in geopolymer precursors initiated and accelerated the polymerization by forming more Si-O-Al bonds, which are more readily to form than Si-O-Si bonds [172], leading to a higher reaction rate and shorter setting time. On the other hand, a higher Na^+ concentration is coupled with a higher OH^- content which can accelerate the dissolution of silicate and aluminate tetrahedrons and thus the rate of polymerization [133]. In addition, since aluminate tetrahedrons in metakaolin are more readily to dissolve [95] than silicate tetrahedrons, the Si-O-Al bonds increased faster with a higher dissolution rate when the Na/Al ratio is higher. Note that SA12 samples set slower (5 hours and 10 mins) than SA14 (1 hour and 30 mins) and SA16 (2 hours and 40 mins). Furthermore, SA12 samples after the final setting time were so crumbled that can be broken with hands; 7 days cured SA12 samples had a very low mechanical strength; and 28 days cured SA12 samples cracked. It illustrates that a Si/Al ratio of 1.2 is too low for the geopolymers to develop mechanical strength.

The effect of Si/Al ratio on the proportion of geopolymer gels is more complex than the reaction rate. Regardless of the curing time, the volumetric population of geopolymer

gels increases with Si/Al molar ratio when Si/Al ≤ 1.7, as depicted in **Figure 5-7** (b). For SA18, the proportion of geopolmer gels after the final setting time is very limited (3.72%), but gradually increases to 89.0% after the curing of 28 days. The mechanical strength and Young's modulus of SA18 largely increased from the final setting time to 7 days, but slightly decreased afterwards, which may be due to the structural defects developed at the later stage of the curing, such as drying cracks. The geopolymer gels of SA20 developed in a similar trend to SA18. As expected, SA22 has a very low population of geopolymer gels even after 28 days' curing because of its excessively high Si/Al molar ratio (> 2.0), which was considered detrimental for geopolymerization in a previous study [115].

The proportion of geopolymer gels increases monotonically with Na/Al ratio regardless of the curing time, as shown in **Figure 5-8** (b). This implies that a higher Na^+ concentration, coupled with a higher OH^- concentration, is favorable for both the dissolution and polymerization processes, thus the formation of geopolymer gels [103].

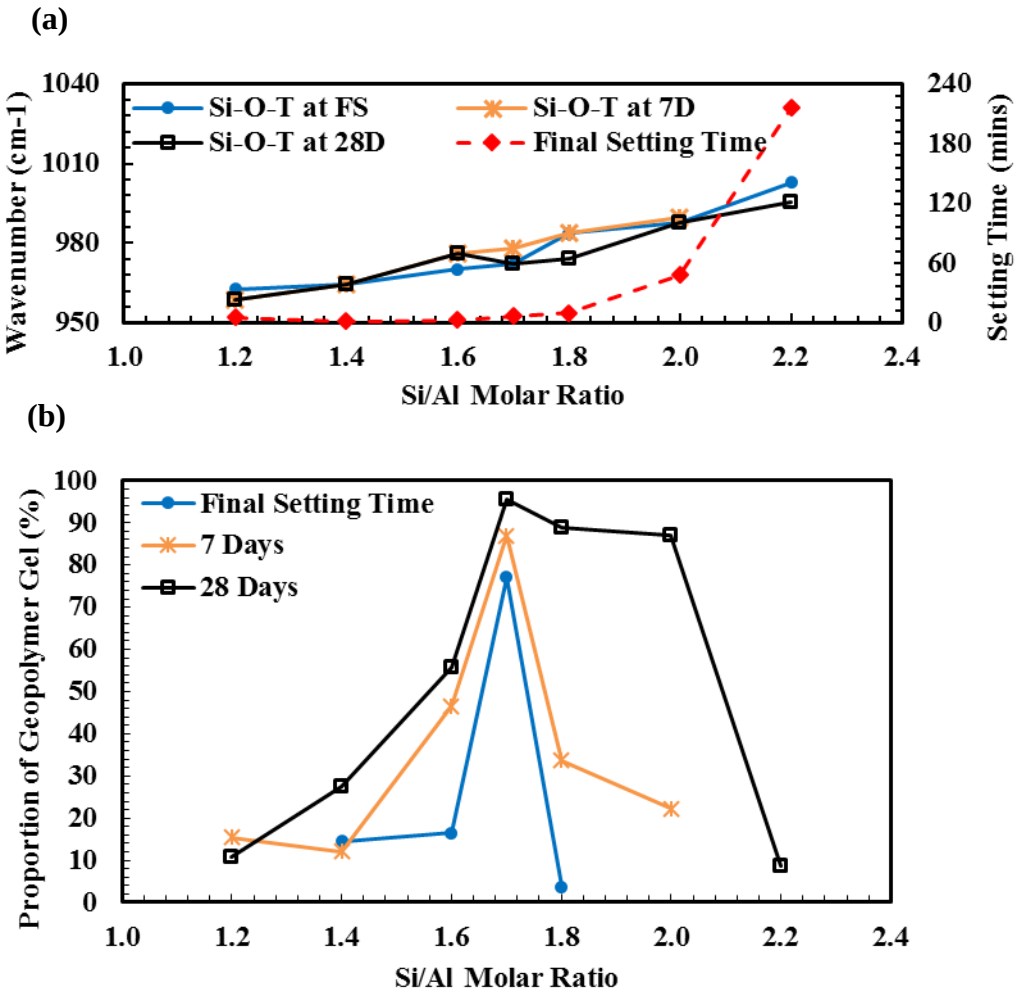

Figure 5-7. Effect of Si/Al molar ratio on (a) the development of Si-O-T band and the final setting time, and (b) volumetric proportion of geopolymer gels in the MKG samples cured for the final setting time, 7 days and 28 days.

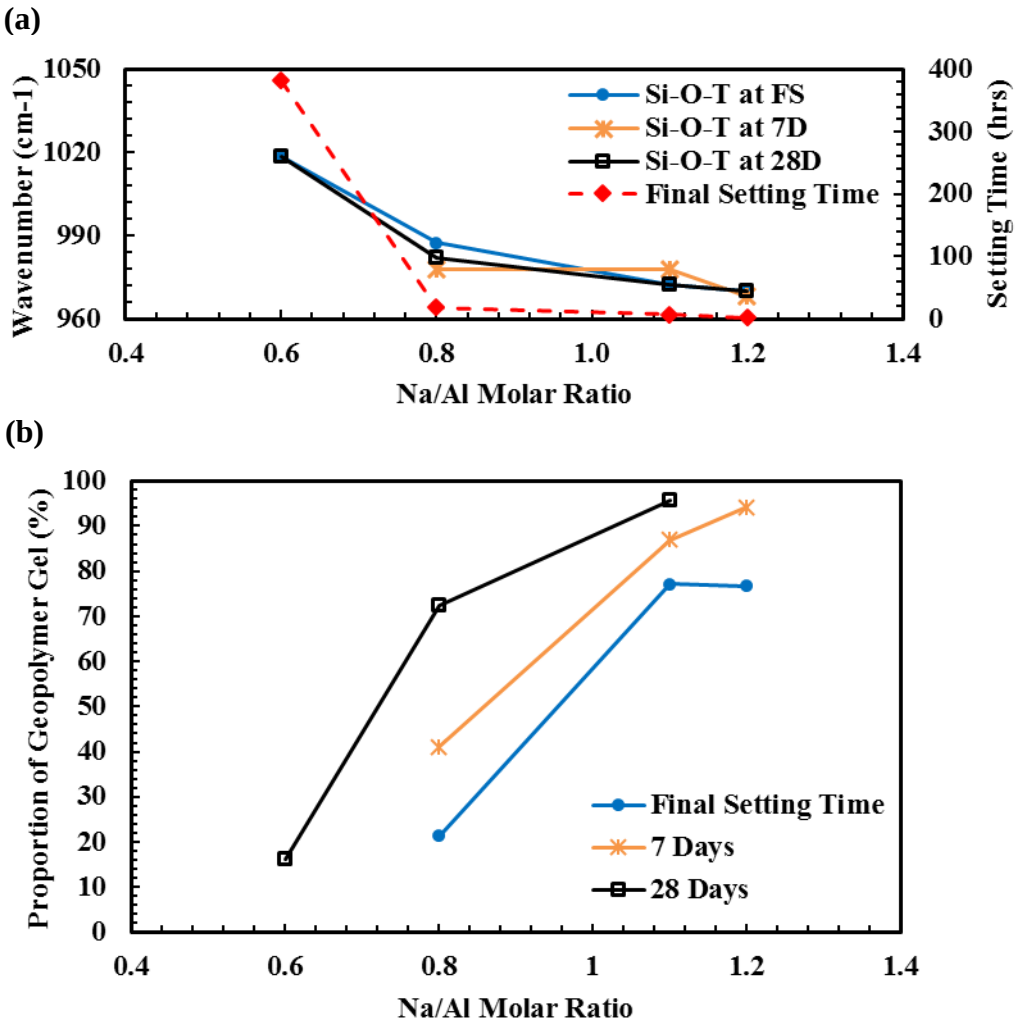

Figure 5-8. Effect of Na/Al molar ratio on (a) the development of Si-O-T band and the final setting time, and (b) volumetric proportion of geopolymer gels in the MKG cured for the final setting time, 7 days and 28 days.

5.3.6. The Effect of Si/Al and Na/Al Ratio on the UCS- and E_m-Proportion of Geopolymer Gel Correlations

The correlation between macro-mechanical strength (UCS), Young's modulus (E_m) and the proportion of geopolymer gels, as well as their dependence on Si/Al ratio and curing

time are demonstrated in **Figure 5-9**. For the samples after the final setting, UCS and E decrease with Si/Al ratio, whereas the proportion of geopolymer gels increases with Si/Al ratio, reaching a maximum value around Si/Al = 1.7, and decreases as Si/Al ratio further increases, as illustrated by the solid trend line of the scattered data. This discrepancy is caused by the results of SA14 which has a low proportion of geopolymer gels, but a very high proportion of partly developed geopolymer gels (see **Table 5-3**) which also contribute to the mechanical properties. This can be verified by the dash trend line of the proportion of geopolymer gels that excluded SA14, which has a consistent trend with the mechanical properties. For the samples cured for 28 days, the macro-mechanical properties (UCS and E_m) and the proportion of geopolymer gels consistently increase with Si/Al molar ratio up to 1.7, and then decrease afterwards for even higher Si/Al ratios. It can be found that (i) the mechanical strength is dominated by the proportion of geopolymer gels, and (ii) a relatively high Si/Al ratio (~1.7) is more favorable for the development of geopolymer gels, and thus the mechanical properties, in a long term; (iii) an excessively high Si/Al ratio is detrimental to the development of mechanical properties of the geopolymers.

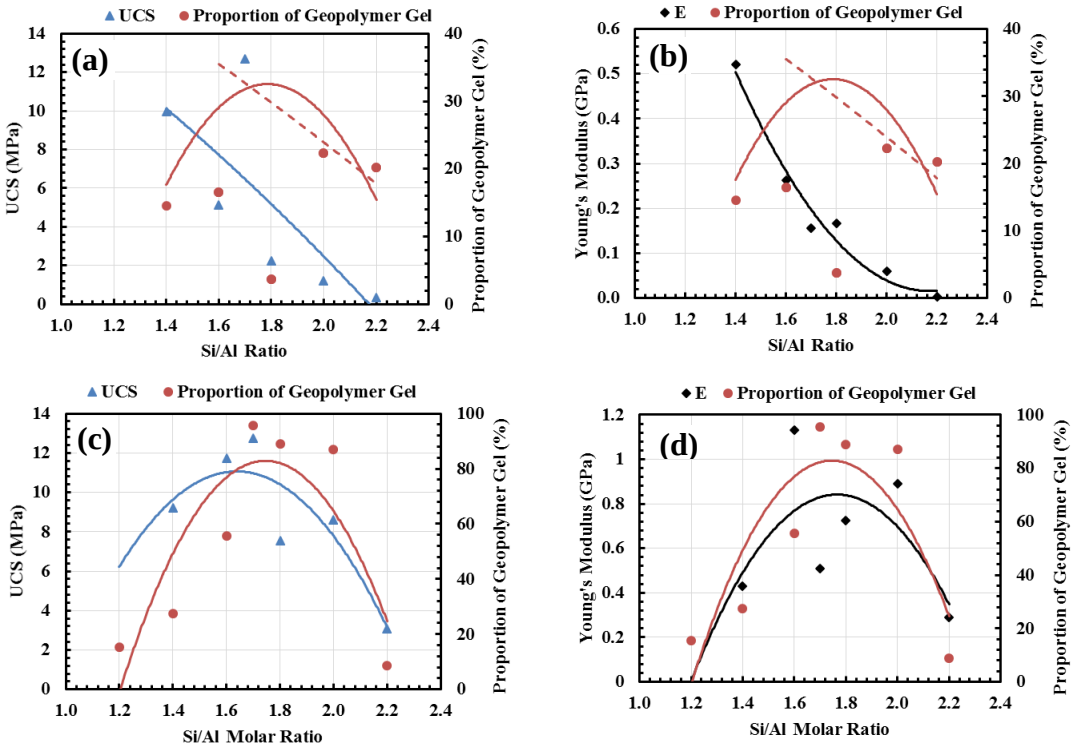

Figure 5-9. Effect of Si/Al molar ratio on the correlation of (a) UCS-proportion of geopolymer gels, (b) E_m-proportion of geopolymer gels after the final setting, and (c) UCS-proportion of geopolymer gels, (d) E_m-proportion of geopolymer gels of 28 days cured MKG.

On the other hand, the proportion of geopolymer gels increases with Na/Al ratio within a range of 0.8 to 1.2, and leveled off around Na/Al = 1.1 regardless of the curing time, as illustrated in **Figure 5-10**. A similar trend is observed for the UCS-geopolymer gels relationship to that of E_m-geopolymer gels regarding the influence of Na/Al ratio. This well illustrates UCS and E_m increase with the increasing proportion of geopolymer gels. The effect of Na/Al ratio on macro-mechanical properties and geopolymer gels might be attributed to two reasons: (i) a higher Na/Al ratio is beneficial for the development of geopolymer gels, but an excessively high alkali concentration leaves extra Na^+ and

weakens the polymerized geopolymeric structure after the polymerization [103], and thus the mechanical strength; and (ii) a higher Na/Al ratio is more favorable for the development of mechanical properties at the early stage, since it can lead to an accelerated dissolution of Si and Al tetrahedrons to form Al-rich gels.

The qualitative characterization of the chemical composition-proportion of geopolymer gels-macro mechanical properties reveals the primary development mechanism for strength and stiffness of MKG is the formation of geopolymer gels. The development of geopolymer gels, which significantly depends on the chemical composition, determines the mechanical performance of geopolymers at early and late stages. The mechanical strength of geopolymers is also affected by the partly developed geopolymer gels at early stage and pores and cracks. A good chemical composition for the high and fast-developed strength and stiffness is Si/Al ratio of 1.7 and Na/Al ratio of 0.9 in this study.

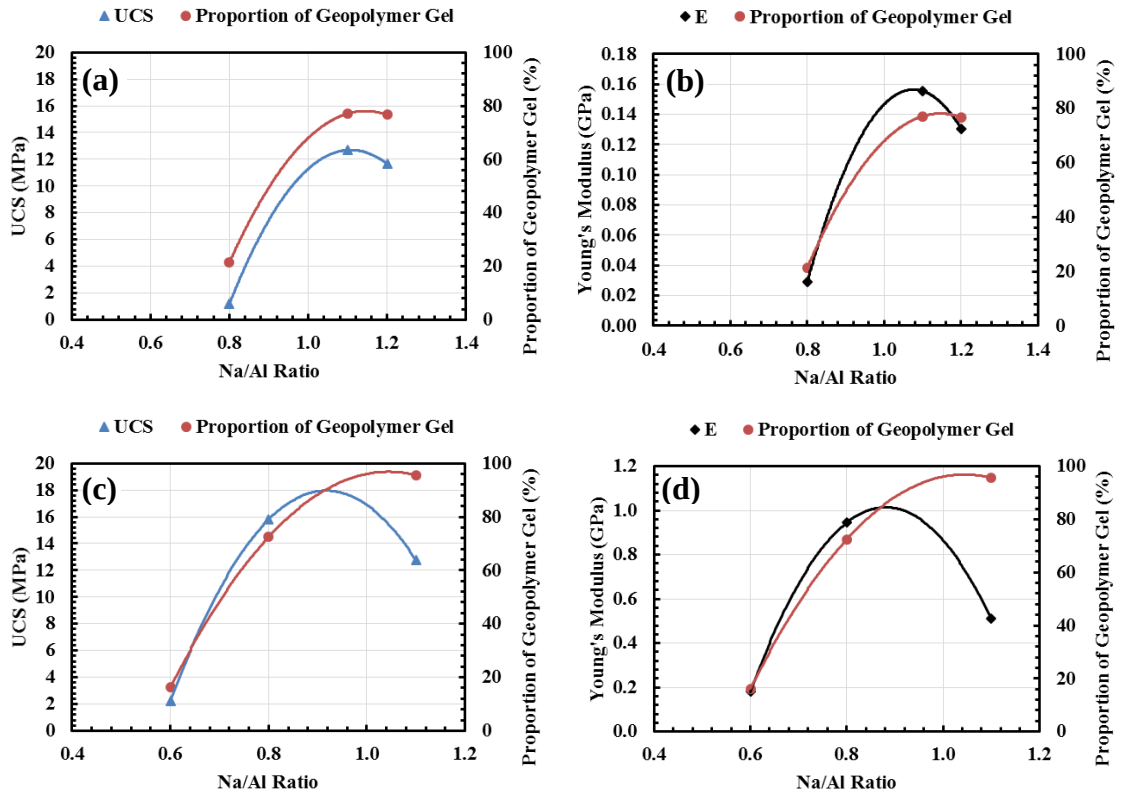

Figure 5-10. Effect of Na/Al molar ratio on the correlation of (a) UCS-proportion of geopolymer gels, (b) E_m- proportion of geopolymer gels of MKG after the final setting, and (c) UCS-proportion of geopolymer gels, (d) E_m- proportion of geopolymer gels of 28 day cured MKG.

5.4. CONCLUSIONS

Young's modulus (E_n) and hardness (H) of metakaolin-based geopolymers (MKG) at nano-scale were characterized with the grid nanoindentation. Four phases were identified from the deconvolution analysis of E_n and H, including porous phase, partly developed geopolymer gels, geopolymer gels and unreacted metakaolin or crystals. These phases were distributed in the resulting geopolymers at different proportions, depending on the chemical compositions of the raw materials. The nanoindentation results and the FTIR

spectra confirmed the formation of geopolymer gels in all the MKG samples, regardless of the chemical compositions.

Si/Al and Na/Al ratios play important roles in the reaction rate, formation of geopolymer gels and mechanical properties of geopolymers. The final setting time increased with Si/Al ratio due to the larger number of Si-O-Si bonds formed at a higher Si concentration, and decreased with Na/Al ratio, attributed to the faster dissolution and polymerization rate with a higher Na^+ concentration. These observations were verified by the fact that Si-O-T (T: Si or Al) FTIR band kept shifting to higher wavenumbers with the increase of Si/Al ratio and decrease of Na/Al ratio, while Si-O-Si bands appear at a higher wavenumber than Si-O-Al bands. With the increasing Si/Al ratio, the proportion of geopolymer gels, as well as the strength and stiffness of geopolymer at early stage (the final setting time) decreased, due to the prolonged polymerization of geopolymer gels. However, a high Si/Al ratio enhanced the formation of geopolymer gels and development of mechanical strength and stiffness of geopolymers for a longer curing time. On the other hand, a high Na/Al ratio is favorable for the formation of geopolymer gels, but an excessively high Na/Al ratio decreased the strength and stiffness of the MKG samples, especially at a later stage, such as 28 days. The optimum chemical composition for the MKG samples with good mechanical properties is Si/Al=1.7 and Na/Al=0.9.

It was observed that the macro-mechanical properties of the MKG samples largely depend on the proportion of geopolymer gels. The MKG samples with a higher strength and stiffness have a higher proportion of geopolymer gels. Furthermore, the mechanical properties are also affected by the partly developed geopolymer gels, which are not

necessarily formed at the early stage but can be converted to geopolymer gels to further improve the mechanical performance when the Si/Al ratio is properly high. The porous phase that may contain drying cracks formed during curing has a low stiffness and hardness and reduces the mechanical strength and stiffness of MKGs at macro-scale.

Based on the results of the current multi-scale study, the development of geopolymer gels and their implications to macro-scale mechanical properties can be better understood. More importantly, the relationship of chemical composition of raw materials-the formation of geopolymer gels-mechanical properties of geopolymers can provide guidance for optimizing geopolymer synthesis to obtain desired mechanical properties.

CHAPTER 6 - MOLECULAR SIMULATIONS OF THE POLYMERIZATION PROCESS FOR GEOPOLYMER SYNTHESIS

6.1. INTRODUCTION

Geopolymers, or alkali activated inorganic binders, are a family of aluminosilicate materials with amorphous to semi-crystalline microstructures, which are composed of silicate and aluminate tetrahedrons that are cross-linked by sharing oxygen atoms [13]. With high mechanical strength and CO_2 emission lower than up to 80% compared to ordinary Portland cement [8, 10], geopolymers have become a promising sustainable alternative to cement. Geopolymers, can also be used in fire/acid resistant coatings [20-22], sewer pipes [34], lightweight foam concrete [43, 44], toxic/radioactive contaminant encapsulation [30], military operations [35], railway sleepers [36], and aircraft manufacturing [37] because of their excellent mechanical, physicochemical and thermal properties. Geopolymers are usually synthesized by using alkaline hydroxide or/and silicate solutions to activate aluminate and silicate rich materials, including natural minerals and some industrial wastes such as metakaolin, fly ash and blast furnace slag [14, 30, 49, 56, 57, 60-62, 103, 235, 236, 239, 240]. However, the wide variability in raw materials and geopolymers' properties complicates the mix design and curing conditions for synthesizing geopolymers. Thus, the applications of geopolymers in practice are still limited.

The final product in the geopolymer synthesis is a composite material composed of unreacted raw materials, geopolymer gels and zeolitic phases [161, 278]. Among the above

constituents, geopolymer gels are the most important because they act as a binding agent and largely govern mechanical properties of the resulting geopolymers. A simplified chemical formula $M_n\{-(SiO_2)_z - AlO_2 -\}_n$ is used for approximately representing the molecular structures of geopolymers without knowing the molecular details. *M* is the cation to balance the negatively charged $Al(OH)_4{}^{-1}$, such as sodium (Na^+) or potassium (K^+). The subscript *z* defines the Si to Al molar ratio, which is a vital factor in determining mechanical properties of the resulting geopolymers. A variety of techniques have been employed to characterize geopolymer gels. Davidovits, Rattanasak and Chindaprasirt, Lyu et al. and Nasab et al. used X-ray diffractometer (XRD) to qualitatively characterize the formation of geopolymer gels that have a hump spanned over 20 °-32 ° 2θ [13, 110, 111]. Scanning electron microscopy (SEM) images and energy dispersive X-ray spectroscopy (EDX) spectra provide the morphologies of "geopolymer gel-like" phases and qualitative estimate of chemical composition of these phases [104]. However, neither of these techniques can quantitatively define the geopolymers' microstructures. Fourier transform infrared spectroscopy (FTIR) spectra have been used to identify the development of main chemical bonds, such as Si-O-T (T: Si or Al), Si-OH, and Al-OH, in geopolymer precursors, but the network and interconnectivity of these bonds are still a "puzzle" [127, 165]. Nuclear magnetic resonance (NMR) spectra can be used to assess the coordination of Si and Al sites and investigate the change in chemical structures during geopolymerization, but some of the sites are difficult to distinguish [141, 142, 170]. X-ray/neutron pair distribution function (PDF) analysis has recently been used as a complementary tool to FTIR and NMR for examining the microstructure of geopolymers [163, 164], but the molecular structures

of geopolymers are still unclear. Despite all these efforts, a conclusive molecular structure of geopolymer gels remain undefined largely due to their amorphous nature.

To tailor geopolymer synthesis for desired properties, the relationship between the synthesis reactions and microstructure/mechanical properties is of particular interest. Unfortunately, key aspects of the relationship between the molecular structure of geopolymer gels and the complex multi-step geopolymerization process remain largely unknown. The geopolymerization process is often approximated by the following reactions [13]: (i) the raw materials are dissolved in alkali solutions, such as NaOH and KOH, to release the reactive aluminate and silicate monomers; and (ii) the aluminosilicate oligomers polymerize in the alkali environment to form geopolymer gels, whose negative charge is balanced by Na^+ or K^+. Water is consumed in the first step and released in the second step. Zhang et al. estimated the geopolymerization rate and degree using the spectrometric analysis of in-situ energy dispersive X-Ray diffractometry and isothermal conduction calorimetry (ICC) data [123, 162]. However, their calculations were based on the models with the thermodynamic parameters of zeolite analcime, not geopolymer gels, because these critical parameters of geoplymeric structures remain unavailable [123, 162].

The amorphous nature of geopolymer gels also presents technical challenges to molecular simulations, although molecular modeling in recent literature studies has provided a new perspective to understand the geopolymeric microstructure and geopolymerization kinetics [284]. Zhang et al. used semi-empirical AM1 method to study the dissolution, ion reorientation, and polycondensation processes of metakaolin based geopolymers in a series of simulations [191-193]. Yang et al. used density functional theory

(DFT) method to assess the stability and structure of various aluminosilicate oligomers that are the basic units for geopolymerization. Subsequently, their group simulated the polymerization between a small oligomer (e.g., silicate monomer, aluminate monomer or aluminosilicate dimer) and an aluminosilicate cluster (e.g., four, six, double four or double six rings) to test the fundamental reaction mechanisms for geopolymerization [194, 195]. These simulation studies have shed light on the initial proportion of the pathways of how geopolymer structures were formed from raw materials, but were not able to obtain the final molecular structure of geopolymer gels. This is because the DFT modeling is limited to relatively small systems (e.g., those with hundreds of atoms), by which prohibitive simulation time will be required for modeling the molecular structure of geopolymer gels that contain a much larger number of atoms. White et al. applied their DFT simulation results in a multiscale model using DFT/Coarse Grain Monte Carlo (CGMC) simulations of alkali activation of metakaolin in three solutions with different silicate concentrations [196, 197]. Their large scale CGMC model was able to simulate the processes from the dissolution to the initial polymerization of a Na-metakaolin based geopolymer precursor system. Most of the aforementioned simulations focused on the early stage of the entire geopolymerization process, whereas geopolymer gels with molecular structures close to those synthesized in the laboratory cannot be generated [198].

Molecular dynamics (MD) modeling with a reactive potential by Feuston and Garofalini (FG) potential [285] was conducted to simulate the polymerization and condensation processes of silicate and aluminate monomers. Previously, the FG potential was used to simulate the polymerization of silicic acid and the effect of simulation temperature and system concentration on the degree of polymerization [286, 287]. Similar

to the polymerization of silicic acid, the dimerization of silicate monomers and aluminate monomers is the essential reaction for the polymerization process in geopolymer synthesis [196]. Therefore, the FG potential was selected in the current work to investigate: (i) the molecular structural change of the aluminosilicate system during the polymerization; (ii) the molecular structure of geopolymer gels; and (iii) the effect of chemical composition and simulation temperature on reaction kinetics and the resulting molecular structures of geopolymer gels.

This chapter is organized as follows: the molecular model and simulation details are introduced in section 2, including the potentials and theory used in this study; the polymerization results are discussed and compared with literature and experimental results in section 3; and section 4 presents the conclusions drawn from this study and suggestions for the future work.

6.2. METHODOLOGY

The molecular dynamics (MD) modeling was carried out to simulate the polymerization process from the aluminate and silicate monomers to the resulting geopolymer gels. The dissolution of raw materials was omitted because it is practically impossible to simulate the entire geopolymerization process with reactive MD modeling. Instead, silicate and aluminate monomers were optimized with DFT method first to represent the released reactive components from the dissolution stage. This approximation was made based on the rational that these monomers are energetically favorable to exist in geopolymer precursor after the dissolution process. Subsequently, the optimized silicate and aluminate monomers were used to simulate polymerization process using reactive MD modeling with

the FG potential. The simulation temperatures from 650K to 1800K were applied on simulation models with a Si/Al ratio of 2 and 3 to investigate the effect of temperature and chemical composition on the polymerization kinetics and molecular structures of computationally predicted geopolymer gels.

6.2.1. Optimization of Silicate and Aluminate Monomers by DFT Modeling

The building blocks used in the reactive MD simulations, silicate monomers and aluminate monomers with sodium as the charge balancing cation, are readily available in the literature. Initial geometries of these molecules were created based on the structural parameters obtained in a previous study [194] and then optimized with DFT simulations. DFT calculations were carried out using the Gaussian and plane wave basis sets approach with Perdew–Burke–Ernzerhof (PBE) exchange-correlation functional, a generalized gradient approximation (GGA) functional, implemented in the CP2K package [288, 289]. Double zeta Gaussian basis sets and Goedecker-Tetter-Hutter pseudopotentials were used during DFT optimization calculations [288, 289].

6.2.2. Molecular Dynamics Simulations

6.2.2.1. Potentials

The reactive Feuston Garofalini (FG) interatomic potentials for Si, O, H, Na, and Al were used, which were implemented in the molecular simulation software Tremolo-X [290] and had been successfully applied in the MD simulations of silicic acid oligomerization [286, 287, 291-293]. The FG potential is composed of two-body and three-body potentials as follows [294].

$$V(\{\boldsymbol{R}_i\}) = \sum_{i,j} V_2(\boldsymbol{r}_i, \boldsymbol{r}_j) + \sum_{i,j,k} V_3(\boldsymbol{r}_i, \boldsymbol{r}_j, \boldsymbol{r}_k) \quad (6.1)$$

$V(\{\boldsymbol{R}_i\})$ is the total potential, where $\{\boldsymbol{R}_i\} = (\boldsymbol{r}_1, \boldsymbol{r}_2, \cdots, \boldsymbol{r}_N)$ are the coordinates for an N-atom system. The modified Born-Mayer-Huggins (BMH) potential and Rahman-Stillinger-Lemberg (RSL2) potential are used to represent the interactions between two atoms (e.g., atom *i* and *j*, atom *j* and *k*, or atom *i* and *k*):

$$V_2(\boldsymbol{r}_i, \boldsymbol{r}_j) = V^{BMH}(r_{ij}) + \sum_k V_k^{RSL2}(r_{ij}) \tag{6.2}$$

The BMH potential is expanded with a short-range repulsion term (the first term in the right side of eq. (6.3)) and a screened Coulomb term (the second term in the right side of eq. (6.3)).

$$V^{BMH}(r_{ij}) = A_{ij} \exp\left(-\frac{\boldsymbol{r}_{ij}}{\rho_{ij}}\right) + \frac{e^2}{4\pi\epsilon_0}\frac{q_i q_j}{\boldsymbol{r}_{ij}} erfc\left(\frac{\boldsymbol{r}_{ij}}{\beta_{ij}}\right) \tag{6.3}$$

In this equation, $r_{ij} = |\boldsymbol{r}_i - \boldsymbol{r}_j|$ which is the distance between atom *i* and *j*; $\boldsymbol{r}_i$and $\boldsymbol{r}_j$ are the coordinates of atom *i* and *j*, respectively; q_i is the electronic charge of atom i; ρ_{ij}, ϵ_0 , A_{ij}, and β_{ij} are all fitting parameters; and $erfc$ is the error function.

The Rahman-Stillinger-Lemberg (RSL2) potential was used to describe the interactions between hydrogen and the other atoms (e.g., O, Si, Al and Na) in the modeling system, as represented by the second term in the right side of eq. (6.2). During the dimerization of aluminate and silicate monomers and the oligomerization of clusters, all the oxygen atoms are treated as interchangeable to dissociate and form water, where RSL2 potential is used here for this purpose and provided below.

$$V^{RSL2}(r_{ij}) = \frac{a_{ij}}{1+\exp(b_{ij}(r_{ij}-c_{ij}))} \tag{6.4}$$

a_{ij}, b_{ij} and c_{ij} are the parameters used in Feuston and Garofalini's paper [294].

The three body term in the right side of Eq. (6.1) was developed by Stilling and Weber for their effective silicon potential [295], as shown in the following formulae:

$$V_3(\boldsymbol{r}_i, \boldsymbol{r}_j, \boldsymbol{r}_k) = v_3(\boldsymbol{r}_{ij}, \boldsymbol{r}_{ik}, \theta_{jik}) + v_3(\boldsymbol{r}_{jk}, \boldsymbol{r}_{ji}, \theta_{kji}) + v_3(\boldsymbol{r}_{ki}, \boldsymbol{r}_{kj}, \theta_{ikj}) \quad (6.5)$$

$$v_3(\boldsymbol{r}_{ij}, \boldsymbol{r}_{ik}, \theta_{jik}) =$$

$$\begin{cases} \lambda_{ijkl} \cdot \exp\left(\frac{\gamma_{ij}}{r_{ij}-r_{ij}^0} + \frac{\gamma_{ik}}{r_{ik}-r_{ik}^0}\right) \times \left(\cos(\theta_{jik}) - \cos(\theta_{jik}^0)\right)^2, & r_{ij} < r_{ij}^0 \; and \; r_{ik} < r_{ik}^0 \\ 0, & r_{ij} \geq r_{ij}^0 \; and \; r_{ik} \geq r_{ik}^0 \end{cases} \quad (6.6)$$

λ_{ijkl}, γ_{ij} (γ_{ik} and γ_{jk}), r_{ij}^0 (r_{ik}^0 and r_{jk}^0) and θ_{jik}^0 are constants, and θ_{jik} is the angle subtended by $\boldsymbol{r}_{ij}$ and $\boldsymbol{r}_{ik}$ with the vertex of atom i.

All the values of the constants in the above equations and more details about the FG potential are available in the articles by Feuston and Garofalini [285, 294].

6.2.2.2. MD Simulation Models

The applicability of the reactive FG potential on aluminosilicate molecular systems was first verified with the simulations of a silicic acid by Garofalini and Martins [286] and an aluminosilicate system with 180 silicate monomers and 36 aluminate monomers at a Si/Al ratio of 5. The molecules in the aluminosilicate system were uniformly distributed in a 30Å×30Å×30Å box with periodic boundaries, giving an initial density of 1.33 g/cm^3. Although the Si/Al ratio of 5 is higher compared to the values used in most geopolymer syntheses, these simulations verified the computational reactivity of aluminate and silicate monomers with the FG potential.

The models for geopolymerization simulations are summarized in **Table 6-1** with the temperature schemes applied during the respective simulations. These models were created with Si/Al ratios of 2 and 3 to investigate the influence of Si/Al ratio on the reaction kinetics. The density for the simulation models was 1.32 g/cm^3. A molecular and domain optimization of the molecules at 0K was carried out first with the modified conjugated gradient (CG) method by Polak-Ribi ére [296]. The optimization was converged once the difference of the mean force between consecutive steps on an atom fell below a fixed threshold, 1.0E-4 eVolt in this case. The model system was then heated up to 300K to randomize the molecules for 1 ps, and then further heated up to "highest temperature" (e.g., 650K, 1000K, 1200K, 1500K and 1800K for scheme a, b, c, d and e, respectively, as shown in the inset in **Table 6-1**) for polymerization. The Si and Al sites, in terms of Si_n and Al_n, were evaluated to examine the degree of oligomerization. The Si_n and Al_n terms are derived from the Q_n term, which are tetrahedral silicate and aluminate connected to n bridging oxygen atoms (n=0, 1, 2, 3 and 4) and (4-n) non-bridging oxygen atoms, respectively, as described by Engelhardt et al. [139]. For example, Si_1 is a Si atom coordinated to four O atoms, one of which is bridging, meaning that the O atom is bonded to two atoms (i.e., T-O-T, where T = Si or Al). Once the Q_n reached a constant number within a reasonable timeframe, the system was gradually cooled down to 300K. The "cooling down" procedures are different depending on the specific temperature schemes (see **Table 6-1**). The temperature was ramped up or reduced at the rate of 0.5 K/step with a time step of 0.1 fs. The NVT ensemble was used with a Verlet propagator and Berendsen thermostat. In physical experiments at room temperature (around 300K), the entire synthesis process, from the mixing of raw materials to the final hardening of geopolymers, usually takes

several hours to several days or weeks, depending on synthesis conditions, whereas the timescale in molecular modeling is on the order of hundreds of picoseconds. Therefore, as a commonly used practice, using higher temperatures in MD simulations is necessary for increasing the reaction rate. In the previous molecular modeling on the polymerization of silicic acid, a high temperature of 2500K was used to increase the polymerization rate [286, 287]. In the current study, the temperatures of 650K ~ 1800K were used to increase the reaction rate and simulate the experimental effect of 'curing temperatures' on the polymerization of geopolymers. After the simulations reached equilibrium, the models were "cooled down" to 300K as the inset temperature schemes shown in **Table 6-1**. The simulation at each respective temperature during the "cool down" process (e.g., 1500K, 1200K, 1000K, 650K and 300K for the simulations at 1800K, including M2e and M3e) lasted for 10 ps to ensure the resulting molecules did not have further changes, such as polymerization or depolymerization. The other simulation parameters of the models are also provided in **Table 6-1**.

Table 6-1. Detailed information of the MD simulation models M2(or 3)a, b, c, d and e which has a Si/Al ratio of 2 (or 3) and were simulated at 650K, 1000K, 1200K, 1500K and 1800K, respectively.

Model	Si/Al Ratio	Building Blocks: Number of the Monomers	Cube Length (Å)	Density (g/cm3)
M2a,b,c,d,e	2	$Si(OH)_4$:144 $NaAl(OH)_4$: 72	30.5	1.32
M3a,b,c,d,e	3	$Si(OH)_4$:150 $NaAl(OH)_4$: 50	29.5	1.32
Temperature Scheme				

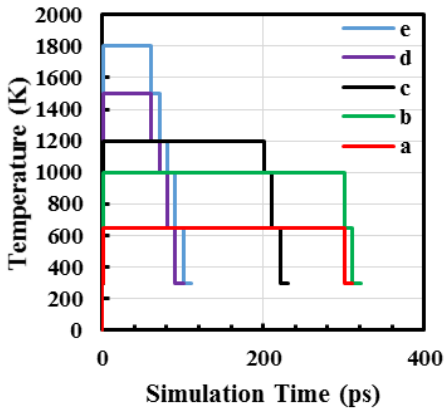

The development of Q_n (Si_n and Al_n) sites, which are indicators of the degree of polymerization for simulated aluminosilicate systems, was monitored during the simulation. Among the five types of four-coordinated Si (Si_0, Si_1, Si_2, Si_3 and Si_4), Si_4(mAl) (m is the number of Al linked to Si_4 through a bridging O atom) can be quantified with NMR spectra [130, 141, 169]. Thus, the development of Si_4(mAl) was also monitored during the simulation and compared to the experimental data reported in the literature. The T-O-T (T being Si or Al) bonds were also counted to elucidate the polymerization degree of the models. The development of Al-O-Al bonds was tracked to assess if the Lowenstein

aluminum avoidance principle holds [297], which states that only one tetrahedral site bridged by the sharing oxygen can be occupied by Al, and Al-O-Al bonds should not exist theoretically. The distribution of Si and Al sites, Si_4(mAl) and T-O-T bonds was determined by Python codes written by the authors. The degree of condensation, c, of each simulation model was calculated using $c = \left(\frac{1}{f}\right)\left(\frac{1}{X}\sum_{m=0}^{f} mq_m + \frac{X-1}{X}\sum_{n=0}^{f} nq_n\right)$, which is modified from the degree of condensation for silicic acid models [298], where f is the coordination number for Si network and Al network, with a value of 4 in this case as both Si and Al are 4-coordinated; m and n are the numbers of bridging oxygen connected to an Al center and a Si center respectively, which ranges between 0~4; X is the Si/Al molar ratio; and q_m and q_n are the fraction of Al_m and Si_n, respectively. The visual configurations and the radial distribution functions of the MD models at representative simulation time steps were obtained with the visualization software VMD [299], and compared to experimental data from X-ray/neutron PDF tests reported in the literature. After the simulation, water molecules were excluded from all the models, and then the models were optimized at 0K. The bulk density of these optimized aluminosilicate molecules was estimated to approximately predict the apparent density of geopolymer gels which include pores and cavities left by the condensation and water extraction.

6.3. RESULTS AND DISCUSSION

6.3.1. Verification of our Approach

The polymerization of the aluminosilicate model is demonstrated by the development of Q_n sites in **Figure 6-1**. There was no polymerization of the aluminosilicate system in the first picosecond at 300K, so only the results at 650K are plotted against the simulation time.

Both Si and Al sites are considered, designated by Si_n and Al_n respectively. As shown in **Figure 6-1** (a), the development trend of Si_n is similar to that of the silicic acid system [294]. Si_0 started to decrease from the very beginning of the simulation, and the other Si_n sequentially increased in the order of Si_1, Si_2, Si_3, and Si_4. The Al sites developed in a similar way, although with more fluctuation, as plotted in **Figure 6-1** (b). The change in the Q_n values for both Si and Al illustrates the polymerization of the silicate and aluminate monomers, which verified the feasibility of FG potential for the simulation of geoplymerization. In the simulation of silicic acid by Garofalini and Martin [286], the final Q_n (Q = Si in their simulations) distribution is 16%, 8%, 20%, 32% and 24% for Q_0, Q_1, Q_2, Q_3 and Q_4, respectively. Herein, the final distribution is 1%, 5%, 34%, 29% and 34% for Si_0, Si_1, Si_2, Si_3 and Si_4, and 0, 2%, 30%, 28% and 12% for Al_0, Al_1, Al_2, Al_3 and Al_4, respectively. Similarly, the Q_2, Q_3 and Q_4 are the dominant sites in the final systems, regardless of the model or the type of the coordination center (Si or Al).

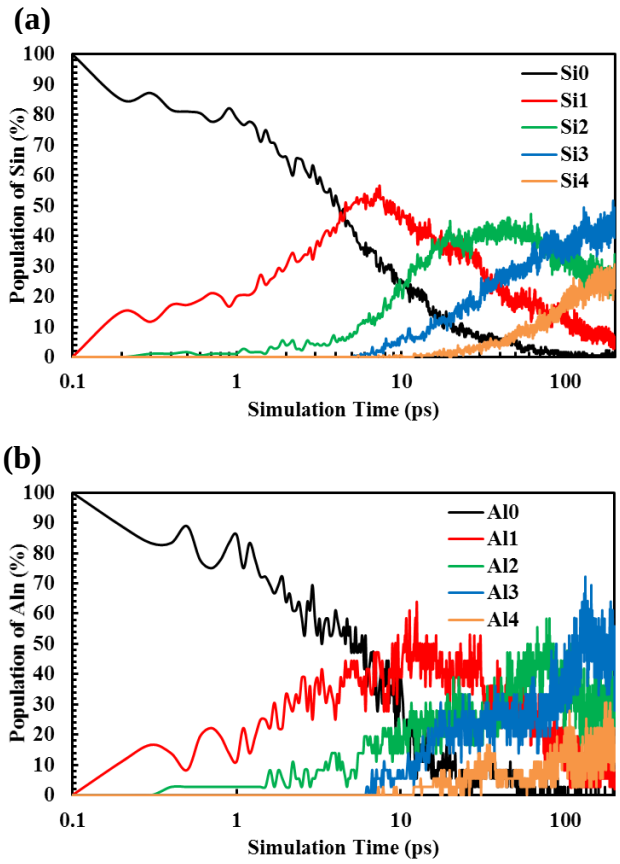

Figure 6-1. Development of Q_n for (a) Si and (b) Al in the simulation of the aluminosilicate model with a Si/Al ratio of 5 at 650K.

6.3.2. Polymerization of Aluminosilicate Precursor

The models of silicate and aluminate monomers at Si/Al ratios of 2 and 3 were simulated at 650K following thermal scheme 'a' shown in **Table 6-1**. After the simulation at 650K for 200ps, almost all the Si and Al sites were still Q_0. For M2a, the final concentrations of Si_0 and Al_0 were 95.14% and 91.67%, respectively; and for M3a, the final concentrations of Si_0 and Al_0 were 98.67% and 100%, respectively. The final degrees of condensation for M2a and M3a were 1.5% and 0.25%, respectively. The simulation systems barely showed any polymerization, or any tendency to polymerize within a reasonable time frame. For the

other simulation schemes with higher simulation temperatures, the development of Q_n exhibited apparent polymerization tendency and equilibrated within a reasonable timeframe. Although the polymerization rates and degrees of these models were dependent on the simulation temperature and Si/Al ratio, the molecules were polymerized in a similar trend. Thus, only the results of molecular structures, represented by Q_n (Si_n and Al_n), degree of condensation and RDF, in the model M2e with a Si/Al ratio of 2 simulated at 1800K are presented for briefness. The effect of simulation temperature and Si/Al ratio on the polymerization is discussed in the following sections.

As shown in **Figure 6-2**, Si_1 and Al_1 started to grow immediately as the simulations began, with a concurrent decrease of Si_0 and Al_0. The concentrations of Si_1 and Al_1 exceeded those of Si_0 and Al_0 at 1.5 ps. As expected, Q_2 started to form later than Q_1. While the concentration of Si_2 exceeded Si_1 at 8.5 ps, Al_2 exceeded Al_1 at 15 ps. Q_3 and Q_4 started to form subsequently while Q_1 started to decrease around 2ps. Finally, Si_4 and Al_4 reached steady-state near 55 ps and 52 ps, respectively. For the polymerized models simulated at 1800K (M2e and M3e) after 110 ps, the most populated Q_n sites are Q_3 and Q_4, while for the other models, M2 (or 3)b, M2 (or 3)c and M2 (or 3)d which were simulated at 1000K, 1200K and 1500K, respectively, the most populated Q_n sites are Q_2 and Q_3, regardless of the Si/Al ratio. This agrees well with the NMR studies reported in the literature, where the experimentally synthesized geopolymer gels are confirmed to be composed of various proportions of Si_1, Si_2, Si_3 and Si_4 and the most prevalent ones are Si_2 or/and Si_3 [136, 279]. The formation of larger Q_n (e.g., Q_3 and Q_4) sites at later stages elucidates that the dimerization between small clusters composed of Q_0, Q_1 and Q_2 is the essential reaction pathway to the condensation.

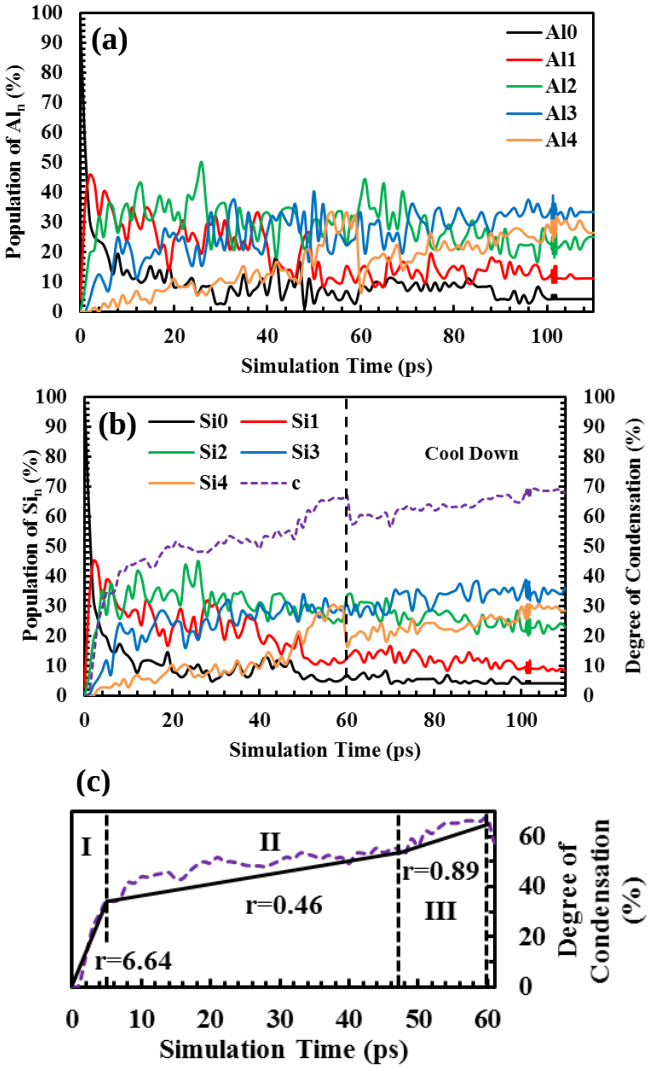

Figure 6-2. Development of (a) Al_n and (b) Si_n and the degree of condensation in the model with Si/Al = 2 at 1800K (M2e), with the three stages of condensation before the cool down process enlarged in (c). Note r is the average slope for the curve of the degree of condensation at each of the three stages.

Degree of Condensation: The degree of condensation, C, was calculated based on the population of Q_n and plotted with the development of Si_n in **Figure 6-2** (b). The increasing trend in degree of condensation suggests that the silicate and aluminate monomers polymerized into a more condensed network gradually. Based on the average slope (r) of the curve for C in **Figure 6-2** (b) and the reaction nature of the simulations for silica

systems [298, 300] that is similar to the simulations herein, the entire polymerization process can be divided into 3 stages, as shown in **Figure 6-2** (c): I. oligomerization, II. ring formation, and III. condensation. The slopes of the degree of condensation curve for these 3 stages are 6.64%/ps, 0.46%/ps and 0.89%/ps, respectively. The boundaries between two consecutive polymerization stages are 5 ps and 47.5 ps, respectively, which correspond to the time instants when Si_2 exceeds Si_0, and Si_3 and Si_4 exceed Si_1 and Si_2, respectively. Si_2 is the main component in the chain structures and single ring clusters, while Si_0 and Si_1 are the characteristic coordination in small oligomers. Therefore, the change in the Si_n coordination at the first stage boundary illustrates the formation of a large number of ring structures. The change in Si_n at the boundary between stage II and III indicates the condensation of the ring clusters, since Si_3 and Si_4 represent the cross-linked tectosilicate frameworks.

Snapshots of Molecular Structures during Simulations: Molecular configurations of the model (M2e) at 1ps, 10ps, 50ps and 110ps, which are within Stage I, II, III and "cool down" process, respectively, are presented in **Figure 6-3**. To show the frameworks of the model, the non-bonded oxygen and all the hydrogen atoms were excluded from the systems in the snapshots for clarity. In Stage I (**Figure 6-3** (a)), because of the high concentration of hydroxyl, the collision of silicate and aluminate monomers became significantly frequent, and then they dimerized to form small oligomers. Therefore, Q_0 decreased, while Q_1 and Q_2 increased rapidly. Subsequently, the increasing concentration of these small clusters enhanced the probability of ring closing activities, and thus Q_3 increased and Q_1 decreased, implying that rings started to form at Stage II (**Figure 6-3** (b)). Ring formation and agglomeration are the main reactions at this stage. At Stage III (**Figure 6-3** (c)), the rings

and clusters polymerized into relatively large clusters via cross-linking activities, illustrated by the large number of formed Q_4, with Si_4 increasing from 10% to 28% at this stage. The change in molecular structure throughout the first two stages well represents the reaction process from reactive silicate and aluminate monomers to aluminosilicate polymers that consist of oligomers in different sizes, while Stage III is consistent with the process from aluminosilicate polymers to geopolymer gels in the conceptual reaction model proposed by Provis et al. [158]. The sudden decrease in temperature at the start of the "cool down" process (**Figure 6-3** (e)) slightly reduced the condensation degree due to the temporary decrease of large Q_n (e.g., Q_3 and Q_4). In the meanwhile, the concentration of the small Q_n increased, implying that some small clusters, such as monomers and dimers, were disassociated from the main molecular network. Along the cooling process, the simulation system reorganized and those small clusters were re-incorporated to the network. Therefore, the final condensation degree and molecular structure are similar to those before the cooling, as shown in **Figure 6-2** and **Figure 6-3** (c) and (d), respectively.

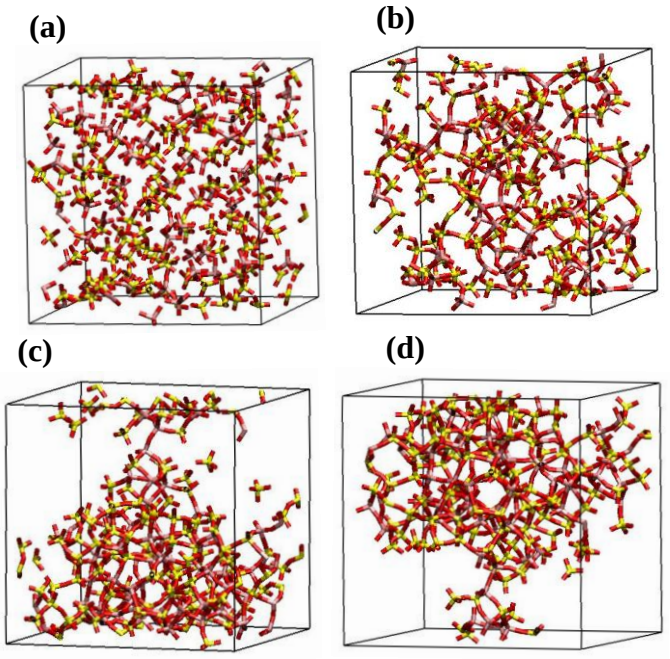

Figure 6-3. Snapshots of the molecular structures in M2e at (a) 1ps, (b) 10ps, (c) 50ps and (d) 120ps during the simulation, respectively. (The color coding is as follows: pink: aluminum, yellow: silicon, and red: oxygen. The non-bonded oxygen and All the hydrogen atoms are excluded for clarity.)

Development of T-O-T bonds: As another main indicator of geopolymerization, the distribution of T-O-T (T: Si or Al) bonds in the model with Si/Al ratios of 2 and 3 at 1800K (M2e and M3e) are plotted as a function of simulation time in **Figure 6-4**. The number of Si-O-Si, Si-O-Al, and Al-O-Al bonds, along with their sum: T-O-T bonds, increased along the simulation in both M2e and M3e models. Before the models were cooled down to lower temperatures, the T-O-T bonds were equilibrated around 52ps and 48ps with a final number of 327 and 288 in model M2e and M3e, respectively. It is reasonable that the T-O-T bonds in M3e model are fewer than those in M2e model, because the monomers in the initial model of M3e are fewer compared to M2e, as detailed in **Table 6-1**. Once the simulation temperature started to decrease at the cooling down stage, the T-O-T bond number reduced

immediately, mainly due to the breaking of Si-O-Al bonds that are weaker than Si-O-Si bonds [171]. However, at the end of the cooling process, the number of Si-O-Al and T-O-T increased back and equilibrated to the level before the cooling. In M2 model series (e.g., M2b, M2c, M2d and M2e), Si-O-Si bonds were always fewer than Si-O-Al, because the dimerization between a Si monomer and an Al monomer is more preferable than that between two Si monomers, illustrated by Yang et al. in their study [195]. However, Si-O-Si bonds were always slightly more than Si-O-Al in M3 model series (e.g., M3b, M3c, M3d and M3e) due to a relatively high Si/Al ratio in the initial model. Although Al-O-Al bonds increasingly formed during the simulation, their number is still much fewer than the other T-O-T bonds in each model, and even more limited in M3e model. The small number of Al-O-Al bonds formed during the simulations is consistent with the findings in a previous ^{29}Si NMR study of geopolymer, which illustrated that Loewenstein's Rule of aluminum avoidance may not apply strictly to geopolymer gels [141]. In addition, Al-O-Al bonds equilibrated at a final concentration of 2.2%, 6.8%, 9.2% and 10.9% in the models with a Si/Al ratio of 2 simulated at 1000, 1200, 1500 and 1800K, respectively. The increasing trend in Al-O-Al bonds with the temperature implies that more energy input may allow the formation of more Al-O-Al bonds. The increase in T-O-T bonds demonstrates that the aluminosilicate networks were gradually formed based on the polymerization of the dispersed silicate and aluminate monomers along the simulation. T-O-T bonds of model M2e increased the fastest in Stage I due to the oligomerization process, consistent with the condensation process shown in **Figure 6-2** (c). They subsequently increased more gently in Stage II as the dominant ring closing and aggregation processes during this stage would not introduce a very large change in T-O-T bonds. In stage III, they

increased faster than stage II, because the condensation process involves a high degree of cross-linking reactions, which increased T-O-T bonds, as depicted in **Figure 6-4** (a). The similar trend is also observed in development of T-O-T bonds shown in **Figure 6-4** (b) for model M3e.

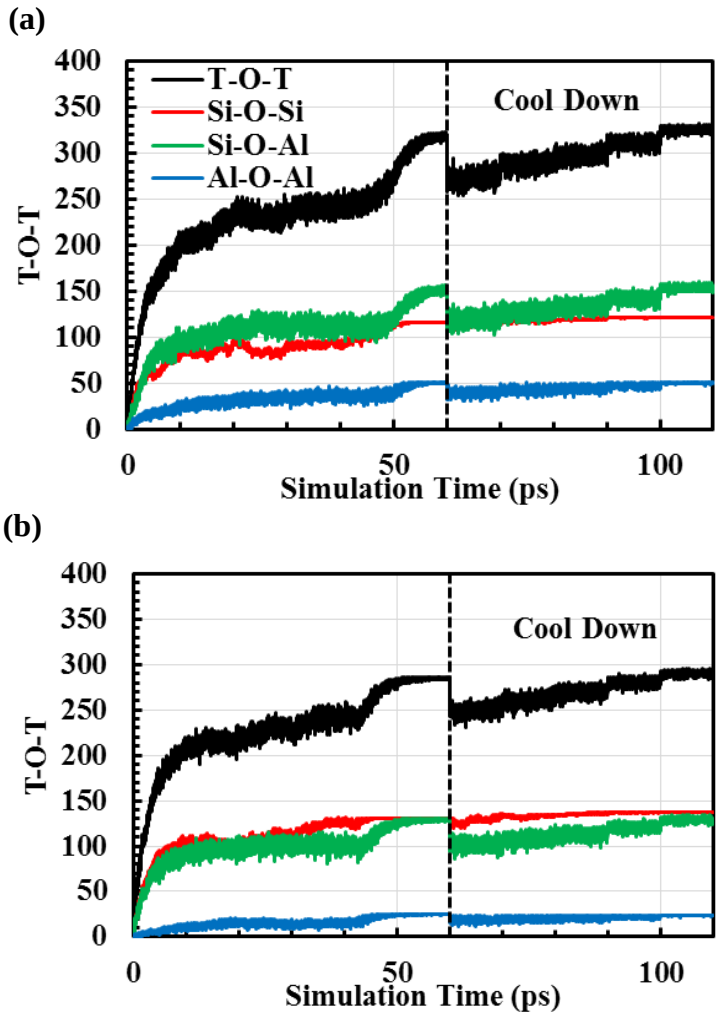

Figure 6-4. Development of T-O-T bonds during the simulation in simulation models with Si/Al ratio of (a) 2 (M2e) and (b) 3 at 1800K (M3e). The quantity of T-O-T is the sum of the other bonds.

Radial Distribution Functions: The radial distribution functions (RDFs) of Si-O, Al-O, O-O and Na-Al for M2e are superimposed and presented in **Figure 6-5** at various time instants within each of the three polymerization stages and at the end of each temperature during cooling process. After the polymerization at 1800K for 60ps, the model was cooled down through the simulation at 1500K, 1200K, 1000K, 650K and 300K orderly. At each cooling temperature, the simulation lasted for 10 ps, as indicated in **Table 6-1**. Therefore, the RDFs at 70ps, 80ps, 90ps, 100ps and 110ps are plotted to interpret the structural change of the model along the cool down process. There are no periodically repeating peaks for any of the atom pairs, indicating the amorphous nature of the molecular system. The most intense peak(s) are shown in the insets of each plot. For M2e model at 1800K, the r(Si-O) (**Figure 6-5** (b)) was centered at 1.55Å after the simulation of 1ps, and then shifted to 1.6Å. From 1ps to 50ps, r(Si-O) was centered at 1.6Å with similar intensities. The bandwidth and intensity increased from 50ps to 60ps. After the temperature decreased from 1800K to 1200K (70 ps to 110 ps), the intensity of r(Si-O) decreased. During the subsequent cooling process, the band of r(Si-O) slightly narrowed with its center shifting to a higher number, which was around 1.64Å, and its intensity gradually increased back to the level at 60ps (i.e., before the cooling). The band of r(Al-O) is less symmetric and wider than r(Si-O), as presented in **Figure 6-5** (c). From 1ps to 50ps, the r(Al-O) was centered at 1.75Å, and gradually increased. The band intensity significantly increased from 50ps to 60ps, and immediately decreased and shifted to 1.65Å after the temperature reduced at the beginning of the cooling process. The band of r(Al-O) increased back to the intensity before the cooling, similar to r(Si-O), and was centered at 1.75Å. The changes in r(Si-O) and r(Al-O) during the simulation are consistent with the development of Si-O-Al bond and the degree

of condensation, as shown in **Figure 6-4** (a) and **Figure 6-2** (b). During the polymerization and condensation of the model at 1800K, the bonds of Si-O and Al-O in monomers were converted to those in geopolymer gels, and reorganized and stabilized during the condensation process while the model gradually cooled down to 300K. \The RDF development of Si-O and Al-O from the MD simulations agrees well with the experimental results of (Si, Al)-O determined with in-situ synchrotron X-ray and neutron pair distribution function by White et al. [163, 164]. The Si-O and Al-O bonds were presented as one single peak in the experimental results in the range of 1.5 to 1.8Å. The RDFs of O-O, plotted in **Figure 6-5** (d) with a peak between 2.3 to 2.9 Å, became narrower along the simulation and its intensity developed in a similar trend to r(Si-O). The correlation between Na and Al is shown in **Figure 6-5** (e), which has multiple peaks before 50ps. After 60ps, only one main peak between 3.0 and 3.5Å became distinct for r(Na-Al). This indicates the molecular structure developed into a more ordered configuration after the simulation. The configurations of r(O-O) and r(Na-Al) are also consistent with the experimental PDFs of O-O and T-Na reported by White et al [164].

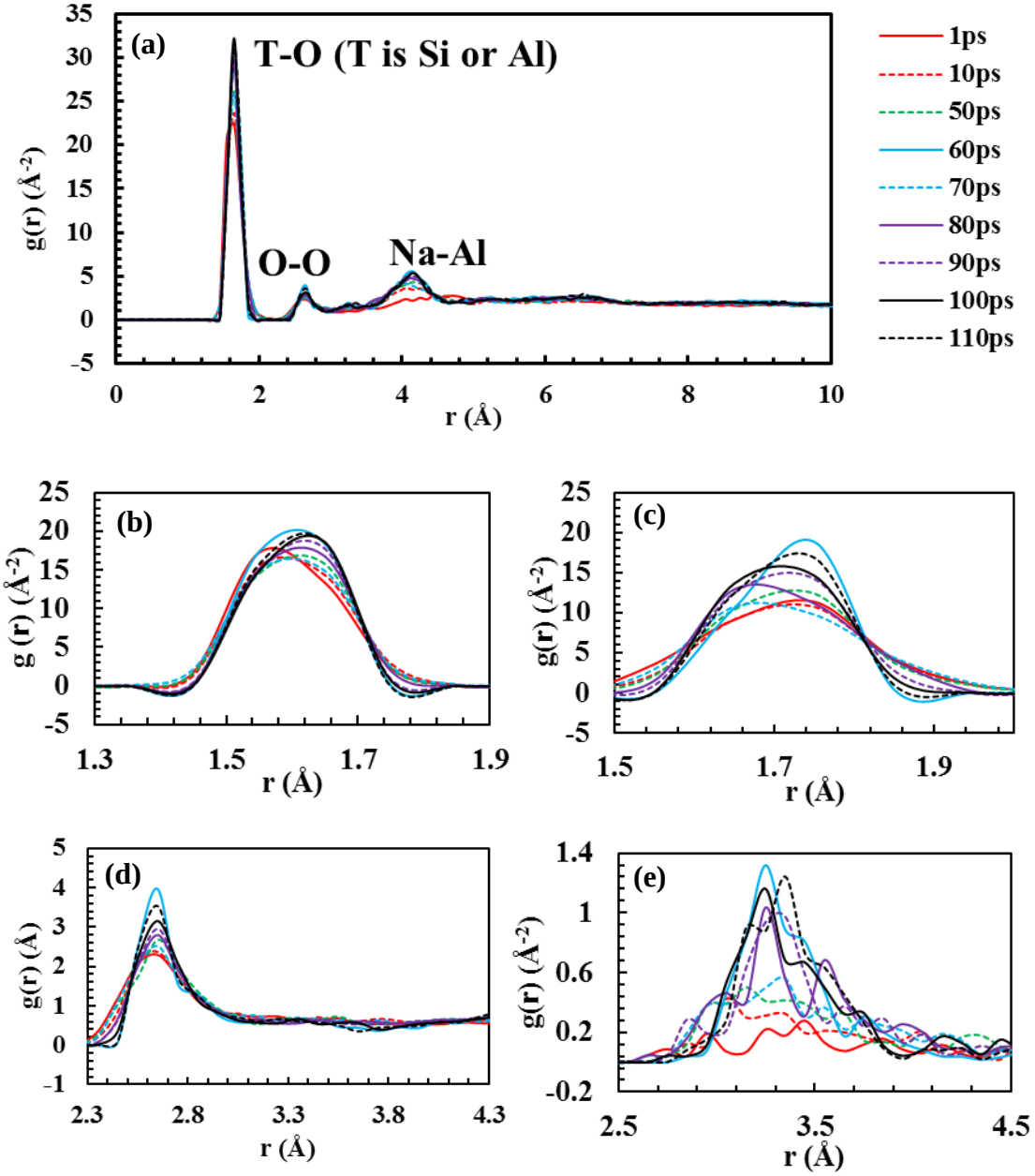

Figure 6-5. Radial distribution functions (RDFs) of molecular model at Si/Al ratio of 2 and simulated at 1800K (M2e): (a) the superimposed RDF for atom pairs, (b) Si-O correlation, (c) Al-O correlation, (d) O-O correlation, and (e) Na-Al correlation; the legends are the same as in (a) and the most intense peak(s) are enlarged in respective insets.

6.3.3. Effect of Si/Al Ratio on Geopolymerization Process

Figure 6-6 shows the development of Si_4(mAl) along the simulations in the models with Si/Al ratios of 2 and 3 at 1800K (M2e and M3e). Silicon tetrahedral centers Si_4(0Al), Si_4(1Al), Si_4(2Al) and Si_4(3Al) gradually increased along the simulations. The population of Si_4(mAl), as an indicator of the Si-Al interconnectivity, well explains the effect of Si/Al ratio on the polymerization. Since Al appears more frequently on the terminal sites of the aluminosilicate network compared to Si, a higher population of Si_4 connecting to fewer Al centers (e.g., Si_4(0Al), Si_4(1Al) and Si_4(2Al)) implies a more polymerized molecular structure. In M2e, the population of all the Si_4(mAl) increased at a low rate in the first 40ps, except for Si_4(4Al) which is always 0. From 40ps to 60ps, Si_4(1Al) and Si_4(2Al) increased rapidly to the highest populations. On the other hand, in M3e model, Si_4(1Al) increased fast immediately from the beginning of the simulation, and Si_4(0Al), Si_4(2Al) and Si_4(3Al) increased at a low rate, while Si_4(4Al) was barely formed during the entire simulation. At the end of the simulations, Si_4(2Al) and Si_4(1Al) are the most populated Si tetrahedral centers in the models with Si/Al ratio of 2 and 3, respectively. This implies that the aluminosilicate systems have been highly polymerized, consistent with the observations in the last section.

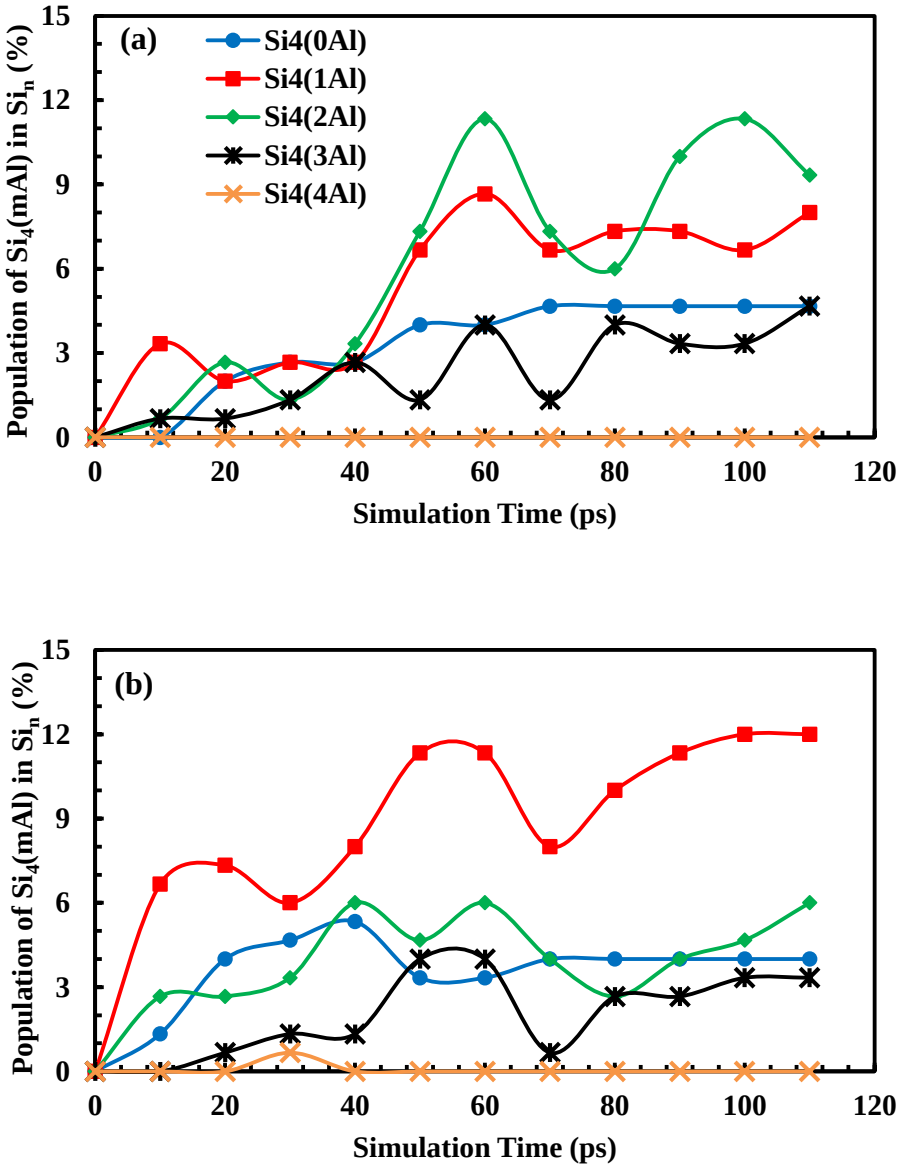

Figure 6-6. Development of $Si_4(mAl)$ as a fraction of Si_n in simulation models with Si/Al ratios of (a) 2 and (b) 3 simulated at 1800K (m = 0, 1, 2, 3 or 4).

The final $Si_4(mAl)$ site distributions of the models simulated at 1800K are also presented in terms of the fraction of the total amount of $Si_4(mAl)$ in **Figure 6-7**, where similar experimental results estimated from the solid state ^{29}Si NMR characterization of

geopolymer gels in the literature are also included for comparison. The experimental results by Duxson et al. were obtained from metakaolin based geopolymers with a nominal Si/Al ratio of 1.9 and 2.1, and the results by Fernandez-Jimenez et al. and Lyu et al. were obtained from fly ash-based geopolymers [142, 170]. The molecular structures generated from the current simulations consist of Si_4(0Al), Si_4(1Al), Si_4(2Al) and Si_4(3Al), where the synthesized geopolymers in the literature are composed of Si_4(1Al), Si_4(2Al), Si_4(3Al) and Si_4(4Al). Compared to the experimental results, the simulation results have more Si(0Al) and Si_4(1Al), but fewer Si_4(4Al). In the NMR study on fly ash based geopolymers by Lyu et al. [170], Si_4(2Al) was found dominant in the final distribution of Si_4(mAl) for all the systems. In the study by Fernandez-Jimenez et al., although the main silicon centers in the fly ash based geopolymer gels were Si_4(1Al), Si_4(2Al) and Si_4(3Al), there still remained an appreciable portion of Si_4(4Al), which might be due to the relatively short curing period (7 days) [142]. The same study showed that for the geopolymers synthesized with the nominal SiO_2/Na_2O ratio of 0 to 1.17, the populations of Si_4(1Al) + Si_4(2Al) and Si_4(3Al) + Si_4(4Al) were in the range of 46%~51% and 31%~35%, respectively. In the current simulation results plotted in **Figure 6-7**, the populations of Si_4(1Al) + Si_4(2Al) and Si_4(3Al) + Si_4(4Al) are in the range of 65%~71% and 13%~18%, respectively. As depicted in previous studies [169, 188], there are more Si_4(3Al) and Si_4(4Al) in Al-rich geopolymer gels, which have a lower mechanical strength; Si_4(1Al) and Si_4(2Al) sites are formed later after certain reaction time, as the major components for Si-rich geopolymer gels that have a higher mechanical strength. This implies that along with the curing time, Si_4(1Al) and Si_4(2Al) sites should gradually increase, so does the mechanical strength of geopolymer gels.

Figure 6-7 indicates that much more Si-rich geopolymer gels were formed in the current simulation study than those in the experimentally synthesized geopolymers in the literature.

The discrepancy between the current simulation and experimental results might be due to the different starting precursors used in the simulation and experimental systems. In the simulation systems, all the monomers are reactive, whereas in the experimental systems, the reactive monomers have to be released first from the raw materials that are not fully dissolvable. In addition, the Si_4(4Al) found in the synthesized geopolymer samples may be attributed to the residues of the raw materials. Unlike the physical experiments, the geopolymerization process in the simulations is not affected by excessive water content, the degree of dissolution of raw materials, excessive silicate or alkali concentrations, or low temperatures. Therefore, the polymerization degree, the proportion of Si_4(0Al) and Si_4(1Al) of the geopolymer gels in the current simulation study are higher.

As demonstrated in **Figure 6-7**, the proportion of Si_4(1Al) in the model with a Si/Al ratio of 2 is lower than that in the model with a Si/Al ratio of 3, whereas the proportions of Si_4(2Al) and Si_4(3Al) are higher in M2 model series. This trend is consistent with the findings reported in the study by Duxson et al. [141], where the Si_4(1Al) in the geopolymers with a nominal Si/Al ratio of 1.90 was lower compared to the counterpart with a Si/Al ratio of 2.15, and the population of the other Si_4(mAl)s was higher. This implies that Si-O-Al bonds in geopolymer gels decreased with the increasing in the nominal Si/Al ratio. The results of the simulation model with a Si/Al ratio of 2 are also qualitatively similar to the NMR results by Duxson et al. [141], where the proportions of Si_4(2Al) and Si_4(4Al) were the most and the least distributed silicate tetrahedrons, respectively, for the systems with

nominal Si/Al ratios of 1.90 and 2.15. This qualitative comparison elucidates that (i) the main Si_4(mAl) sites in the current simulated geopolymer systems are Si_4(1Al) and Si_4(2Al), whose populations are qualitatively consistent with the experimental results; and (ii) the Si/Al ratio plays an important role in the resulting molecular structures of geopolymer gels.

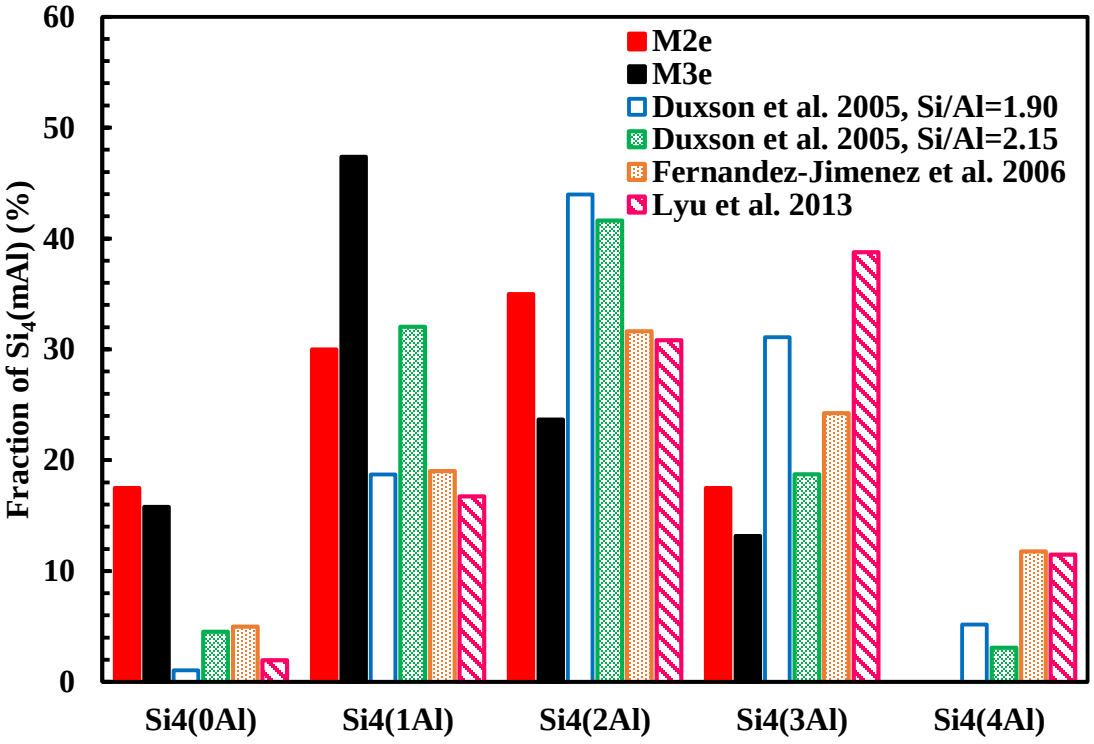

Figure 6-7. Fraction of Si_4(mAl) in simulation models with Si/Al ratio of 2 and 3 at 1800K compared with the experimental Si_4(mAl) sites obtained with ^{29}Si NMR characterization [141, 142, 170].

The effect of Si/Al ratio on the polymerization is further elucidated by the final percentages of Q_n, final degrees of condensation and T-O-T bonds in **Figure 6-8.** As shown in **Figure 6-8** (a) and (b), in most of the M2 model series (Si/Al=2), the final portions of Q_0 and Q_3 were lower than those in M3 model series (Si/Al=3), but the Q_1 and Q_2 were higher than M3 counterparts. The dependence of the final portions of Si_4 on Si/Al ratio is different

from that of Al_4, which is affected by the simulation temperatures. The final proportion of Si_4 in M2 models at 1000K, 1200K and 1800K were higher than those in M3 counterparts, while the final portions of Al_4 in M2 models at 1000K, 1200K and 1500K were slightly lower than those in M3 counterparts. Since Si tetrahedrons are the major components in geopolymeric networks and Si_4 represents the polymerization degree better than Al_4, the final molecules of geopolymer gels formed from the M2 models should be more cross-linked than those resulted from the M3 models in general. Consistently, the degrees of condensation of M2 models simulated at 1000K, 1200K and 1800K were higher than the M3 counterparts (see **Figure 6-8** (c)). As illustrated in 0, the differences in T-O-T bond developments are: (i) Si-O-Si bonds were always more than Si-O-Al bonds in M2 models, while the M3 models followed the opposite trend; and (ii) more Al-O-Al bonds formed in M2 models than those in M3 models. This phenomenon is also illustrated by the number of resulting T-O-T bonds in the final simulation systems at different temperatures, as shown in **Figure 6-8** (d). More Si-O-Al and Al-O-Al bonds are formed in the resulting molecular models with a Si/Al ratio of 2 than the models with a Si/Al ratio of 3, for all the simulation temperatures. On the other hand, more Si-O-Si bonds were formed in the models with a Si/Al ratio of 3 than those in the models with the Si/Al ratio of 2. These discrepancies are mainly due to the different Si/Al ratios, where Al-O bonds have a lower probability but it is more likely for Si-O to form in the models with a relatively higher Si/Al ratio.

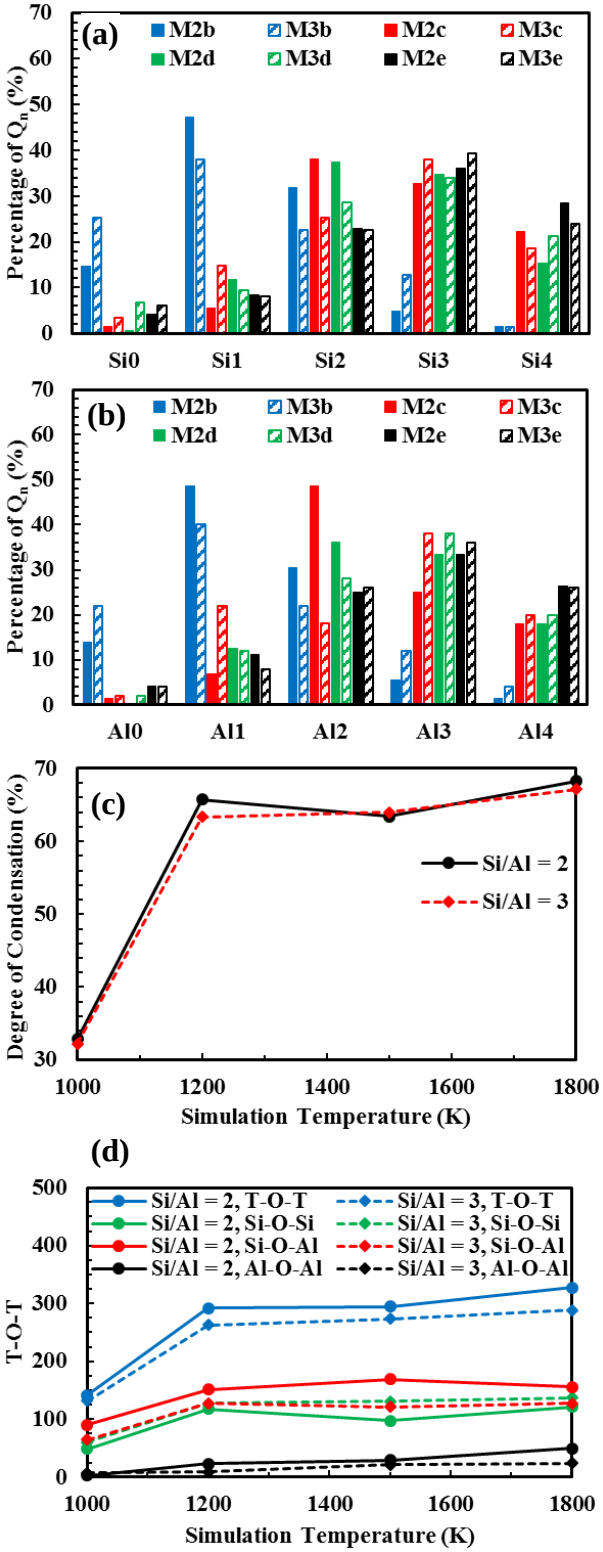

Figure 6-8. Effect of Si/Al ratio on the of (a) Si_n, (b) Al_n, (c) degree of condensation and (d) T-O-T bonds in the polymerized models at different temperatures.

6.3.4. Effect of Simulation Temperature on Geopolymerization Process

The fractions of Si_4(mAl) in the final Si_4 sites of all the models simulated at different temperatures are depicted in **Figure 6-9**. In the models simulated at 1000K (M2b and M3b), only a small number of Si_4(1Al) and Si_4(2Al) was formed due to low degree of polymerization. For the models with a Si/Al ratio of 3 (M3 model series), the total Si_4(mAl), Si_4(1Al) and Si_4(2Al) increased with the increasing in simulation temperatures. For the models with a Si/Al ratio of 2 (M2 model series), Si_4(2Al) and Si_4(3Al) increased with the simulation temperature; the concentrations of Si_4(0Al), Si_4(1Al) and Si_4(2Al) in M2d (1500K) are lower than those in M2c (1200K), and thus the total Si_4(mAl) in M2d is fewer than that in M2c. As evident from **Figure 6-9**, the effect of simulation temperatures on the molecular structures of the models is also dependent on the Si/Al ratio. Such intertwining effects of curing temperature and Si/Al ratio on geopolymerization are also reported in experimental synthesis studies in the literature [123].

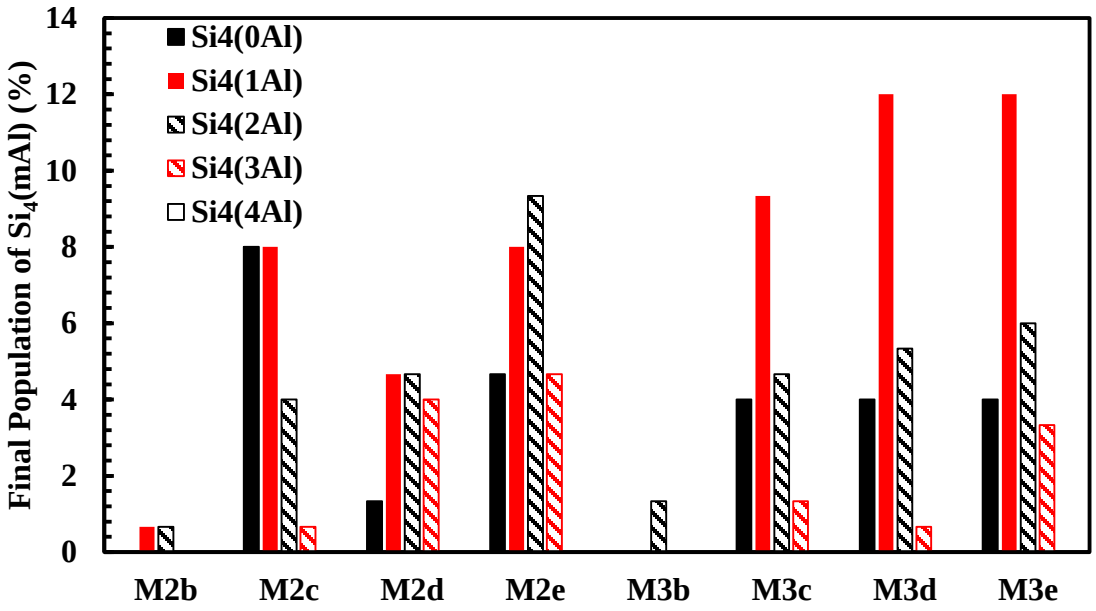

Figure 6-9. Final distribution of Si_4(mAl) in the models with Si/Al ratio of 2 and 3 at the temperature of 1000K (M2b and M3b), 1200K (M2c and M3c), 1500K (M2d and M3d) and 1800K (M2e and M3e).

The effect of simulation temperatures on the polymerization can be better demonstrated by the degree of condensation, as shown in **Figure 6-10**. The degree of condensation for M3 model series (Si/Al=3) exhibited a similar dependence on the simulation temperature as that for M2 counterparts (Si/Al=2), so only the results of M2 models are presented. The condensation degree increased with simulation time and reached a steady state near 250, 180, 48 and 52ps for the models at 1000, 1200, 1500 and 1800K, respectively. In other words, the higher simulation temperatures are applied, the shorter simulation time is required to reach the final degree of condensation. In each of the models, the condensation degree dropped once the temperature started to decrease during the 'cool down' and then increased to the similar level before the cooling. The final degrees of condensation of M2b, M2c, M2d and M2e are 33.3%, 65.7%, 63.5% and 67.8%, respectively. For the models

heated to 1000K and 1200K (M2b and M2c), no apparent boundary between stage I (oligomerization) and II (ring formation) can be found, but stage III (condensation) is able to distinguish from the early stages. For the model simulated at 1500K (M2d), the boundaries between two consecutive stages are 13ps and 35ps, respectively. The higher simulation temperature resulted in a shorter Stage I (M2d: 0ps to13ps and M2e: 0ps to 5ps) and III (M2d: 35ps to 60ps and M2e: 47.5ps to 60ps) but a longer Stage II (M2d: 13ps to 35ps and M2e: 5ps to 47.5ps), as shown in **Figure 6-10** (c) and (d). A higher temperature speeded up the oligomerizaiton process and also increased the oligomerization degree, where the degree of condensation (c) value of M2e (67.8%) is higher than M2d (63.5%) at the end of Stage I. A shorter Stage II in M2d compared to M2e might be attributed to the less availability of oligomers for the ring formation. Consequently, the final condensation degree of M2e is higher than that of M2d. For the models simulated at 1000K and 1200K, ring formation and cluster-cluster aggregation occurred simultaneously with the oligomerization due to the relatively low temperature, thus the resulting condensation degrees are relatively low. The slightly higher condensation degree of M2c compared to M2d might be due to much longer simulation time, as shown in **Table 6-1**. Apparently in **Figure 6-10**, the degree of condensation at the same simulation time instant increased with the simulation temperature. This illustrates that the temperature can effectively enhance the reaction rate, consistent with the experimental results in previous research [52, 185, 187].

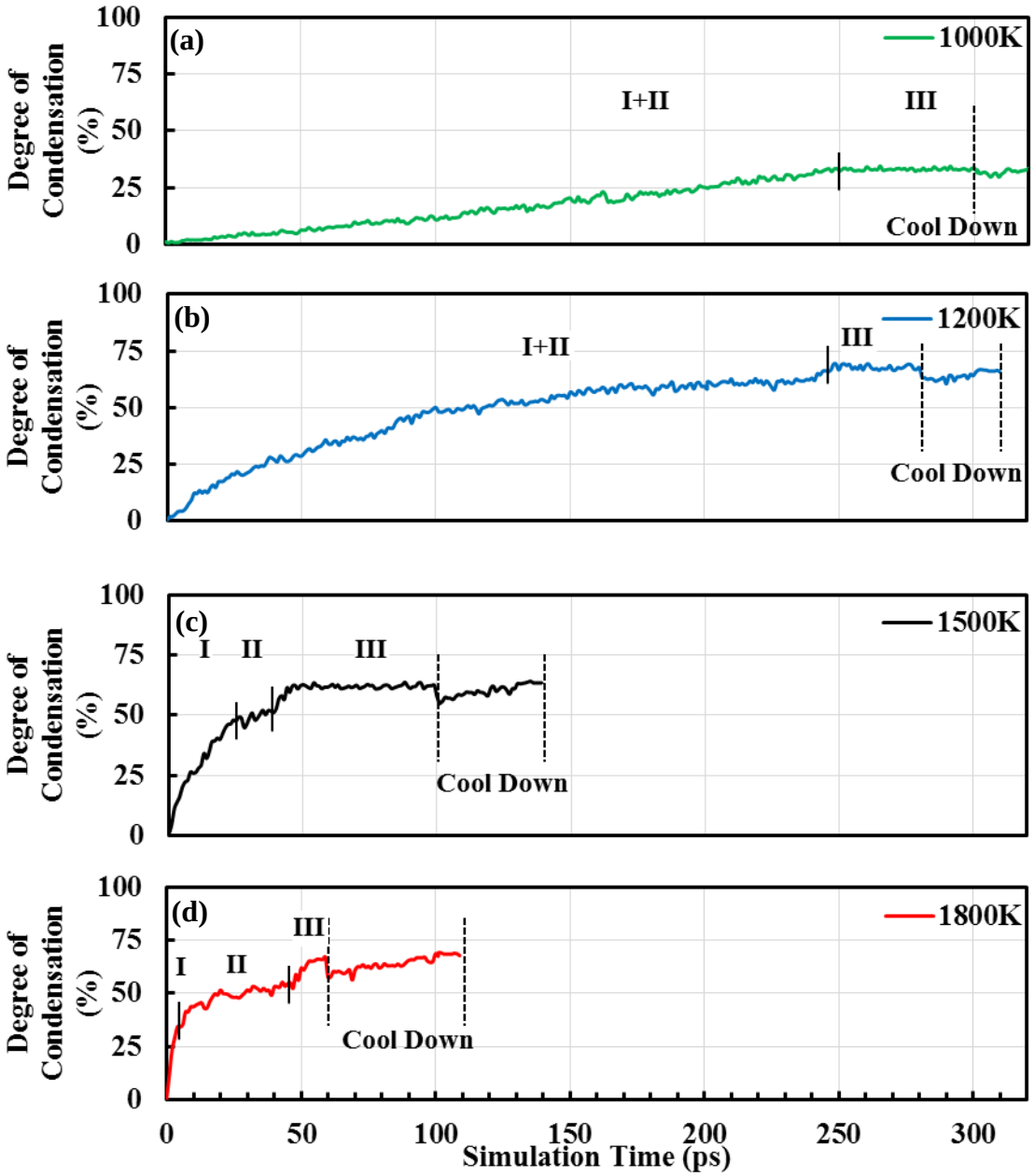

Figure 6-10. Degree of condensation of M2 models with a Si/Al ratio of 2 at (a) 1000K, (b) 1200K, (c) 1500K and (d) 1800K. Stage I, II and III are the process of oligomerization, ring formation and condensation, respectively.

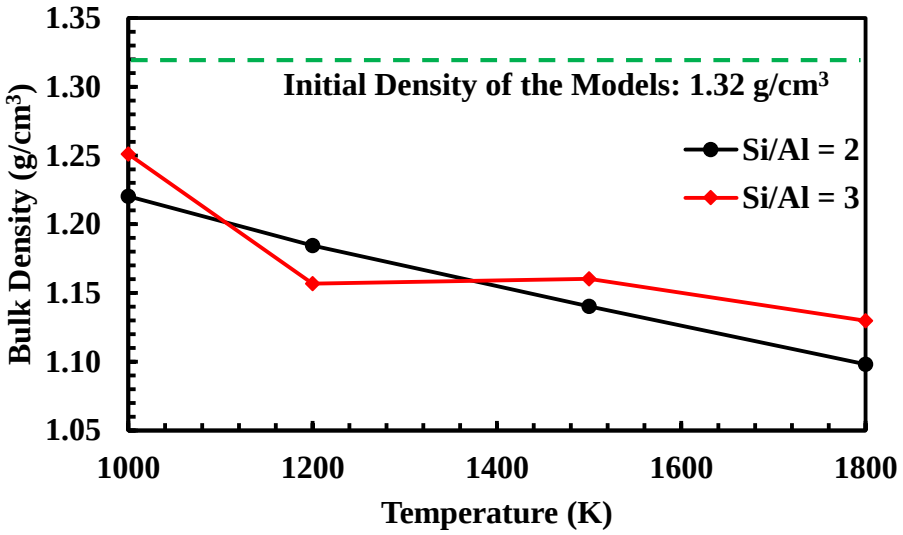

Figure 6-11. Bulk density of the polymerized models with the Si/Al ratio of 2 and 3, where the dotted line indicates the initial density of the models.

The bulk densities of the model systems simulated at different temperatures were estimated by using the total mass of the atoms in the final model divided by the volume of the simulation domain, as plotted in **Figure 6-11**. Free water molecules were excluded for the estimation. The densities of the final models are all lower than the initial density due to the removal of the water molecules that left a large proportion of pores and cavities in the models. The density of the "geopolymer gels" predicted from the simulations is in the range of 1.10 to 1.25 g/cm^3, which is lower compared to the bulk density of metakaolin based geopolymers, 1.31g/cm^3, experimentally synthesized in a previous study by the authors [109]. This discrepancy in the bulk density is expected because the cavities in experimentally synthesized metakaolin-based geopolymers were filled with the remaining impurity and unreacted constituents. For both M2 and M3 series (with Si/Al ratios of 2 and 3, respectively), their bulk densities decreased with the simulation temperature due to the

increasing amount of water exclusion. This agrees well with the effect of curing temperature on the density of geopolymers observed in physical experiments [57]. The density of the polymerized model with a Si/Al ratio of 2 is slightly lower than its counterpart with a Si/Al ratio of 3 except the one at 1200 K, implying (i) the porosity in M2 models is higher than M3 models, and (ii) more water molecules were extracted from M2 models than those from M3 models. Therefore, the geopolymer frameworks with the Si/Al ratio of 2 were more compact than those with the Si/Al ratio of 3.

6.4. CONCLUSIONS

A combined DFT-reactive MD simulation procedure was developed in this study to simulate the polymerization process and computationally "synthesize" amorphous geopolymer gels from aluminate and silicate monomers to final geopolymer gels. The influence of curing temperature and Si/Al ratio on the geopolymerization was simulated by applying 5 simulation temperatures from 650K to 1800K on the models with a Si/Al ratio of 2 and 3.

Based on the analysis of the degree of condensation and the nature of geopolymerization, the entire polymerization process was divided into 3 stages: oligomerization, ring formation and condensation, similar to the polymerization of silica models. Along with the polymerization, the models with dispersed monomers gradually developed into a more condensed and ordered structure. For the first time, geopolymer gels close to the ones synthesized experimentally were computationally "synthesized", which were verified with the experimental NMR and X-ray/neutron PDF results reported in the literature. The good agreement between the current simulations and NMR results in the

distribution of Si_4(mAl) indicated that the polymerized models are consistent with the experimentally synthesized geopolymer gels. The single-peak RDF patterns for the atom pair Si-O, Al-O, O-O and Na-Al of the models illustrated the amorphous nature of the simulated geopolymer gel structures. These RDF patterns also agreed with the experimental PDF results and further confirmed the consistency of molecular structure between the computationally and experimentally synthesized geopolymer gels. After excluding the free water molecules from the models, the bulk densities of the simulated geopolymer gels were estimated, which ranged between 1.10 and 1.25 g/cm^3.

Similar to the experimental observations, the polymerization rate and degree derived from the simulation results were both accelerated by the increase of temperature. As a result, the bulk density of the resulting geopolymer gels decreased with the increasing simulation temperature. This implies that geopolymer gels simulated at a higher temperature tend to have more water evaporated and result in a higher porosity, consistent with the experimental results. The simulation results suggest that a low temperature extends the reaction time at the early stage of polymerization and results in a relatively low degree of condensation. This agrees qualitatively with the experimental findings that reaction rate and degree at low curing temperatures are relatively low. The polymerization process and the properties of the resulting geopolymer gels show apparent dependence on Si/Al ratio of the initial simulation models. T-O-T bonds, Si_4 and degrees of condensation in the models with a Si/Al ratio of 2 are higher than their counterparts with a Si/Al ratio of 3, so the molecular structures obtained in the former models are more compact than those in the latter ones. The lower bulk densities of the models with a lower Si/Al ratio implied a higher degree of water extraction and higher pore volume in the corresponding geopolymeric

models. Furthermore, Si/Al ratio plays an important role in the effect of simulation temperature on the polymerization process. Although the polymerization was enhanced by the increase of temperature for all the models, more Al atoms were connected to the Si_4 sites in the models with a lower Si/Al ratio (Si/Al ratio = 2 in this case). This was verified with the distribution of T-O-T bonds and Si_4(mAl) and agreed well the experimental findings that the effect of different synthesis factors on geopolymerization are intertwined.

The reaction kinetics of geopolymer synthesis is better understood with the aid of the reactive MD modeling. More importantly, the molecular structures of geopolymer gels predicted from MD simulations in this study can be used for assessing their other properties, such as strength, stiffness and permeability. Lastly, the simulation approach to computationally synthesize amorphous geopolymer gels using both first principle DFT-based and reactive molecular dynamics (MD) simulations can be extended for studying other amorphous materials.

CHAPTER 7 - EXPERIMENTAL FEASIBILITY STUDY OF GEOPOLYMER AS THE NEXT-GENERATION SOIL STABILIZER

7.1. INTRODUCTION

Soft or highly compressible soils are often encountered on many civil engineering project sites, which lack sufficient strength to support the loading either during construction or throughout the service life [301, 302]. To improve the strength and stiffness of those less competent soils, chemical stabilization with cementitious materials has been widely practiced. The commonly used stabilizers include ordinary Portland cement (OPC) and lime, with their stabilization mechanisms being relatively well understood [54, 138, 303-305]. In cement stabilized soils, the stabilization mechanisms are associated with hydration and pozzolanic reactions [304, 306]. When lime is mixed with clayey soils, the clay particles become closer and the soil is stabilized through flocculation and pozzolanic reactions [54, 307]. A major issue with conventional soil stabilizers (i.e., OPC and lime) is that their production processes are energy intensive and emit a large quantity of CO_2. For instance, approximately one ton of CO_2 is emitted for the production of one ton of cement [308]. Furthermore, the raw materials readily available for cement production are being over-consumed. Therefore, civil engineering industry is always searching for new, viable sustainable alternatives to replace Portland cement as soil stabilizers.

Geopolymer is an inorganic aluminosilicate material formed through polycondensation of tetrahedral silica (SiO_4) and alumina (AlO_4), which are linked alternatingly by sharing

all the oxygen atoms [13, 75]. The chemical structure of geopolymer can generally be expressed as [75]:

$$M_n\{-(SiO_2)_z - AlO_2 -\}_n$$

where M is an alkali cation such as potassium (K^+) or sodium (Na^+) that balances the negative charge for Al, n is the degree of polycondensation, and z is the Si/Al molar ratio, ranging from 1 to 15, and up to 300 [13, 75]. Three typical structures of geopolymer are: $M_n\{-Si-O-Al-O-\}_n$, $M_n\{-Si-O-Al-O-Si-O-\}_n$, and $M_n\{-Si-O-Al-O-Si-O-Si-O-\}_n$. Geopolymers exhibit different physicochemical properties with varying Si/Al molar ratios [309]: low ratios (<3) result in three-dimensional and cross-linked networks with stiff and brittle properties, and hence can be used as cementitious and ceramic materials; and higher ratios (>3) result in two-dimensional and linearly linked networks with adhesive and rubbery properties [309]. The geopolymerization can be simplified as two major steps that interact with each other along the reaction: (1) amorphous aluminosilicate materials are firstly dissolved by alkali hydroxide solution and/or alkaline silicate solution to form reactive silica and alumina, and (2) the dissolved species then poly-condense into amorphous or semi-crystalline oligomers which further polymerize and harden into synthetic aluminosilicate materials [161, 234]. The reasonable synthesis temperature of geopolymer is in the range of 25 ℃ to 80 ℃ [174]. Consequently, energy consumption and CO_2 emission can be largely reduced by replacing OPC with geopolymer [310]. Moreover, geopolymers have excellent mechanical properties (e.g., compressive strength and stiffness) and exceptional resistance to heat, organic solvents and acids. In addition, geopolymers can be synthesized from a wide range

of low-cost aluminosilicate materials or even industrial wastes, such as metakaolin, fly ash, furnace slag, red mud, and rice husk ash [46, 75, 242, 311, 312]. Considering all the above advantages [236], geopolymer renders itself to be a promising alternative to OPC in civil infrastructure construction. Finally, geopolymers also have low shrinkage potential and excellent adhesion to aggregates, suggesting that they can be an effective soil stabilizer [126, 161].

Recently, some researchers have investigated the effectiveness of both low calcium- and high calcium-fly ash based geopolymers in deep soft soil improvement (i.e., grouting process) [38, 39]. These studies were conducted by thoroughly mixing alkali activated fly ash slurry, the geopolymer precursor, with soft soils, and their results indicated that fly ash based geopolymers were comparable to cement and lime in the stabilization of deep soft soils.

This paper describes a different potential application of geopolymers: soil stabilization at shallow depth (e.g., subgrade, subbase or base in pavement and airport construction, shallow foundation, embankment, etc.). Alkali activated metakaolin (MK) was selected to treat a lean clay, in an attempt to examine the feasibility of using geopolymer as a soil stabilizer. Metakaolin is an anhydrous aluminosilicate produced by the calcination of kaolin at a temperature of 650-900 ℃ [9, 313], so it contains nearly exclusively amorphous silica and alumina, and hence is highly reactive during the alkali activation [161, 314]. Although metakaolin is not necessarily more cost-effective or ‘greener’ than OPC, it is an ideal raw material that results in relatively pure geopolymer binders. Therefore, it was chosen as a starting point for this exploratory study to avoid complexity and uncertainties

associated with impurity present in other low-cost materials with complex compositions (e.g., fly ash, red mud, furnace slag).

In this study, a synthesis recipe that yields metakaolin based geopolymers (MKG) with adequate mechanical properties was determined first. The mechanical properties and workability of geopolymers are significantly affected by Si/Al molar ratio and water content in the precursor. Therefore, MKG with nominal Si/Al molar ratios ranging from 1.5 to 2.0, as reported in the literature that these Si/Al ratios render geopolymer with high mechanical strength, were synthesized for an optimal geopolymer precursor. A Na/Al molar ratio of 1 was selected in this study also because this value proved to yield MKG with high mechanical strength according to previous studies [31, 115, 315]. To investigate the feasibility of MKG as a soil stabilizer, the following properties of the treated soil were determined: unconfined compressive strength (UCS), failure strain (ε_f), Young's Modulus (E) and volumetric shrinkage strain during curing period. One-way analysis of variance (ANOVA) was performed to determine the statistical trend of the dependence of mechanical properties on curing period and geopolymer concentrations. Furthermore, the microstructural change of the soil before and after the stabilization was investigated to elucidate the geopolymer stabilization mechanisms, with the aid of X-ray diffraction (XRD), scanning electron microscopy (SEM), and energy dispersive X-ray spectroscopy (EDX) analyses.

7.2. MATERIALS AND METHODS

7.2.1. Soil

The studied soil was synthesized in the laboratory by mixing a soil collected from a construction site on Worcester Polytechnic Institute (WPI) campus and an ACTI-MIN CR kaolin clay at a dry mass ratio of 5:3. The minus 425 μm fraction (or passing the No. 40 sieve) has a plasticity index (PI) of 15% and a liquid limit (LL) of 29% (ASTM D4318-00) [316]. Particle size analysis was performed on this soil by following the standard methods (ASTM D2487 and D422) [317, 318], and the result is shown in **Figure 7-1**. According to the Unified Soil Classification System (USCS), this soil is a CL (lean clay or low-plasticity clay). About 65% of the soil is finer than 0.2 mm, so clay and fine sand are the major components in this soil. This type of soil is often too soft and weak to support the upper infrastructures in constructions. Therefore, this soil was used for the feasibility study on the use of geopolymer as a soil stabilizer. The standard Proctor compaction tests were also performed on the soil (ASTM D698) [319] to determine the maximum dry density (ρ_{max}) and the optimum water content (OWC). The ρ_{max} and OWC of the soil are not appreciably affected by the addition of the geopolymer precursor, on the basis of the authors' preliminary experiments and a previous research [320], so the ρ_{max} of 1.8g/cm^3 and OWC of 15% of unstabilized soil were used to prepare all the soil specimens in this study for consistency and practical consideration.

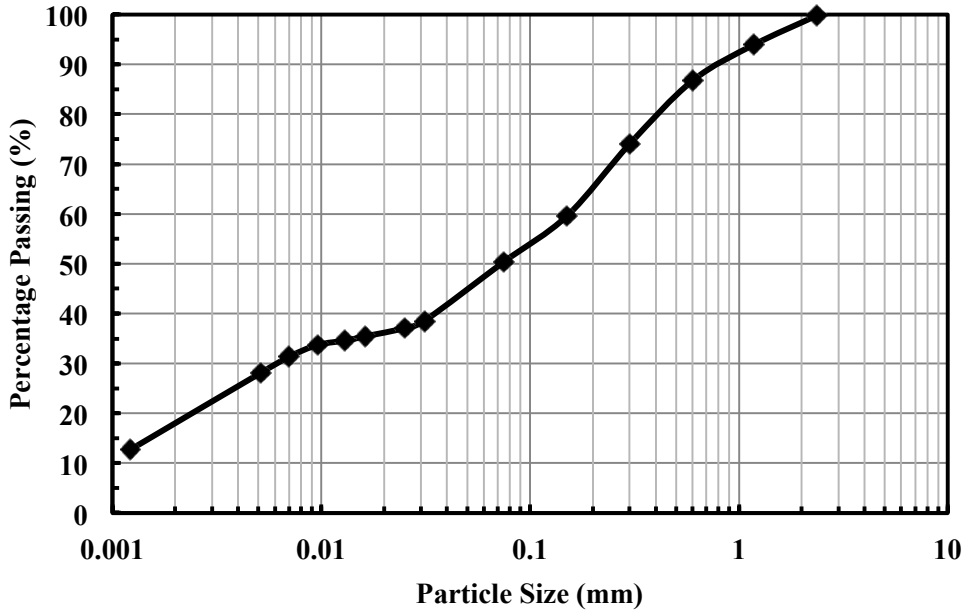

Figure 7-1. The particle size distribution curve of the studied soil.

7.2.2. Geopolymer synthesis

In order to synthesize an appropriate geopolymer precursor that can successfully stabilize the soil, geopolymer samples with Si/Al molar ratios of 1.6, 1.7 or 1.8 and a constant Na/Al ratio of unity were prepared. The Si/Al molar ratios were calculated by dividing the amount of Si element in metakaolin and the activator by the amount of Al element in metakaolin. Similarly, Na/Al ratio was obtained. A water content of 50% was used in the synthesis to produce a geopolymer precursor with desired workability [53], where the water content is calculated as the water in the activator divided by the mass of metakaolin and the activator mixture. The chemical and physical properties of the MK are summarized in **Table 7-1**. The used activator was a mixture of sodium hydroxide solution (NaOH~50%, and H_2O~50%) and reagent grade sodium silicate solution (Na_2O~10.6%; SO_2~26.5%, 1.39g/mL at 25 ℃). In the synthesis sequence, the MK was mixed with the activator for

20 minutes, and then transferred into 4 cm (diameter) × 10 cm (height) cylindrical molds. The samples were cured at ambient temperature and humidity conditions (temperature ≈ 23 ℃, and relative humidity ≈ 40-50%) before testing. Unconfined compression tests were performed after the curing period of 7 or 28 days. SEM and XRD tests were also conducted on the MKG samples to characterize their mineralogical and microstructural properties.

For comparison, a Type II OPC was also used to stabilize the soil, and its chemical and physical properties are listed in **Table 7-1**.

Table 7-1. Chemical and physical properties of portland cement and metakaolin.

Properties	Type II (MH) Portland cement	Metakaolin
Chemical composition		
SiO_2 (wt.%)	19.80	52.20
Al_2O_3 (wt.%)	4.80	43.11
Fe_2O_3 (wt.%)	3.00	1.53
CaO (wt.%)	61.90	0.07
MgO (wt.%)	3.80	0.06
Na_2O (wt.%)	0.61	0.07
K_2O (wt.%)	--	0.22
SO_3 (wt.%)	3.00	0.99
Insoluble residue (wt.%)	0.49	--
Moisture content (wt.%)	--	0.33
Loss on ignition (wt.%)	2.24	0.18
Physical properties		
Amount passing No. 325 sieve (wt.%)	91.6	92.9
Blaine Fineness (m^2/kg)	380	2690

7.2.3. Soil Stabilization with MKG and Characterization Tests

7.2.3.1. Sample Preparation and Unconfined Compressive Strength (UCS) Test

The soil samples for UCS test were prepared using cylindrical molds, which have an inner diameter of 3.6 cm and a height/diameter ratio of 2.0 for reducing the end effects during

UCS testing. For geopolymer stabilized soils, the MKG precursor was prepared and poured into soils at predetermined concentrations. Then extra water was added to the soil to meet the OWC, and the soil was mixed for about 10 minutes to achieve a homogeneous mixture. All samples were statically compacted in three layers with the aid of a loading machine. The compacted specimens were extruded with a Harvard Miniature Compaction Apparatus immediately after compaction, wrapped with plastic film, and cured in a plastic chamber that was equipped with a humidifier that maintained a nearly constant relative humidity (RH) (~40%) and temperature (~23 ℃). After two days curing, the specimens were unwrapped and continued to cure in the chamber until UCS testing. During the curing process, the diameter and height of each sample were measured at the following time intervals: right after extrusion, unwrapping (i.e., 2 days), 3, 4, 7, 14, and 28 days, to determine its volumetric changes. The sample matrix and the corresponding designations are listed in **Table 7-2**. The soils were stabilized with geopolymers at the concentrations of 3, 5, 8, 11, or 15%, where the concentration is the mass percentage of the soil and stabilizer mixture. Note that these concentrations were used in this study since they are practically reasonable values and very little information is available in the literature on the concentration of geopolymer for soil stabilization. For soil stabilization with OPC, 5% is a typical value to provide a baseline for the stabilization efficacy of OPC as the most common soil stabilizer. The samples of unstabilized soil (MKG0) were also prepared as control group 1. Three replicates of each sample set were prepared to assure reproducibility.

The UCS and εf of the cured samples were determined in an Instron Compression Machine at a loading rate of 0.2 in./min. The Young's modulus (*E*) of each sample was derived as the slope of the stress-strain curve, as illustrated in . According to ASTM E-111

[321], the tangent modulus or chord modulus of the stress-strain curve from UCS testing can be used as the estimate of Young's modulus. To exclude the artifactual stiffening effect, as indicated by the initial concave up portion of the curve in **Figure 7-2**, on the soil samples due to the testing conditions, a tangent line of the linear part of the curve was drawn and its slope was used as the Young's Modulus, as shown in **Figure 7-2**. The stiffening feature of the observed stress-strain curves may be caused by the samples' uneven end surfaces, and hence a better contact was achieved after some load was applied.

Table 7-2. Soil sample matrix and corresponding designations.

Samples	Concentration of MKG (%)	Concentration of OPC (%)
MKG0 (Control 1)	0	0
OPC5 (Control 2)	0	5
MKG3	3	0
MKG5	5	0
MKG8	8	0
MKG11	11	0
MKG15	15	0

Note: the concentration is the mass percentage of the soil and stabilizer mixture.

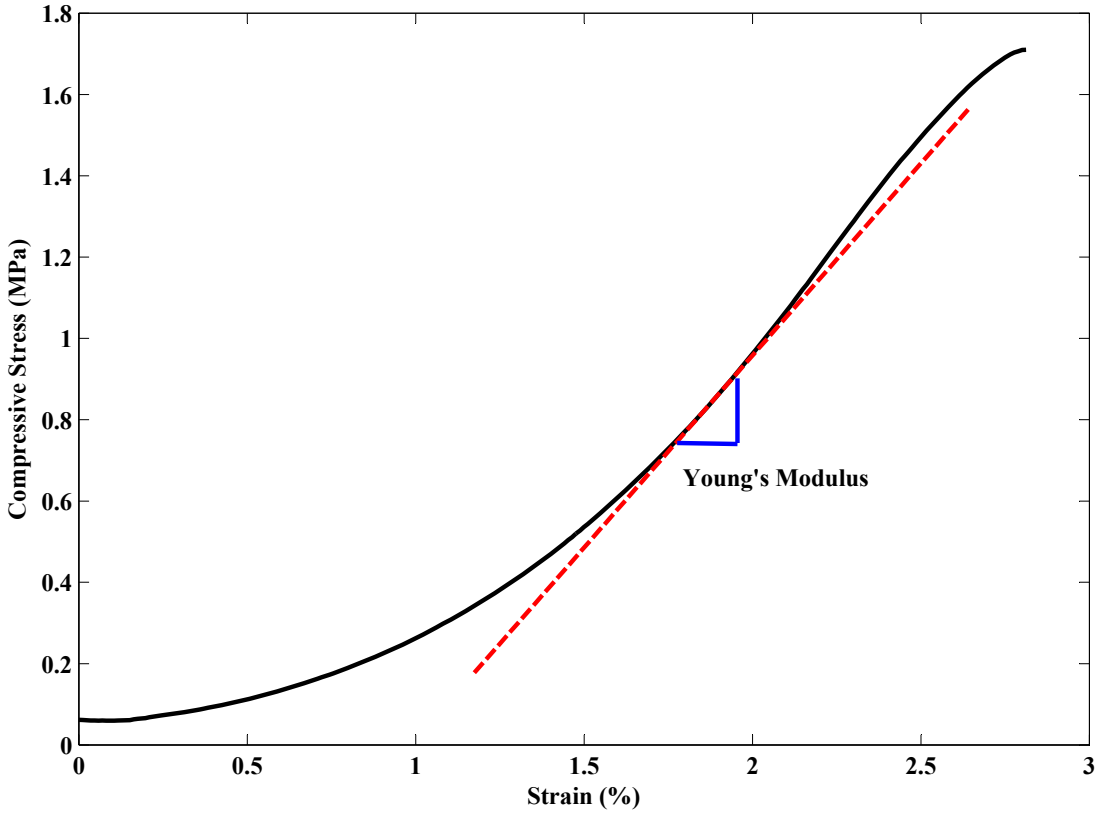

Figure 7-2. An example stress-strain curve showing how Young's Modulus is determined.

7.2.3.2. Statistical Analysis of the Mechanical Properties of MKG Stabilized Soils

To aid in interpreting the results of aforementioned mechanical testing, statistical analyses with the one-way analysis of variance (ANOVA) method were conducted with the IBM SPSS v.17. Such analysis is used to test whether more than two population means are equal, with the hypotheses given in Equation (1) [250].

H_0: $\mu_1=\mu_2=\mu_3$

H_a: at least one of the population means is different from the others. (7.1)

Where: H_0 is the null hypothesis, H_a is the alternative hypothesis, and μ_1, μ_2, and μ_3 are the population means of Group 1, 2, and 3, respectively. To be consistent, the one-way ANOVA analysis was also used to test the equality of two population means herein. The standard significance α was assumed to be 0.05 for all the statistical tests, which means that if the *P*-value of a statistical test is less than 0.05, at least one of the population means is different from the others; otherwise the difference among the population means is not statistically significant [250]. The statistical testing groups are summarized in **Table 7-3**, with the means of UCS, ε_f and *E* being tested individually. For example, if the *P*-value of Testing 1a is greater than 0.05, the 7-day and 28-day UCS of MKG3 would be viewed as the same statistically. For Testing 2 and 3, a *P*-value of <0.05 represents at least the UCS mean at one MKG concentration is different from the other counterparts, and the post hoc analysis would be conducted to study the UCS trend against the MKG concentrations.

Table 7-3. The testing groups of one-way ANOVA analyses for UCS, ε_f, and E of MKG stabilized soil specimens.

Testing No.	Samples	Objectives
1a	MKG3: 7 days and 28 days	To assess the influence of curing time (7 vs. 28 days) on mechanical properties of stabilized soil samples (*UCS, ε_f, or E*)
1b	MKG5: 7 days and 28 days	
1c	MKG8: 7 days and 28 days	
1d	MKG11: 7 days and 28 days	
1e	MKG15: 7 days and 28 days	
2	7 days curing: MKG3, MKG5, MKG8, MKG11 and MKG15	To assess the influence of MKG concentration on mechanical properties of stabilized soil samples (UCS, ε_f, or E) after 7-day curing
3	28 days curing: MKG3, MKG5, MKG8, MKG11 and MKG15	To assess the influence of MKG concentration on mechanical properties of stabilized soil samples (*UCS, ε_f, or E*) after 28 day curing

7.2.3.3. Microstructural Characterization

To examine the micromorphological change of the stabilized samples and shed lights on the stabilization mechanisms, SEM imaging was performed on selected soil samples in a JEOL JSM-7000F field emission SEM under the backscatter mode. The EDX spectra were also acquired using an OXFORD INCA x-act instrument installed in the same SEM device. The EDX spectra were collected within the selected areas of SEM samples in order to verify whether any geopolymer gels were formed. SEM samples were prepared by following a procedure suggested in previous studies [301, 322]. The same cylindrical samples used for UCS tests were prepared and wrapped with plastic bags for 2 days curing.

A 1 ×1 ×1 cm cubic specimen was trimmed off and then air dried in a desiccator at ambient temperature for a total curing time of 28 days. The dried specimen was cut in the center with a V-shaped groove and broken into two parts by pulling and bending. The debris on the surface of the specimens was removed with an adhesive tape. The specimen was mounted on an alumina stud with conductive tapes, and then sputter coated with gold-palladium alloy.

7.2.3.4. Mineralogical Characterization

To investigate the mineralogical changes of the stabilized soil, XRD patterns were taken on 28 day-cured, broken samples after UCS tests. The crushed soil sample was first ground with a mortar and pestle, and 10 g ground soil was sieved through a 45 μm sieve. The minus45 μm portion was collected and kept in a desiccator at room temperature until XRD testing. The prepared powder sample was side-loaded on the sample holder. The purpose of XRD test was to determine whether any reaction occurs between the geopolymer precursor and the soil, which can be identified by observing any new peaks (i.e., new mineral) formed. Consequently, the simpler oriented-mounting method was good enough and adopted in this study because the full spectrum of clay minerals is more complicated and not necessary [323]. The powder samples were scanned with a Rigaku Geigerflex X-ray powder diffractometer using a CuKα radiation with a voltage of 37.5 kV and a current of 25 mA at 1 sec/step. The data were collected from 5° to 70° 2θ at 0.02 °/step and analyzed with MDI Jade 5.0.

7.3. RESULTS AND DISCUSSION

7.3.1. Geopolymer Samples

The UCS of MKG was maximized at a Si/Al molar ratio of 1.7 based on the preliminary results by the authors, and the corresponding synthesis recipe was used for subsequent soil stabilization experiments. The UCS, ε_f and E of this geopolymer were determined after the curing of 7 days and 28 days, as shown in **Table 7-4**. These values are the average results of three identical samples. It should be noted that metakaolin based geopolymer samples are totally different from the MKG stabilized soil samples discussed in the following sections. **Figure 7-3** shows the XRD patterns of metakaolin and the MKG cured for 28 days. Some of the sharp peaks belong to quartz and kaolinite in the metakaolin, which are the impurities inherited from the source material. A characteristic broad hump in the range of 18 ° to 37 ° in the MKG pattern indicates the formation of geopolymer gel due to their amorphous nature [104]. The SEM image of the MKG cured for 28 days is shown in **Figure 7-4**. Similar to what was reported in the literature [31], the microstructure of MKG is highly homogeneous, where some unreactive grains are closely bonded with the geopolymer gel. The micro-cracks shown in the image may be due to the drying shrinkage during curing or the stress during sample preparation (i.e., cutting and breaking).

Table 7-4. The mechanical properties of selected MKG with a Si/Al ratio of 1.7.

Curing period	UCS (MPa)	Failure strain (%)	Young's modulus (GPa)	Bulk density (g/cm^2)
7 days	20.27	2.35	0.82	1.31
28 days	31.22	4.06	0.81	1.31

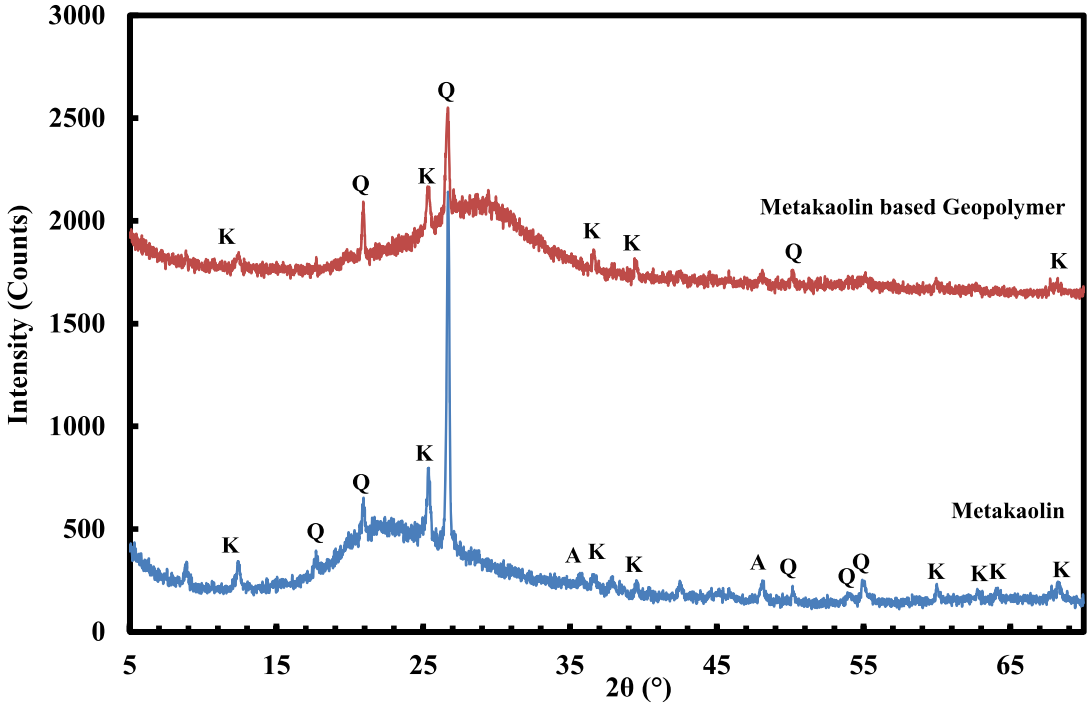

Figure 7-3. XRD pattern of metakaolin and metakaolin based geopolymer (K: Kaolinite, Q: Quartz, and A: Anatase).

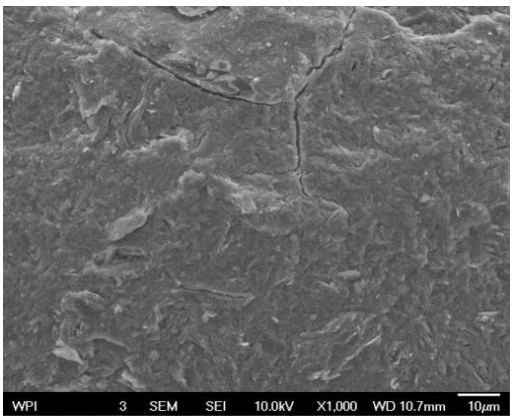

Figure 7-4. The SEM image of metakaolin based geopolymer after 28 day curing.

7.3.2. Mechanical Properties of MKG stabilized Soil samples

UCS, ε_f (failure strain), and E of all the soil samples after the curing of 7 or 28 days are shown in **Figure 7-5** to **Figure 7-7**. Since the UCS of untreated soil did not further develop after 7 days, its 28-day UCS is not shown. As expected, the UCS values of all the MKG stabilized soils were much higher than the untreated counterpart. The strength of MKG15 was higher than PC5, both after 7 and 28 days curing. As shown in **Figure 7-5**, the UCS values of MKG stabilized soil samples did not increase significantly after 7 days curing, which may be due to quick reactions of metakaolin-based geopolymer precursor. The quick reaction of metakaolin led to the near completion of geopolymerization and strength development of geopolymer gels in the first 7 days. For MKG3 and MKG11, it seems that the UCS may have even decreased slightly with curing time. In general, the UCS increases with the MKG concentrations ranging from 5 to 11%. However, there is no statistical difference in the UCS values between MKG 3 and MKG 5, based on the one-way ANOVA analysis shown in the following sections; similarly no statistical difference between MKG 11 and MKG 15, as seen in **Figure 7-5**. Essentially, the MKG at all dosages used in this study are effective soil stabilizers, because an increase in UCS of 345 KPa or more for soil treatment can be considered effective, according to ASTM D4609 [324]. The improved binding of soil particles by the geopolymer gels was the most likely reason for the strength improvement. This can be demonstrated by the SEM images of unstabilized and MKG stabilized soil samples in the following sections.

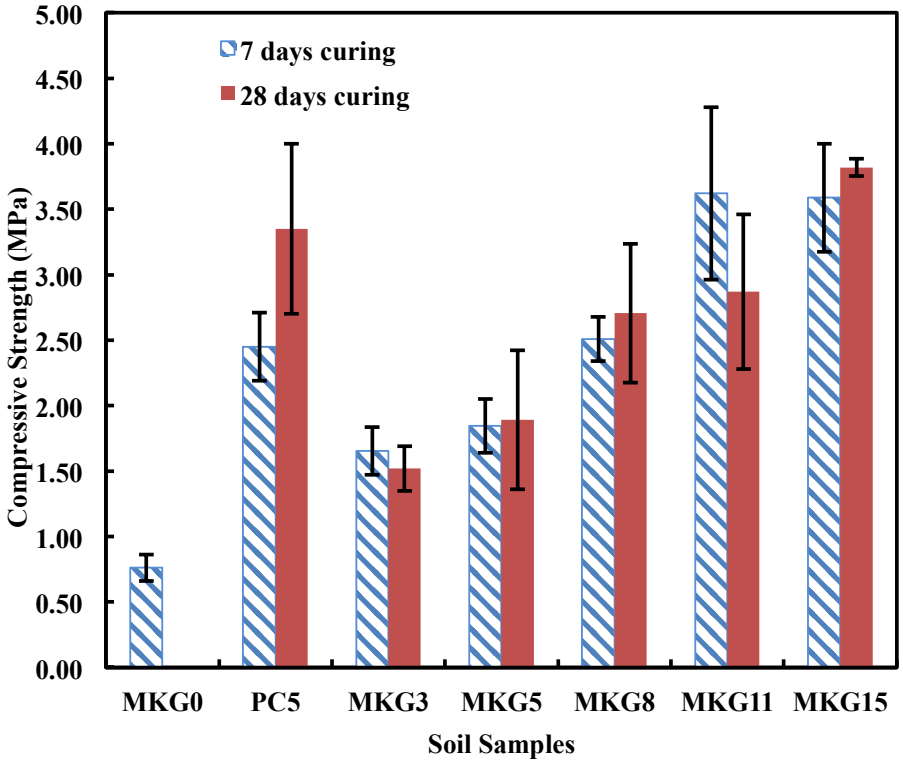

Figure 7-5. The UCS of MKG stabilized soils, soil, and Portland cement stabilized soil samples after 7 and 28 day curing.

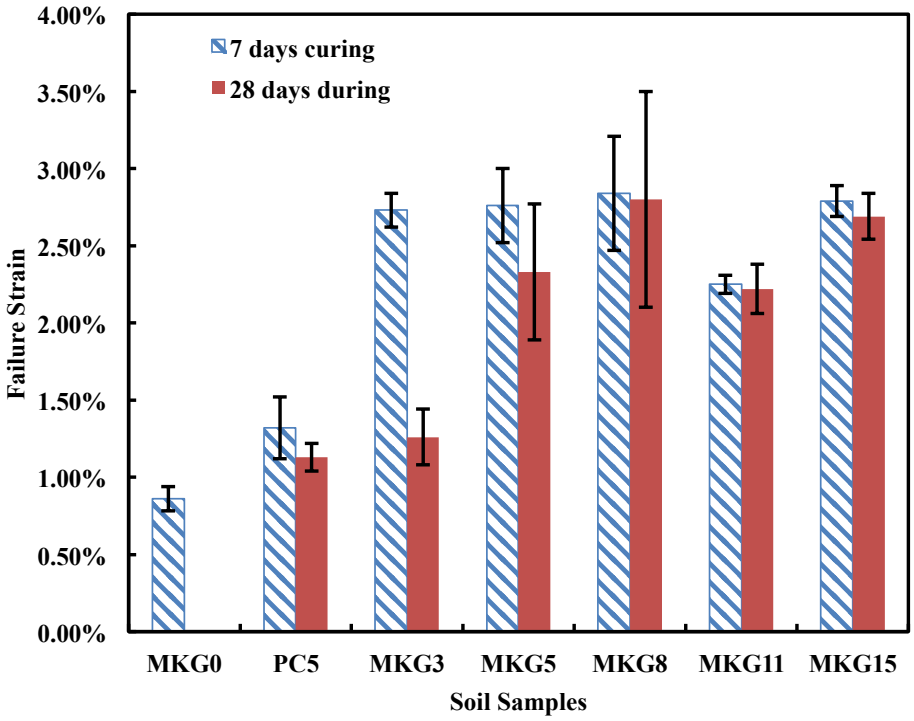

Figure 7-6. Failure strains of MKG stabilized soil, soil, and Portland cement stabilized soil samples after 7 and 28 day curing.

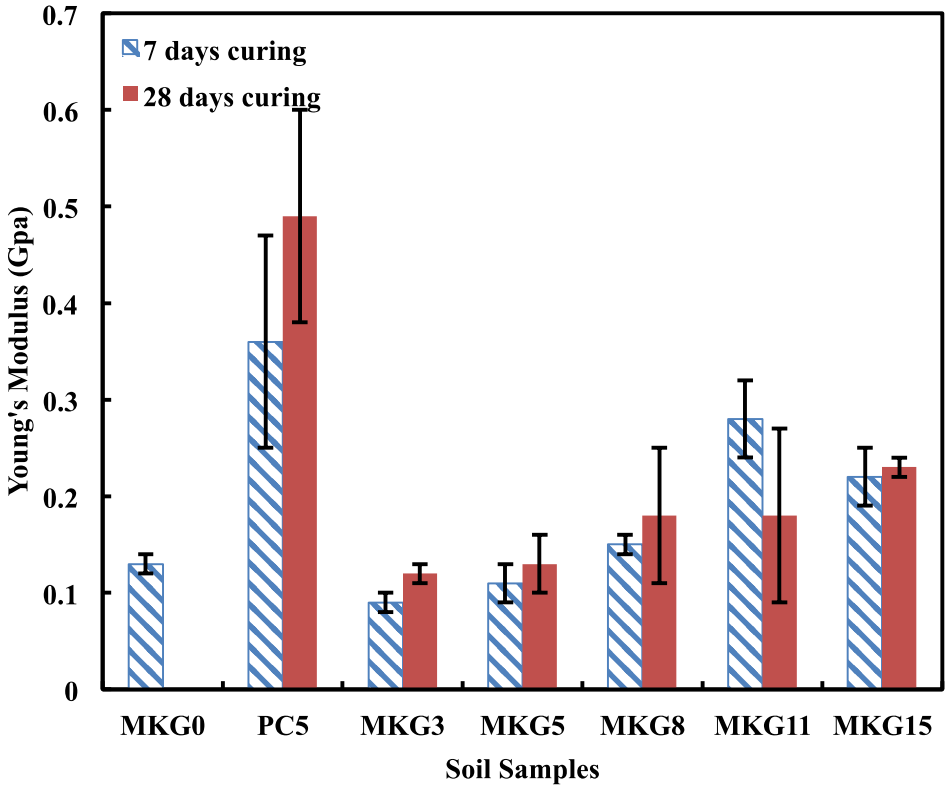

Figure 7-7. Young's Modulus of MKG stabilized soil, soil, and Portland cement stabilized soil after 7 and 28 day curing.

Figure 7-6 shows that the failure strains of the MKG stabilized soils were higher than the MKG0 and PC5 samples. This means that the MKG stabilized soils were more ductile compared to the two control groups. The failure strains of metakaolin based geopolymer, which has been used in the soil stabilization in this study, are higher than the unstabilized soil and the soil stabilized with OPC, as seen in **Table 7-4** and **Figure 7-6**. This illustrated that the addition of geopolymer enhanced the soil's ductility.

As seen in **Figure 7-7**, the Young's Moduli of the MKG stabilized soils are similar to that of unstabilized soil when the MKG concentration is less than 8%. This might be caused

by non-uniform mixing when geopolymer precursors were added to soil or inadequacy of the formed geopolymer gel within the soil matrix to form a microstructure more resistant to deformation. When the MKG concentration is larger than 8%, there are probably enough geopolymer gels dispersed within the soil matrix to form a more deformation-resistant microstructure that renders a high Young's modulus. Therefore the Young's Moduli of the soil stabilized with more than 8% of MKG are higher than unstabilized soil. This might indicate that the improvement of stiffness for soil by MKG is not as significant as the improvement of UCS, or there are different mechanisms between strength- and stiffness-related failures. The influence of curing time and MKG concentrations on either failure strain or Young's Modulus is not illustrated well by the bar-chart, which was therefore further studied by the statistical analyses in the next section.

7.3.3. ANOVA Analyses on Mechanical Properties of Soil Specimens Stabilized by MKG

All the P-values from the one-way ANOVA analyses are listed in **Table 7-5**, for studying the statistical trend of UCS, ε_f and E against the curing time and MKG concentrations. For UCS, the P-values of testings 1a to 1e are all larger than 0.05, indicating that the compressive strength of MKG stabilized soils at each concentration did not have appreciable change after 7 days curing. The P-values of testing 2 and testing 3 for UCS were less than 0.05, so the post hoc analyses were further conducted on 7-day UCS and 28-day UCS against MKG concentrations, respectively, as shown in **Figure 7-8** (a). The compressive strength of the stabilized soils generally increased with the MKG concentration, either cured for 7 days or 28 days. Although there was a slight decrease of

7 day-strength from MKG11 to MKG15, these two groups can be viewed as the same statistically because of negligible difference in their UCS values.

Table 7-5. The P-values of one-way ANOVA analysis on the influence of curing time and MKG concentration on UCS, ε_f, and E of MKG stabilized soil.

P-value ($\alpha = 0.05$)	Testing No.						
	1a	1b	1c	1d	1e	2	3
P (UCS)	0.404	0.661	0.579	0.218	0.391	0.000	0.001
P (ε_f)	0.000	0.208	0.923	0.721	0.515	0.036	0.005
P (E)	0.021	0.808	0.559	0.170	0.692	0.000	0.171

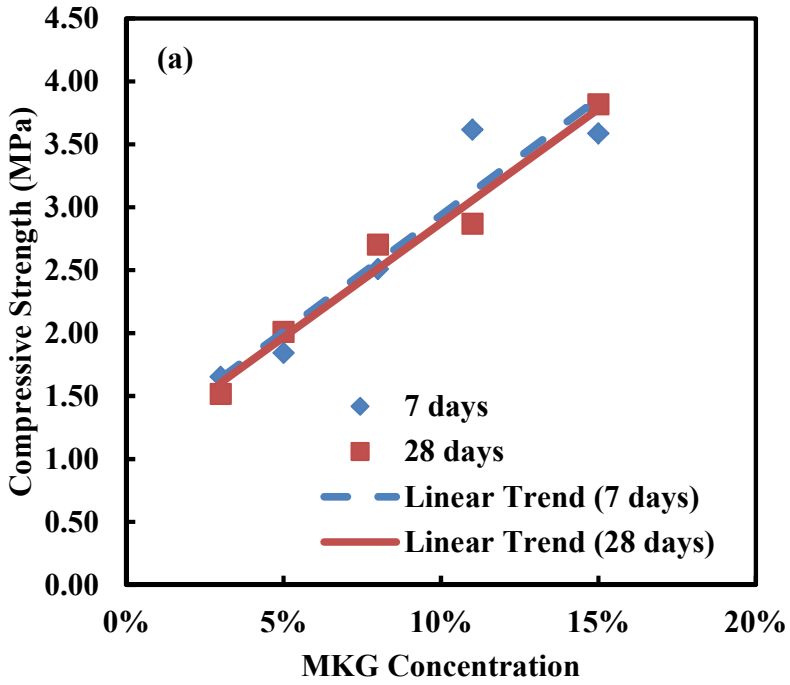

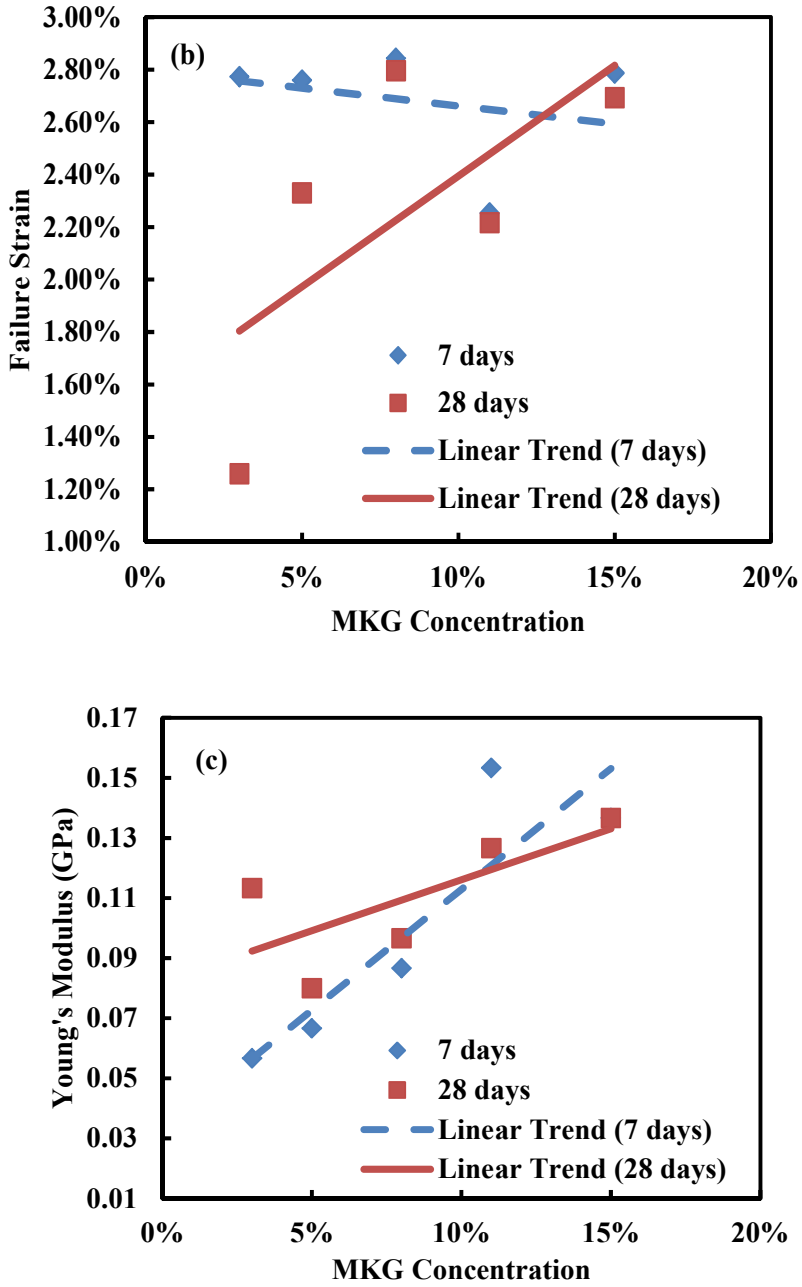

Figure 7-8. The influence of MKG concentrations on: (a) UCS; (b) failure strain; and (c) Young's Modulus of the MKG stabilized soils cured for 7 and 28 days.

For failure strain, the P-values of testing 1b to 1e are larger than 0.05, whereas testing 1a has a P-value less than 0.05, demonstrating that the failure strain of MKG stabilized soils

at the concentration higher than 3% was generally steady after 7 days curing. As seen in **Figure 7-5**, the soil stabilized with 3% MKG became more brittle along with the curing time. The P-values of testing 2 and 3 for ε_f shown in **Table 7-5** were less than 0.05, indicating that the soil stabilized with MKG at different concentrations are distinguishable in ductility. However, there is no apparent trend on the failure strain against MKG concentration. As shown in **Figure 7-8** (b) developed with post hoc analysis, the failure strain increased when the MKG dosage increased from 3% to 8%, became lower at 11%, and bounced back at 15% to the similar level as MKG8, after both 7 days and 28 days curing. The lower failure strain of soil stabilized with 11% MKG needs to be further studied.

As shown in **Table 7-5**, the P-values of testing 1b to 1e for Young's Modulus are all larger than 0.05, whereas the P-value of testing 1a is less than 0.05. These results indicated that the Young's Moduli of MKG stabilized soils were generally steady after 7 days curing, except that MKG 3 showed an appreciable improvement of stiffness with the curing time. The P-value of testing 2 for Young's Modulus is less than 0.05, but the P-value of testing 3 is larger than 0.05. The post hoc analyses were conducted, as the curves shown in Figure 8(c). The *E* after 7 days curing increased from MKG3 to MKG11, but decreased from MKG11 to MKG15. The 28 day-curing samples also showed an increasing trend of Young's Moduli. The influence of MKG concentrations on the stiffness of MKG stabilized soils needs to be further studied.

7.3.4. Shrinkage Behavior of MKG Stabilized Soil Samples

The volumetric change of stabilized samples during curing was quantified with volumetric strain, which was calculated by dividing the original volume by the volume difference

between the as-prepared sample and the sample before UCS testing. The volumetric strains of all the soil samples are shown in **Figure 7-9**. The shrinkage of the samples is expressed with a negative volumetric strain while the expansion with a positive number. Both after 7 days and 28 days curing, the MKG stabilized soil samples shrunk much less than MKG0. The shrinkage may be reduced by the low shrinkage potential of metakaolin based geopolymer [9, 315]. As reported in the previous literature, slight expansion occurred with MK-based geopolymer during curing under proper curing conditions [118]. The MKG stabilized soils were sealed for 2 days immediately after the demolding in this study, so the geopolymer might have expanded slightly offsetting the shrinkage of the soil. In general, the higher the MKG dosage, the less shrinkage strain was developed in the stabilized soil samples.

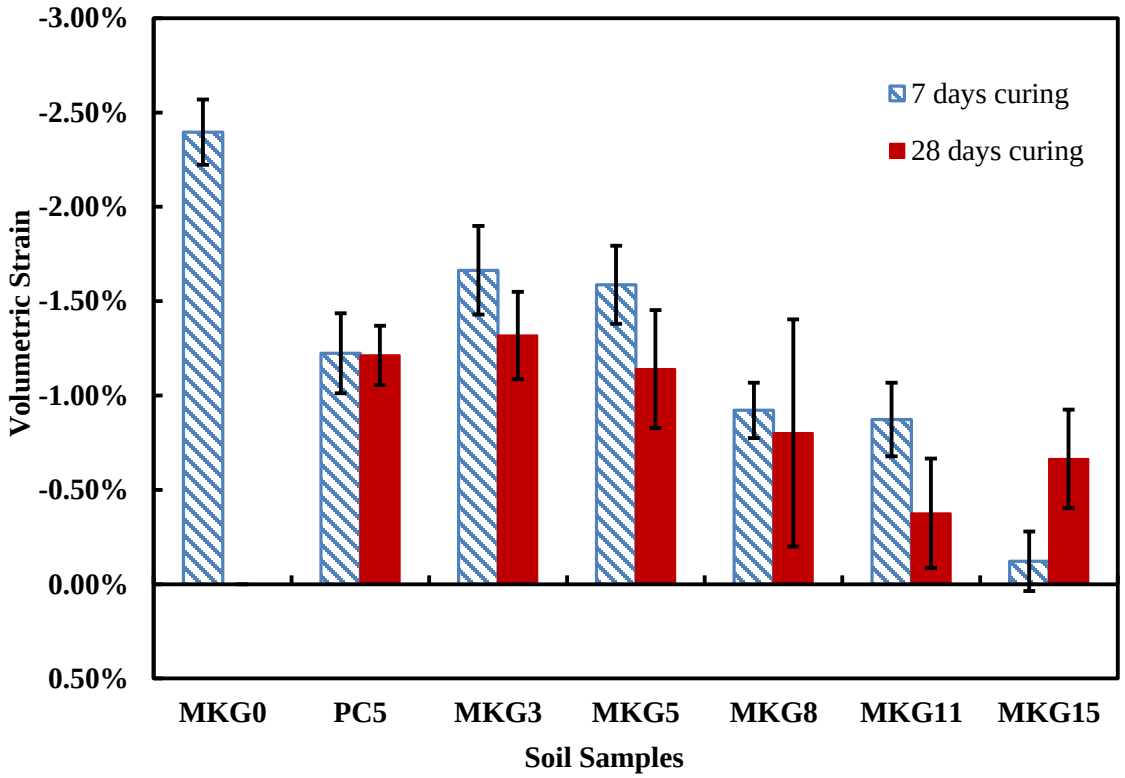

Figure 7-9. The volumetric strain of MKG stabilized soil samples during the curing of 7 days and 28 days (the unstabilized soil samples were cured for 7 days, since there is no volumetric change after 7 days).

The shrinkage strains of MKG stabilized samples versus curing period are shown in **Figure 7-10**. Because the samples were unwrapped from the plastic film after curing for 2 days, there was a large amount of water evaporated from the 2nd to the 3rd day, which explains the shrinkage jump in **Figure 7-10**. The trend of the volumetric change of the stabilized soil samples with different MKG dosages varies to some degree. For MKG 3, the sample expanded consistently after the 3rd day, and then kept nearly constant. MKG5 and MKG8 expanded on the 4th day, shrank back for the rest of the curing period, and then kept steady from the 7th to 28th day. For MKG11and 15, the samples continued to shrink from the 3rd

to the 7th day, and then expanded slightly. The soil stabilized with geopolymer, especially at a high concentration, formed a more compact structure with smaller and more distributed pores. The compact microstructure made it more difficult for the pore water to evaporate from the soil, which may be another explanation for lower shrinkage strains in the soil samples stabilized with higher MKG concentrations. This can be illustrated with the remaining moisture content of the broken soil samples after 28 days curing, shown in **Figure 7-11**: The more MKG was added in the soil, the higher was the remaining moisture content. The more compact microstructure of the MKG stabilized soil was indicated from the SEM images that are presented in the next section.

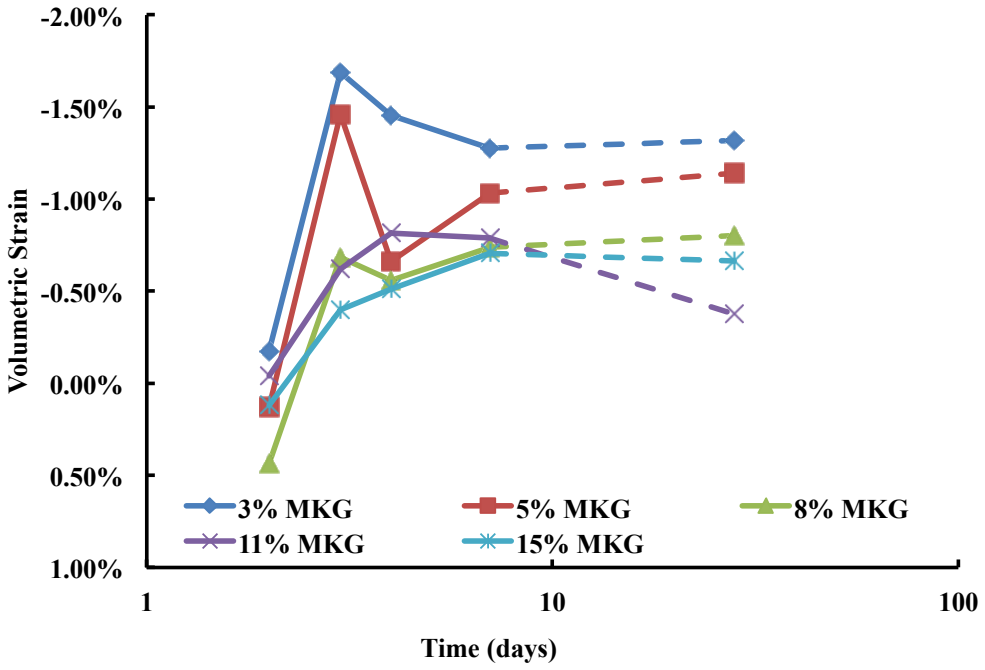

Figure 7-10. The shrinkage strains of MKG stabilized soils along with the curing period.

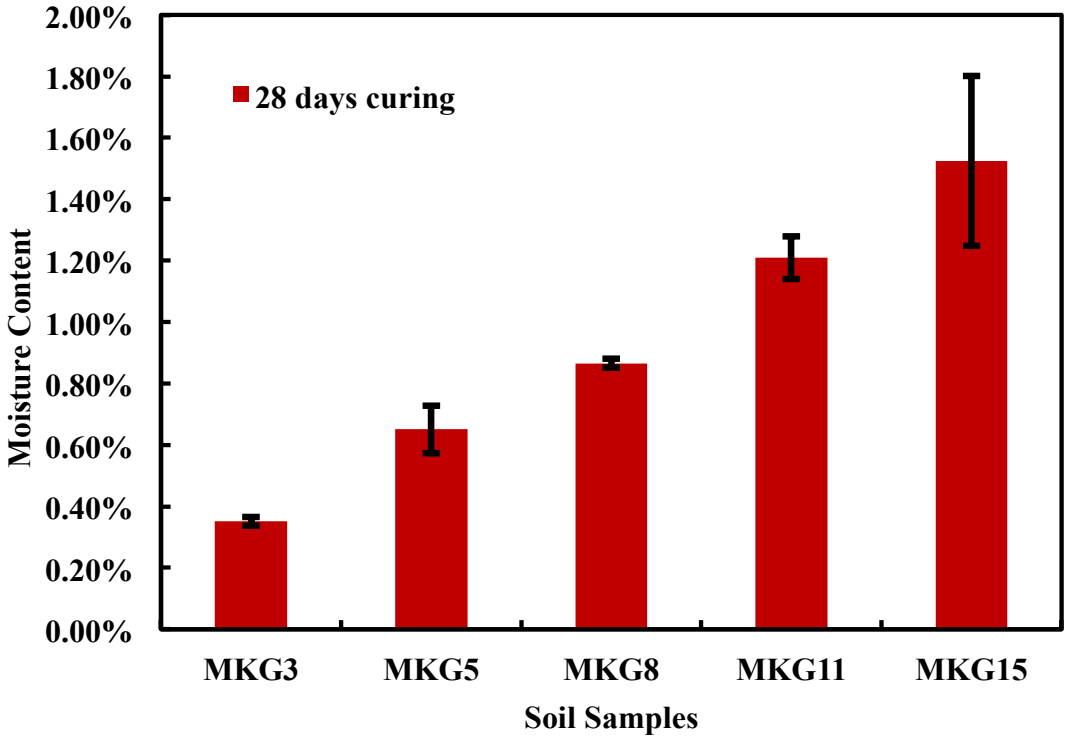

Figure 7-11. The remaining moisture content of MKG stabilized soils after the curing of 28 days.

7.3.5. SEM-EDX Characterization of MKG Stabilized Soil Samples

The micromorphology of the fractured surface of 28 day-cured soil samples is shown in **Figure 7-12**. The homogeneity of the microstructure clearly improves as the dosage of the MKG increases from 0 to 15%, explaining why the UCS, ε_f and E of the 28 day cured-samples increased with MKG concentration. As seen in **Figure 7-12** (a) and (b), although the microstructure of MKG3 is still rough, the discrete particles of MKG3 were bonded significantly more closely than MKG0 and the gaps among the particles were more thoroughly filled. Nevertheless, geopolymer gels at low concentration are not adequate on the binding of soil particles. This microstructural observation agreed well with the mechanical property variation that the increases of UCS, ε_f and E from MKG0 to MKG3

were limited. The microstructures of MKG3 and MKG 5 (**Figure 7-12** (b) and (c)) are not distinguishable, which can explain that their mechanical properties were similar, as previously shown in **Figure 7-8**. The same explanation can be applied to MKG 8 and MKG 11, whose images are not distinguishable either. The microstructure of MKG15 is significantly different from that of MKG0 and more similar to metakaolin based geopolymer. This is not unexpected because the soil stabilized with 15% MKG showed much higher UCS, ε_f and E, and much lower shrinkage strain, as shown in **Figure 7-8** and **Figure 7-9**, respectively. The higher degree of binding and more compact microstructure are believed to result in: (i) higher strength, ductility and stiffness of the stabilized soil; and (ii) lower shrinkage strains by effectively decelerating the evaporation of pore water from the soil.

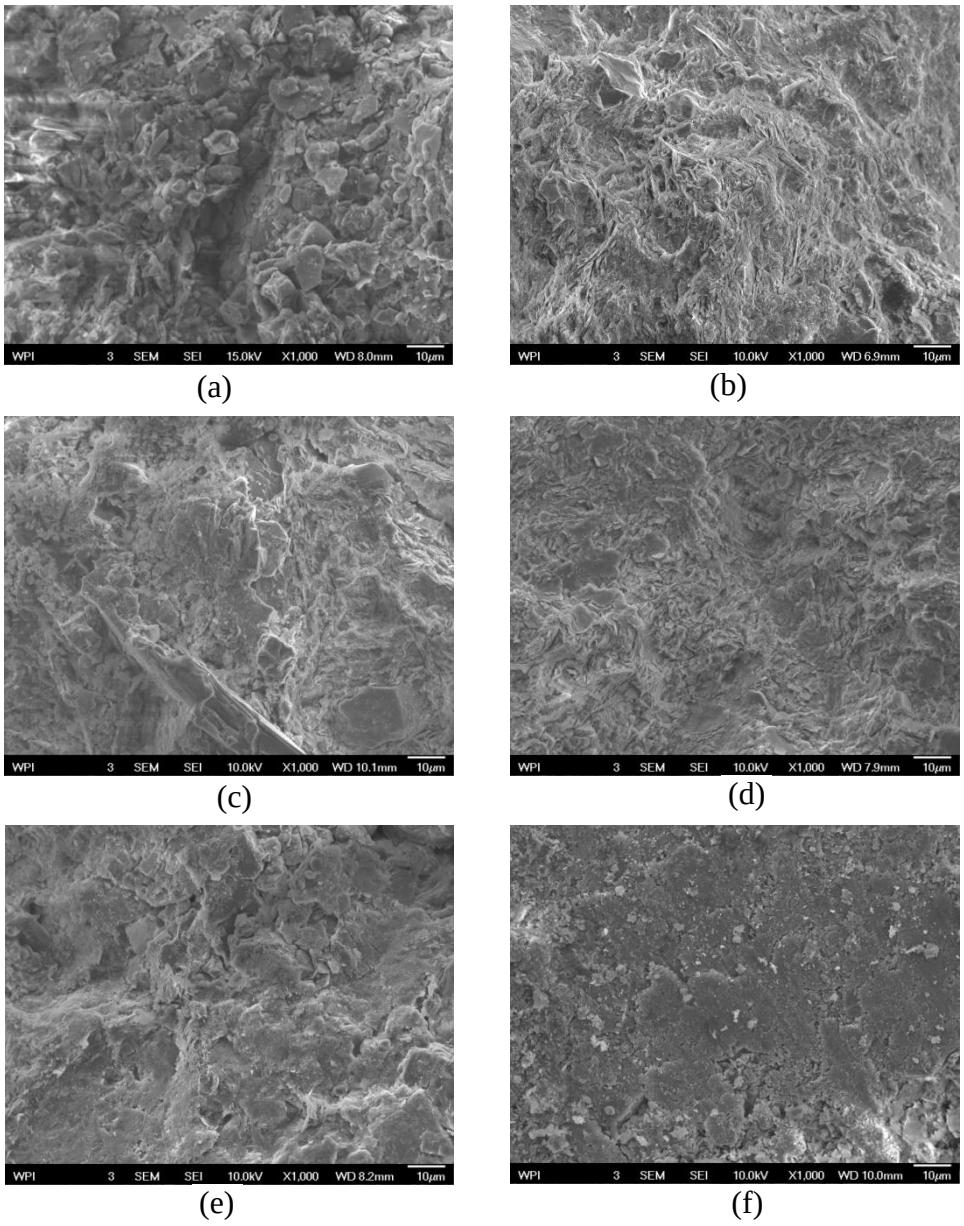

Figure 7-12. The SEM images of (a) MKG0, (b) MKG3, (c) MKG5, (d) MKG8, (e) MKG11, and (f) MKG15 after 28 day curing.

The EDX spectra of the selected areas within MKG8, MKG11, and MKG15 SEM samples after 28 days curing are shown in **Figure 7-13**. The spectra and the inserted tables provided

the average chemical composition of the detected elements contained in the circled location over the measurements of 10 points. The EDX results are used to provide a qualitative evidence for the formation of geopolymer gels in soil, rather than a quantitative indication. The estimated elemental composition of the MKG5, MKG8, and MKG11 shown in **Figure 7-13** are listed in **Table 7-6** as Si/Al and Na/Al molar ratios.

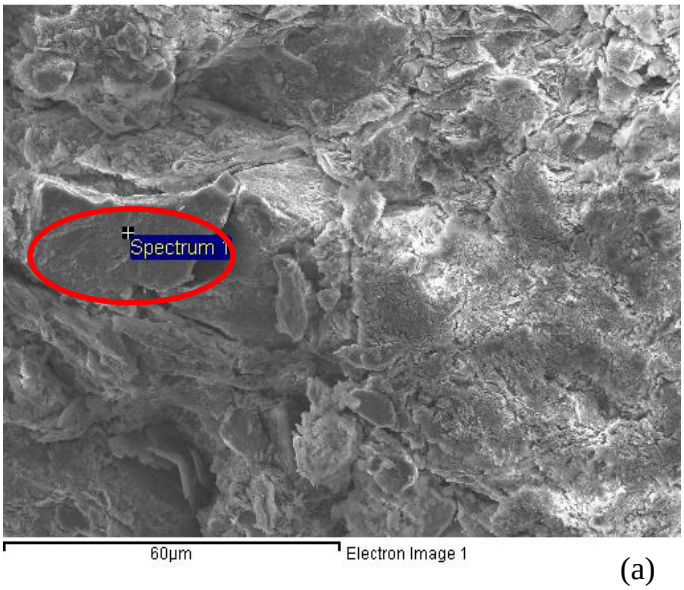

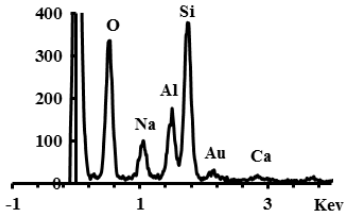

Element	Weight%	Atomic%
O K	42.81	59.19
Na K	5.43	5.22
Al K	12.18	9.99
Si K	30.04	23.66
Ca K	1.95	1.08
Au M	7.59	0.85
Totals	100.00	

(a)

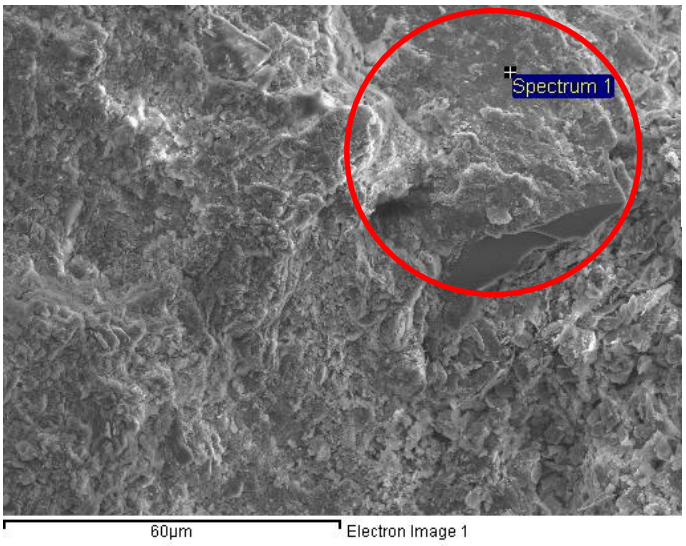

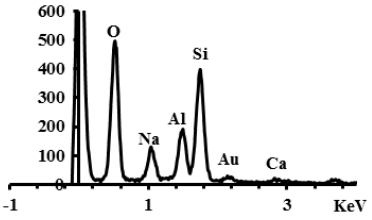

Element	Weight%	Atomic%
O K	52.62	67.21
Na K	6.37	5.66
Al K	9.57	7.25
Si K	25.03	18.21
Ca K	2.48	1.26
Au M	3.94	0.41
Totals	100.00	

(b)

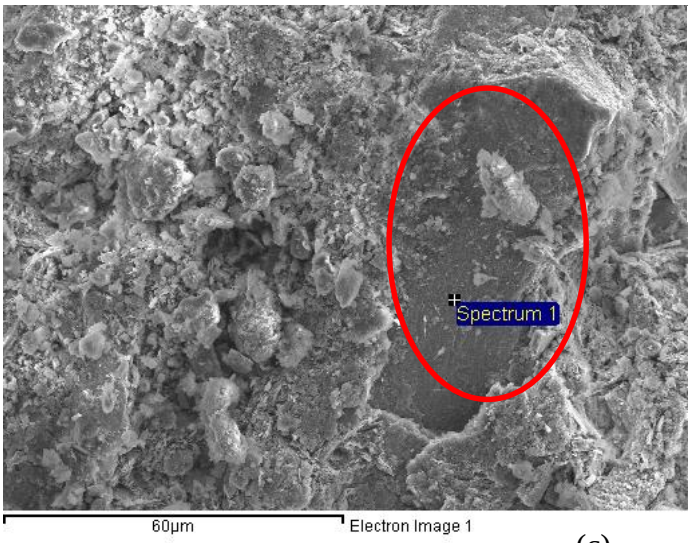

Element	Weight%	Atomic%
O K	46.40	65.66
Na K	5.03	4.96
Al K	9.25	7.76
Si K	22.37	18.03
Ca K	2.63	1.48
Pd L	4.72	1.00
Au M	9.61	1.10
Totals	100.00	

(c)

Figure 7-13. The EDX spectra of the selected samples of (a) MKG5, (b) MKG8, and (c) MKG11 after 28 day curing.

Table 7-6. Si/Al and Na/Al molar ratios of the selected portions of MKG5, MKG8 and MKG11 tested with EDX.

EDX sample	Si/Al (Molar Ratio)	Na/Al (Molar Ratio)
MKG5	2.36	0.51
MKG8	2.15	0.54
MKG11	2.26	0.43

The Na element was only detected in these samples stabilized with geopolymer, but not in the MKG0 sample. Noticeably shown in **Figure 7-13**, the Na percentages are obtained in the circled areas in the SEM images, which represent the likely geopolymer gels in soil. For geopolymer gel, Na percentage should fall within a relatively narrow value range, so its value in different stabilized samples are similar and not affected by geopolymer concentration in soil. Additionally, Si/Al ratios are in the range of 2~3, very close to the

pure MKG gel [13]. Although Si and Al can come from both the soil and geopolymer gel, the ratios can still be qualitative indicators illustrating that geopolymer gels were formed in the stabilized soil samples. The reaction of MKG was very quick because of high amorphous content and very high Blaine fineness of metakaolin, so the detected Na most likely belongs to Na element in the geopolymer rather than that in the activator, which has been consumed in the reaction [325]. Note that Na/Al ratios (~0.5) from the EDX estimation are much lower than 1, the typical value of geopolymers reported in the literature [115]. These Na/Al ratios were probably underestimated, because the soil itself contained Al but no Na. Therefore, the detected Al could include the element both existing in the geopolymer and the soil residue adhering to the geopolymer.

7.3.6. XRD Characterization of MKG Stabilized Soil Samples

The XRD patterns of MKG stabilized and unstabilized soils are shown in **Figure 7-14**. There is no significant change in the patterns of stabilized samples, except that the intensity of the peaks associated with kaolinite and quartz between 18° and 37 °2θ decreased. This is due to masking effect by the broad hump in this range associated with the amorphous MKG gel. The lack of change in the XRD patterns of the stabilized soil demonstrates that no new minerals were formed with the introduction of the MKG precursor to the soil (i.e., there was no direct chemical reaction between the geopolymer precursor and soil minerals). Therefore, the enhancement of mechanical properties is largely due to binding effects of geopolymer gels.

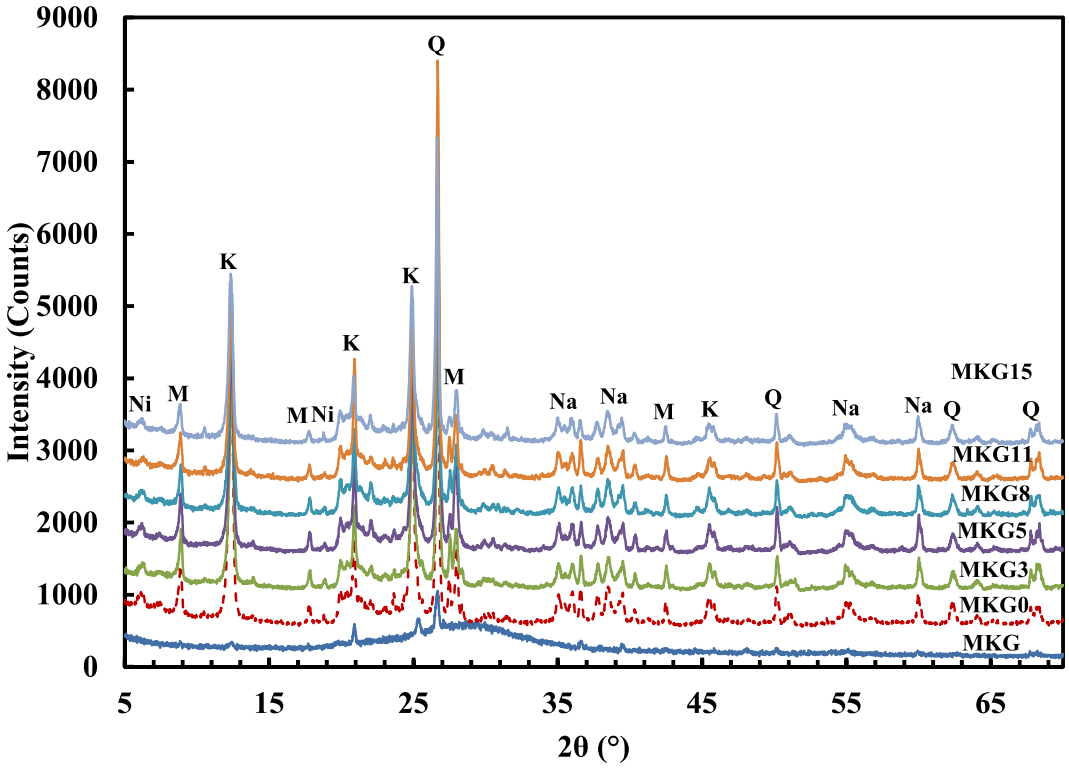

Figure 7-14. The XRD patterns of metakaolin based geopolymer, unstabilized soil and soil stabilized with MKG at different concentrations (Ni: Nimite, M: Muscovite; K: Kaolinite; Q: Quartz: and Na: Nacrite).

7.4. CONCLUSIONS

In this study, the feasibility of using metakaolin based geopolymer as a soil stabilizer at shallow depth was confirmed. SEM-EDX and XRD results showed that MKG gels effectively developed in the soil, which assist the soil particles to form more compact micro-structures and improve its mechanical properties and volume stability.

The UCS values of MKG stabilized soils are much higher than the soil, and higher than 5% PC stabilized soil when MKG concentration is higher than 11%. However, the strength increase from 7-day curing to 28-day curing is not appreciable, which might be due to

quick reactions of MK-based geopolymer precursor. The long-term performance of MKG stabilized soil in terms of UCS needs further investigated. The compressive strength of MKG stabilized soils increased with the concentration of MKG. As indicated by more compact microstructures of the soil samples stabilized with MKG higher than 8%, the stabilization mechanism is largely attributed to the binding effect of metakaolin based geopolymer gel.

The soil samples stabilized with MKG became less brittle than the unstabilized counterpart, which is beneficial for the performance of flexible pavement. In addition, higher Young's modulus can be achieved in the stabilized soil after 28-day curing. The mechanical properties of geopolymer are affected by various factors, including the properties of source materials (types, particle size distributions, and amorphous content), curing conditions (temperature, humidity, pressure, and curing time), water content and chemical composition of the precursor (Si/Al and Na/Al ratios) [206, 255, 315, 326-328]. Therefore, by adjusting the above parameters during geopolymer synthesis, it is possible to stabilize soil with geopolymers to achieve both high compressive strength and high stiffness.

The shrinkage strains of MKG stabilized soil were much lower than those of the unstabilized soil and 5% PC stabilized soil when the concentration of MKG is higher than 8%. Reduced shrinkage strain in chemically stabilized pavement sublayers is desirable for reducing shrinkage induced cracks in pavements. The shrinkage generally decreased as MKG concentration increased. This may be due to the low shrinkage potential of metakaolin based geopolymer gels, and the slower evaporation of pore water in the

stabilized soil with more compact microstructure when stabilized with higher concentration of MKG.

With the aid of the SEM-EDX, the formation of geopolymer gels in the soil was qualitatively confirmed. Since there was no new mineral formed after the stabilization in the XRD patterns, the improvement in mechanical properties of the stabilized soil was most likely provided by the binding effect of the geopolymer gels.

The exploration of geopolymer as the next-generation soil stabilizer has significant implications for civil engineering practices. Geopolymer stabilized soils need less time in the development of high early strength than OPC. The more ductile property of geopolymer stabilized soils can effectively mitigate cracking during the pavement construction, curing and operation. Additionally, the lower shrinkage than OPC can reduce the damage caused by the shrinkage cracking of the soils. Although it seems a higher dosage is required (e.g., 5% OPC vs. 10-15% MKG) for stabilizing soils, the cost issue can be addressed if industrial wastes or byproducts are used to synthesis geopolymer instead of metakaolin.

CHAPTER 8 - CONCLUSIONS AND RECOMMENDATIONS

Geopolymers, as the next generation sustainable construction materials, have been systematically investigated on their synthesis, mechanical properties, microstructures, molecular structure, durability, environmental impact and engineering applications in this Ph.D. study. A multi-scale experimental and computional study was carried out to better understand the relationship of chemical composition-reaction kinetics-microstructures-mechanical properties of geopolymers such that mechanical properties of geopolymers can be optimized. Two types of geopolymers: red mud-class F fly ash based geopolymers (RFFG) and metakaolin based geopolymers (MKG) were synthesized and characterized. For RFFG, the experimental work was firstly focused on assessing the influence of synthesis factors (e.g., nominal Si/Al and Na/Al molar ratios of the starting materials and fly ash sources) and curing conditions (e.g., temperature, humidity and time) on microstructure and mechanical properties of RFFG. Subsequently, the RFFG samples cured at different temperatures were characterized with Fourier transform infrared spectroscopy (FTIR), X-ray diffractometer (XRD), isothermal conduction calorimeter (ICC), Micro-CT and N_2-BJH along the curing time up to 120 days to examine the correlation of their reaction kinetics-microstructure-porosity-mechanical properties. For MKG, the geopolymer samples synthesized with different nominal Si/Al and Na/Al molar ratios were tested with unconfined compression tests and grid-nanoindentation for macro- and nano-mechanical properties. Their final setting time and change in chemical bonding were also determined with Vicat needle tests and FTIR, respectively, to understand the reaction rate and development of geopolymer gels. The relation between the development

of geopolymer gels and mechanical properties of geopolymers and its dependence on the chemical compositions were addressed. Density functional theory (DFT) simulation and reactive molecular dynamic (MD) modeling were applied to simulate the polymerization process from silicate and aluminate monomers at different Si/Al ratios to geopolymer gels at different temperatures. The influence of Si/Al ratio and temperature on the final geopolymeric structure, polymerization mechanisms and the degree of condensation was therefore examined. In addition, this Ph.D. study also shed light on the durability, environmental impact and potential applications of geopolymers. The resistance of RFFG to sulfuric acid was evaluated by soaking the RFFG samples in the sulfuric acid and measuring the residual mechanical properties, including unconfined compressive strength (UCS), failure strength (ε_f), Young's modulus (E) and flexural strength. The concentrations of heavy metals leached from RFFG by sulfuric acid were measured to study the leaching behavior of the heavy metals in RFFG. Lastly, the applications of geopolymers in geotechnical engineering were explored by using MKG to stabilize a lean clay. The stabilization effectiveness and mechanisms were investigated by testing the mechanical properties and the change in the microstructures of stabilized soils with scanning electron microscopy-energy dispersive X-ray spectroscopy (SEM-EDX) and XRD.

This Ph.D. work started with the synthesis of geopolymers with two abundant industrial wastes, red mud and class F fly ash. The RFFG with high mechanical strength was synthesized at room temperature around 23 ℃ and under a relative humidity (RH) at 40% ~ 50%. This study found that the pre-curing at 100% RH had little effect on the mechanical properties. In addition, the mechanical properties (e.g., UCS, ε_f and E) of RFFG increased along the curing under ambient conditions for 180 days. A nominal chemical composition

at Si/Al molar ratio of 2.0 and Na/Al molar ratio of 0.6 ~ 0.8 was recommended to synthesize RFFG with good mechanical properties. The reaction kinetics and its correlation to the mechanical properties of geopolymers were investigated for RFFG. The geopolymerization started with the dissolution of the raw materials, and the released aluminate and silicate monomers gradually developed into Al-rich gels, Si-rich gels and more cross-linked aluminosilicate gels. The mechanical strength of geopolymers is primarily governed by the development of geopolymer gels but also affected by other factors, such as pore volume, pore size, and partly developed geopolymer gels. During the reaction, the formation of Si-rich gels was slower than the Al-rich gels, but led to a higher mechanical strength for RFFG, as indicated by the shift of the main FTIR band (i.e., Si-O-T) during the course of syntheis. The Si-O-T band shifted to a lower wavenumber (from 1031.0 cm^{-1} to a wavenumber lower than 1000 cm^{-1}) at Stage I while raw materials were dissolved and Al-rich gels started to form. Subsequently, the Si-O-T band shifted to a higher wavenumber at Stage II while Al-rich gels kept growing and Si-rich gels started to form. In the third stage, the Si-O-T band shifted back to a relatively higher wavenumber and Si-rich gels gradually converted to more cross-linked networks. The mechanical strength of RFFG barely developed in the first stage, increased within a low range in the second stage and highly increased in Stage III. A high curing temperature was found to enhance the development of geopolymer gels, and thus the mechanical properties of RFFG at the early stage. Nonetheless, an excessively high temperature resulted in a high pore volume, which is detrimental for the long-term mechanical strength of RFFG. Subsequently from the perspective of practical applications, the resistance and leaching behavior of heavy metals in sulfuric acid of RFFG were examined. The resistance of RFFG

to sulfuric acid after soaking in pH 3.0 sulfuric acid for up to 120 days was comparable to that of ordinary Portland cement. With the FTIR characterization, the Si-O-T band shifted to a higher wavenumber (from 972 cm^{-1} to 987~993cm^{-1}) after one-day soaking in sulfuric acid and deionized water, but did not further shift after the longer term soaking. The XRD hump of geopolymer gels shifted from 17~38 ° 2θ to 15~32 ° 2θ after one-day soaking, regardless of the solutions, and further narrowed to 15°~30° 2θ after 56 days' soaking in the sulfuric acid. These implied that the depolymerization and dealumination were the main deterioration mechanisms for the soaked RFFG samples. Furthermore, the concentration of heavy metals, including Cu, As, Cr and Cd, leached from the soaked RFFG samples in sulfuric acid, even in their powder form with a size less than 45 μm was much lower than the respective US EPA standards for soil contamination. Therefore, the applications of RFFG in sulfuric acid environments will not introduce excessive heavy metals to the surrounding soils.

The second part of this Ph.D work focused on the nano-scale mechanical properties and molecular structure characterization of geopolymer gels by nano-scale experimental testing and computational modeling, respectively. With grid-nanoindentation measurements, four phases were identified in the MKG samples based on the statistical devonvolution of the nanoindentation results (i.e., Young's modulus, E_n, and hardness, H): porous phases (E_n < 2 GPa and H < 0.1 GPa), partly developed geopolymer gels (2 GPa ≤ E_n < 5.5 GPa and 0.1 GPa ≤ H < 0.35 GPa), geopolymer gels (5.5 GPa ≤ E_n <25 GPa and 0.35 GPa ≤ H < 1.5 GPa) and unreacted metakaolin or crystals (E_n ≥ 25 GPa and H ≥1.5 GPa). The proportion of geopolymer gels was found to be the most important

governing factor for the mechanical strength of the resulting geopolymers. The partly developed geopolymer gels, which can further developed into geopolymer gels, also improved the mechanical strength of the MKG. A high Si/Al ratio in the range of 1.6 to 1.8 enhanced development of geopolymer gels and long-term mechanical properties of MKG. This is due to the formation of a larger number of Si-O-Si bonds, despite a slower reaction rate. On the other hand, a high Na/Al ratio accelerated the dissolution process, and thus the early reaction rate, development of geopolymer gels and mechanical properties at the early stage. These observations were verified by the fact that Si-O-T (T: Si or Al) FTIR band kept shifting to higher wavenumbers with the increase of Si/Al ratio and decrease of Na/Al ratio, while Si-O-Si bands appear at a higher wavenumber than Si-O-Al bands. Si-rich gels contribute more to the development of mechanical strength of geopolymers than Al-rich gels. Subsequently, the molecular structure of geopolymer gels and geopolymerization were investigated using the combined density function theory and reactive molecular dynamics simulations. The simulation results indicate that the geopolymer gels were gradually formed from the dispersed aluminate and silicate monomers along three stages: oligomerization, ring formation and condensation. The division of these three stages was based on the reaction nature of polymerization process of geopolymer synthesis. The amorphous nature of the simulated geopolymeric structure was verified by the radial distribution function (RDF) of Si-O, Al-O, O-O and Al-Na, which did not show periodically repeating peaks. In addition, the RDF of the above mentioned atom pairs agreed well with the X-ray/neutron pair distribution function results of geopolymers from previous literature. The simulation results were further verified by comparing the distribution of the $Si_4(mAl)$ (i.e., the 4-coordinated Si connected to m Al) of the MD

geopolymer gels with that in the synthesized geopolymers measured by solid state 29Si nuclear magnetic resonance (NMR) in the literature. The Si_4(1Al) and Si_4(2Al) were found to be the most dominant in both the simulated and experimental geopolymer gels. The MD simulation results also demonstrated that the temperature and Si/Al ratio have important but intertwining effects on the polymerization. A higher temperature enhanced the reaction rate while a higher Si/Al ratio resulted in a more compact geopolymer gel framework that had a higher bulk density and a higher proportion of Si_4(mAl).

The applications of geopolymer in shallow soil stabilization were explored for the first time in the last part of this Ph.D. study. The mechanical properties of the clayey soils were largely improved after the stabilization with MKG. The degree of soil stabilization by metakaolin-based geopolymers at a concentration higher than 11 wt.% was comparable to or even better than ordinary Portland cement. The SEM images and EDX spectra of the stabilized soil samples indicate that the binding effect of geopolymer gels dispersed within the soil matrix was the main reason for the improvement of mechanical properties of the stabilized soils.

Since industrial wastes are more favorable for synthesizing geopolymers from an economic point of view, the grid-nanoindentation technique can be applied on the RFFGs to further assess its nano-mechanical properties and formation of geopolymer gels for optimizing the RFFG synthesis. The final properties of RFFGs were significantly affected by the properties of fly ash, such as the amorphous aluminate and silicate content and particle size. Therefore, more fly ash sources should be used in the RFFG synthesis to obtain a consistent chemical composition of raw materials to achieve good mechanical

properties and durability based on the relationship of chemical composition-reaction kinetics-mechanical properties obtained in this dissertation. The resistance of RFFG and the derived concrete to other aggressive environments, such as freeze-thaw cycles, salt scaling, alkali silicon reactions and other acids (e.g., HCl and HNO_3) at different concentrations, needs to be further studied to explore other potential applications of RFFG.

The geopolymer gels 'synthesized' from reactive MD simulations can be used to derive the mechanical and other properties of geopolymer gels, such as stiffness and permeability, which remain poorly understood. Corrosive ions, such as Cl-, SO_4^{2-} and H^+, can be introduced to the geopolymer gels in MD simulations, of which the diffusive behavior can be determined, and thus the deterioration mechanisms of geopolymer gels in these corrosive environments can be evaluated. Based on the predictions with the MD simulations, mechanical properties and durability of geopolymer gels can be further improved with the relationship between the chemistry, molecular structure and macro-properties of geopolymer gels.

The feasibility of using the geopolymers synthesized from industrial wastes, such as RFFG, to stabilize different weak and soft soils needs to be verified. In addition, the synthesis procedure, chemical composition and concentration of the geopolymers can be further adjusted to improve the stabilization effectiveness on the soils.

REFERENCES

1. *US Geological Survey*, in *Cement statistics 2006*. 2006.
2. Development, W.B.C.f.S. and I.E. Agency, *Cement Technology Roadmap 2009, Carbon emissions reductions up to 2050*. 2009.
3. Ltd, O.S.C., *Press release announcement, Global cement to 2020*. 2006, Ocean Shipping Consultants Ltd, Surrey, UK.
4. Hoagland-Grey, H., *Environmental Impact Assessments for Cement Plants*. 2011, Inter-American Development Bank.
5. Habert, G., J.B. d'Espinose de Lacaillerie, and N. Roussel, *An environmental evaluation of geopolymer based concrete production: reviewing current research trends.* Journal of Cleaner Production, 2011. **19**(11): p. 1229-1238.
6. Van den Heede, P. and N. De Belie, *Environmental impact and life cycle assessment (LCA) of traditional and 'green' concretes: Literature review and theoretical calculations.* Cement and Concrete Composites, 2012. **34**(4): p. 431-442.
7. Chen, C., et al., *Environmental impact of cement production: detail of the different processes and cement plant variability evaluation.* Journal of Cleaner Production, 2010. **18**(5): p. 478-485.
8. McLellan, B.C., et al., *Costs and carbon emissions for geopolymer pastes in comparison to ordinary portland cement.* Journal of Cleaner Production, 2011. **19**(9-10): p. 1080-1090.
9. Provis, J.L. and J.S.J. Van Deventer, *Geopolymers: structures, processing, properties and industrial applications*. 2009: Elsevier.
10. Duxson, P., et al., *The role of inorganic polymer technology in the development of 'green concrete'.* Cement and Concrete Research, 2007. **37**(12): p. 1590-1597.
11. Provis, J., *Introduction and Scope*, in *Alkali Activated Materials*, J.L. Provis and J.S.J. van Deventer, Editors. 2014, Springer Netherlands. p. 1-9.
12. Davidovits, J., *Geopolymer Chemistry and Applications*. 2008: Geopolymer Institute.
13. Davidovits, J. *Properties of geopolymer cements*. in *First International Conference on Alkaline Cements and Concretes*. 1994.
14. Chindaprasirt, P., et al., *High-Strength Geopolymer Using Fine High-Calcium Fly Ash.* Journal of Materials in Civil Engineering, 2011. **23**(3): p. 264-270.
15. Puertas, F., et al., *Alkali-activated fly ash/slag cements: Strength behaviour and hydration products.* Cement and Concrete Research, 2000. **30**(10): p. 1625-1632.
16. Davidovits, J. and J.L. Sawyer, *Early high-strength mineral polymer*. 1985, Google Patents.
17. Sumajouw, D.M.J., et al., *Fly ash-based geopolymer concrete: study of slender reinforced columns.* Journal of Materials Science, 2007. **42**(9): p. 3124-3130.
18. Pacheco-Torgal, F., J.P. Castro-Gomes, and S. Jalali, *Adhesion characterization of tungsten mine waste geopolymeric binder. Influence of OPC concrete substrate surface treatment.* Construction and Building Materials, 2008. **22**(3): p. 154-161.
19. Davidovits, J., *Mineral polymers and methods of making them*. 1982, Google Patents.
20. Temuujin, J., et al., *Preparation of metakaolin based geopolymer coatings on metal substrates as thermal barriers.* Applied Clay Science, 2009. **46**(3): p. 265-270.

21. Medri, V., et al., *SiC-based refractory paints prepared with alkali aluminosilicate binders.* Journal of the European Ceramic Society, 2011. **31**(12): p. 2155-2165.
22. Temuujin, J., et al., *Preparation and thermal properties of fire resistant metakaolin-based geopolymer-type coatings.* Journal of Non-Crystalline Solids, 2011. **357**(5): p. 1399-1404.
23. Bakharev, T., *Resistance of geopolymer materials to acid attack.* Cement and Concrete Research, 2005. **35**(4): p. 658-670.
24. Temuujin, J., et al., *Characterisation of class F fly ash geopolymer pastes immersed in acid and alkaline solutions.* Cement and Concrete Composites, 2011. **33**(10): p. 1086-1091.
25. Thokchom, S., P. Ghosh, and S. Ghosh, *Durability of Fly Ash Geopolymer Mortars in Nitric Acid–effect of Alkali (Na2o) Content.* Journal of Civil Engineering and Management, 2011. **17**(3): p. 393-399.
26. Sata, V., A. Sathonsaowaphak, and P. Chindaprasirt, *Resistance of lignite bottom ash geopolymer mortar to sulfate and sulfuric acid attack.* Cement and Concrete Composites, 2012. **34**(5): p. 700-708.
27. Reddy, D., et al. *Experimental Evaluation of the Durability of Fly Ash-based geopolymer Concrete in the Marine Environment*. in *9th Latin American & Caribbean Conference*. 2011.
28. Lee, W.K.W. and J.S.J. van Deventer, *The effect of ionic contaminants on the early-age properties of alkali-activated fly ash-based cements.* Cement and Concrete Research, 2002. **32**(4): p. 577-584.
29. Fernando, P.-T. and J. Said, *Resistance to acid attack, abrasion and leaching behavior of alkali-activated mine waste binders.* Materials and Structures, 2011. **44**(2): p. 487-498.
30. Yunsheng, Z., et al., *Synthesis and heavy metal immobilization behaviors of slag based geopolymer.* Journal of Hazardous Materials, 2007. **143**(1): p. 206-213.
31. Duxson, P., et al., *Understanding the relationship between geopolymer composition, microstructure and mechanical properties.* Colloids and Surfaces a-Physicochemical and Engineering Aspects, 2005. **269**(1-3): p. 47-58.
32. ŠKVÁRA, F., et al., *MICROSTRUCTURE OF GEOPOLYMER MATERIALS BASED FLY ASH.* Ceramics-Silikáty, 2006. **50**(4): p. 208-215.
33. Hardjito, D. and B.V. Rangan, *Development and properties of low-calcium fly ash-based geopolymer concrete.* Perth, Australia: Curtin University of Technology, 2005.
34. Gourley, J.T. and G.B. Johnson. *Developments in Geopolymer Precast Concrete*. in *International Workshop on Geopolymers and Geopolymer Concrete*. 2005. Perth, Australia.
35. Malone, P.G., C.A. Randall Jr, and T. Kirkpatrick, *Potential applications of alkali-activated alumino-silicate binders in military operations*. 1985, DTIC Document.
36. Palomo, A., et al., *Railway sleepers made of alkali activated fly ash concrete.* Revista Ingeniería, 2007. **22**(2): p. 75-80.
37. Davidovits, J. *30 years of successes and failures in geopolymer applications. Market trends and potential breakthroughs*. in *Keynote Conference on Geopolymer Conference*. 2002.

38. Cristelo, N., S. Glendinning, and A.T. Pinto, *Deep soft soil improvement by alkaline activation.* Proceedings of the ICE-Ground Improvement, 2011. **164**(2): p. 73-82.
39. Cristelo, N., et al., *Effect of calcium content on soil stabilisation with alkaline activation.* Construction and Building Materials, 2012. **29**: p. 167-174.
40. Zoulgami, M., et al., *Synthesis and physico-chemical characterization of a polysialate-hydroxyapatite composite for potential biomedical application.* The European Physical Journal - Applied Physics, 2002. **19**(03): p. 173-179.
41. Derrien, A.C., et al., *Thermal behaviour of composites aluminosilicate-calcium phosphates.* Journal of Thermal Analysis and Calorimetry, 2004. **75**(3): p. 937-946.
42.He, J., et al., *Geopolymer-Based Smart Adhesives for Infrastructure Health Monitoring: Concept and Feasibility.* Journal of Materials in Civil Engineering, 2011. **23**(2): p. 100-109.
43. Zhang, Z., et al., *Geopolymer foam concrete: An emerging material for sustainable construction.* Construction and Building Materials, 2014. **56**: p. 113-127.
44. Strozi Cilla, M., P. Colombo, and M. Raymundo Morelli, *Geopolymer foams by gelcasting.* Ceramics International, 2014. **40**(4): p. 5723-5730.
45. Sakulich, A.R., S. Miller, and M.W. Barsoum, *Chemical and Microstructural Characterization of 20-Month-Old Alkali-Activated Slag Cements.* Journal of the American Ceramic Society, 2010.
46. Pan, Z., et al., *Properties and microstructure of the hardened alkali-activated red mud–slag cementitious material.* Cement and Concrete Research, 2003. **33**(9): p. 1437-1441.
47. Andini, S., et al., *Coal fly ash as raw material for the manufacture of geopolymer-based products.* Waste Management, 2008. **28**(2): p. 416-423.
48. Wang, S. and L. Baxter, *Comprehensive study of biomass fly ash in concrete: Strength, microscopy, kinetics and durability.* Fuel Processing Technology, 2007. **88**(11-12): p. 1165-1170.
49. de Vargas, A.S., et al., *The effects of Na2O/SiO2molar ratio, curing temperature and age on compressive strength, morphology and microstructure of alkali-activated fly ash-based geopolymers.* Cement and Concrete Composites, 2011. **33**(6): p. 653-660.
50. Škvára, F., T. Jílek, and L. Kopecký, *Geopolymer materials based on fly ash.* Ceram.-Silik, 2005. **49**(3): p. 195-204.
51. Duxson, P., et al., *The effect of alkali and Si/Al ratio on the development of mechanical properties of metakaolin-based geopolymers.* Colloids and Surfaces A: Physicochemical and Engineering Aspects, 2007. **292**(1): p. 8-20.
52. Rovnan ĭk, P., *Effect of curing temperature on the development of hard structure of metakaolin-based geopolymer.* Construction and Building Materials, 2010. **24**(7): p. 1176-1183.
53. Lizcano, M., et al., *Effects of Water Content and Chemical Composition on Structural Properties of Alkaline Activated Metakaolin-Based Geopolymers.* Journal of the American Ceramic Society, 2012. **95**(7): p. 2169-2177.
54. Yao, X., et al., *Geopolymerization process of alkali–metakaolinite characterized by isothermal calorimetry.* Thermochimica Acta, 2009. **493**(1-2): p. 49-54.

55. Latella, B., et al., *Mechanical properties of metakaolin-based geopolymers with molar ratios of Si/Al ≈ 2 and Na/Al ≈ 1.* Journal of Materials Science, 2008. **43**(8): p. 2693-2699.
56. He, J., et al., *Synthesis and characterization of red mud and rice husk ash-based geopolymer composites.* Cement and Concrete Composites, 2013. **37**: p. 108-118.
57. Zhang, M., et al., *Synthesis factors affecting mechanical properties, microstructure, and chemical composition of red mud–fly ash based geopolymers.* Fuel, 2014. **134**(0): p. 315-325.
58. Andalib, R., et al., *Structural Performance of Sustainable Waste Palm Oil Fuel Ash-Fly Ash Geo-polymer Concrete Beams.* Journal of Environmental Treatment Techniques, 2014. **2**(3): p. 115-119.
59. Liu, M.Y.J., et al., *Utilization of Palm Oil Fuel Ash as Binder in Lightweight Oil Palm Shell Geopolymer Concrete.* Advances in Materials Science and Engineering, 2014. **2014**: p. 1-6.
60. Zhang, L., S. Ahmari, and J. Zhang, *Synthesis and characterization of fly ash modified mine tailings-based geopolymers.* Construction and Building Materials, 2011. **25**(9): p. 3773-3781.
61. Songpiriyakij, S., et al., *Compressive strength and degree of reaction of biomass- and fly ash-based geopolymer.* Construction and Building Materials, 2010. **24**(3): p. 236-240.
62. Brew, D.R.M. and K.J.D. MacKenzie, *Geopolymer synthesis using silica fume and sodium aluminate.* Journal of Materials Science, 2007. **42**(11): p. 3990-3993.
63. Molino, B., et al., *Recycling of Clay Sediments for Geopolymer Binder Production. A New Perspective for Reservoir Management in the Framework of Italian Legislation: The Occhito Reservoir Case Study.* Materials, 2014. **7**(8): p. 5603-5616.
64. Zhao, R. and F.L. Han, *Preparation of Geopolymer Using Electrolytic Manganese Residue.* Key Engineering Materials, 2014. **591**: p. 130-133.
65. Ridzuan, A.R.M., et al., *Alkaline Activators Concentration Effect to Strength of Waste Paper Sludge Ash-Based Geopolymer Mortar*, in *InCIEC 2013*, R. Hassan, et al., Editors. 2014, Springer Singapore. p. 169-175.
66. Jiao, X., et al., *Geopolymerisation of a silica-rich tailing.* Minerals Engineering, 2011. **24**(15): p. 1710-1712.
67. Tchakoute Kouamo, H., et al., *Synthesis of volcanic ash-based geopolymer mortars by fusion method: Effects of adding metakaolin to fused volcanic ash.* Ceramics International, 2013. **39**(2): p. 1613-1621.
68. Moon, J., et al., *Characterization of natural pozzolan-based geopolymeric binders.* Cement and Concrete Composites, 2014. **53**: p. 97-104.
69. Zivica, V., M.T. Palou, and T.I.Ľ. Bágeľ, *High strength metahalloysite based geopolymer.* Composites Part B: Engineering, 2014. **57**: p. 155-165.
70. Li, C., T. Zhang, and L. Wang, *Mechanical properties and microstructure of alkali activated Pisha sandstone geopolymer composites.* Construction and Building Materials, 2014. **68**: p. 233-239.

71. He, J., et al., *The strength and microstructure of two geopolymers derived from metakaolin and red mud-fly ash admixture: A comparative study.* Construction and Building Materials, 2012. **30**: p. 80-91.
72. Hamada, T. *Environmental management of bauxite residue - A review*. in *International Conference on Bauxite Tailings.* 1986. The Jamaica Bauxite Institute, The University of the West Indies, Kingston, Jamaica.
73. Power, G., M. Gräfe, and C. Klauber, *Bauxite residue issues: I. Current management, disposal and storage practices.* Hydrometallurgy, 2011. **108**(1-2): p. 33-45.
74. Gräfe, M., G. Power, and C. Klauber, *Bauxite residue issues: III. Alkalinity and associated chemistry.* Hydrometallurgy, 2011. **108**(1-2): p. 60-79.
75. Zhang, G., J. He, and R.P. Gambrell, *Synthesis, Characterization, and Mechanical Properties of Red Mud-Based Geopolymers.* Transportation research record, 2010. **2167**(01).
76. Hajjaji, W., et al., *Composition and technological properties of geopolymers based on metakaolin and red mud.* Materials & Design, 2013. **52**(0): p. 648-654.
77. Ye, N., et al., *Synthesis and Characterization of Geopolymer from Bayer Red Mud with Thermal Pretreatment.* Journal of the American Ceramic Society, 2014. **97**(5): p. 1652-1660.
78. Ahmaruzzaman, M., *A review on the utilization of fly ash.* Progress in Energy and Combustion Science, 2010. **36**(3): p. 327-363.
79. ASTMC618, *Standard Specification for Coal Fly Ash and Raw or Calcined Natural Pozzolan for Use in Concrete*. 2013, ASTM International.
80. Gamage, N., et al., *Overview of different types of fly ash and their use as a building and construction material.* 2013.
81. Fernández-Jiménez, A. and A. Palomo, *Characterisation of fly ashes. Potential reactivity as alkaline cements ☆.* Fuel, 2003. **82**(18): p. 2259-2265.
82. Kolias, S., V. Kasselouri-Rigopoulou, and A. Karahalios, *Stabilisation of clayey soils with high calcium fly ash and cement.* Cement and Concrete Composites, 2005. **27**(2): p. 301-313.
83. Chancey, R.T., et al., *Comprehensive phase characterization of crystalline and amorphous phases of a Class F fly ash.* Cement and Concrete Research, 2010. **40**(1): p. 146-156.
84. Fernández-Jiménez, A., A. Palomo, and M. Criado, *Microstructure development of alkali-activated fly ash cement: a descriptive model.* Cement and Concrete Research, 2005. **35**(6): p. 1204-1209.
85. Kumar, S. and R. Kumar, *Mechanical activation of fly ash: Effect on reaction, structure and properties of resulting geopolymer.* Ceramics International, 2011. **37**(2): p. 533-541.
86. Palomo, A., M.W. Grutzeck, and M.T. Blanco, *Alkali-activated fly ashes: A cement for the future.* Cement and Concrete Research, 1999. **29**(8): p. 1323-1329.
87. Winnefeld, F., et al., *Assessment of phase formation in alkali activated low and high calcium fly ashes in building materials.* Construction and Building Materials, 2010. **24**(6): p. 1086-1093.
88. Swanepoel, J.C. and C.A. Strydom, *Utilisation of fly ash in a geopolymeric material.* Applied Geochemistry, 2002. **17**(8): p. 1143-1148.

89. Bakharev, T., *Geopolymeric materials prepared using Class F fly ash and elevated temperature curing.* Cement and Concrete Research, 2005. **35**(6): p. 1224-1232.
90. Komljenovic, M., Z. Bascarevic, and V. Bradic, *Mechanical and microstructural properties of alkali-activated fly ash geopolymers.* J Hazard Mater, 2010. **181**(1-3): p. 35-42.
91. Puertas, F., et al., *Alkali-activated fly ash slag cements Strength behaviour and hydration products.* Cement and Concrete Research, 2000. **30**: p. 1625-1632.
92. Snellings, R., G. Mertens, and J. Elsen, *Supplementary cementitious materials.* Reviews in Mineralogy and Geochemistry, 2012. **74**(1): p. 211-278.
93. Badogiannis, E., G. Kakali, and S. Tsivilis, *Metakaolin as supplementary cementitious material.* Journal of Thermal Analysis and Calorimetry, 2005. **81**(2): p. 457-462.
94. Rocha, J., J.M. Adams, and J. Klinowski, *The rehydration of metakaolinite to kaolinite: Evidence from solid-state NMR and cognate techniques.* Journal of Solid State Chemistry, 1990. **89**(2): p. 260-274.
95. Provis, J.L. and J.S.J. van Deventer, *5. Nanostructure/Microstructure of Metakaolin Geopolymers*, in *Geopolymers - Structure, Processing, Properties and Industrial Applications*. Woodhead Publishing.
96. Palomo, A., et al., *Chemical stability of cementitious materials based on metakaolin.* Cement and Concrete Research, 1999. **29**(7): p. 997-1004.
97. Davidovits, J., *Synthetic mineral polymer compound of the silicoaluminates family and preparation process*. 1984, Google Patents.
98. Provis, J.L. and J.S.J. van Deventer, *3. Geopolymer Precursor Design*, in *Geopolymers - Structure, Processing, Properties and Industrial Applications*. Woodhead Publishing.
99. Zuhua, Z., et al., *Role of water in the synthesis of calcined kaolin-based geopolymer.* Applied Clay Science, 2009. **43**(2): p. 218-223.
100. Perera, D.S., et al., *Influence of curing schedule on the integrity of geopolymers.* Journal of Materials Science, 2006. **42**(9): p. 3099-3106.
101. Kuenzel, C., et al., *Ambient Temperature Drying Shrinkage and Cracking in Metakaolin-Based Geopolymers.* Journal of the American Ceramic Society, 2012. **95**(10): p. 3270-3277.
102. Zhang, Z., et al., *Using fly ash to partially substitute metakaolin in geopolymer synthesis.* Applied Clay Science, 2014. **88–89**(0): p. 194-201.
103. Rowles, M. and B. O'connor, *Chemical optimisation of the compressive strength of aluminosilicate geopolymers synthesised by sodium silicate activation of metakaolinite.* journal of Materials Chemistry, 2003. **13**(5): p. 1161-1165.
104. Williams, R.P., R.D. Hart, and A. van Riessen, *Quantification of the Extent of Reaction of Metakaolin-Based Geopolymers Using X-Ray Diffraction, Scanning Electron Microscopy, and Energy-Dispersive Spectroscopy.* Journal of the American Ceramic Society, 2011. **94**(8): p. 2663-2670.
105. Steveson, M. and K. Sagoe-Crentsil, *Relationships between composition, structure and strength of inorganic polymers-Part II Fly ash-derived inorganic polymers.* Journal of Materials Science, 2005. **40**(16): p. 4247-4259.

106. Kovalchuk, G., A. Fernández-Jiménez, and A. Palomo, *Alkali-activated fly ash: Effect of thermal curing conditions on mechanical and microstructural development – Part II.* Fuel, 2007. **86**(3): p. 315-322.
107. Criado, M., A. Palomo, and A. Fernandezjimenez, *Alkali activation of fly ashes. Part 1: Effect of curing conditions on the carbonation of the reaction products.* Fuel, 2005. **84**(16): p. 2048-2054.
108. Fletcher, R.A., et al., *The composition range of aluminosilicate geopolymers.* Journal of the European Ceramic Society, 2005. **25**(9): p. 1471-1477.
109. Zhang, M., et al., *Experimental feasibility study of geopolymer as the next-generation soil stabilizer.* Construction and Building Materials, 2013. **47**: p. 1468-1478.
110. Rattanasak, U. and P. Chindaprasirt, *Influence of NaOH solution on the synthesis of fly ash geopolymer.* Minerals Engineering, 2009. **22**(12): p. 1073-1078.
111. Lyu, S.-J., et al., *Main factors affecting mechanical characteristics of geopolymer revealed by experimental design and associated statistical analysis.* Construction and Building Materials, 2013. **43**(0): p. 589-597.
112. Nasab, G.M., F. Golestanifard, and K.J.D. MacKenzie, *The Effect of the SiO2/Na2O Ratio in the Structural Modification of Metakaolin-Based Geopolymers Studied by XRD, FTIR and MAS-NMR.* Journal of Ceramic Science and Technology, 2014. **5**(3): p. 185-192.
113. Chen, C., et al., *Kinetics of fly ash geopolymerization.* Journal of Materials Science, 2010. **46**(9): p. 3073-3083.
114. Lloyd, R., J. Provis, and J.J. van Deventer, *Microscopy and microanalysis of inorganic polymer cements. 2: the gel binder.* Journal of Materials Science, 2009. **44**(2): p. 620-631.
115. Rowles, M.R. and B.H. O'Connor, *Chemical and Structural Microanalysis of Aluminosilicate Geopolymers Synthesized by Sodium Silicate Activation of Metakaolinite.* Journal of the American Ceramic Society, 2009. **92**(10): p. 2354-2361.
116. Jaggi, N. and D.R. Vij, *FOURIER TRANSFORM INFRARED SPECTROSCOPY*, in *Handbook of Applied Solid State Spectroscopy*, D.R. Vij, Editor. 2006, Springer US. p. 411-450.
117. García-Lodeiro, I., et al., *Effect of Calcium Additions on N-A-S-H Cementitious Gels.* Journal of the American Ceramic Society, 2010.
118. Criado, M., A. Fernández-Jiménez, and A. Palomo, *Alkali activation of fly ash: Effect of the SiO2/Na2O ratio.* Microporous and Mesoporous Materials, 2007. **106**(1-3): p. 180-191.
119. Ismail, I., et al., *Drying-induced changes in the structure of alkali-activated pastes.* Journal of Materials Science, 2013. **48**(9): p. 3566-3577.
120. Guo, X., H. Shi, and W.A. Dick, *Compressive strength and microstructural characteristics of class C fly ash geopolymer.* Cement and Concrete Composites, 2010. **32**(2): p. 142-147.
121. Liew, Y.M., et al., *Optimization of solids-to-liquid and alkali activator ratios of calcined kaolin geopolymeric powder.* Construction and Building Materials, 2012. **37**: p. 440-451.

122. Asadi, M., et al., *Synthesis and microstructural properties of a geopolymer cement with high silica materials.* Journal of Ceramic Processing Research, 2012. **13**(4): p. 425-428.
123. Zhang, Z., et al., *Quantitative kinetic and structural analysis of geopolymers. Part 1. The activation of metakaolin with sodium hydroxide.* Thermochimica Acta, 2012. **539**: p. 23-33.
124. Zhang, Z., et al., *Quantitative kinetic and structural analysis of geopolymers. Part 2. Thermodynamics of sodium silicate activation of metakaolin.* Thermochimica Acta, 2013. **565**(0): p. 163-171.
125. Fernández-Jiménez, A. and A. Palomo, *Composition and microstructure of alkali activated fly ash binder: Effect of the activator.* Cement and Concrete Research, 2005. **35**(10): p. 1984-1992.
126. Yunsheng, Z., S. Wei, and L. Zongjin, *Composition design and microstructural characterization of calcined kaolin-based geopolymer cement.* Applied Clay Science, 2010. **47**(3-4): p. 271-275.
127. Rees, C.A., et al., *In Situ ATR-FTIR Study of the Early Stages of Fly Ash Geopolymer Gel Formation.* Langmuir, 2007. **23**(17): p. 9076-9082.
128. Lyu, S.-J., et al., *Main factors affecting mechanical characteristics of geopolymer revealed by experimental design and associated statistical analysis.* Construction and Building Materials, 2013. **43**: p. 589-597.
129. Prud'homme, E., et al., *Defining existence domains in geopolymers through their physicochemical properties.* Applied Clay Science, 2013. **73**(0): p. 26-34.
130. Lyu, S.-J., et al., *Microstructure of geopolymer accounting for associated mechanical characteristics under various stress states.* Cement and Concrete Research, 2013. **54**: p. 199-207.
131. Jozić1, D., et al., *INSITU SAXS WAXS STUDY OF THE DEVELOPING PROCESS OF GEOPOLYMER STRUCTURES*, in *ECCM15 - 15TH EUROPEAN CONFERENCE ON COMPOSITE MATERIALS*. 2012: Venice, Italy.
132. Rahier, H., et al., *Reaction mechanism, kinetics and high temperature transformations of geopolymers.* Journal of Materials Science, 2007. **42**(9): p. 2982-2996.
133. Gao, K., et al., *Effects SiO2/Na2O molar ratio on mechanical properties and the microstructure of nano-SiO2 metakaolin-based geopolymers.* Construction and Building Materials, 2014. **53**(0): p. 503-510.
134. Rees, C.A., *Mechanisms and kinetics of gel formation in geopolymers*. 2007, The University of Melbourne.
135. Bass, J.L. and G.L. Turner, *Anion Distributions in Sodium Silicate Solutions. Characterization by 29SI NMR and Infrared Spectroscopies, and Vapor Phase Osmometry.* The Journal of Physical Chemistry B, 1997. **101**(50): p. 10638-10644.
136. Singh, P., T. Bastow, and M. Trigg, *Structural studies of geopolymers by 29Si and 27Al MAS-NMR.* Journal of Materials Science, 2005. **40**(15): p. 3951-3961.
137. Skvara, F., et al., *Material and structural characterization of alkali activated low-calcium brown coal fly ash.* J Hazard Mater, 2009. **168**(2-3): p. 711-20.
138. Barbosa, V.F.F., K.J.D. MacKenzie, and C. Thaumaturgo, *Synthesis and characterisation of materials based on inorganic polymers of alumina and silica:*

sodium polysialate polymers. International Journal of Inorganic Materials, 2000. **2**(4): p. 309-317.
139. Engelhardt, G. and D. Michel, *High-resolution solid-state NMR of silicates and zeolites*. Other Information: From review in Analytical Chemistry, Vol. 60, No. 18 (15 Sep 1988). 1987. Medium: X; Size: Pages: 499.
140. Criado, M., A. Fernández-Jiménez, and A. Palomo, *Alkali activation of fly ash. Part III: Effect of curing conditions on reaction and its graphical description.* Fuel, 2010. **89**(11): p. 3185-3192.
141. Duxson, P., et al., *29Si NMR Study of Structural Ordering in Aluminosilicate Geopolymer Gels.* Langmuir, 2005. **21**(7): p. 3028-3036.
142. Fernández-Jiménez, A., et al., *Quantitative determination of phases in the alkaline activation of fly ash. Part II: Degree of reaction.* Fuel, 2006. **85**(14-15): p. 1960-1969.
143. Ma, Y., J. Hu, and G. Ye, *The pore structure and permeability of alkali activated fly ash.* Fuel, 2013. **104**: p. 771-780.
144. Lloyd, R.R., et al., *Spatial distribution of pores in fly ash-based inorganic polymer gels visualised by Wood's metal intrusion.* Microporous and Mesoporous Materials, 2009. **126**(1–2): p. 32-39.
145. Kriven, W.M., J.L. Bell, and M. Gordon, *Microstructure and Nanoporosity of as-Set Geopolymers*, in *Mechanical Properties and Performance of Engineering Ceramics II: Ceramic Engineering and Science Proceedings*. 2008, John Wiley & Sons, Inc. p. 491-503.
146. Collins, F. and J.G. Sanjayan, *Effect of pore size distribution on drying shrinking of alkali-activated slag concrete.* Cement and Concrete Research, 2000. **30**(9): p. 1401-1406.
147. Provis, J.L., et al., *X-ray microtomography shows pore structure and tortuosity in alkali-activated binders.* Cement and Concrete Research, 2012. **42**(6): p. 855-864.
148. Li, R., et al., *Characterization of multi-scale porous structure of fly ash/phosphate geopolymer hollow sphere structures: From submillimeter to nano-scale.* Micron, 2015. **68**(0): p. 54-58.
149. Pelisser, F., et al., *Micromechanical characterization of metakaolin-based geopolymers.* Construction and Building Materials, 2013. **49**(0): p. 547-553.
150. Škvára, F., et al., *Microstructure of geopolymer materials based on fly ash.* Ceramics-Silikaty, 2006. **50**(4): p. 208-215.
151. Steinerova, M. and J. Schweigstillova, *POROUS MICROSTRUCTURE OF THE INTERFACIAL TRANSITION ZONE IN GEOPOLYMER COMPOSITES.* Ceramics–Silikáty, 2013. **57**(4): p. 328-335.
152. Jennings, H.M., et al., *A multi-technique investigation of the nanoporosity of cement paste.* Cement and Concrete Research, 2007. **37**(3): p. 329-336.
153. Constantinides, G. and F.-J. Ulm, *The nanogranular nature of C–S–H.* Journal of the Mechanics and Physics of Solids, 2007. **55**(1): p. 64-90.
154. Ulm, F.-J., et al., *Statistical Indentation Techniques for Hydrated Nanocomposites: Concrete, Bone, and Shale.* Journal of the American Ceramic Society, 2007. **90**(9): p. 2677-2692.

155. Beleña, I. and W. Zhu, *Nanoindentation Study of Na-Geopolymers Exposed to High Temperatures*, in *Nanotechnology in Construction 3*, Z. Bittnar, et al., Editors. 2009, Springer Berlin Heidelberg. p. 169-174.
156. Němeček, J., V. Šmilauer, and L. Kopecký, *Nanoindentation characteristics of alkali-activated aluminosilicate materials.* Cement and Concrete Composites, 2011. **33**(2): p. 163-170.
157. Glukhovsky, V.D., *Soil silicates*, in *Gosstroyizdat*. 1959: Kiev. p. 154pp.
158. Provis, J.L. and J.S.J. van Deventer, *Geopolymerisation kinetics. 2. Reaction kinetic modelling.* Chemical Engineering Science, 2007. **62**(9): p. 2318-2329.
159. Swaddle, T.W., *Silicate complexes of aluminum(III) in aqueous systems.* Coordination Chemistry Reviews, 2001. **219–221**(0): p. 665-686.
160. Swaddle, T.W., J. Salerno, and P.A. Tregloan, *Aqueous aluminates, silicates, and aluminosilicates.* Chemical Society Reviews, 1994. **23**(5): p. 319-325.
161. Duxson, P., et al., *Geopolymer technology: the current state of the art.* Journal of Materials Science, 2006. **42**(9): p. 2917-2933.
162. Provis, J. and J.J. van Deventer, *Direct measurement of the kinetics of geopolymerisation by in-situ energy dispersive X-ray diffractometry.* Journal of Materials Science, 2007. **42**(9): p. 2974-2981.
163. White, C.E., et al., *Evolution of Local Structure in Geopolymer Gels: AnIn SituNeutron Pair Distribution Function Analysis.* Journal of the American Ceramic Society, 2011. **94**(10): p. 3532-3539.
164. White, C.E., et al., *In situ synchrotron X-ray pair distribution function analysis of the early stages of gel formation in metakaolin-based geopolymers.* Applied Clay Science, 2013. **73**: p. 17-25.
165. Rees, C.A., et al., *Attenuated total reflectance fourier transform infrared analysis of fly ash geopolymer gel aging.* Langmuir, 2007. **23**(15): p. 8170-8179.
166. Fernández-Jiménez, A. and A. Palomo, *Mid-infrared spectroscopic studies of alkali-activated fly ash structure.* Microporous and Mesoporous Materials, 2005. **86**(1-3): p. 207-214.
167. Lee, W.K.W. and J.S.J. van Deventer, *Use of Infrared Spectroscopy to Study Geopolymerization of Heterogeneous Amorphous Aluminosilicates.* Langmuir, 2003. **19**(21): p. 8726-8734.
168. Hajimohammadi, A., J.L. Provis, and J.S.J. van Deventer, *Effect of Alumina Release Rate on the Mechanism of Geopolymer Gel Formation.* Chemistry of Materials, 2010. **22**(18): p. 5199-5208.
169. Fernández-Jiménez, A., et al., *The role played by the reactive alumina content in the alkaline activation of fly ashes.* Microporous and Mesoporous Materials, 2006. **91**(1-3): p. 111-119.
170. Criado, M., et al., *Effect of the SiO2/Na2O ratio on the alkali activation of fly ash. Part II: 29Si MAS-NMR Survey.* Microporous and Mesoporous Materials, 2008. **109**(1-3): p. 525-534.
171. Davidovits, J., *Geopolymers: Inorganic Polymeric New Materials.* Journal of Thermal Analysis, 1991. **37**: p. 1633-1656.

172. Silva, P.D., K. Sagoe-Crenstil, and V. Sirivivatnanon, *Kinetics of geopolymerization: Role of Al2O3 and SiO2.* Cement and Concrete Research, 2007. **37**(4): p. 512-518.
173. Cioffi, R., L. Maffucci, and L. Santoro, *Optimization of geopolymer synthesis by calcination and polycondensation of a kaolinitic residue.* Resources, Conservation and Recycling, 2003. **40**(1): p. 27-38.
174. Sindhunata, et al., *Effect of curing temperature and silicate concentration on fly-ash-based geopolymerization.* Industrial & Engineering Chemistry Research, 2006. **45**(10): p. 3559-3568.
175. Lee, W.K.W. and J.S.J. van Deventer, *Structural reorganisation of class F fly ash in alkaline silicate solutions.* Colloids and Surfaces A: Physicochemical and Engineering Aspects, 2002. **211**(1): p. 49-66.
176. Criado, M., et al., *An XRD study of the effect of the SiO2/Na2O ratio on the alkali activation of fly ash.* Cement and Concrete Research, 2007. **37**(5): p. 671-679.
177. De Silva, P. and K. Sagoe-Crenstil, *Medium-term phase stability of Na2O–Al2O3–SiO2–H2O geopolymer systems.* Cement and Concrete Research, 2008. **38**(6): p. 870-876.
178. Kamseu, E., et al., *Design of inorganic polymer cements: Effects of matrix strengthening on microstructure.* Construction and Building Materials, 2013. **38**: p. 1135-1145.
179. Steveson, M. and K. Sagoe-Crentsil, *Relationships between composition, structure and strength of inorganic polymers-Part I Metakaolin-derived inorganic polymers.* Journal of Materials Science, 2005. **40**(8): p. 2023-2036.
180. Rahier, H., et al., *Low-temperature synthesized aluminosilicate glasses: Part III Influence of the composition of the silicate solution on production, structure and properties.* Journal of Materials Science, 1997. **32**(9): p. 2237-2247.
181. Phair, J.W. and J.S.J. Van Deventer, *Effect of silicate activator pH on the leaching and material characteristics of waste-based inorganic polymers.* Minerals Engineering, 2001. **14**(3): p. 289-304.
182. van Jaarsveld, J.G.S. and J.S.J. van Deventer, *Effect of the Alkali Metal Activator on the Properties of Fly Ash-Based Geopolymers.* Industrial & Engineering Chemistry Research, 1999. **38**(10): p. 3932-3941.
183. Cheng, T.W. and J.P. Chiu, *Fire-resistant geopolymer produced by granulated blast furnace slag.* Minerals Engineering, 2003. **16**(3): p. 205-210.
184. Hos, J.P., P.G. McCormick, and L.T. Byrne, *Investigation of a synthetic aluminosilicate inorganic polymer.* Journal of Materials Science, 2002. **37**(11): p. 2311-2316.
185. Mo, B.-h., et al., *Effect of curing temperature on geopolymerization of metakaolin-based geopolymers.* Applied Clay Science, 2014. **99**(0): p. 144-148.
186. Kada-Benameur, H., E. Wirquin, and B. Duthoit, *Determination of apparent activation energy of concrete by isothermal calorimetry.* Cement and concrete research, 2000. **30**(2): p. 301-305.
187. Granizo, N., A. Palomo, and A. Fernandez-Jiménez, *Effect of temperature and alkaline concentration on metakaolin leaching kinetics.* Ceramics International, 2014. **40**(7, Part A): p. 8975-8985.

188. Palomo, Á., et al., *Alkaline Activation of Fly Ashes: NMR Study of the Reaction Products.* Journal of the American Ceramic Society, 2004. **87**(6): p. 1141-1145.
189. Andini, S., et al., *Coal fly ash as raw material for the manufacture of geopolymer-based products.* Waste Manag, 2008. **28**(2): p. 416-23.
190. Muñiz-Villarreal, M.S., et al., *The effect of temperature on the geopolymerization process of a metakaolin-based geopolymer.* Materials Letters, 2011. **65**(6): p. 995-998.
191. Yunsheng, Z. and S. Wei, *Semi-empirical AM1 calculations on 6-memebered alumino-silicate rings model: implications for dissolution process of metakaoline in alkaline solutions.* Journal of Materials Science, 2007. **42**(9): p. 3015-3023.
192. Yunsheng, Z., et al., *Study of ion cluster reorientation process of geopolymerisation reaction using semi-empirical AM1 calculations.* Cement and Concrete Research, 2009. **39**(12): p. 1174-1179.
193. Yunsheng, Z., et al. *Study of polycondensation process of metakaolin-based geopolymeric cement using semi-empirical AM1 calculations*. Advances in Cement Research, 2009. **21**, 67-73.
194. Yang, C.-S., J.M. Mora-Fonz, and C.R.A. Catlow, *Stability and Structures of Aluminosilicate Clusters.* The Journal of Physical Chemistry C, 2011. **115**(49): p. 24102-24114.
195. Yang, C.-S., J.M. Mora-Fonz, and C.R.A. Catlow, *Modeling the Polymerization of Aluminosilicate Clusters.* The Journal of Physical Chemistry C, 2012. **116**(42): p. 22121-22128.
196. White, C.E., et al., *Density functional modelling of silicate and aluminosilicate dimerisation solution chemistry.* Dalton Trans, 2011. **40**(6): p. 1348-55.
197. White, C.E., et al., *Molecular mechanisms responsible for the structural changes occurring during geopolymerization: Multiscale simulation.* AIChE Journal, 2012. **58**(7): p. 2241-2253.
198. Provis, J.L., et al., *Modeling Speciation in Highly Concentrated Alkaline Silicate Solutions.* Industrial & Engineering Chemistry Research, 2005. **44**(23): p. 8899-8908.
199. Thokchom, S., P. Ghosh, and S. Ghosh, *Effect of Na2O content on durability of geopolymer mortars in sulphuric acid.* International Journal of Chemical and Biomolecular Engineering, 2009. **2**(1): p. 20-25.
200. Thokchom, S., P. Ghosh, and S. Ghosh, *Resistance of fly ash based geopolymer mortars in sulfuric acid.* ARPN Journal of Engineering and Applied Sciences, 2009. **4**.
201. Allahverdi, A. and F. Skvara, *Sulfuric acid attack on hardened paste of geopolymer cements Part 1. Mechanism of corrosion at relatively high concentrations.* Ceramics-Silikaty, 2005. **49**(4): p. 225-229.
202. Allahverdi, A. and F. Skvara, *Sulfuric acid attack on hardened paste of geopolymer cements - part 2. Corrosion mechanism at mild and relatively low concentrations.* Ceramics-Silikaty, 2006. **50**(1): p. 1-4.
203. Lloyd, R.R., J.L. Provis, and J.S.J. Deventer, *Acid resistance of inorganic polymer binders. 1. Corrosion rate.* Materials and Structures, 2011. **45**(1-2): p. 1-14.

204. Zhang, H.Y., et al., *Development of metakaolin–fly ash based geopolymers for fire resistance applications.* Construction and Building Materials, 2014. **55**: p. 38-45.
205. Zhao, R. and J.G. Sanjayan, *Geopolymer and Portland cement concretes in simulated fire.* Magazine of concrete research, 2011. **63**(3): p. 163-173.
206. Rickard, W.D.A., et al., *Assessing the suitability of three Australian fly ashes as an aluminosilicate source for geopolymers in high temperature applications.* Materials Science and Engineering: A, 2011. **528**(9): p. 3390-3397.
207. Kong, D.L.Y. and J.G. Sanjayan, *Damage behavior of geopolymer composites exposed to elevated temperatures.* Cement and Concrete Composites, 2008. **30**(10): p. 986-991.
208. Kong, D.L.Y., J.G. Sanjayan, and K. Sagoe-Crentsil, *Comparative performance of geopolymers made with metakaolin and fly ash after exposure to elevated temperatures.* Cement and Concrete Research, 2007. **37**(12): p. 1583-1589.
209. Kong, D.Y., J. Sanjayan, and K. Sagoe-Crentsil, *Factors affecting the performance of metakaolin geopolymers exposed to elevated temperatures.* Journal of Materials Science, 2008. **43**(3): p. 824-831.
210. Davidovits, J. *Geopolymer chemistry and properties*. in *Geopolymer*. 1988.
211. Buchwald, A., R. Oesterheld, and H. Hilbig, *Incorporation of Aluminate into Silicate Gels and its Effect on the Foamability and Water Resistance.* Journal of the American Ceramic Society, 2010. **93**(10): p. 3370-3376.
212. Sukhanevich, M.V. and S.G. Guzii, *The Effect of Technological Factors on Properties of Alkali Aluminosilicate Systems Used for Preparation of Fireproof Coatings.* Refractories and Industrial Ceramics, 2004. **45**(3): p. 217-219.
213. Temuujin, J., et al., *Fly ash based geopolymer thin coatings on metal substrates and its thermal evaluation.* J Hazard Mater, 2010. **180**(1-3): p. 748-52.
214. Porcherie, O. and E. Pershikova, *Pumpable geopolymer formulation for oilfield application*. 2009, Google Patents.
215. Barlet-Gouedard, V., B. Zusatz-Ayache, and O. Porcherie, *Geopolymer composition and application for carbon dioxide storage*. 2010, Google Patents.
216. Rego, S.R., et al., *Application of Geopolymeric Adhesives in Ceramic Systems Subjected to Cyclic Temperature Environments.* The Journal of Adhesion, 2013. **90**(1): p. 120-133.
217. Yunsheng, Z., et al., *Impact properties of geopolymer based extrudates incorporated with fly ash and PVA short fiber.* Construction and Building Materials, 2008. **22**(3): p. 370-383.
218. Vaidya, S. and E.N. Allouche, *Strain sensing of carbon fiber reinforced geopolymer concrete.* Materials and Structures, 2011. **44**(8): p. 1467-1475.
219. Tang, C., et al., *Strength and mechanical behavior of short polypropylene fiber reinforced and cement stabilized clayey soil.* Geotextiles and Geomembranes, 2007. **25**(3): p. 194-202.
220. Reed, M., W. Lokuge, and W. Karunasena, *Fibre-reinforced geopolymer concrete with ambient curing for in situ applications.* Journal of Materials Science, 2014. **49**(12): p. 4297-4304.
221. Schneider, M., et al., *Sustainable cement production—present and future.* Cement and Concrete Research, 2011. **41**(7): p. 642-650.

222. Josa, A., et al., *Comparative analysis of available life cycle inventories of cement in the EU.* Cement and Concrete Research, 2004. **34**(8): p. 1313-1320.
223. Yamamoto, J.K., et al., *Environmental impact reduction on the production of blended portland cement in Brazil.* Environmental Geosciences, 1997. **4**(4): p. 192-206.
224. Humphreys, K. and M. Mahasenan, *Substudy 8: climate change. In: Toward a sustainable cement industry; 2002.* 2002. p. 34.
225. Flower, D.M. and J. Sanjayan, *Green house gas emissions due to concrete manufacture.* The International Journal of Life Cycle Assessment, 2007. **12**(5): p. 282-288.
226. Turner, L.K. and F.G. Collins, *Carbon dioxide equivalent (CO2-e) emissions: A comparison between geopolymer and OPC cement concrete.* Construction and Building Materials, 2013. **43**(0): p. 125-130.
227. Gäbel, K. and A.-M. Tillman, *Simulating operational alternatives for future cement production.* Journal of Cleaner Production, 2005. **13**(13–14): p. 1246-1257.
228. Books, D., *An Economic and Embodied Energy Comparison of Geo-polymer, Blended Cement and Traditional Concretes.*
229. Perez Fernandez, N., *The influence of construction materials on life-cycle energy use and carbon dioxide emissions of medium size commercial buildings.* 2008.
230. Al Bakri Abdullah, M.M., et al., *Study on Fly Ash Based Geopolymer for Coating Applications.* Advanced Materials Research, 2013. **686**: p. 227-233.
231. Temuujin, J., et al., *Thermal properties of spray-coated geopolymer-type compositions.* Journal of Thermal Analysis and Calorimetry, 2011. **107**(1): p. 287-292.
232. Van Jaarsveld, J.G.S., J.S.J. Van Deventer, and L. Lorenzen, *The potential use of geopolymeric materials to immobilise toxic metals: Part I. Theory and applications.* Minerals Engineering, 1997. **10**(7): p. 659-669.
233. Pacheco-Torgal, F., J. Castro-Gomes, and S. Jalali, *Investigations about the effect of aggregates on strength and microstructure of geopolymeric mine waste mud binders.* Cement and Concrete Research, 2007. **37**(6): p. 933-941.
234. Khale, D. and R. Chaudhary, *Mechanism of geopolymerization and factors influencing its development: a review.* Journal of Materials Science, 2007. **42**(3): p. 729-746.
235. Barbosa, V.F., K.J. MacKenzie, and C. Thaumaturgo, *Synthesis and characterisation of materials based on inorganic polymers of alumina and silica: sodium polysialate polymers.* International Journal of Inorganic Materials, 2000. **2**(4): p. 309-317.
236. Pacheco-Torgal, F., et al., *Composition, strength and workability of alkali-activated metakaolin based mortars.* Construction and Building Materials, 2011. **25**(9): p. 3732-3745.
237. Buchwald, A., et al., *The suitability of thermally activated illite/smectite clay as raw material for geopolymer binders.* Applied Clay Science, 2009. **46**(3): p. 300-304.

238. Najafi Kani, E., A. Allahverdi, and J.L. Provis, *Efflorescence control in geopolymer binders based on natural pozzolan.* Cement and Concrete Composites, 2012. **34**(1): p. 25-33.
239. Fernandez-Jimenez, A., I. Garc á-Lodeiro, and A. Palomo, *Durability of alkali-activated fly ash cementitious materials.* Journal of Materials Science, 2006. **42**(9): p. 3055-3065.
240. Cheng, T. and J. Chiu, *Fire-resistant geopolymer produced by granulated blast furnace slag.* Minerals Engineering, 2003. **16**(3): p. 205-210.
241. Dimas, D.D., I.P. Giannopoulou, and D. Panias, *UTILIZATION OF ALUMINA RED MUD FOR SYNTHESIS OF INORGANIC POLYMERIC MATERIALS.* Mineral Processing & Extractive Metall. Rev., 2009. **30**: p. 211-239.
242. Detphan, S. and P. Chindaprasirt, *Preparation of fly ash and rice husk ash geopolymer.* International Journal of Minerals, Metallurgy and Materials, 2009. **16**(6): p. 720-726.
243. Joshi, R.C., *Fly ash in concrete: production, properties and uses*. Vol. 2. 1997: Taylor & Francis.
244. Mukherjee, A.B., et al., *Mercury flow via coal and coal utilization by-products: A global perspective.* Resources, Conservation and Recycling, 2008. **52**(4): p. 571-591.
245. ASTMC618, *Standard Specification for Coal Fly Ash and Raw or Calcined Natural Pozzolan for Use in Concrete*. 2013, ASTM International.
246. Klauber, C., M. Gr äfe, and G. Power, *Bauxite residue issues: II. options for residue utilization.* Hydrometallurgy, 2011. **108**(1-2): p. 11-32.
247. Kumar, A. and S. Kumar, *Development of paving blocks from synergistic use of red mud and fly ash using geopolymerization.* Construction and Building Materials, 2013. **38**: p. 865-871.
248. Gr äfe, M. and C. Klauber, *Bauxite residue issues: IV. Old obstacles and new pathways for in situ residue bioremediation.* Hydrometallurgy, 2011. **108**(1-2): p. 46-59.
249. Badanoiu, A. and G. Voicu, *Influence of Raw Materials Characteristics and Processing Parameters on The Strength of Geopolymer Cements Based on Fly Ash.* Environmental Engineering and Management Journal, 2011. **10**(5): p. 673-681.
250. Triola, M.F., *Elementary Statistics*. 10 ed. 2007: Addison Wesley.
251. Ahmari, S., et al., *Production of geopolymeric binder from blended waste concrete powder and fly ash.* Construction and Building Materials, 2012. **35**: p. 718-729.
252. ASTMC150, *Standard Specification for Portland Cement*. 2012, ASTM International.
253. Chindaprasirt, P., U. Rattanasak, and S. Taebuanhuad, *Resistance to acid and sulfate solutions of microwave-assisted high calcium fly ash geopolymer.* Materials and Structures, 2012. **46**(3): p. 375-381.
254. Inada, M., et al., *Microwave-assisted zeolite synthesis from coal fly ash in hydrothermal process.* Fuel, 2005.
255. Diaz, E.I., E.N. Allouche, and S. Eklund, *Factors affecting the suitability of fly ash as source material for geopolymers.* Fuel, 2010. **89**(5): p. 992-996.

256. Provis, J.L. and J.S.J. van Deventer, *Geopolymerisation kinetics. 1. In situ energy-dispersive X-ray diffractometry.* Chemical Engineering Science, 2007. **62**(9): p. 2309-2317.
257. Xu, H. and J.S.J. van Deventer, *The effect of alkali metals on the formation of geopolymeric gels from alkali-feldspars.* Colloids and Surfaces A: Physicochemical and Engineering Aspects, 2003. **216**(1–3): p. 27-44.
258. ASTMC191-13, *Standard Test Methods for Time of Setting of Hydraulic Cement by Vicat Needle*. 2013, ASTM International.
259. Sweet, J. and W. White, *Study of sodium silicate glasses and liquids by infrared reflectance spectroscopy.* Physics and Chemistry of Glasses, 1969. **10**(6): p. 246-&.
260. Roy, B.N., *Infrared Spectroscopy of Lead and Alkaline-Earth Aluminosilicate Glasses.* Journal of the American Ceramic Society, 1990. **73**(4): p. 846-855.
261. Flanigen, E.M., *Structural analysis by infrared spectroscopy*, in *Zeolite Chemistry and Catalysis*, J.A. Rabo, Editor. 1976, American Chemical Society: Washington, DC. p. 80-117.
262. Celik, O., E. Damci, and S. Piskin, *Characterization of fly ash and it effects on the compressive strength properties of Portland cement.* Indian Journal of Engineering and Materials Sciences, 2008. **15**(5): p. 433.
263. Lee, W.K.W. and J.S.J. van Deventer, *The effects of inorganic salt contamination on the strength and durability of geopolymers.* Colloids and Surfaces A: Physicochemical and Engineering Aspects, 2002. **211**(2–3): p. 115-126.
264. Adriano, D.C., et al., *Utilization and Disposal of Fly Ash and Other Coal Residues in Terrestrial Ecosystems: A Review1*. J. Environ. Qual., 1980. **9**(3): p. 333-344.
265. ALLAHVERDI, A. and F. SKVARA, *Nitric acid attack on hardened paste of geopolymeric cements. Part 1.* Ceramics, 2001. **45**(3): p. 81-88.
266. Fernández-Jiménez, A. and F. Puertas, *The alkali–silica reaction in alkali-activated granulated slag mortars with reactive aggregate.* Cement and Concrete Research, 2002. **32**(7): p. 1019-1024.
267. García-Lodeiro, I., A. Palomo, and A. Fernández-Jiménez, *Alkali–aggregate reaction in activated fly ash systems.* Cement and Concrete Research, 2007. **37**(2): p. 175-183.
268. *Impact of Alkali Silica Reaction on Fly Ash-Based Geopolymer Concrete.* Journal of Materials in Civil Engineering, 2013. **25**(1): p. 131-139.
269. Jo, B.-w., S.-k. Park, and J.-b. Park, *Properties of concrete made with alkali-activated fly ash lightweight aggregate (AFLA).* Cement and Concrete Composites, 2007. **29**(2): p. 128-135.
270. Fu, Y., L. Cai, and W. Yonggen, *Freeze–thaw cycle test and damage mechanics models of alkali-activated slag concrete.* Construction and Building Materials, 2011. **25**(7): p. 3144-3148.
271. Xie, S., L. Qi, and D. Zhou, *Investigation of the effects of acid rain on the deterioration of cement concrete using accelerated tests established in laboratory.* Atmospheric Environment, 2004. **38**(27): p. 4457-4466.

272. De Belie, N., et al., *Durability of Building Materials and Components in the Agricultural Environment, Part III: Concrete Structures.* Journal of Agricultural Engineering Research, 2000. **76**(1): p. 3-16.
273. Bertron, A., J. Duchesne, and G. Escadeillas, *Degradation of cement pastes by organic acids.* Materials and Structures, 2007. **40**(3): p. 341-354.
274. Ariffin, M.A.M., et al., *Sulfuric acid resistance of blended ash geopolymer concrete.* Construction and Building Materials, 2013. **43**(0): p. 80-86.
275. ASTMC78, *Standard Test Method for Flexural Strength of Concrete (Using Simple Beam with Third-Point Loading)*. 2010.
276. Agency, E.P., *Toxicity characteristic leaching procedure: method 1311*. 2003, U.S., EPA.
277. USEPA, *PART 503—Standards for the use or disposal of sweage sludge. Electronic Code of Federal Regulations (e-CFR)*. 2007.
278. Provis, J.L., G.C. Lukey, and J.S.J. van Deventer, *Do Geopolymers Actually Contain Nanocrystalline Zeolites? A Reexamination of Existing Results.* Chemistry of Materials, 2005. **17**(12): p. 3075-3085.
279. Singh, P.S., et al., *Geopolymer formation processes at room temperature studied by 29Si and 27Al MAS-NMR.* Materials Science and Engineering: A, 2005. **396**(1–2): p. 392-402.
280. Zhu, W., et al., *Nanoindentation mapping of mechanical properties of cement paste and natural rocks.* Materials Characterization, 2007. **58**(11–12): p. 1189-1198.
281. Li, X. and B. Bhushan, *A review of nanoindentation continuous stiffness measurement technique and its applications.* Materials Characterization, 2002. **48**(1): p. 11-36.
282. Oliver, W.C. and G.M. Pharr, *An improved technique for determining hardness and elastic modulus using load and displacement sensing indentation experiments.* Journal of Materials Research, 1992. **7**(06): p. 1564-1583.
283. Constantinides, G., et al., *Grid indentation analysis of composite microstructure and mechanics: Principles and validation.* Materials Science and Engineering: A, 2006. **430**(1–2): p. 189-202.
284. White, C., et al., *The Synergy Between Total Scattering and Advanced Simulation Techniques: Quantifying Geopolymer Gel Evolution*. 2012, Los Alamos National Laboratory (LANL).
285. Feuston, B.P. and S.H. Garofalini, *Empirical three-body potential for vitreous silica.* The Journal of Chemical Physics, 1988. **89**(9): p. 5818.
286. Garofalini, S.H. and G. Martin, *Molecular Simulations of the Polymerization of Silicic Acid Molecules and Network Formation.* The Journal of Physical Chemistry, 1994. **98**(4): p. 1311-1316.
287. Rao, N.Z. and L.D. Gelb, *Molecular Dynamics Simulations of the Polymerization of Aqueous Silicic Acid and Analysis of the Effects of Concentration on Silica Polymorph Distributions, Growth Mechanisms, and Reaction Kinetics.* The Journal of Physical Chemistry B, 2004. **108**(33): p. 12418-12428.
288. VandeVondele, J., et al., *Quickstep: Fast and accurate density functional calculations using a mixed Gaussian and plane waves approach.* Computer Physics Communications, 2005. **167**(2): p. 103-128.

289. Lippert, G., J. Hutter, and M. Parrinello, *The Gaussian and augmented-plane-wave density functional method for ab initio molecular dynamics simulations.* Theoretical Chemistry Accounts, 1999. **103**(2): p. 124-140.
290. Griebel, M., S. Knapek, and G. Zumbusch, *Numerical simulation in molecular dynamics: numerics, algorithms, parallelization, applications*. Vol. 5. 2007: Springer Science & Business Media.
291. Manzano, H., et al., *A molecular dynamics study of the aluminosilicate chains structure in Al-rich calcium silicate hydrated (C-S-H) gels.* physica status solidi (a), 2008. **205**(6): p. 1324-1329.
292. Dolado, J.S., M. Griebel, and J. Hamaekers, *A Molecular Dynamics Study of Cementitious Calcium Silicate Hydrate (C-S-H) Gels.* J Am Chem Soc, 2007. **90**: p. 3938-3942.
293. Manzano, H., et al., *A molecular dynamics study of the aluminosilicate chains structure in Al-rich calcium silicate hydrate (C-S-H) gels.* Phys Status Solidi A., 2008. **205**(6): p. 1324-1329.
294. Feuston, B.P. and S.H. Garofalini, *Oligomerization in silica sols.* The Journal of Physical Chemistry, 1990. **94**(13): p. 5351-5356.
295. Stillinger, F.H. and T.A. Weber, *Computer simulation of local order in condensed phases of silicon.* Physical Review B, 1985. **31**(8): p. 5262-5271.
296. Griebel, M. and J. Hamaekers, *Molecular dynamics simulations of the mechanical properties of polyethylene-carbon nanotube composites.* Handbook of Theoretical and Computational Nanotechnology, 2005. **9**: p. 409-454.
297. Rabdel Ruiz-Salvador, A., et al., *Silicon-aluminium distribution in dehydrated calcium heulandite.* Physical Chemistry Chemical Physics, 1999. **1**(7): p. 1679-1685.
298. Malani, A., S.M. Auerbach, and P.A. Monson, *Monte Carlo Simulations of Silica Polymerization and Network Formation.* The Journal of Physical Chemistry C, 2011. **115**(32): p. 15988-16000.
299. Humphrey, W., A. Dalke, and K. Schulten, *VMD - Visual Molecular Dynamics.* J. Molec. Graphics, 1996. **14**: p. 33-38.
300. Yamahara, K. and K. Okazaki, *Molecular dynamics simulation of the structural development in sol–gel process for silica systems.* Fluid phase equilibria, 1998. **144**(1): p. 449-459.
301. Barden, L. and G. Sides, *Sample Disturbance in the Investigation of Clay Structure.* Géotechnique, 1971. **21**(3): p. 211-222.
302. Zhang, Z. and M. Tao, *Durability of Cement Stabilized Low Plasticity Soils.* Journal of Geotechnical and Geoenvironmental Engineering, 2008. **134**(2): p. 203-213.
303. Beeghly, J.H. *Recent experiences with lime-fly ash stabilization of pavement subgrade soils, base, and recycled asphalt*. 2003.
304. George, K.P., *Interim Report I, SOIL STABILIZATION FIELD TRIAL*. 2001, DEPARTMENT OF CIVIL ENGINEERING UNIVERSITY OF MISSISSIPPI.
305. Horpibulsuk, S., C. Phetchuay, and A. Chinkulkijniwat, *Soil Stabilization by Calcium Carbide Residue and Fly Ash.* Journal of Materials in Civil Engineering, 2012. **24**(2): p. 184-193.

306. Nicholson, C., et al., *Building innovation through geopolymer technology.* Chemistry in New Zealand, 2005. **69**(3): p. 10.
307. Adaska, W.S., et al. *Control of reflective cracking in cement stabilized pavements*. 2004. RILEM Publications SARL.
308. Khedari, J., P. Watsanasathaporn, and J. Hirunlabh, *Development of fibre-based soil–cement block with low thermal conductivity.* Cement and Concrete Composites, 2005. **27**(1): p. 111-116.
309. MacKenzie, K.J., et al., *Advances in understanding the synthesis mechanisms of new geopolymeric materials.* Novel Processing of Ceramics and Composites: Ceramic Transactions Series, Volume 195, 2006: p. 185-199.
310. Davidovits, J., *Geopolymer, green chemistry and sustainable development solutions: proceedings of the World Congress Geopolymer 2005*. 2005.
311. Giannopoulou, I., et al., *Utilization of metallurgical solid by-products for the development of inorganic polymeric construction materials.* Global NEST Journal, 2009. **11**(2): p. 127-136.
312. Mymrin, V.A. and A.J. Vazquez-Vaamonde, *Red mud of aluminium production waste as basic component of new construction materials.* Waste Management & Research, 2001. **19**(5): p. 465-469.
313. George, K., *Mechanism of Shrinkage Cracking of Soil-Cement Bases.* Highway research record, 1973(442).
314. Bell, F.G., *Lime stabilization of clay minerals and soils.* Engineering Geology, 1996. **42**(4): p. 223-237.
315. Maitland, C.F., et al., *Characterization of the pore structure of metakaolin-derived geopolymers by neutron scattering and electron microscopy.* Journal of Applied Crystallography, 2011. **44**(4): p. 697-707.
316. International, A., *ASTM D4318-Standard Test Methods for Liquid Limit, Plastic Limit, and Plasticity Index of Soils*. 2014.
317. International, A., *ASTM422, Standard Test Method for Particle-Size Analysis of Soils*. 2010.
318. International, A., *ASTM2487, Standard Practice for Classification of Soils for Engineering Purposes (Unified Soil Classification System)*. 2011.
319. International, A., *ASTM Standard D698, Standard Test Methods for Laboratory Compaction Characteristics of Soil Using Standard Effort (12 400 ft-lbf/ft3(600 kN-m/m3))*. 2012.
320. Horpibulsuk, S., et al., *Analysis of strength development in cement-stabilized silty clay from microstructural considerations.* Construction and Building Materials, 2010. **24**(10): p. 2011-2021.
321. International, A., *ASTM E111-04(2010), Standard Test Method for Young's Modulus, Tangent Modulus, and Chord Modulus*. 2010.
322. Smart, P. *Particle arrangements in kaolin*. in *The 15th national conference of clays and clay mineral*. 1967.
323. Ulery, A.L. and L.R. Drees, *Methods of soil analysis: mineralogical methods*. Vol. 5. 2008: ASA-CSSA-SSSA.
324. International, A., *ASTM D4609, Standard Guide for Evaluating Effectiveness of Admixtures for Soil Stabilization*. 2008.

325. Šmilauer, V., et al., *Micromechanical multiscale model for alkali activation of fly ash and metakaolin.* Journal of Materials Science, 2011. **46**(20): p. 6545-6555.
326. Nugteren, H.W., et al. *High strength geopolymers from fractionated and pulverized fly ash*. 2009. Lexington, KY, United states: Unavailable.
327. Somna, K., et al., *NaOH-activated ground fly ash geopolymer cured at ambient temperature.* Fuel, 2011. **90**(6): p. 2118-2124.
328. Williams, R.P. and A. van Riessen, *Determination of the reactive component of fly ashes for geopolymer production using XRF and XRD.* Fuel, 2010. **89**(12): p. 3683-3692.